Robust Carrier Tracking Techniques for GNSS Receivers affected by Ionospheric Scintillation

Sergi Locubiche-Serra

Universitat Autònoma de Barcelona

Ph.D. Dissertation

Programme in Electronic and Telecommunication Engineering

Robust Carrier Tracking Techniques for GNSS Receivers affected by Ionospheric Scintillation

Sergi Locubiche-Serra

Thesis Advisors: José Antonio López-Salcedo
Gonzalo Seco-Granados

Department of Telecommunications and Systems Engineering
Universitat Autònoma de Barcelona (UAB)

Bellaterra, June 2019

Abstract

Global Navigation Satellite Systems (GNSS) have become an indispensable tool in different areas in our modern society for positioning purposes using radio-frequency ranging signals. Some application examples are the positioning and navigation in ground, maritime and aviation environments, as well as their use in agriculture, surveying and precise timing and synchronization in communication systems and finances. The tracking stage is one of the core tasks within a GNSS receiver to keep aligned with the satellites and, to date, most receivers equip conventional tracking techniques with ease of implementation that suffice to operate in environments with favorable working conditions. However, in the recent years, the success of GNSS in open-sky environments has led to the emergence of applications that expand toward scenarios with harsher conditions, such as urban canyons and soft-indoor environments. The trend is to provide user mobile terminals such as smartphones with positioning capabilities in scenarios where receivers face new technological challenges owing to the abounding propagation impairments. In this sense, the so-called ionospheric scintillation is one of the issues degrading the performance of GNSS receivers, particularly in equatorial regions and at high latitudes. It introduces rapid carrier phase and signal power variations, and has a detrimental effect particularly onto the tracking stage.

The objective of this thesis is to design and develop new techniques for the robust tracking of GNSS signals affected by ionospheric scintillation disturbances. The presented approach is based on the use of Kalman filtering techniques, and the main contributions of the thesis are three. First, the analysis of ionospheric scintillation and the tracking of carrier dynamics despite the presence of the former. We design a Kalman filter with a hybrid formulation that allows the robust monitoring of both contributions separately. This arises from carrying out a detailed analysis of ionospheric scintillation which concludes that scintillation phase variations can be characterized through autoregressive processes, and thus be dealt with within the Kalman filter in a natural manner. Second, the design of adaptive Kalman filter-based techniques that allow self-adjusting their loop bandwidth

to the actual scintillation conditions, which are rather time-varying in practice. This part includes a scintillation detector, a real-time estimator of the autoregressive model parameters, and an implementation to address the problem of non-linear signal amplitude attenuation introduced by scintillation itself. The goodness of the proposed techniques is later validated by carrying out an extensive simulation campaign using both synthetic data and real scintillation time series, and the outperformance region with respect to conventional tracking techniques is quantified. Third, a novel method for the derivation of expressions for the termed Bayesian Cramér-Rao bound (BCRB), which allow characterizing the behavior of Kalman filters in a closed-form manner, thus becoming a contribution to the literature of practical usefulness to design Kalman filters for any kind of application.

Resumen

Las tecnologías de posicionamiento por satélite (GNSS, del inglés *global navigation satellite systems*) se han convertido en una herramienta indispensable en diferentes ámbitos de nuestra sociedad moderna. Algunos ejemplos de aplicaciones son el posicionamiento y la navegación en entornos terrestre, marítimo y aéreo, así como usos destinados a la agricultura, topografía o aplicaciones de sincronización precisa en sistemas de telecomunicaciones o finanzas. El módulo de *tracking* es una de las etapas centrales para mantener los receptores alineados con los satélites, y hasta ahora se han empleado técnicas de tracking convencionales de fácil implementación que son suficientes para operar en escenarios con unas condiciones de trabajo favorables. Sin embargo, en los últimos años, el éxito de GNSS en entornos a cielo abierto ha propiciado su expansión hacia aplicaciones en escenarios más exigentes, tales como cañones urbanos o interiores. La tendencia es dotar a los terminales móviles (smartphones) de capacidades de posicionamiento en entornos en donde se enfrentan a nuevos retos tecnológicos dados por los problemas de propagación que abundan. En este sentido, el centelleo ionosférico (*ionospheric scintillation* en inglés), es uno de los problemas que degradan las prestaciones de los receptores, particularmente en zonas equatoriales y a altas latitudes. Es un efecto que introduce rápidas variaciones aleatorias en la fase y la potencia de la señal, y tiene un efecto perjudicial precisamente en la etapa de tracking del receptor.

El objetivo de esta tesis es diseñar y desarrollar nuevas técnicas para el tracking robusto de señales GNSS afectadas por el efecto de centelleo ionosférico. La propuesta que se presenta está basada en el uso de técnicas de filtrado de Kalman, y las contribuciones principales de esta tesis son tres. En primer lugar se estudia el efecto de centelleo ionosférico y el tracking de la dinámica del receptor a pesar de su presencia. Diseñamos un filtro de Kalman con una formulación híbrida que permite monitorizar ambas contribuciones por separado de manera robusta. Esto surge de realizar un análisis detallado del centelleo ionosférico en el que se concluye que las variaciones de fase se pueden caracterizar a través de procesos autoregresivos, los cuales se pueden tratar mediante el filtro de Kalman de

manera natural. En segundo lugar se diseñan técnicas de filtrado de Kalman adaptativas que permiten ajustar su ancho de banda en función de las condiciones de centelleo, las cuales suelen ser variantes en el tiempo en la práctica. Esta parte incluye un detector de presencia de centelleo, un estimador en tiempo real de los parámetros del modelo autoregresivo, y una implementación para lidiar con las atenuaciones no lineales introducidas por el mismo centelleo. El funcionamiento de las técnicas propuestas se valida posteriormente mediante una campaña extensiva de simulaciones utilizando tanto datos sintéticos como datos reales de centelleo ionosférico, y se cuantifica la región de ganancia respecto a las técnicas convencionales. Por último se propone un innovador método para derivar expresiones para la denominada cota Bayesiana de Cramér-Rao (BCRB, del inglés *Bayesian Cramér-Rao bound*) que permiten caracterizar el comportamiento de los filtros de Kalman de manera cerrada. Esto supone una contribución a la literatura de gran interés práctico para diseñar filtros de Kalman para cualquier tipo de aplicación.

Agradecimientos

Me gustaría agradecer y dedicar esta tesis a las siguientes personas.

En primer lugar a mis supervisores de tesis, José Salcedo y Gonzalo Seco. Dentro de su ajetreada agenda siempre han encontrado un hueco para resolver mis dudas y para debatir conceptos y resultados. Gracias por vuestros consejos y por proporcionarme ese inestimable volumen de conocimiento durante estos años.

A mis compañeros de despacho, Vicente, Dani, David, José Del Peral, Toni, Rubén y Alessio por las interesantes conversaciones mientras comíamos el tupper, y por prestar su ayuda y su punto de vista ante problemas que me costaba resolver.

A Adrià, Roger y José Del Peral (sí, otra vez) por su acogida cuando estuve en Holanda, y a José Molina por su recibimiento y dedicación durante mi estancia en ESTEC.

A mis amigos Óscar, José Manuel, Noemí, Dani, Mireia y compañía, que a base de paseos por la montaña, Escape Rooms e incontables sesiones de cine me han ayudado a desconectar del trabajo cuando lo necesitaba y a afrontar las jornadas con más energía.

A mi familia por aguantar mis neuras durante estos años. Ciertamente, esta tesis no habría sido posible sin esas terapias con mis padres que me ayudaban a restarle importancia a mis penas y me animaban a seguir adelante.

A mi abuela, a quien de bien seguro le habría gustado verme acabar esta tesis y ser doctor antes de irse.

Y finalmente, a mis gatos por hacerme compañía mientras escribía esta tesis.

Gracias a todos por vuestra inestimable ayuda y apoyo.

This work was supported by the Spanish Ministry of Economy and Competitiveness projects TEC2014-53656-R and TEC2017-89925-R, and the FI-DGR PhD grant with file number 9015-376195/2014 from Generalitat de Catalunya.

Contents

List of Figures

List of Tables

Notation

In the sequel, matrices are indicated by uppercase boldface letters, vectors are indicated by lowercase boldface letters, and scalars are indicated by italic letters. Other specific notation has been introduced as follows:

$\|a\|$	Absolute value of scalar a.
$\|\|\mathbf{a}\|\|$	Norm 2 of vector $\mathbf{a}$.
$\approx$	Approximately equal to.
$\doteq$	Defined as.
$\mathbf{A}^*$, $\mathbf{A}^T$, $\mathbf{A}^H$, $\mathbf{A}^{-1}$	Complex conjugate, transpose, conjugate transpose (Hermitian) and inverse of matrix $\mathbf{A}$, respectively.
$[\mathbf{a}]_i$, $[\mathbf{A}]_{i,j}$, $\mathbf{A}_{i,j}$	ith element of vector $\mathbf{a}$, and element from ith row, jth column of matrix $\mathbf{A}$, respectively.
$\mathbf{I}_n$	Identity matrix with dimension m.
$\mathbf{a}_n$, $\mathbf{A}_n$	Vector $\mathbf{a}$ and matrix $\mathbf{A}$ whose dimensions depend on the scalar n with unspecified value.
$\mathbf{a}(n)$, $\mathbf{A}(n)$	Vector $\mathbf{a}$ and matrix $\mathbf{A}$ whose values depend on the scalar n.
$\mathrm{E}[\mathbf{a}]$, $\mathrm{E}[\mathbf{A}]$	Expectation operation on vector $\mathbf{a}$ and matrix $\mathbf{A}$, respectively.
$\mathrm{Tr}(\mathbf{A})$	Trace of matrix $\mathbf{A}$ as the sum of the diagonal elements.
$\mathrm{diag}(\mathbf{A})$	Vector containing the diagonal elements of matrix $\mathbf{A}$.
$\mathbf{1}$	Vector of ones.
$\mathbf{0}_{r\times c}$	Matrix of zeros with r rows ans c columns.

Acronyms

ACF	Autocorrelation Function
ADC	Analog-to-Digital Converter
A-GNSS	Assisted Global Navigation Satellite Systems
AHL	Adaptive Hard-Limiting
AIC	Akaike's Information Criterion
AR	Autoregressive (process)
ARIMA	Autoregressive Integrated Moving Average (process)
ARMA	Autoregressive Moving Average (process)
ATAN2	Four-quadrant Arctangent Phase Discriminator
ATAN	Two-quadrant Arctangent Phase Discriminator
AWGN	Additive White Gaussian Noise
BCRB	Bayesian Cramér-Rao Bound
BER	Bit Error Rate
BIM	Bayesian Information Matrix
BLUE	Best Linear Unbiased Estimator
BOC	Binary Offset Carrier
BPSK	Binary Phase Shift Keying
C/A	Coarse-Acquisition (code)
CAF	Cross-Ambiguity Function
CBOC	Composite Binary Offset Carrier
CCF	Cross-Correlation Function
CDMA	Code-Division Multiple Access
Chi2	Chi-Square Distribution
C/N_0	Carrier-to-Noise Ratio

CPU	Central Processing Unit
CRB	Cramér-Rao Bound
CSM	Cornell Scintillation Model
DARE	Discrete Algebraic Riccati Equation
DLL	Delay-Lock Loop
ECEF	Earth-Centered Earth-Fixed (coordinates)
EKF	Extended Kalman Filter
ESA	European Space Agency
ESTEC	European Space Research and Technology Center
FDMA	Frequency-Division Multiple Access
FIM	Fisher Information Matrix
GCS	Ground Control Segment
GGTO	GPS-to-Galileo Time Offset
GNSS	Global Navigation Satellite Systems
GoF	Goodness of Fit
GPS	Global Positioning System
GPST	GPS Time
GST	Galileo System Time
HPF	High-Pass Filter
HS-GNSS	High-Sensitivity GNSS
I&D	Integrate & Dump
IQ	In-phase and Quadrature (signal components)
ISM	Ionospheric Scintillation Monitoring
KF	Non-hybrid Kalman Filter for carrier dynamics-only tracking
KF-AR	Hybrid Autoregressive Kalman Filter
KL	Kullback-Leibler Divergence
LBS	Location-Based Services
LMMSE	Linear Minimum Mean Squared Error
LNA	Low-Noise Amplifier
LoL	Loss of Lock (probability)
LOS	Line of Sight
LPF	Low-Pass Filter

LS	Least Squares
MCS	Master Control Station
MDL	Minimum Description Length
MEO	Medium-Earth Orbit
ML	Maximum Likelihood (approach, estimation)
MMSE	Minimum Mean Squared Error
MSE	Mean Squared Error
MVU	Minimum Variance Unbiased
NBP	Narrow Bandwidth Power
NCO	Numerically-Controlled Oscillator
NF	Near-Far
NLOS	Non-Line of Sight
NWPR	Narrow-Wideband Power Ratio
OS	Open Service (signals)
P	Precision (code)
PDI	Post-Detection Integration
PLL	Phase-Lock Loop
PRN	Pseudo-Random Noise
PRS	Public Regulated Service (Galileo)
PSD	Power Spectral Density
PVT	Position, Velocity, Time
RMSE	Root MSE
SNR	Signal-to-Noise Ratio
SS	Space Segment
SV	Satellite Vehicle
TOA	Time of Arrival
TOW	Time of Week
TTFF	Time to First Fix
US	User Segment
WBP	Wide Bandwidth Power
WLS	Weighted Least Squares
YW	Yule-Walker (method, equations)

Chapter 1

Thesis Introduction

1.1 Motivation

In the recent years, Global Navigation Satellite Systems (GNSS) have become an indispensable tool in our modern society to provide a real-time estimation of one's position using ranging radio-frequency signals. Nowadays, the use of GNSS ranges from scientific applications such as surveying and geodesy, to agriculture or precise timing in finances, to safety-critical applications such as aviation and maritime navigation, just to mention a few. One of the core tasks performed within GNSS receivers is *signal tracking*, which is carried out by the so-called *tracking stage*. It is in charge of keeping the receiver synchronized with the signals received from different satellites orbiting around the Earth, as well as precisely monitoring any variation in the dynamics observed between these and the receiver. In this sense, an upward trend is to employ the carrier phase measurements instead of pseudorange ones, as they are of better quality and provide ultra-precise positioning information, and thus their exploitation by means of *carrier tracking* becomes of paramount importance for high-accuracy positioning applications, and the computation of navigation and integrity data for GNSS ground segments [Mac12].

The most mature and widespread GNSS is the American Global Positioning System (GPS). The initial user receiving equipments date from the mid-1970s and were originally devoted to military applications; they were large, bulky and heavy [Kap05], designed to operate in open-sky environments with clear visibility of the satellites. For this reason, most of the existing GNSS receivers implement carrier tracking using a very simple technique, the well-known *phase-locked loop* (PLL), which provides good performance in these

environments with ease of implementation. It is a closed-loop architecture that compares a local replica with the received signal and drives the resulting error to zero by adjusting the phase of the local oscillator. However, technology trends in component miniaturization, low-power consumption and large-scale manufacturing have led current and future GNSS receivers to be compact, light and low-cost. As a matter of fact, current GNSS receivers are embedded in many of the items we use in our daily lives, such as smartphones and automobiles, which are considered to be the next-generation GNSS receivers thanks to their growing computational capabilities. Indeed, smartphones account for almost 80% of the global installed base of GNSS devices, and the number of units in use is expected to exceed 9 bilion by 2025 [GSA17]. Therefore, there exists a commercial push for providing user mobile terminals with ubiquitous positioning capabilities that has led to the emergence of a new era of GNSS applications taking place in scenarios very different from those for which GNSS was originally conceived [Mis06]. A clear example is autonomous vehicle navigation, or automatic guidance and airplane landing, and we are referring to the urban and soft-indoor arena, where propagation impairments and time-varying working conditions abound.

On the other hand, the expansion of GNSS in emerging countries has unveiled the need to cope with the so-called *ionospheric scintillation* effect [Kin07]. The ionosphere is the upper Earth's atmosphere ionized by solar radiation, and has a significant influence on transionospheric radio wave propagation. The ionospheric electron density irregularities introduce rapid random amplitude and phase fluctuations onto GNSS signals when crossing the ionosphere, as illustrated in Figure 1.1, thus hampering the proper determination of the receiver synchronization parameters. The effect of ionospheric scintillation is known to be highly dependent on the solar activity and the location on the Earth, as illustrated in Figure 1.2. For instance, at high latitudes (*i.e.* auroral and polar regions), phase scintillations are more frequent than amplitude scintillations [Jia13, Sko05]. At mid latitudes ionospheric scintillation is observed particularly after intense magnetic storms originated from solar eruptions [Mac12]. However, the effects are more prominent at low-latitude/equatorial regions, where scintillation events are found to be more intense in both amplitude and phase [Kin09, Jia15, Seo09], thus posing serious concerns to the widespread deployment of GNSS in those areas.

The weak link in GNSS receivers under the presence of scintillation disturbances is the carrier tracking loop, especially the conventional PLL architecture [Lee17], which is known to experience serious trouble to deal with such impairment. This motivates the research and development of new signal processing techniques for robust carrier tracking

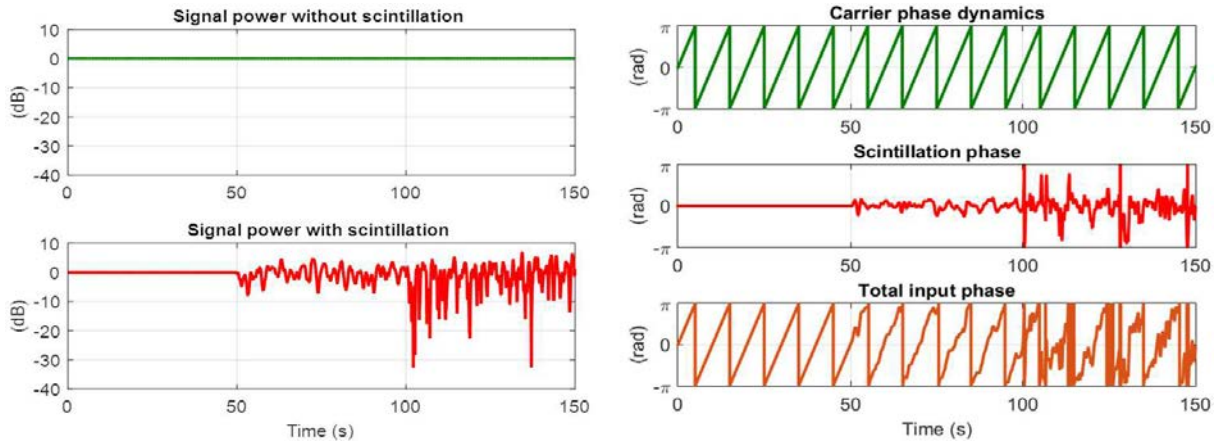

Figure 1.1: Illustrative example of signal amplitude (left) and phase variations (right) introduced by ionospheric scintillation.

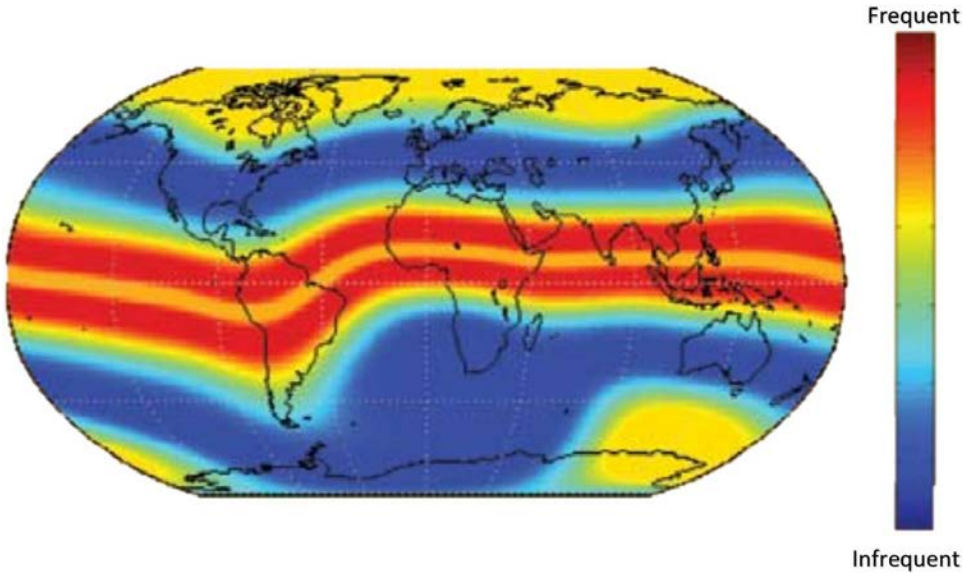

Figure 1.2: Scintillation map showing the frequency of ionospheric disturbances onto the different regions of the Earth [Kin09].

to deal with the challenges to be faced by next generation GNSS receivers, with special emphasis on ionospheric scintillation. Indeed, this necessity has been identified by the European Space Agency (ESA) and materialized in form of the "Robust Carrier Phase Tracking" (ROCAT) project, within whose framework this thesis has been developed, as an opportunity to enhance the positioning accuracy of GNSS receivers under the presence of scintillation disturbances.

1.2 Objectives

Ionospheric scintillation is certainly a critical challenge having a detrimental impact in conventional GNSS receivers. In order to deal with it at the tracking stage, this thesis tackles the carrier tracking problem through the use of Kalman filter-based techniques, as a result of considering the general framework of optimal minimum mean squared error (MMSE) estimation. The main contribution of this thesis is the design of Kalman filter-based techniques to deal with scintillation disturbances in a natural manner. In GNSS positioning applications, the idea is to estimate carrier dynamics and ionospheric scintillation separately, so that the latter can be virtually eliminated from the input signal and thus clean scintillation-free carrier phase measurements can be provided. Notwithstanding, it is worth noting that the problem could also be seen the other way around. That is, to estimate scintillation in the presence of carrier dynamics, so that the latter can be virtually eliminated and clean scintillation estimates can eventually be provided. Therefore, the proposed approach could ultimately be used for scientific applications relying on ionospheric scintillation monitoring (ISM).

On the other hand, from the practical standpoint, during the design of Kalman filters it is often interesting to determine the best achievable performance and predict its behavior before implementation. This is usually addressed by means of the so-called Bayesian Cramér-Rao bound (BCRB) which, unfortunately, does not present a solution in closed-form, thus hampering the analysis of the filter in practice. This thesis also tackles this limitation by proposing a novel method for the derivation of closed-form expressions in order to characterize the performance of Kalman filters in a straightforward manner. To the best of the author's knowledge, the proposed approach is a novel contribution to the literature with great practical interest for any kind of application.

Based on the above observations, the main objectives of this thesis are to:

1. Following the recent trends, present the Kalman filter as the natural improvement to conventional PLLs in order to deal with the technological challenges to be faced by next-generation receivers.

2. Propose a method for the derivation of closed-form expressions for the BCRB of Kalman filters, which provide a better understanding on the Kalman filter behavior without having to solve for the BCRB by means of numerical evaluations.

3. Perform a thorough characterization of ionospheric scintillation disturbances. Ex-

plore the feasibility of modeling scintillation phase variations through a linear Gaussian model, so that it can be encompassed by Kalman filter-based techniques in a natural manner. Analyze the impact of thermal noise onto the scintillation modeling process for a better characterization in realistic scenarios.

4. Propose a Kalman filter-based architecture to estimate scintillation phase variations, with the aim of subtracting them from the input signal and thus be able to provide accurate scintillation-free carrier phase measurements.

5. Design and develop adaptive implementations to deal with the time-varying nature of ionospheric scintillation and provide optimal performance in these conditions.

6. Carry out an extensive simulation campaign using synthetic scintillation data, and evaluate the performance of the different proposed techniques. Quantify their outperformance with respect to that of conventional PLLs. Validate the results obtained with synthetic data using real scintillation time series.

1.3 Thesis Outline and Publications

This section provides a summary of the content of this dissertation. The work in this thesis has led to a number of international conference and journal publications, which are also listed below.

Chapter 2 presents the basic notions of GNSS technologies. The space and ground deployments are briefly described, and the positioning principle is explained, which mainly consists in measuring the distance from the receiver to several satellites. Then, the different stages of GNSS receivers are presented, placing special emphasis onto the tracking stage. The aim is to provide fine estimates of the parameters used to keep synchronized with the satellites. To this end, the carrier and code loops are employed, and the solutions adopted in conventional receivers are described. Then, the mathematics for the position determination are explained, where some guidelines for positioning in high-sensitivity receivers are also provided.

Chapter 3 introduces the fundamentals of the Kalman filtering problem. Some guidelines for the set-up and tuning of the filter are provided, and the formulation for the particular problem of GNSS carrier dynamics tracking is presented. The main contribution of this chapter is the derivation of closed-form expressions for the BCRB characterizing the

Kalman filter performance. On the one side, an approximate upper bound for the convergence time of Kalman filters encompassing second-order kinematic models with nonzero process noise, as well as approximate lower bounds for the performance in steady state. On the other side, an extension of the aforementioned convergence time upper bound to Kalman filters encompassing a kinematic model with any nonrestricted order. These two contributions have led to the publication of two journal papers, respectively:

- S. Locubiche-Serra, G. Seco-Granados, J. A. López-Salcedo, "Closed-Form Approximation for the Steady-State Performance of Second-Order Kalman Filters", *IEEE Signal Processing Letters*, vol. 25, no. 2, pp. 268-272, Feb 2018.
- S. Locubiche-Serra, G. Seco-Granados, J. A. López-Salcedo, "Closed-Form Approximation for the Convergence Time of pth-order Kalman Filters", *IEEE Signal Processing Letters*, vol. 25, no. 10, pp. 1505-1509, Oct 2018.

Chapter 4 provides a detailed characterization of random phase variations introduced by ionospheric scintillation. The key observation is that these can be modeled through a process with some correlated Gaussian distribution. In that sense, this chapter presents the class of autoregressive processes as the proposed way to model scintillation phase variations. To do so, the problem of autoregressive fitting is presented as that of finding the set of model parameters that best fit a given scintillation time series. To this end, two equivalent methods are proposed, namely the Yule-Walker equations and the Least-Squares method. Then, several preliminary tests using both synthetic data and real scintillation time series are carried out to confirm the fitting of autoregressive processes to scintillation phase. This is done by comparing the power spectral density of the actual data to that which the estimated model parameters lead to. Finally, the problem of autoregressive model order selection is addressed. A brief literature review on the most common criteria for optimal order determination of a random process is provided. Among them, a consistent criterion is presented as the choice in this thesis, namely the minimum description length. Some test results are provided to confirm those of the power spectral densities.

Chapter 5 presents the core of a novel Kalman filter with an augmented state-space formulation that hybridizes separate kinematic and autoregressive models. The idea is to deal with both carrier dynamics and ionospheric scintillation phase variations, respectively, in the presence of one another but in a decoupled manner. In general terms, we will denote this technique as the hybrid autoregressive Kalman filter. This chapter also introduces a qualitative analysis of the BCRB for this kind of techniques. In this sense,

in the same way as in Chapter 3, this thesis also contributes with the derivation of novel closed-form expressions for the performance characterization of autoregressive Kalman filter-based techniques. The contribution is twofold. On the one hand, closed-form expressions for the convergence time of a KF-AR encompassing a second-order kinematic and a first-order AR models. On the other hand, closed-form expressions for the steady-state performance of pure first- and second-order autoregressive Kalman filters. This chapter also proposes some adaptive implementations for the hybrid Kalman filter to self adapt to the actual scintillation conditions, which are rather time-varying in practice. Two implementations are proposed. The first one is a technique implementing online estimators of the autoregressive model parameters and order. At this point, an analysis on how the presence of thermal noise may hinder the proper detection of the autoregressive parameters is carried out. Moreover, a novel adaptive hard-limiting implementation is also proposed in order to deal with the nonlinear signal amplitude fades introduced by scintillation. Then, a second implementation is proposed, consisting in a semi-adaptive technique that preserves the adaptive hard limit, while the Kalman filter employs fixed autoregressive parameters and order, instead of computing them in an online manner. In addition, it includes a scintillation detector in order to commute to a dynamics-only Kalman filter when scintillation is absent and the hybrid autoregressive one when it is present. The rationale of this second implementation is to provide optimal performance regardless of the nature of the input signal, at a significantly smaller computational cost.

The contributions in this chapter on the closed-form expressions for the BCRB have led to the preparation of two journal publications, respectively:

- S. Locubiche-Serra, G. Seco-Granados, J. A. López-Salcedo, "Closed-Form Approximations for the Convergence time of Hybrid Autoregressive Kalman Filters", *submitted to IEEE Signal Processing Letters, in review progress.*
- S. Locubiche-Serra, G. Seco-Granados, J. A. López-Salcedo, "Closed-Form Lower Bounds for the Steady-State Performance of Autoregressive Kalman Filters", *to be submitted to IEEE Signal Processing Letters.*

Chapter 6 presents the experimental results of the Kalman filter implementations proposed in Chapter 5. These arise from an extensive simulation campaign by using a GNSS carrier tracking simulator implemented in MATLAB. Two different cases of input scintillation are considered, namely for synthetic and real scintillation time series, both based on GPS L1 C/A signals (*i.e.* with binary phase shift keying modulation, BPSK). The simulations are divided into three categories. First, a set of simulations with stationary synthetic

scintillation. The idea is to test the performance of fixed KF-AR configurations and compare them to that provided by the solutions adopted in conventional GNSS receivers. In addition, the BCRB is employed as a tool to check on the optimality of the proposed techniques. Second, simulations considering time-varying scintillation conditions. The objective is twofold. On the one hand, to evaluate the agility of the adaptive implementations to self-adapt when the working conditions change, and their ability to provide optimal performance. On the other hand, to compare their convergence and steady-state performance to that of fixed techniques. Third, simulations considering real scintillation time series obtained from ESA's scintillation monitoring network. The objective here is to test the performance of the proposed fixed and adaptive techniques and to validate the goodness and performance obtained with synthetic data. Finally, this chapter culminates with the determination of the region within which the hybrid autoregressive Kalman filter does provide an advantage with respect to the approach adopted in conventional receivers. The limits of this region are quantified in terms of both signal-to-noise ratio and input dynamics tracking capabilities.

As already mentioned in Section 1.1, the work presented in Chapters 4 to 6 has been performed within the framework of the ROCAT project funded by ESA, and has led to the following conference publication, and the preparation of a journal manuscript that is to be submitted shortly:

- S. Locubiche-Serra, G. Seco-Granados, J. A. López-Salcedo, "Doubly-Adaptive Autoregressive Kalman Filter for GNSS Carrier Tracking under Scintillation Conditions", *Proc. International Conference on Localization and GNSS (ICL-GNSS)*, Jun 28 2016.
- S. Locubiche-Serra, G. Seco-Granados, J. A. López-Salcedo, "Robust GNSS Carrier Tracking under Ionospheric Scintillation using Semi-Adaptive Hybrid Autoregressive Kalman Filter", *to be submitted to GPS Solutions.*

Other contributions

Even though remaining out of the scope of this dissertation, efforts for improving the acquisition stage of high-sensitivity snapshot GNSS receivers have additionally been made during this thesis. In harsh environments such as urban canyons, the presence of propagation impairments such as high signal attenuation, non-line-of-sight (NLOS) issues, multipath and near-far severely hampers the proper satellite acquisition. Among these, multipath and near-far are certainly one of the most limiting effects, the former having

been recently addressed using the framework of quickest detection [Ege15, Ege17]. As for the latter, it is defined as the situation in which a strong signal captures the receiver and consequently impedes the acquisition of weaker signals, thus posing a serious concern to GNSS service availability [Rap02]. Near-far is caused by the different attenuation losses incurred in the different propagation paths, and it is thence an impairment abounding in the above scenarios, where the presence of obstacles and tall buildings may lead the difference in power among signals to exceed 30 dB. The underlying idea is that the orthogonality property of the spreading codes on which individual satellite detection and identification relies is not fully fulfilled. The practical consequence is that the autocorrelation of a given satellite with the corresponding local replica becomes hindered by the cross-correlation with other satellites with stronger received signal power [Mor03].

In that sense, we have developed different techniques to address the problem of near-far detection and mitigation. Near-far detection becomes of paramount importance to discard those unreliable satellites that may introduce an error of several meters in the positioning solution. To this end, the common approach in the literature is to simply observe whether the autocorrelation function (ACF) presents fluctuations over time. However, since this phenomenon is not necessarily caused by near-far, we proposed a different approach based on observing the ACF from the statistical point of view, and do a statistical hypothesis testing analysis [Alb14]. That is, when near-far is absent, the squared ACF follows a chi-square distribution, χ^2. When near-far is present, the squared ACF departs from a χ^2 distribution. The proposed techniques exploit this phenomenon by measuring the distance of the actual CAF to a χ^2 distribution, and these are mainly the chi-square goodness of fit (GoF), the Kullback-Leibler divergence [Mac03], which has been rarely used in GNSS [Pin13], and the threshold-surpassing method. The application of these techniques to the problem of near-far detection is a novel contribution of this work, and simulations with synthetic Galileo E1BC signals have shown promising results: statistical techniques have been found to outperform conventional ones based on mere ACF observation, with a slight advantage of the threshold-surpassing method.

The problem of near-far mitigation has also been addressed. The aim is to cancel the cross-correlation effect of strong signals onto weak ones, in such a way that the latter can be acquired and further enabled for positioning. To this end, we have proposed the subspace projection technique, which is based on dissociating the received signal into two separate contributions, one for the strong signals and another one for the weak ones. These form the strong and weak signal subspaces, respectively. The interfering signals are identified and a local version of the strong signal subspace is constructed within

the receiver. Then, by using projection operations, the local reconstruction is employed to obtain an interference-free signal that is orthogonal to the subspace spanned by the strong signals. Simulation results have shown the technique to successfully achieve this goal, providing an additional protection against near-far beyond that already provided by spreading codes, thus enhancing the GNSS service availability in harsh environments.

This work has been developed within the framework of the "Techniques for High-Sensitivity GNSS Receivers" (HISENS) project funded by the European Space Agency (ESA), and has led to the following conference publications:

- S. Locubiche-Serra, J. A. López-Salcedo, G. Seco-Granados, "Statistical Near-Far Detection Techniques for GNSS Snapshot Receivers", *Proc. IEEE International Conference on Acoustics, Speech and Signal Processing (ICASSP)*, Mar 20 2016.
- S. Locubiche-Serra, J. A. López-Salcedo, G. Seco-Granados, "Sensitivity of Projection-Based Near-Far Mitigation Techniques in High-Sensitivity GNSS Software Receivers", *Proc. Seventh International Conference on Indoor Positioning and Indoor Navigation (IPIN)*, Oct 04 2016.
- E. Domínguez, A. Pousinho, P. Boto, D. Gómez-Casco, S. Locubiche-Serra, G. Seco-Granados, J. A. López-Salcedo, H. Fragner, F. Zangerl, O. Peña, D. Jiménez-Baños, "Performance Evaluation of High-Sensitivity GNSS Techniques in Indoor, Urban and Space Environments", *Proc. ION GNSS+*, Sep 12 2016.

Research Stay at ESTEC (ESA)

During this thesis the author has also performed a research stay at the European Space Research and Technology Center (ESTEC), at ESA in The Netherlands from January to July 2016. Several tasks have been carried out. On the one hand, to give support in the development and implementation of a high-sensitivity software GNSS receiver in MATLAB. The software was initially devoted to the acquisition and tracking of high-order BOC signals, and the first task has been to extend its applicability to BPSK and low-order BOC signals. On the other hand, to implement a fully-operative module to estimate the receiver's position in high-sensitivity conditions. This implies that a reliable decoding of the navigation message embedded within the received signals may not be feasible due to low signal power. Therefore, the positioning module has been implemented so as to solve for the position without requiring to decode the navigation message, by using orbital parameters downloaded from an external source and estimating the satellite

transmit time as part of the navigation solution. In addition, the module has also been implemented so as to combine measurements coming from satellites belonging to different GNSS constellations. This is often termed *multi-constellation hybridization*, and implies that the module provide a positioning solution using signals with BPSK, low- and high-order BOC modulations indistinctly. The aim was to enhance the positioning accuracy with respect to that of conventional GNSS receivers. GPS and Galileo satellites have been mainly used, and the time offset between both constellations is usually embedded into the navigation messages. However, since it is such time offset has also been treated as a new unknown in the navigation solution. Then, the implemented software has been tested by processing real signals captured at ESTEC by handling a 3-meter directive dish antenna and lab equipment such as USRPs and spectrum analyzers.

The work performed during the research stay at ESTEC has led to the following conference publication:

- S. Locubiche-Serra, D. Gómez-Casco, A. Gusi-Amigó, J. A. López-Salcedo, G. Seco-Granados, J. A. García-Molina, "Positioning Performance analysis of High-Order BOC Signals in Advanced Multi-Constellation High-Sensitivity GNSS Receivers", *Proc. 6th International Colloquium on Scientific and Fundamental Aspects of GNSS / Galileo*, Oct 2017.

Chapter 2

Fundamentals of GNSS

2.1 Introduction

One of the recurrent concerns in human history has been that of determining the geographical position of a given subject [Kar07]. In ancient civilizations, this was originally carried out by observing celestial bodies. However, the problem is nowadays addressed by the use of radio-frequency signals [For08] emitted from different satellites orbiting around the Earth, leading to the so-called *global navigation satellite systems* (GNSS). Their global coverage, technological maturity, deployment cost, user privacy and excellent accuracy in open-sky environments [Par96a, Van02] have led GNSS to become the quintessential enabling technology for positioning and precise timing applications, being nowadays an indispensable tool in our modern society.

The most known GNSS technology is the American *global positioning system* (GPS), which originated back in the 1970s from the interest of United States governmental institutions to develop a positioning system for military purposes. However, the use of GPS rapidly spread to commercial applications, and its success motivated the deployment of similar systems (*i.e.* satellite constellations) by European and Asian institutions to provide location-based services (LBS) without having to depend on GPS [Mis06]. This is the case of GLONASS, managed by the Russian government, or Compass-BeiDou, managed by the Chinese one. In Europe, the corresponding GNSS is the so-called *Galileo*, a GNSS that is fully compatible with GPS but can also provide global positioning coverage in a standalone manner (*i.e.* independently from GPS).

Any GNSS technology is based on the same principle, which is that of receiving the

signals emitted by several satellites and process them to compute the receiver's position. In that sense, this chapter presents the fundamentals of operation of GNSS technologies. We start Section 2.2 by presenting the basic concepts on the deployment and operation principle of GNSS technologies, including a brief description on the employed signal modulations. Next, Section 2.3 explains the general architecture of GNSS receivers, which consists of four consecutive stages, namely the receiver's front-end, acquisition, tracking, and the position-velocity-time (PVT) module. The elements conforming each of these stages are detailed, particularly those within the tracking and PVT modules. In the latter, the foundations to compute the user's position by hybridizing measurements from different satellite constellations, particularly GPS and Galileo, are provided. Finally, Section 2.4 draws the conclusions.

2.2 GNSS Foundations

The main purpose of GNSS is to estimate the user PVT solution. In that sense, this section provides a brief introduction to the basic GNSS concepts related to the deployment and the main principle of GNSS operation for PVT determination. The foundations explained below are based on the following references: [Kap05, Mis06, Par96a, Par96b, Ló12], to which the reader is encouraged to refer for a more in-depth explanation.

2.2.1 GNSS Deployment

The deployment of any GNSS technology is generally divided into three segments: the space segment, the ground control segment, and the user segment.

Space Segment

The space segment (SS) is formed by the satellite constellation, which is the set of satellites orbiting around the Earth that provide signals with data messages that are used to eventually compute the navigation solution. These signals are referred to as *ranging* signals, and include information about the satellite position at a given time instant, as well as clock and atmospheric (*i.e.* tropospheric, ionospheric) corrections.

As previously explained, there exist four main satellite constellations in operation at the time of this writing: GPS, Galileo, GLONASS and COMPASS-BeiDou. The

common feature is that they consist of around 30 satellites orbiting at MEO (medium-Earth orbit) at an altitude in the order of 20000 km. The satellites within a constellation are strategically placed so that at least four satellites (*i.e.* the minimum needed for PVT determination) are in the receiver's line of sight (LOS) anytime and anywhere, thus allowing to provide a worldwide service. The main characteristics of the above-mentioned constellations are summarized in Table 2.1 [ESA11a, ESA11c, ESA17, USG19].

	GPS	**Galileo**	**GLONASS**	**COMPASS-BeiDou**
Owner	USA	Europe	Russia	China
Altitude (km)	20200	23222	19100	27878 MEO
				42164 GEO
Period	11h 58min	14h 7min	11h 15min	12h 38min
# Orbital planes	6	3		
# SV	24	30	24	27 MEO
				5 GEO

Table 2.1: Main characteristics of current existing GNSS satellite constellations.

Ground Control Segment

In general terms, the ground control segment (GCS) is formed by stations on the Earth's surface that track the satellites in space and monitor their proper functioning: health, signal integrity and orbital configuration maintenance. In the latter, the stations send maneuvering signals to the satellites in order to adjust their orbital position. On the other hand, the GCS also tracks and updates a number of parameters that are crucial to perform navigation, such as satellite clock corrections, almanac and ephemerides, which are updated at least once per day. The ephemerides refer to the complete set of parameters needed for PVT determination, while the almanac is a reduced-precision subset of the ephemeris parameters that is usually employed to predict the approximate satellite position and aid in satellite signal acquisition. In order to determine the above-mentioned parameters, pseudorange and carrier phase measurements are collected at the monitoring stations.

To accomplish these functions, the GCS is formed by the following elements:

- **Master control station** (MCS), in charge for processing the information com-

ing from the monitoring stations, and tracking the system status: health of satellites, satellite orbits, and synchronization of system timing service. Furthermore, it predicts satellite ephemerides and clock parameters, while also generating satellite maneuvering commands and the navigation messages.

- **Monitoring stations** at L band, consisting of dual-frequency receivers that collect satellite ranging and status data, and local meteorological data. They are usually located at sites near the Earth equator for coverage maximization.
- **Ground uplink antennae** at S band, used for satellite commanding and data transmission of the correction information processed by the MCS. In addition, they receive satellite telemetry data that is forwarded to the MCS.

User Segment

The user segment (US) consists of the GNSS receivers in ground, marine, air and space applications. The main purpose of GNSS receivers is to process the downlink signals received from the different satellites at L band and decode the navigation message to determine their PVT.

The set of GNSS receivers that form the user segment can be classified into two main categories:

- **Type of user**: can be **civilian** or **military**. In the former, open-service (OS) but accuracy-limited signals are employed. This is the case of GPS L1 C/A and Galileo E1BC signals. On the other hand, a military use refers to restricted-access signals that are thought to provide an enhanced accuracy. This is the case of GPS L2-P and Galileo-PRS codes.
- **Frequency capabilities**. **Single-frequency** receivers are standard receivers operating at one single frequency band. In contrast, **dual** (or **multiple**)**-frequency** receivers can process signals obtained from different frequency bands. Their main advantage is the ability to compensate for ionospheric, geometry and carrier-phase ambiguity effects by combining measurements obtained at different bands, and thus improve the estimation of the user's position [San13].

2.2.2 GNSS Signal Structure and Frequency Bands

GNSS signals fall into a broad category of signals known as *direct-sequence spread-spectrum* (DSSS) signals. This type of signals is based on using (nearly-) orthogonal codes, where the orthogonality property is achieved by employing the so-called cyclic *pseudo-random noise* (PRN) sequences. The rationale of this nomenclature is that the cross-correlation between two different PRN codes is (nearly) zero, while the auto-correlation of a given code results in a high peak when aligned with itself, and ideally zero cross-correlation otherwise, thus resembling the behavior of white noise. Within a given GNSS constellation, each satellite transmits a different pseudo-random code, meaning that the satellites can be uniquely identified by their corresponding code. As will be explained in Section 2.3.2, this concept is the basis to dissociate among satellites, detect their presence individually and measure the different propagation times to the receiver.

DSSS are signals that employ all the available communication channel bandwidth, and are transmitted simultaneously without interfering with each other. That is, they all share the same time and frequency slots (*i.e.* no multiplexing), and are uniquely identified by the PRN codes thanks to their orthogonality property. This type of communication is referred to as *code-division multiple access* (CDMA) and is widely employed in wireless mobile communications systems. Except for the Glonass constellation, which employs *frequency-division multiple access* (FDMA) [Reu11, Wan11], GNSS utilize CDMA, which provides the following advantages:

- PRN codes allow obtaining precise range measurements.
- PRN codes cause the signal energy to distribute along a broader spectrum, which enhances the robustness against narrowband interferences.

The signals employed in GNSS are characterized by the following four elements:

- A suitable **carrier frequency** onto which the signal can be transmitted through the propagation path. In GPS and Galileo, different bands are employed: L1/E1 (1575.42 MHz), L2 (1227.60 MHz), L5/E5a (1176.45 MHz) and E6 (1278.75 MHz).
- The **navigation data**: a binary-coded message containing information about the satellites status, ephemeris, clock bias and parameters to compute atmospheric corrections.

- The **ranging code**: the PRN code that statistically behaves as white noise, as stated above, and allows dissociating among the different satellites. In GPS L1 C/A, the PRN sequences are formed by 1023 bits termed *chips* that repeat with a period of 1 ms and thus transmit at a chip rate of $f_{\text{ref}} = 1.023$ MHz. In open-service (OS) Galileo E1BC, the number of chips carrying the navigation data is 4092 repeating with a period of 4 ms. Each of them is then multiplied by one bit of a secondary code, the latter consisting in a 25-bit known sequence that repeats in a cyclic manner, thus leading to a total duration of 100 ms.

- The **modulation**. GPS L1 C/A employs a simple BPSK modulation, whereas Galileo E1BC employs BOC modulations. The latter are based on multiplying a pseudo-random code with a sub-carrier f_{sc} with frequency equal to or higher than the chip rate. This allows widening the signal spectrum (*i.e.* Gabor bandwidth) with respect to that of BPSK, which ultimately translates into a sharper autocorrelation peak and enhanced positioning accuracy. However, the drawback is the occurrence of secondary peaks that may hamper the proper capture of the main one. A BOC-modulated signal is usually denoted as BOC(m, n), with $m \doteq f_{\text{sc}}/f_{\text{ref}}$, $n \doteq f_{\text{c}}/f_{\text{ref}}$ and f_{c} is the modulated chip frequency. Galileo E1BC employs BOC(1,1) modulations. However, more advanced Galileo signals are implementing higher-order BOC modulations, namely BOC(15, 2.5), which further exploit the above phenomenon at the expense of severely aggravating the problem of false locks. These concepts will be further detailed when introducing the principle of GNSS satellite detection in the acquisition stage in Section 2.3.2.

2.2.3 GNSS Positioning Principle

GNSS positioning is based on computing range estimates obtained by measuring the so-called *time-of-arrival* (TOA) as the propagation delay between each visible satellite and the receiver. To this end, each satellite transmits a signal with a time stamp t_k that refers to the time instant at which the signal leaves the kth satellite. When the receiver captures the signal, it decodes the time stamp t_k after synchronizing a local replica of the PRN code under study to the received one[1], while at the very same moment it measures the time of reception t_r by reading its internal clock [Mis06, Ch. 5]. The propagation time is then computed as the difference between both measurements, $\tau_k = t_k - t_r$, and the

[1]This will be the main function of the acquisition and tracking stages presented next in Sections 2.3.2 and 2.3.3, respectively.

distance between the satellite and the receiver is determined using the speed of light c as $d_k = c\tau_k$. The presented approach for position estimation based on distance measurements is referred to as *trilateration* [Fre96].

The position of a satellite at a given time instant can be determined by employing the ephemerides transmitted by the satellite itself. Hence, the estimated distance provides the radius of the spherical surface centered at the satellite and containing the user's location. This is graphically described by the straight circles in Figure 2.1. However, the time measurement t_r is referred to the receiver's internal clock, which may present some unknown offset with respect to the time reference shared by all satellites of a given constellation, the latter referred to as GNSS time which varies from one constellation to another [Mou05]. As a consequence, the measurements from all satellites are shifted by a common offset δt_u owing to the receiver running an independent clock. This phenomenon can be observed in the dotted circles in Figure 2.1, and must be compensated for to determine the correct user's position.

The key point underlying GNSS positioning is that the three dotted circumferences in Figure 2.1 share a unique intersection point for an appropriate value of δt_u [Sec12]. This is considered to be the user's position, and this means that measurements from at least four satellites are needed to determine the solution. In that sense, the unknowns are the position coordinates in Earth-centered Earth-fixed (ECEF) system (*i.e.* X, Y and Z with origin the center of the Earth), plus the receiver clock offset δt_u. It is worth noting that, by estimating the latter, the receiver can be synchronized to the GNSS time scale, and since satellites equip high-precision atomic clocks on board, this is what opens the door to applying GNSS for precise timing applications.

2.3 Architecture of GNSS Receivers

This section aims at providing the details of the modules that form a GNSS receiver. These are namely the receiver's front-end, the acquisition and tracking stages, and the PVT module which ultimately determines the user's position using the information coming from the previous stages. The general scheme of the modules of a GNSS receiver is shown in Figure 2.2.

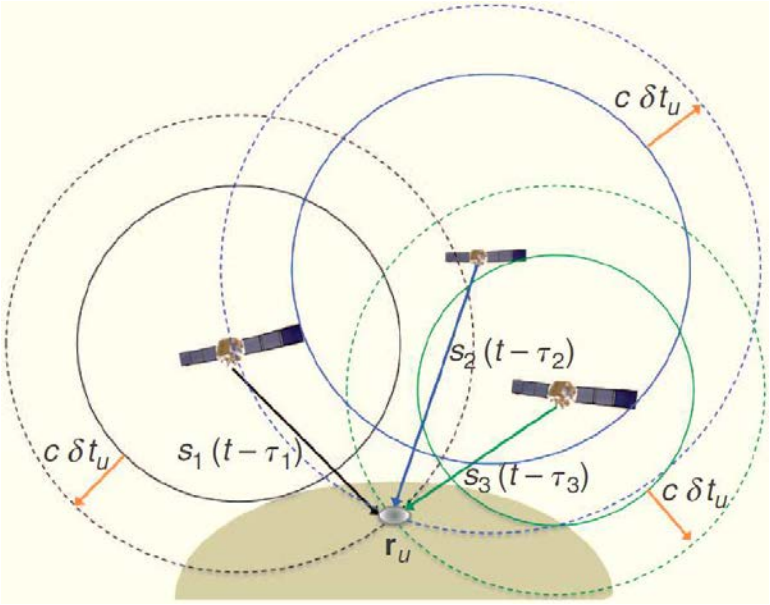

Figure 2.1: Illustration of the GNSS positioning principle, and effect of receiver clock offset [Sec12].

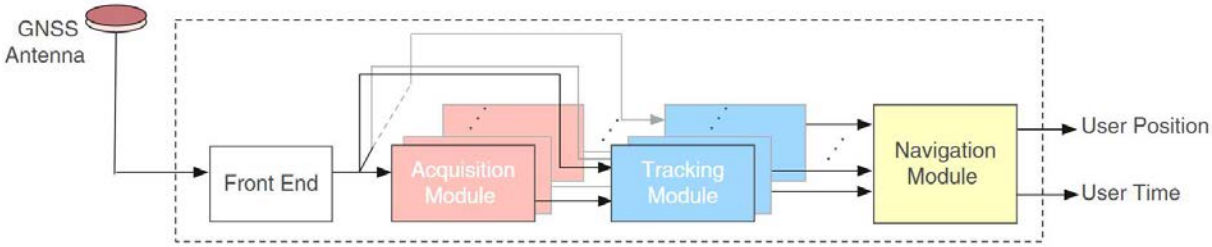

Figure 2.2: General box diagram of a GNSS receiver [Sec12].

2.3.1 Receiver's Front-End

The receiver's front-end is in charge of the analog processing of the signal. That is, the conversion of the captured bandpass signal to baseband. The main operations include low-noise amplification (LNA), filtering, frequency down-conversion to baseband [ESA11b] and analog-to-digital (ADC) conversion. Once the signal has been conditioned and converted, the subsequent stages of the receiver are based on digital signal processing.

2.3.2 Acquisition stage

The acquisition stage of a GNSS receiver consists in detecting the satellites that are present in the received signal. These will serve as anchor nodes from which the receiver

will determine its position by measuring the propagation time from the different satellites to the receiver, based on the starting point of the cyclic PRN codes.

Satellite detection must be carried out, though, in the presence of a residual frequency that still remains after down-conversion in the receiver's front-end. That is, the PRN code of each satellite is received with some Doppler shift caused by the relative motion between the satellite under study and the receiver: either both the satellite and the receiver are in movement, or the receiver is static, in which case it still sees the satellite movement. In addition, the possible misaccuracy of the receiver's oscillator may also introduce some residual frequency shift.

In that sense, the signal at the ADC output can be written as the sum of L signals coming from L different satellites with their respective Doppler shifts, plus some white noise (considered additive white Gaussian, AWGN):

$$r(n) = \sum_{k=1}^{L} \sqrt{P_k(n)} D_k(n - \tau_k - \delta t_u) C_k(n - \tau_k - \delta t_u) e^{j\left(2\pi f_{d,k} n + \theta_k\right)} + w(n) \tag{2.1}$$

where $P_k(n)$ is the power of the received kth satellite at time instant n, $D_k(n)$ is the navigation message, $C_k(n)$ is the PRN sequence, $(\tau_k + \delta t_u)$ is the propagation time from the kth satellite to the receiver including the receiver clock offset, $f_{d,k}$ is the Doppler shift, θ_k is some carrier phase offset owing to the propagation path, and $w(n)$ is the noise term. The presence of an unknown code delay and Doppler shift forces to perform the detection of the kth satellite in a two-dimensional search (*i.e.* in time and frequency). To this end, the orthogonality property of PRN codes is exploited: the received signal is correlated with a local replica of the PRN code under analysis generated with trial values of both code delay and Doppler shift. The process is repeated for several trial values until the cross-correlation exceeds some detection threshold, which occurs for a given combination of code delay and Doppler shift that makes the local replica to be aligned with the code in the received signal. In this situation the satellite is declared to be present, while the tentative values of code delay and Doppler shift at which the signal of interest is located is also provided.

An example of the acquisition architecture of a generic GNSS receiver is shown in Figure 2.3. The cross-correlation is carried out by multiplying the received signal with the local replica, plus a coherent integration with length T_{code} (or N_{scode}, the PRN code duration in samples) through the *integrate and dump* (I&D) block. Notwithstanding, in harsh environments with LOS difficulties, the correlation peak usually suffers from severe attenuation and may become imperceptible. In this situation, it is necessary to

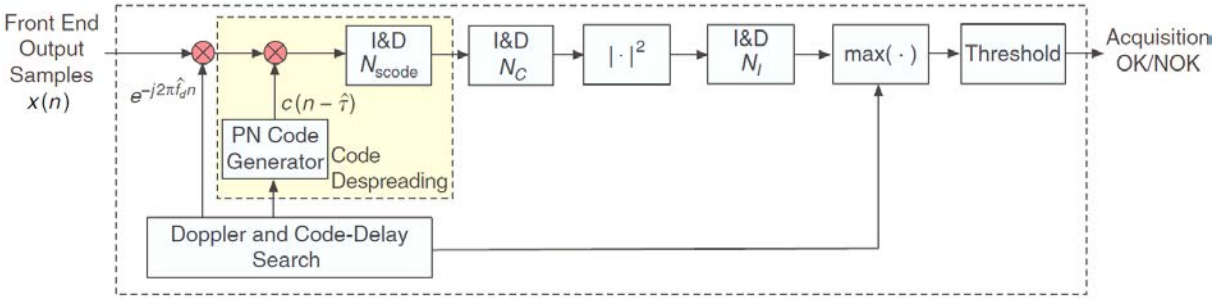

Figure 2.3: Example of acquisition architecture for a GNSS receiver, which incorporates non-coherent integrations to extend the correlation time (*i.e.* high-sensitivity GNSS receiver) [Sec12].

implement *high-sensitivity* detection techniques. Their underlying principle is that the signal component of a few consecutive correlations is strongly correlated, whereas the noise component is completely uncorrelated. Therefore, the addition of several CAFs allows the receiver to accumulate enough energy to detect the signal. As can be observed in Figure 2.3, these techniques are implemented by extending the coherent correlation time N_c times (thus leading to a total coherent integration time of $N_c T_{\text{code}}$). However, it cannot be extended without bound due to the presence of Doppler shift, navigation data bits and phase noise. Thence, coherent integrations are complemented by adding N_I of them in a non-coherent manner (*i.e.* using some non-linear function) [Van02, Lac04]. These are generally named *post-detection integration* (PDI) techniques, a good overview of which can be found in [Gó16].

The 3-D representation of the cross-correlation above for all the possible combinations of trial values is the so-called *cross-ambiguity function* (CAF). Figures 2.4, 2.5 and 2.6 show the CAF for BPSK, $\text{BOC}_{\sin}(1,1)$ and $\text{BOC}_{\cos}(15,2.5)$ modulations presented in Section 2.2.2, respectively, as well as their projection onto the frequency and time domains. The three modulations differ in the latter domain. The use of BOC modulations allows reducing the width of the main triangle and sharpening the main peak of interest, thus improving the accuracy of the measured code delay and, consequently, the user's position. However, secondary peaks at each side of the main one do conversely appear. Even though this may not be problematic for $\text{BOC}_{\sin}(1,1)$, it becomes a serious issue for $\text{BOC}_{\cos}(15,2.5)$: the presence of secondary lobes that are very little apart from the main correlation peak and present similar amplitude poses serious difficulties to distinguish the main peak, particularly in scenarios with low carrier-to-noise ratio (C/N_0). This leads to the problem of *false locks*: due to the ambiguity in the correlation function, the receiver captures a secondary peak instead of the main correct one, which eventually leads

to measured pseudoranges with errors of several meters. Dealing with the detection and mitigation of false locks is a challenging problem, particularly in high-sensitivity GNSS receivers [Gar14], and several methods can already be found in the literature, namely the BPSK-like envelope technique [Bur06], bump jumping [Fin99], double estimator [Hod08], code-subcarrier smoothing [Gal13] and other maximum likelihood (ML)-based techniques such as the double optimization multi-correlator-based estimator (DOME) [Gar15].

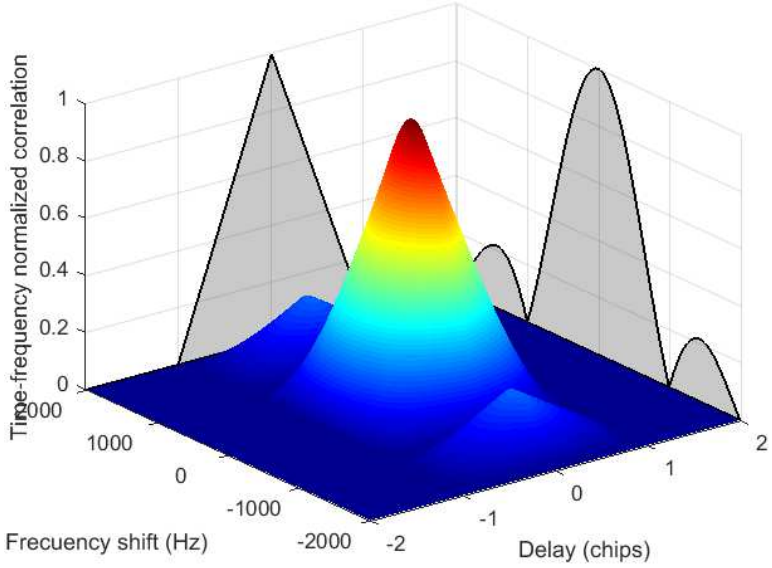

Figure 2.4: CAF for BPSK signal employed in GPS L1 C/A.

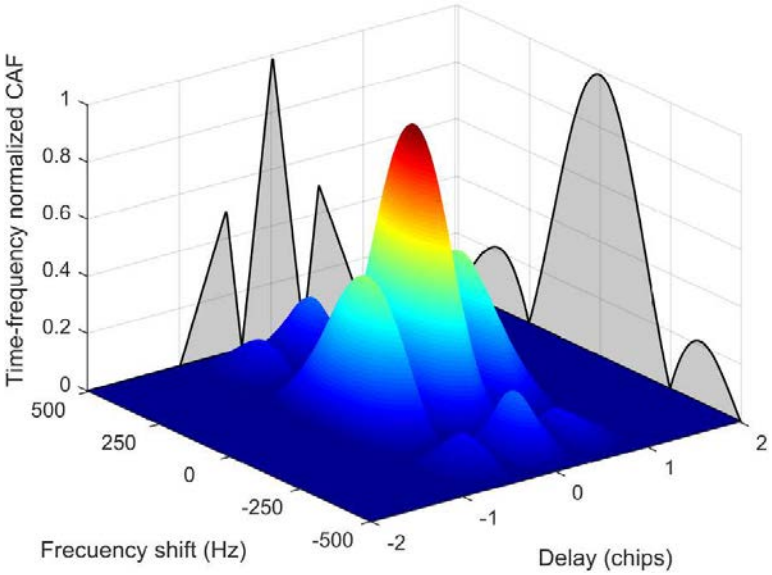

Figure 2.5: CAF for $\mathrm{BOC}_{\sin}(1,1)$ signal employed in Galileo E1BC [Gó18].

As can be anticipated, the code-delay and Doppler-shift discretization scale of the

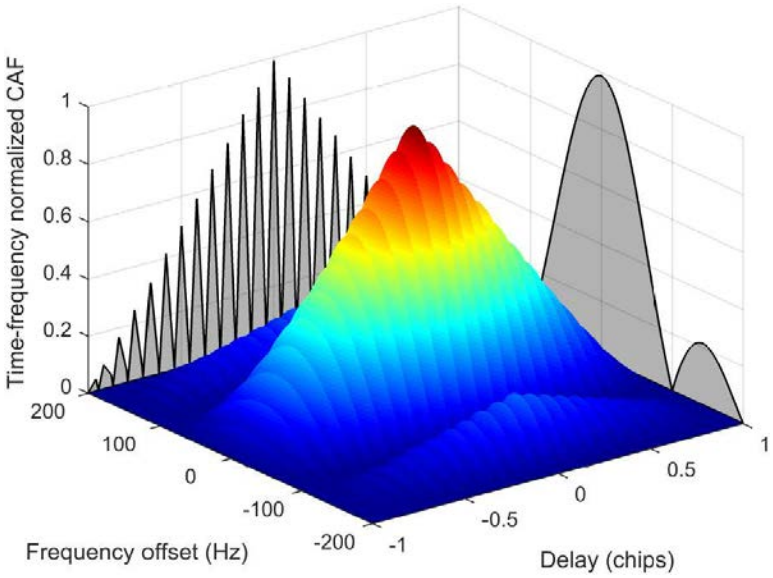

Figure 2.6: CAF for $\mathrm{BOC}_{\cos}(15, 2.5)$ signal being implemented in the Galileo E1 band [Gó18].

CAF determines a trade-off between computational load and speed, and accuracy of the coarse estimates. A way to optimize this aspect is by the use of assisted data, leading to the concept of *assisted GNSS* (A-GNSS). That is, to facilitate to the receiver *a priori* information about the parameters of interest so that the search scale be focused around the true values, thus considerably reducing the computational load and enhancing accuracy. However, assisted data is not always available. In that case, in the efforts made to optimize the computation of the CAF to date, particularly in high-sensitivity GNSS receivers, one of the most relevant methods is the termed *double-FFT* algorithm [Lop06]. It allows implementing the acquisition steps with only simple operations such as additions, products, circular shifts, and the extensive use of FFT processors [Sec12], and becomes one of the most efficient methods to perform a time-frequency search in a wide bi-dimensional region. Moreover, an approach that is coming into vogue at the time of this writing is the use of *cloud computing services* [Luc16a, Luc16b]. In these, the receiver only needs to collect the received samples and send them to the cloud where all the signal processing is carried out remotely using virtually unlimited resources. In this way, the receiver is set free from almost any heavy computational load, thus becoming a suitable solution for handheld receivers where the power supply relies on batteries, such as smartphones.

2.3.3 Tracking stage

The code-delay and Doppler-shift values provided by the acquisition stage are just coarse (*i.e.* rough) estimates that have been obtained by performing a search discretized with some granularity. Such discretization does usually not provide a GNSS receiver with enough accuracy; note that an error in the code delay becomes enormously magnified by the speed of light $c \approx 3 \cdot 10^8$ m/s when converted into meters. Therefore, it is necessary to refine the estimated synchronization parameters obtained from the acquisition stage, so that an accurate solution to the user's position can be provided.

Such refinement can be performed through *open-loop* and *closed-loop* architectures, the latter conforming the so-called tracking stage [Tah12]. Open-loop architectures, also termed snapshot-based architectures, are usually employed in high-sensitivity GNSS receivers by computing the CAF from time to time with a narrow search for the Doppler frequency. They provide robustness advantages in front of signal fading effects versus closed-loop architectures. However, they present the drawbacks of being only implementable when the Doppler shift is small, and the estimated parameters are not as accurate as when employing a tracking stage. For these reasons, the latter is the most commonly used since it is the one allowing to obtain fine estimates of the synchronization parameters. Then, techniques to enhance robustness against signal impairments are designed based on such architecture.

The main objective of the tracking stage is twofold. On the one hand, to refine the code-delay and Doppler-shift estimates provided by the acquisition stage. On the other hand, to accurately follow any possible variation that these parameters may present over time. The underlying idea is to find the set of code-delay and Doppler-shift values so as to generate a local replica of the signal of interest that keeps aligned with the received one by recursively driving the resulting error signal to zero when compared with one another. The estimation is carried out in a joint manner, where each parameter must be determined in the presence of the other one. An illustrative example of a generic closed-loop tracking architecture is shown in Figure 2.7 and, as observed, it can be divided into two parallel sub-architectures: one devoted to carrier tracking, and another one devoted to code tracking.

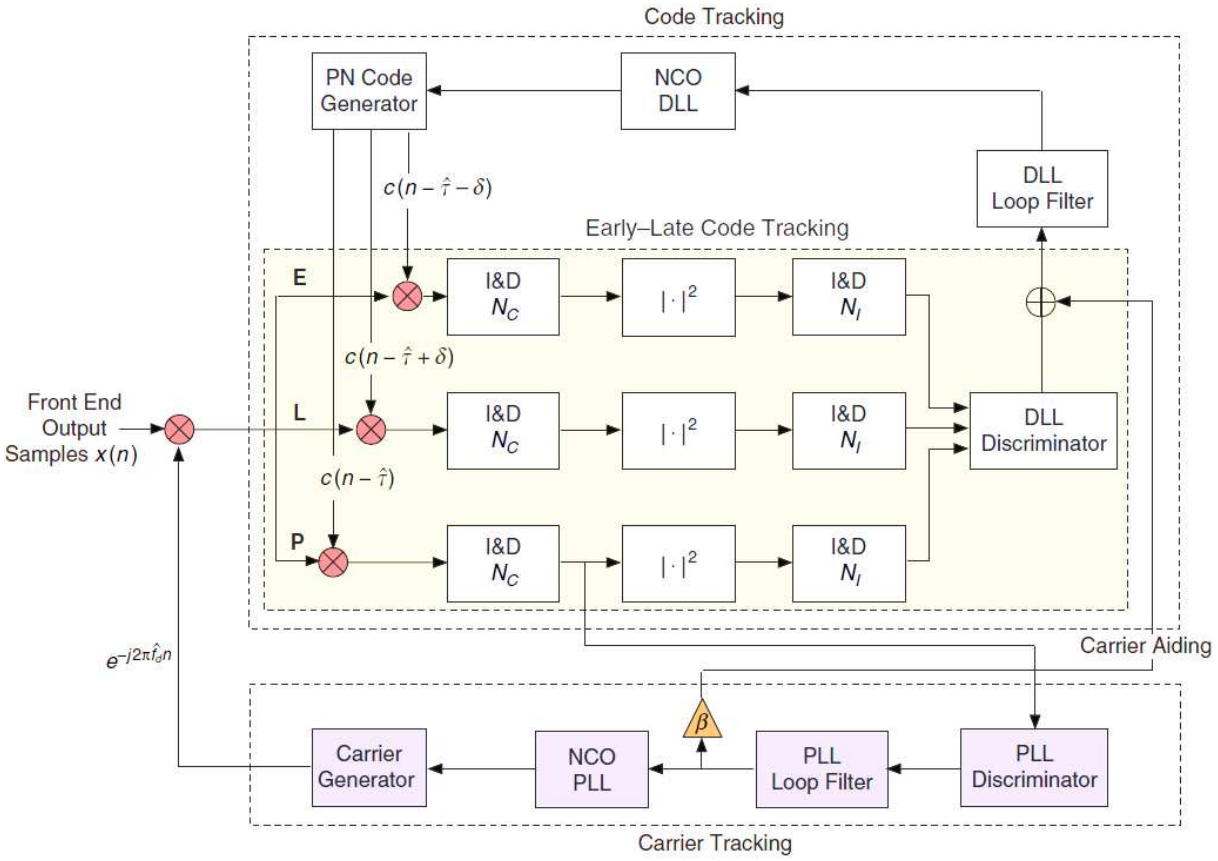

Figure 2.7: General architecture of tracking stage in GNSS receivers [Sec12].

2.3.3.1 Carrier tracking. Phase-Lock Loop

The input signal of the tracking stage for the kth satellite is a baseband signal, with a carrier frequency owing only to the residual Doppler shift:

$$x_k(n) = c_k(n - \tau_k - \delta t_u)e^{j2\pi f_{d,k}n}. \tag{2.2}$$

Therefore, in order to compensate for $f_{d,k}$, the PLL local replica is a carrier generator providing a complex exponential with negative phase given by the estimated Doppler shift at a given time instant n. Then, it is multiplied to the input signal so as to compensate for the complex exponential in (2.3), thus leading to:

$$y_k(n) = c_k(n - \tau_k - \delta t_u)e^{j2\pi f_{d,k}n}e^{-j2\pi \hat{f}_{d,k}n} = c(n - \tau_k - \delta t_u)e^{j2\pi \Delta f_{d,k}n}. \tag{2.3}$$

with $\Delta f_{d,k}$ the possible error in the estimated Doppler shift. The objective is to find the value of $\hat{f}_{d,k}$ so as to drive $\Delta f_{d,k}$ to zero by iterating in the loop. To this end, at iteration n, the result $y_k(n)$ is correlated with a local replica of the code through the so-called *prompt* correlator, which centers such local replica at the last code-delay estimate provided by the

code-tracking loop (see Section 2.3.3.2). Similarly to the acquisition stage, the correlation is carried out by multiplying both signals and adding them in the I&D block in Figure 2.7. The prompt correlator output is then fed to the PLL discriminator, which provides at its output a signal that is proportional to the error in the estimated Doppler shift that still has to be corrected. This result is then filtered through the so-called *loop filter* in order to obtain a smoothed version of the correction to be applied, since the discriminator output is contaminated by the input noise. This is then fed to a *numerically-controlled oscillator* (NCO), which accumulates the loop filter output over time in order to provide the updated Doppler shift to the carrier generator in terms of phase, thus closing the loop.

PLL Discriminators

Carrier disciminators obtain a signal that is proportional to the local replica error to be corrected by applying some function onto the prompt correlator output, denoted as $y_{\mathrm{P}}(\hat{\tau}_k)$, with $\hat{\tau}_k$ representing the estimated code delay. Based on that, there exist two main groups of carrier discriminators:

- **Pure-PLL discriminators** are the most typical ones providing pure phase error estimates at their output. The pure-PLL discriminator most commonly employed in practice is the four-quadrant arctangent (ATAN2),

$$\Delta\theta_{\mathrm{ATAN2}}(\theta_\epsilon) = \arctan 2\left(\frac{\mathrm{Im}\left[y_{\mathrm{P}}(\hat{\tau}_k)\right]}{\mathrm{Re}\left[y_{\mathrm{P}}(\hat{\tau}_k)\right]}\right). \tag{2.4}$$

- **Costas-PLL discriminators** are PLL-type discriminators that tolerate the presence of data modulation on the baseband signal. That is, they are insensitive to abrupt phase changes owing to the bit modulation in the navigation message. The most common Costas-PLL discriminator is the two-quadrant arctangent (ATAN),

$$\Delta\theta_{\mathrm{ATAN}}(\theta_\epsilon) = \arctan\left(\frac{\mathrm{Im}\left[y_{\mathrm{P}}(\hat{\tau}_k)\right]}{\mathrm{Re}\left[y_{\mathrm{P}}(\hat{\tau}_k)\right]}\right). \tag{2.5}$$

Even though they require a high computational burden, pure- and Costas-PLL discriminators have the advantages of presenting a linear response for all input phase values, and providing pure phase error signals at their outputs. Moreover, they constitute the optimal (*i.e.* maximum likelihood) phase estimators at high and low signal-to-noise ratio (SNR). Between both discriminators, an important inconvenient of the Costas ones is that there is a 180-degree ambiguity causing that the detected data bit stream may be normal or inverted. This ambiguity has to be solved, in contrast to pure-PLL discriminators,

thus making the latter the most convenient ones to be employed. Their advantage is that their pull-in range is twice the one for the ATAN. However, the drawback is that they can only be applied on dataless signals, or signals that have undergone some data wipe-off preprocessing. The presence of data bits is usually unavoidable, particularly in GPS L1 C/A. Notwithstanding, it is important to note that all modernized GNSS signals make provisions for dataless carrier tracking in addition to providing data. This is the case, for instance, of Galileo E1BC, which employs a pilot signal (*i.e.* the known secondary code) used purely for signal processing purposes, plus the data channel from which the navigation message is obtained once the signal is captured. In this way, a pure PLL discriminator can eventually be employed.

Although pure- and Costas-PLL discriminators provide the most accurate response, they present the inconvenient of being sensitive to dynamic stress. In that sense, there actually exists a third type of carrier discriminators, the so-called *frequency lock loop* (FLL) discriminators, which present the advantage of being more robust in front of rapid dynamics. However, they monitor the frequency error instead of the phase error, which could eventually be obtained by integrating the former, but again there exists a carrier phase ambiguity that has to be solved afterwards. In addition, when detecting the data bits, they present higher bit error rate (BER) than PLL-based discriminators. FLLs are usually employed during initial signal acquisition, where it is easier to maintain frequency lock than phase lock while performing bit synchronization. Nonetheless, when tracking is in steady state, pure-PLL discriminators are more often used since they produce the most accurate measurements [Kap05].

Third-order loop filters

The input signal of the tracking stage is affected by the thermal noise introduced by the receiver, and thus so is the discriminator output. For this reason, the latter must go through some filtering process in order to remove signal instabilities. As mentioned earlier, this is achieved by the loop filter, which employs a set of gains and integrators in charge for smoothing the noisy signal.

In the carrier loop, a third-order loop filter is usually employed. That is, a filter that is able to track a signal whose dynamics presents a constant non-zero second derivative. This is so because filters with higher order than three are known to suffer from instability issues. The structure of a third-order loop filter is depicted in Figure 2.8. As will be shown in the next section, the filtering performance of a loop filter is determined through the

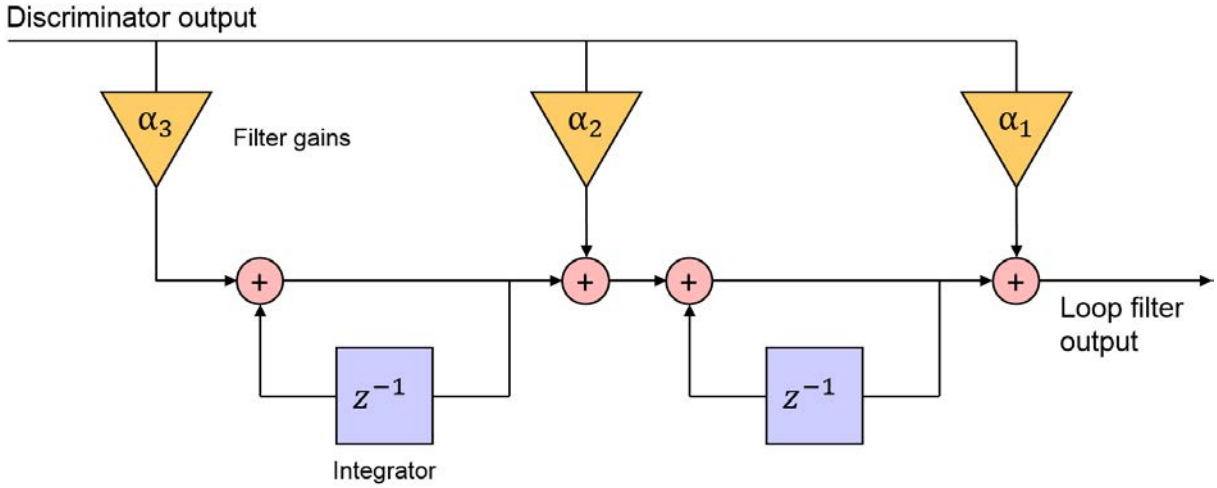

Figure 2.8: Block diagram of third-order loop filter.

filter gains by the so-called *equivalent loop bandwidth*, which becomes a trade-off between noise filtering and dynamics tracking capabilities. That is, the larger the bandwidth, the more reactive to variations in the input dynamics the filter is, but the noise filtering capability degrades in contrast. In practice, a balance between both properties is sought, and the chosen value becomes then reflected onto the filter gains as follows.

Let B_L be the equivalent loop bandwidth in Hz. The natural frequency of a third-order loop filter can be expressed as,

$$\omega_n^{(3)} = \frac{4(bc-1)}{bc^2+b^2-c} \tag{2.6}$$

where $b = 1.1$, $c = 2.4$ [Kap05], and the superscript (3) denotes a filter with third order. The filter gains are then given by,

$$\alpha_1^{(3)} = c\left(\omega_n^{(3)} T_s\right) \tag{2.7}$$

$$\alpha_2^{(3)} = b\left(\omega_n^{(3)} T_s\right)^2 \tag{2.8}$$

$$\alpha_3^{(3)} = \left(\omega_n^{(3)} T_s\right)^3 \tag{2.9}$$

with T_s the sampling time in seconds.

Tracking Threshold and PLL Performance Bounds

The dominant sources of phase error in a GNSS receiver PLL are *phase jitter* and *dynamic stress* errors [Kap05]:

- Jitter owing to **thermal noise**. It is sometimes treated as the only source of carrier tracking error, since the other sources of PLL jitter may be either transient or

negligible. For the ATAN2 discriminator and assuming AWGN reception conditions, it can be computed in dimensions of radians in one-sigma terms as:

$$\sigma_{\theta_{\text{AWGN}}} = \sqrt{\frac{B_L}{C/N_0}\left(1 + \frac{1}{2C/N_0 T_s}\right)} \tag{2.10}$$

with the C/N_0 in linear scale. The jitter in (2.10) can be understood as the performance lower bound (as far as thermal noise is concerned) that a PLL can achieve in terms of mean squared error (MSE) for a given loop bandwidth and C/N_0. When designing PLLs, the statement in the opposite direction is often taken. That is, for a given C/N_0, expression (2.10) can be employed to determine the required loop bandwidth to achieve a given target performance. Expression (2.10) also manifests that, in order to keep a target performance when the C/N_0 varies, the loop bandwidth must also vary accordingly to counteract the former effect. The lower C/N_0, the smaller bandwidth, and viceversa. As will be seen next, this is at odds with the jitter owing to dynamic stress.

- Jitter owing to **dynamic stress**. In a loop filter, the loop order is sensitive to the same order of dynamics [Kap05]. However, the input signal may present higher-order dynamics that exceeds the loop order, and the fact that this is not being accounted for in the filter set-up may also introduce some jitter if its magnitude is considerable. In that sense, for a third-order PLL, the jitter contribution owing to dynamic stress is computed as:

$$\theta_{\text{d}}^{(3)} = 0.4808 \frac{\frac{\delta^3 R}{\delta t^3}}{B_L^3} \tag{2.11}$$

where $\frac{\delta^3 R}{\delta t^3}$ refers to the higher-order dynamics that exceed the PLL loop order, and has dimensions of degrees. For the GNSS tracking problem, this term refers to the *doppler jerk* (*i.e.* the third derivative of phase). In expression (2.11) it is observed that the loop bandwidth is inversely proportional to the jitter. That is, the smaller the bandwidth, the larger the dynamic stress error. This manifests that the loop bandwidth must be wide enough to accommodate the signal (higher-order) dynamics, which becomes at odds with the case for the thermal noise jitter, where the loop bandwidth must be reduced for better noise filtering, as explained above. Therefore, the selection of the PLL loop bandwidth becomes a trade-off between noise filtering and dynamics tracking capabilities; the bandwidth must be as small as possible for better noise filtering, but simultaneously wide enough to be able to track dynamics. Since the dynamic stress jitter is also sensitive to the loop order

(*i.e.* a higher order leads to better dynamic-stress performance), some strategies to find the optimal loop bandwidth rely on increasing the loop order and reducing the noise bandwidth, thus allowing to compensate for both effects simultaneously.

The sources of error affecting the PLL performance are then employed to determine if the estimation error is below the tracking threshold. In practice, under AWGN reception conditions, a conservative rule of thumb for the tracking threshold is that the 3-sigma jitter comprising both thermal noise and dynamic stress contributions must not exceed one fourth of the pull-in range of the PLL discriminator. For the ATAN one used when there is data modulation, the pull-in range equals to π radians. Therefore, the 3-sigma rule must satisfy:

$$3\sigma^{(3)}_{\text{PLL}} = 3\sigma^{(3)}_{\theta_{\text{AWGN}}} + \theta^{(3)}_{\text{d}} \leqslant \frac{\pi}{4} \text{ rad.} \tag{2.12}$$

On the other hand, for the ATAN2 discriminator used when the signal is dataless, the pull-in range equals to 2π radians. Therefore, the 3-sigma rule must satisfy:

$$3\sigma^{(3)}_{\text{PLL}} = 3\sigma^{(3)}_{\theta_{\text{AWGN}}} + \theta^{(3)}_{\text{d}} \leqslant \frac{\pi}{2} \text{ rad.} \tag{2.13}$$

From (2.12) and (2.13), it is observed that the total PLL jitter can be expressed as:

$$\sigma^{(3)}_{\text{PLL}} = \sigma^{(3)}_{\theta_{\text{AWGN}}} + \frac{\theta^{(3)}_{\text{d}}}{3} \tag{2.14}$$

and, as mentioned above, it can be used for design purposes.

2.3.3.2 Code Tracking. Delay-Lock Loop

Once the residual Doppler shift at a given time instant is compensated, the code-tracking loop is in charge of determining the code delay that keeps the local replica aligned with the received signal in the time domain. To this end, the procedure is analogous to the carrier-tracking loop. Notwithstanding, the code loop employs two additional correlators besides the prompt one, the so-called *early* and *late* correlators. These are centered at the code delay of interest plus some shift at each side:

$$y_E(\tau_k) = y_P\left(\tau_k + \frac{\Delta\tau_{E-L}}{2}\right) \tag{2.15}$$

$$y_L(\tau_k) = y_P\left(\tau_k - \frac{\Delta\tau_{E-L}}{2}\right) \tag{2.16}$$

with $\Delta\tau_{E-L}$ the early-late distance which typically corresponds to one chip, and they are employed to facilitate the identification of the main correlation peak. The rest of the loop

remains as in carrier tracking: the correlation results are fed into the DLL discriminator and further smoothed by the loop filter, which indicates to the NCO the corrections to be applied by the PRN code generator for the local replica at the next iteration, thus closing the loop.

It is worth noting that the code tracking loop shown in the previous Figure 2.7 implements the possibility of extending the integration time by combining coherent and non-coherent integrations, in a similar way as in the acquisition stage in Figure 2.3.

DLL Discriminators

Code disciminators obtain a signal that is proportional to the local replica error to be corrected by applying some function of the early, prompt and late correlators, $\{y_{\mathrm{E}}(\tau_k), y_{\mathrm{P}}(\tau_k), y_{\mathrm{L}}(\tau_k)\}$. Code discriminators can be divided into two main groups:

- **Coherent discriminators**. They assume that the carrier frequency is perfectly known. The most common coherent discriminator is the *early-minus-late*, where the output error signal is the difference between the early and late correlators,

$$\Delta\tau_{\mathrm{E\text{-}L,c}}(\tau_k) = \frac{1}{2}\left[y_{\mathrm{E}}(\tau_k) - y_{\mathrm{L}}(\tau_k)\right]. \tag{2.17}$$

- **Non-coherent discriminators**. They are employed when the assumption that the carrier frequency is perfectly known is not true, and thus the prompt correlator output is affected by some carrier phase error. This is the most common situation in practice, and thus we will focus on non-coherent discriminators. There exist several of them in this group: the *non-coherent early-minus-late* operates on the signal envelope instead of the carrier phase error; the *normalized-envelope early-minus-late* includes a normalizing term to reduce the discriminator sensitivity to changes in the signal amplitude, at the expense of higher computational cost; the *quasi-coherent dot-product* discriminator avoids using the non-linearity of raising the correlator output to the second power, while requiring low computational load.

The main advantage of the early-minus-late coherent discriminator is that its response to input code delays is linear. In that sense, the non-coherent discriminator resembling the coherent behavior the most is the termed *coherent dot-product*, which can be employed when the carrier loop is in lock and presents low computational load. In practice, a normalized version is usually employed, the termed *coherent dot-product normalized* to

the power of the prompt correlator output,

$$\Delta\tau_{\text{E-L,normDotProd}}(\tau_\epsilon) = \frac{1}{4}\text{Re}\left[\frac{y_\text{E}(\tau_k) - y_\text{L}(\tau_k)}{y_\text{P}(\tau_k)}\right] \tag{2.18}$$

which is the one providing the most accurate code measurements [Kap05].

Second-order loop filters

In contrast to the third-order loop filter employed in the carrier loop, the code loop usually implements a second-order loop filter, thanks to the use of *carrier aiding* which allows the order of DLL loop filters to be smaller than that of PLL ones, as will be explained next in Section 2.3.3.3. The structure of a second-order loop filter is depicted in Figure 2.9. In this case, the natural frequency of the filter can be expressed as,

$$\omega_n^{(2)} = \frac{4a}{B_L} \tag{2.19}$$

with $a = \sqrt{2}$, and B_L is expressed in Hz. From this, the filter gains are given by,

$$\alpha_1^{(2)} = a\left(\omega_n^{(2)} T_s\right) \tag{2.20}$$

$$\alpha_2^{(2)} = \left(\omega_n^{(2)} T_s\right)^2. \tag{2.21}$$

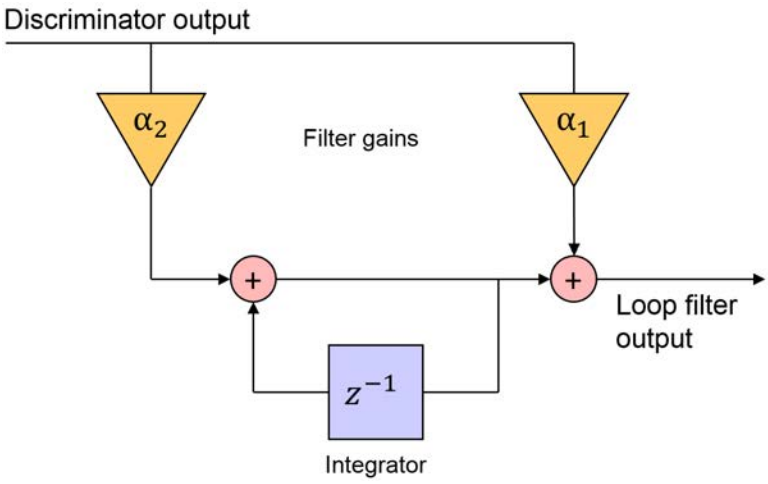

Figure 2.9: Block diagram of second-order loop filter.

DLL Performance Bounds

Similarly to the PLL, the dominant sources of phase error in a GNSS receiver DLL are the *delay jitter* and *dynamic stress* errors.

- Jitter owing to **thermal noise**. For the normalized dot-product discriminator, it can be expressed for a second-order DLL as,

$$\sigma^{(2)}_{\tau_{\text{AWGN}}} = \sqrt{\frac{B_L \Delta\tau_{E-L}}{2C/N_0}\left(1 + \frac{2}{C/N_0 T_s}\right)} \tag{2.22}$$

  with dimensions of chips.

- Jitter owing to **dynamic stress**. For a second-order DLL, it is determined by,

$$\tau^{(2)}_{\text{d}} = \frac{\frac{\delta^2 R}{\delta t^2}}{\omega^{(2)}_n} \tag{2.23}$$

  where $\frac{\delta^2 R}{\delta t^2}$ refers to the higher-order dynamics exceeding the DLL loop order, and has dimensions of chips. For the GNSS tracking problem, this term refers to the *delay jerk* (*i.e.* the second derivative of code delay).

In reality, though, the use of carrier-aided code is practically a universal design practice that effectively removes the code dynamics, as will be explained in the next section. As a consequence, the DLL jitter owing to the dynamic stress is usually negligible with respect to the one owing to thermal noise, and the total DLL jitter becomes practically $\sigma^{(2)}_{\text{DLL}} \approx \sigma^{(2)}_{\tau_{\text{AWGN}}}$.

2.3.3.3 Carrier Aiding of Code Loop

As already explained, GNSS receivers base their position estimation on the observed distance to the different satellites in terms of transmission time. However, such observations are distorted by the presence of residual dynamics, which is a physical magnitude that affects both code and carrier measurements and must be compensated for.

In that sense, the concept of carrier aiding is based on the fact that carrier phase measurements are much less noisy than code delay measurements [Kap05] in about an order of magnitude [Mit13], and thus present much better quality. The idea of carrier aiding is to take advantage of this feature by providing the information about the estimated carrier dynamics to the code-delay estimation, as *a priori* information, in such a way that the dynamics contribution onto the code delay can be virtually eliminated. This allows the DLL to significantly reduce its order and loop bandwidth, so that it presents an enhanced robustness and the effect of noise onto the code-delay measurements can be further reduced.

Carrier aiding was already devised in the previous Figure 2.7, where the output of the PLL loop filter was added to the output of the DLL discriminator. In order to apply the concept in the tracking stage, though, it must be noted that the effect of residual dynamics is not the same in both carrier-phase and code-delay measurements. This is due to the fact that the chip rate is much smaller than the carrier frequency. For the case of GPS L1 C/A and Galileo E1BC, the spreading code chip rate equals to $R_{\text{chip}} = 1.023$ Mchips/s, which can be understood as a chip frequency of 1.023 MHz. On the other hand, the carrier frequency equals to $f_c = 1575.42$ MHz. As a consequence, the carrier dynamics is a factor of,

$$\beta \doteq \frac{f_c}{R_{\text{chip}}} = \frac{1575.42 \text{ MHz}}{1.023 \text{ MHz}} \approx 1540 \tag{2.24}$$

times faster than code-delay dynamics. Therefore, for the particular case of GPS L1 C/A and Galileo E1BC, the Doppler aiding to be introduced to the DLL corresponds to the estimated carrier dynamics (*i.e.* the frequency shift at the output of the PLL loop filter) divided by the constant factor β in (2.24).

2.3.4 PVT Module

The PVT module is in charge of determining the user's position by making use of the information coming from the tracking stage. As already explained, the process is based on measuring the propagation time of a given point within the signals (*i.e.* a given chip) since they leave from the different satellites, until reaching the receiver. For each satellite, such propagation time can be determined by reading the time stamp in the signal, and also the receiver clock at the very same time instant. In the former, the information coming from the tracking stage is employed to keep the receiver synchronized with the received signal to then successfully decode the navigation message and retrieve the time stamp, a process that requires a time to first fix (TTFF) of around 6 seconds to be carried out [Mut12]. In terms of PVT, such time stamp is also referred to as the *time-of-week* (TOW). Then, by multiplying the difference of both time measurements by the speed of light, one obtains the distance between the satellite under study and the receiver, the so-called *range*, which for the kth satellite equals to the geometric distance:

$$r_k = ||\mathbf{r}_k - \mathbf{r}_u|| = \sqrt{(x_k - x_u)^2 + (y_k - y_u)^2 + (z_k - z_u)^2} \tag{2.25}$$

where $\{x_k, y_k, z_k\}$ and $\{x_u, y_u, z_u\}$ are respectively the satellite and user positions in ECEF coordinates. In practice, though, the obtained measurements present a bias δt_u due to

the receiver clock offset with respect to the GNSS time, as previously explained, plus additional error sources such as the delay introduced when propagating through the ionosphere and troposphere. As a consequence, the measured distances are not absolute distance measurements, and they are therefore referred to as *pseudoranges*, and can be expressed as follows,

$$\rho_k = r_k + c\delta t_u + I_k + T_k + \epsilon_k \tag{2.26}$$

where I_k and T_k are the ionospheric and tropospheric propagation delays from the kth satellite to the receiver, and ϵ_k refers to other effects that may remain unmodeled (*i.e.* additional measurement errors).

Expression (2.26) is the basis for computing the user's position. In practice, the navigation messages usually include correction parameters to compensate ionospheric and tropospheric effects. This means that atmospheric corrections are readily subtracted from the pseudorange equation in (2.26),

$$\tilde{\rho}_k \doteq r_k + c\delta t_u + \epsilon_k \tag{2.27}$$

and the positioning problem mainly boils down to finding the set of $\{x_u, y_u, z_u\}$ parameters in (2.25), plus the receiver clock offset δt_u. That is, 4 unknowns that have thus to be solved using at least 4 measurements of the form in (2.26), leading to the following system:

$$\begin{bmatrix} \tilde{\rho}_1 \\ \tilde{\rho}_2 \\ \vdots \\ \tilde{\rho}_L \end{bmatrix} = \begin{bmatrix} r_1 \\ r_2 \\ \vdots \\ r_L \end{bmatrix} + c\delta t_u \begin{bmatrix} 1 \\ 1 \\ \vdots \\ 1 \end{bmatrix} + \begin{bmatrix} \epsilon_1 \\ \epsilon_2 \\ \vdots \\ \epsilon_L \end{bmatrix}. \tag{2.28}$$

which is nonlinear due to the norm operator within r_k.

There exist two main families of approaches to solve for the nonlinear problem in (2.28):

- **Linearization-based** methods. They are based on the linearization with respect to the position solution, $\mathbf{r}_u \doteq [x_u, y_u, z_u]^T$. They are iterative methods that require an approximate value of the receiver's position to start operating.
- **Closed-form** methods. They are based on the Bancroft algorithm [Ban85] and have the advantage of providing the solution in closed form, thus not being iterative methods and not requiring an initial estimate of the user's position.

In this section we will focus on the linearization-based methods, since very few iterations are actually needed in practice, and they provide better accuracy than closed-form methods [Ló12]. The geometric distance r_k is linearized around a tentative value of the user's position, $\mathbf{r}_{u,0} \doteq [x_{u,0}, y_{u,0}, z_{u,0}]^T$, by keeping the first-order term of the Taylor series expansion:

$$r_k = ||\mathbf{r}_k - \mathbf{r}_u|| \approx ||\mathbf{r}_k - \mathbf{r}_{u,0}|| - \frac{(\mathbf{r}_k - \mathbf{r}_{u,0})^T}{||\mathbf{r}_k - \mathbf{r}_{u,0}||}\mathbf{\Delta r}_u \tag{2.29}$$

where $\mathbf{\Delta r}_u \doteq \mathbf{r}_u - \mathbf{r}_{u,0}$, and $\mathbf{r}_k \doteq [x_k, y_k, z_k]^T$ is the position of the kth satellite, which can be determined using the ephemerides decoded from the navigation message. For convenience, we define the following parameters that will be used to build the system of equations to be solved:

$$\alpha_{x,k} \doteq \frac{x_k - x_{u,0}}{||\mathbf{r}_k - \mathbf{r}_{u,0}||} \tag{2.30}$$

$$\alpha_{y,k} \doteq \frac{y_k - y_{u,0}}{||\mathbf{r}_k - \mathbf{r}_{u,0}||} \tag{2.31}$$

$$\alpha_{z,k} \doteq \frac{z_k - z_{u,0}}{||\mathbf{r}_k - \mathbf{r}_{u,0}||}. \tag{2.32}$$

Now, using the approximation above and collecting the measurements from all L satellites, the system to be solved is as follows:

$$\mathbf{\Delta}\rho = \mathbf{H}\mathbf{\Delta u} + \epsilon \tag{2.33}$$

where,

$$\mathbf{\Delta}\rho \doteq \begin{bmatrix} \tilde{\rho}_1 - r_1, & \tilde{\rho}_2 - r_2, & \cdots & \tilde{\rho}_L - r_L \end{bmatrix}^T \tag{2.34}$$

$$\mathbf{H} \doteq \begin{bmatrix} \alpha_{x,1} & \alpha_{y,1} & \alpha_{z,1} & 1 \\ \alpha_{x,2} & \alpha_{y,2} & \alpha_{z,2} & 1 \\ \vdots & \vdots & \vdots & \vdots \\ \alpha_{x,L} & \alpha_{y,L} & \alpha_{z,L} & 1 \end{bmatrix} \tag{2.35}$$

$$\mathbf{\Delta u} \doteq \begin{bmatrix} \mathbf{\Delta r}_u \\ c\Delta t_u \end{bmatrix} = \begin{bmatrix} x_u - x_{u,0} \\ y_u - y_{u,0} \\ z_u - z_{u,0} \\ c\left(\delta t_u - \delta t_{u,0}\right) \end{bmatrix} \tag{2.36}$$

$$\epsilon \doteq \begin{bmatrix} \epsilon_1, & \epsilon_2, & \cdots & \epsilon_L \end{bmatrix}^T. \tag{2.37}$$

In order to minimize the impact of the latter, the system in (2.33) is solved through a weighted least-squares (WLS) approach,

$$\widehat{\boldsymbol{\Delta}\mathbf{u}}_{\mathrm{WLS}} = \left(\mathbf{H}^T\mathbf{W}\mathbf{H}\right)^{-1}\mathbf{H}^T\mathbf{W}\boldsymbol{\Delta}\rho \tag{2.38}$$

where $\mathbf{W}$ is a positive-definite weighting matrix that introduces weighting factors to give more or less importance to each of the measurements according to some criterion. For instance, they can be used to emphasize the contributions of those osbervables that are deemed to be more reliable [Kay93]. On the other hand, note that the obtained solution refers to the corrections to be applied onto the tentative user position $\mathbf{r}_{u,0}$. This process is iterated again, until the estimated corrections are close to zero.

For simplicity, the standard least-squares (LS) solution to the problem in (2.33) is often employed:

$$\widehat{\boldsymbol{\Delta}\mathbf{u}}_{\mathrm{LS}} = \left(\mathbf{H}^T\mathbf{H}\right)^{-1}\mathbf{H}^T\boldsymbol{\Delta}\rho \tag{2.39}$$

which is nothing but the WLS solution in (2.38) substituting the weighting matrix $\mathbf{W}$ by an identity matrix. Notwithstanding, the WLS is found to provide better performance when it is known that some measurements are of better quality than others. Several criteria to quantify the quality of GNSS measurements can be found in the literature. Some works [Kap05] base the weights on the elevation angle of the satellite as seen by the receiver, as a measurement related to multipath and tropospheric errors. The lower the elevation angle, the more prone to suffer from these effects the receiver is. Other works base the weights on the measured C/N_0 [Li11, Wez14] as a global parameter encompassing the overall quality of signals. More advanced efforts combine the two previous criteria into one single way to compute an overall set of weights [Tay13].

Positioning Solutions for High-Sensitivity GNSS Receivers

As explained above, the receiver decodes the navigation message coming from the satellites in order to retrieve the TOW at which signals have been sent. This approach is sometimes referred to as *fine-time* positioning. Notwithstanding, in high-sensitivity receivers, the low C/N_0 poses a serious concern in decoding the navigation message. That is, the navigation message cannot be decoded reliably, and the orbital parameters must therefore be downloaded from some external source. As a consequence, the satellites transmit time is also unknown, thus hampering the operation of GNSS receivers since pseudoranges cannot be built.

In short, when the navigation message from the received signal cannot be used, the receiver must rely on external assistance data to compute a reliable position fix, and

sometimes only coarse data is available, particularly the TOW. In this situation, the mostly-adopted solution is to fine-estimate the TOW as part of the navigation solution [Ako02, Ako09]. That is, by introducing an additional unknown to the system in (2.33). This approach presents some inconvenients, such as the need for one more satellite measurement, a more precise tentative user position $\mathbf{r}_{u,0}$, an approximate TOW accurate to within a few seconds, and requiring to solve for integer millisecond ambiguity and to correct integer-millisecond rollovers [Van09]. However, estimating the TOW presents succulent advantages even for non-high-sensitivity receivers, such as faster TTFF (*i.e.* the 6-second transient period is eliminated), and the ability to obtain a position fix without having to decode the navigation message even in harsh environments, which leads to energy saving in handheld receivers.

The solution presented above is referred to as *coarse-time* positioning, and it relies on computing the radial velocity of the different satellites, or pseudorange rates. That is, for the kth satellite, the pseudorange rate or radial velocity is determined as,

$$v_k = \frac{f_{d,k}}{f_c} c \tag{2.40}$$

where $f_{d,k}$ is the Doppler shift for the kth satellite provided by the tracking stage. Then, the system in (2.33) remains as is, but a new element is introduced into matrices $\mathbf{H}$ and $\mathbf{\Delta u}$,

$$\mathbf{H} \doteq \begin{bmatrix} \alpha_{x,1} & \alpha_{y,1} & \alpha_{z,1} & 1 & v_1 \\ \alpha_{x,2} & \alpha_{y,2} & \alpha_{z,2} & 1 & v_2 \\ \vdots & \vdots & \vdots & \vdots & \vdots \\ \alpha_{x,L} & \alpha_{y,L} & \alpha_{z,L} & 1 & v_N \end{bmatrix} \tag{2.41}$$

$$\mathbf{\Delta u} \doteq \begin{bmatrix} x_u - x_{u,0} \\ y_u - y_{u,0} \\ z_u - z_{u,0} \\ c\left(\delta t_u - \delta t_{u,0}\right) \\ c\left(\tau_s - \tau_{s,0}\right) \end{bmatrix} \tag{2.42}$$

with τ_s the TOW to be fine-estimated, thus manifesting that at least 5 measurements are needed for PVT computation. In this way, high-sensitivity GNSS receivers can compute their position without decoding the navigation message, as long as the initial tentative TOW is located in the vicinity of the true TOW.

Multi-Constellation Hybridization

The advent of new GNSS constellations operating complementarily to GPS opens the door to multi-constellation positioning. That is, the determination of the user position by simultaneously combining measurements coming from satellites belonging to different constellations. This has been already done by the author of this thesis during his research stay at ESA-ESTEC in [Loc17], and the main advantage comes in terms of enhanced positioning availability owing to the increased number of operative satellites, as well as enhanced accuracy particularly when using Galileo BOC signals.

We will now explain the notions of multi-constellation positioning by combining open service measurements from GPS and Galileo. The main aspect to be taken into account is that GPS measurements are referenced to the GPS time (GPST), whereas the ones for Galileo are referenced to the Galileo system time (GST). GPST and GST are not equal time references, and hence there exists an additional time offset between GPS and Galileo measurements, known in the literature as the GPS-Galileo time offset (GGTO) [Van07], which must be accounted for to successfully determine the PVT.

There are two main ways to determine the GGTO:

- Determination at **system level**. The GGTO information is comprised within the navigation message, and can thus be retrieved from the received signal if decoding is possible. The main advantage is that no additional measurements are required, but it presents the inconvenient of requiring a minimum acceptable C/N_0.
- Determination at **user level**. Similarly to the TOW, the GGTO can be estimated as part of the navigation solution by considering an additional unknown into the system in (2.33). This has the advantage of enabling PVT computation when the navigation message cannot be decoded, but the main drawback is that one more measurement is required.

To estimate the GGTO as part of the navigation solution, it is enough to think that the GGTO is nothing but a time offset between GPS and Galileo measurements. Therefore, it suffices to select either GPST or GST as the reference time scale, and indicate in the system in (2.33) whether the corresponding measurements are either from GPS or Galileo.

That is, an additional unknown is introduced as follows:

$$\mathbf{H} \doteq \begin{bmatrix} \alpha_{x,1} & \alpha_{y,1} & \alpha_{z,1} & 1 & v_1 & \phi_1 \\ \alpha_{x,2} & \alpha_{y,2} & \alpha_{z,2} & 1 & v_2 & \phi_2 \\ \vdots & \vdots & \vdots & \vdots & \vdots & \vdots \\ \alpha_{x,L} & \alpha_{y,L} & \alpha_{z,L} & 1 & v_L & \phi_L \end{bmatrix} \tag{2.43}$$

$$\mathbf{\Delta u} \doteq \begin{bmatrix} x_u - x_{u,0} \\ y_u - y_{u,0} \\ z_u - z_{u,0} \\ c\left(\delta t_u - \delta t_{u,0}\right) \\ c\left(\tau_s - \tau_{s,0}\right) \\ c\left(\tau_{\mathrm{GGTO}} - \tau_{\mathrm{GGTO},0}\right) \end{bmatrix} \tag{2.44}$$

with τ_{GGTO} the GGTO to be estimated, and ϕ_k equals either 1 or 0 depending on the chosen time scale. If GPST has been selected, those ϕ_k corresponding to Galileo satellites are set to 1, whereas those corresponding to GPS are set to 0. If GST has been selected, the opposite applies.

2.4 Conclusions

This chapter has introduced the foundations on GNSS operation and the principles for finding one's position using ranging signals coming from different satellites orbiting around the Earth. A description of the three main segments conforming a GNSS deployment has been provided, and the basic concepts regarding the structure of the employed signals have been presented, placing the main focus on GPS and Galileo OS signals. Then, the different stages that GNSS receivers implement to process the satellite signals have been widely described. These are mainly the receiver's front-end for analog-to-digital signal processing, the acquisition and tracking stages, and the PVT module. The latter is the one that determines the navigation solution using the information processed in the previous modules, and with a look into the future of GNSS, some practical strategies to enable GNSS positioning under harsh environments and by using multi-constellation measurements have been explained. These are namely the estimation of the inter-constellation

time offset and the TOW as part of the navigation solution, the latter opening the door to positioning without decoding the navigation message.

Once the fundamental concepts of GNSS have been introduced, the main focus of this dissertation is on the tracking stage. It is in charge of refining the code delay and frequency shift estimates provided by the acquisition stage, and tracking any possible variations of these parameters over time using a closed-loop architecture. A fine estimation of these parameters is indispensable to provide a positioning solution with high accuracy. In that sense, the tracking stage is divided into two sub-functions, namely the carrier- and code-delay tracking loops. Both are based on the same idea: to find the synchronization parameters that keep the local replica aligned with the received signal. To this end, the discriminators provide signals that are functions of the synchronization errors that still have to be corrected. These signals are usually noisy, and thus they are then filtered through the PLL and DLL loop filters. However, this conventional solution is known to experience serious robustness troubles when operating in harsh environments, while in addition, the presence of ionospheric scintillation has a detrimental effect onto the received measurements, thus severely hampering the proper determination of the synchronization parameters. Therefore, it is necessary to deal with the above phenomena and provide clean estimates of the synchronization parameters in spite of the presence of ionospheric scintillation, in order to ultimately provide a high-accuracy positioning solution. This dissertation addresses this problem at the tracking stage throughout the remaining chapters by means of Kalman filter-based techniques.

Chapter 3

Kalman Filter-Based Techniques for GNSS Carrier Tracking

3.1 Motivation

Carrier tracking is one of the core tasks carried out within a GNSS receiver, with the aim of determining the synchronization parameters that keep the receiver aligned with the measured signal, and tracking any possible variation over time of these parameters. To this end, conventional GNSS receivers equip the PLL architecture presented in Chapter 2 with a loop filter, which is an easy-to-implement structure that suffices to properly operate in open-sky environments for which GNSS was originally conceived. Notwithstanding, the extension of GNSS toward environments with harsher working conditions poses a serious concern to the operation of conventional PLLs, which are known to experience serious trouble owing to propagation impairments and rapidly-time-varying channel conditions.

A way to circumvent the above limitation is to reformulate the problem of carrier tracking by making use of the general framework of optimal minimum mean squared error (MMSE) estimation. For stationary signal and noise, the solution to this problem is known to be given by the Wiener filter. As a matter of fact, a generalization of this filter is available for the case of signals whose parameters evolve according to some state-space model. Interestingly, this is the case of carrier phase (and its successive derivatives) in GNSS systems. Such a generalization is the so-called Kalman filter [Kal60], which estimates the parameters of interest in a sequential (*i.e.* sample-by-sample) manner [Kay93].

There exists a tight and natural link between Kalman filtering and conventional PLL-based tracking, since the latter can be proven to be nothing but a particular case of the Kalman filter with constant gains [Pol73, Pat99]. Notwithstanding, the key advantage of the Kalman filter is that it can keep on with the estimation process even if the signal dynamics assumed in the model does not coincide exactly with the actual signal one, thus adding a very valuable degree of robustness. This is certainly the main reason why Kalman filter architectures are widely being proposed for robust carrier tracking in the existing literature [Cas80, Hin88, Hae89, Cla93, Zha08b, Zha08a, Del10]. The Kalman filter fits very well into the closed-loop architecture of the tracking stage in GNSS receivers, thus becoming the optimal way to perform GNSS carrier tracking owing to the reasons above. The use of Kalman filters can thus be understood as the natural improvement to conventional PLLs.

This chapter presents the foundations of linear Kalman filtering. First, the underlying idea is introduced, as well as the formulation of the state-space and observation models. The recursive equations for parameter estimation are presented, and the basic guidelines for the filter set-up and tuning are provided. Then, the formulation of the Kalman filter for the particular problem of GNSS carrier tracking is presented, leading to the carrier-dynamics Kalman filter denoted henceforth as KF, for which the theoretical bounds that allow predicting the filter performance are then described as well. Such bounds are typically expressions that are solved by numerical or recusive evaluation. In this sense, in Section 3.5 we propose the derivation of an approximation for the convergence time of kinematic Kalman filters with any order in form of a closed-form upper bound. In the same line, in Section 3.7 we propose the derivation of an approximation for the steady-state performance of second-order kinematic Kalman filters in form of a closed-form lower bound.

3.2 Fundamentals of Kalman Filtering

The basic idea of the Kalman filter can be described using the representation shown in Figure 3.1. There is a given system whose behavior as a function of time is internally controlled by a set of parameters, denoted henceforth as states, which are stacked into the so-called state vector $\mathbf{x}(n)$. The objective of the Kalman filter is to provide an estimate of $\mathbf{x}(n)$. However, a direct access to the system state vector is unfortunately not available. Instead, the system provides a set of outputs that are stacked into the vector $\mathbf{y}(n)$ and are related to the system states through some function. In addition, the system outputs are

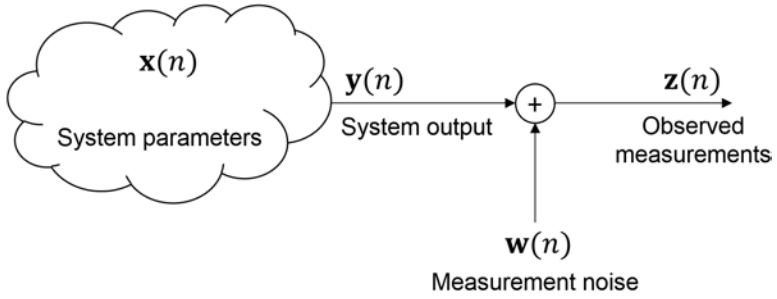

Figure 3.1: Schematic model describing the fundamental idea of the Kalman filter.

usually corrupted by some measurement noise $\mathbf{w}(n)$, thus giving rise to the measurements $\mathbf{z}(n)$ which are actually the ones the observer can work with.

In this context, the aim of the Kalman filter is to provide an estimate of the state vector $\mathbf{x}(n)$ at every time instant n based on observing the set of noisy measurements $\mathbf{z}(n)$.

3.2.1 State-Space and Observation Models

The Kalman estimation problem is an iterative process based on propagating two signal models over time: one describing the time evolution of the system parameters and one for the noisy measurements that are obtained from such system.

- **State-space model**. The time evolution of the system parameters is governed by some function that is modeled within the Kalman filter using a given state-space model. That is, the propagation from $\mathbf{x}(n-1)$ to $\mathbf{x}(n)$ follows a signal model that, in the linear case, corresponds to a linear transformation given by the so-called *transition matrix* $\mathbf{F}(n)$. When the Kalman model does not fully match the actual model of the system parameters, some model mismatch errors appear in addition. The latter are modeled through the so-called *process noise* $\mathbf{q}(n)$, which is usually zero-mean with covariance matrix $\mathbf{V}(n)$. The process noise propagates to the Kalman states through a *state-weighting matrix* $\mathbf{G}(n)$.

  With these observations, the so-called *Kalman state transition equation* is built:

$$\mathbf{x}(n) = \mathbf{F}(n-1)\mathbf{x}(n-1) + \mathbf{G}(n-1)\mathbf{q}(n-1) \tag{3.1}$$

  where the overall process noise covariance matrix becomes $\mathbf{Q}(n) \doteq \mathrm{E}\left[\mathbf{G}(n)\mathbf{q}(n)\mathbf{q}^H(n)\mathbf{G}^H(n)\right]$.

- **Observation model**. As explained above, the observed measurements consist of the system outputs corrupted by some *measurement noise* $\mathbf{w}(n)$, which is usually modeled as a zero-mean Gaussian process with covariance matrix $\mathbf{R}(n)$. The system outputs are related to the system states through some function. Thus, in the linear case, the system outputs can be expressed as a linear transformation of the states given by the so-called *observation matrix* $\mathbf{H}(n)$. This leads to the following *measurement equation*:

$$\mathbf{z}(n) = \mathbf{H}(n)\mathbf{x}(n) + \mathbf{w}(n) \tag{3.2}$$

3.2.2 The Kalman Filter Recursion

In the Kalman filtering problem, the optimal estimate of $\mathbf{x}(n)$ under the MMSE criterion can be formulated as the mean value conditioned to the available information,

$$\hat{\mathbf{x}}(n) = \mathrm{E}\left[\mathbf{x}(n)|z(0), z(1), ..., z(n)\right]. \tag{3.3}$$

which is the estimated state vector at time instant n, with associated state estimation covariance matrix,

$$\mathbf{\Sigma}_{\mathbf{x}}(n) \doteq \mathrm{E}\left[\left(\hat{\mathbf{x}}(n) - \mathbf{x}(n)\right)\left(\hat{\mathbf{x}}(n) - \mathbf{x}(n)\right)^{H}\right]. \tag{3.4}$$

The solution to this MMSE estimation problem can be iteratively computed (*i.e.* in a sequential manner), and considering (3.3) as the starting point, leads to the following recursion [Kay93, Sim06]:

1. **State propagation**. Generate a prediction of the state vector for time instant n based on the measurements up to time instant $n-1$. To do so, apply the optimal MMSE estimate of $\mathbf{x}(n)$ in (3.1) according to (3.4):

$$\mathrm{E}\left[\mathbf{x}(n)\right] = \mathrm{E}\left[\mathbf{F}(n-1)\mathbf{x}(n-1)\right] + \mathrm{E}\left[\mathbf{G}(n-1)\mathbf{w}(n-1)\right] = \mathbf{F}(n-1)\mathrm{E}\left[\mathbf{x}(n-1)\right] \tag{3.5}$$

   where the zero-mean property of $\mathbf{w}(n)$ has been employed, eventually leading to,

$$\hat{\mathbf{x}}(n|n-1) = \mathbf{F}(n-1)\hat{\mathbf{x}}(n-1). \tag{3.6}$$

   The associated state prediction covariance matrix is given by,

$$\mathbf{\Sigma}_{\mathbf{x}}(n|n-1) = \mathbf{F}(n-1)\mathbf{\Sigma}_{\mathbf{x}}(n-1)\mathbf{F}^{H}(n-1) + \mathbf{Q}(n-1) \tag{3.7}$$

   where the transition matrix $\mathbf{F}(n)$ is used to propagate the matrix in a similar way as in the state vector.

2. **Measurement propagation**. Generate a prediction of the measurement for time instant n based on the predicted state vector in (3.6). This is done similarly to the state vector prediction, in the sense that the optimal MMSE estimate for $\mathbf{z}(n)$ is the expected value of (3.2):

$$\hat{\mathbf{z}}(n) = \mathrm{E}\left[\mathbf{z}(n)\right] = \mathrm{E}\left[\mathbf{H}(n)\mathbf{x}(n)\right] + \mathrm{E}\left[\mathbf{w}(n)\right] = \mathbf{H}(n)\mathrm{E}\left[\mathbf{x}(n)\right] \tag{3.8}$$

where the zero-mean property of $\mathbf{w}(n)$ has been employed, eventually leading to,

$$\hat{\mathbf{z}}(n) = \mathbf{H}(n)\hat{\mathbf{x}}(n|n-1). \tag{3.9}$$

This is then subtracted from the actual input measurement $\mathbf{z}(n)$, thus giving an error as a result that is usually denoted as the *innovation sequence*:

$$\mathbf{e}(n) \doteq \mathbf{z}(n) - \hat{\mathbf{z}}(n) \tag{3.10}$$

3. **State correction**. Employ the information provided by the new observable (contained within the innovation sequence) to correct the predicted state using the Kalman gains at time instant n:

$$\hat{\mathbf{x}}(n) = \hat{\mathbf{x}}(n|n-1) + \mathbf{K}(n)\mathbf{e}(n) \tag{3.11}$$

where the Kalman gains can be computed using the predicted state covariance matrix as follows,

$$\mathbf{K}(n) = \mathbf{\Sigma}_{\mathbf{x}}(n|n-1)\mathbf{H}^H(n)\left(\mathbf{R}(n) + \mathbf{H}(n)\mathbf{\Sigma}_{\mathbf{x}}(n|n-1)\mathbf{H}^H(n)\right)^{-1}. \tag{3.12}$$

Associated to (3.11) is the corrected state covariance matrix $\mathbf{\Sigma}_{\mathbf{x}}(n)$, which reduces the variance of the state prediction and can also be computed as a correction onto the predicted state covariance matrix using the Kalman gains in (3.12),

$$\mathbf{\Sigma}_{\mathbf{x}}(n) = \left(\mathbf{I} - \mathbf{K}(n)\mathbf{H}(n)\right)\mathbf{\Sigma}_{\mathbf{x}}(n|n-1). \tag{3.13}$$

With this, the loop is closed and the algorithm starts over at step 1 for the next time instant.

The steps above implementing the recursive Kalman filter are depicted in a more visual manner in Figure 3.2.

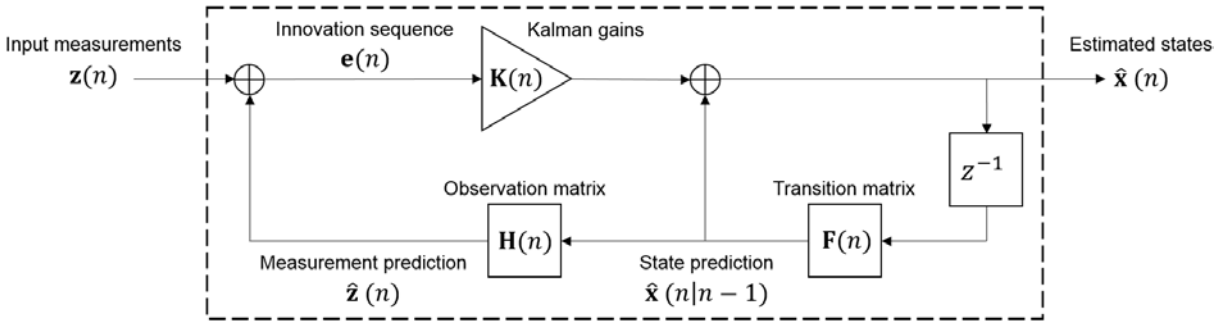

Figure 3.2: Block diagram of the Kalman filter closed-loop (*i.e.* recursive) architecture.

3.2.3 Kalman Filter Set-Up and Tuning

The Kalman filter performance is driven by the Kalman gains. In that sense, according to (3.12), there are other matrices apart from $\mathbf{F}(n)$ and $\mathbf{H}(n)$ that also play a key role in the estimation performance. These are namely the initial state, measurement noise and process noise covariance matrices.

The interesting point about these matrices is that they allow providing the Kalman filter with some *a priori* information about the parameters to be estimated, or the actual working conditions, which helps the Kalman throughout the estimation process. This is indeed a differential feature of the Kalman filter with respect to the PLL, and the way to set-up or tune these matrices to optimize performance is explained next.

Measurement Noise Covariance Matrix

The measurement noise covariance matrix $\mathbf{R}(n)$ depends directly on the noise of the Kalman input measurements. Typically, this information can be estimated during operation of the Kalman filter, or even known in advance, and thus it can be readily provided to the Kalman filter so as to be aware of the actual working conditions. For the problem at hand, the measurement noise variance corresponds to the phase noise power, which can easily be obtained by estimating the C/N_0 at the GNSS receiver and thus leads to a scalar variance $R(n)$, as will be shown in Section 3.3.

Process Noise Covariance Matrix

The process noise covariance matrix $\mathbf{Q}(n)$ is in charge for covering the possible mismatch between the state-space model used within the Kalman filter, and the model that the system parameters of interest truly follow. In the recursion in Section 3.2.2, this

is used when sequentially updating the state covariance matrix $\mathbf{\Sigma}_{\mathbf{x}}(n)$. Therefore, such mismatch is internally modeled by increasing the uncertainties (*i.e.* variances) of the Kalman estimates through $\mathbf{\Sigma}_{\mathbf{x}}(n)$. This effect denotes that model discrepancies incur into some degradation in the estimation performance, introducing a lower saturation effect (*i.e.* steady state) as will be shown in Section 3.4, as well as it makes the Kalman more or less reactive to possible variations in the input signal.

The process noise covariance matrix is usually modeled as $\mathbf{Q}(n) \doteq \mathrm{E}\left[\mathbf{G}(n)\mathbf{q}(n)\mathbf{q}^H(n)\mathbf{G}^H(n)\right]$, where $\mathbf{G}(n)$ is typically a known matrix. Hence, $\mathbf{Q}(n)$ is adjusted by properly setting the power of the mismatch errors through $\mathbf{V}(n)$. However, in many practical applications such as GNSS carrier tracking, the mismatch errors turn out to be a scalar zero-mean random process $v(n)$ with variance σ_v^2. Therefore, the problem boils down to properly setting σ_v^2.

Initial State Covariance Matrix

Intuitively, the state covariance matrix denotes the quality of the estimates that its elements refer to. That is, it contains the variances of the estimated states. The lower the variances, the more accurate the estimates. Due to the recursive nature of this matrix, as previously shown, some initial value must be set before running the very first iteration of the Kalman filter. We refer to $\mathbf{\Sigma}_{\mathbf{x}}(0)$, which reflects the initial uncertainty about the parameters to be estimated.

In that sense, when no *a priori* information about the parameters of interest is available, it is possible to set $\mathbf{\Sigma}_{\mathbf{x}}(0) \to \infty$ to inform the Kalman about the complete lack of knowledge. In contrast, when some *a priori* information is available, this can be informed to the Kalman through $\mathbf{\Sigma}_{\mathbf{x}}(0)$ in order to speed up convergence. For instance, if a Kalman state is known to be comprised within a given range of values, we can set the state initial variance to that of a uniformly-distributed random process within such range. As will be seen in Section 3.3, this is actually the case of carrier phase, which is already known to be comprised within $[-\pi,\ \pi]$ radians, and the corresponding initial uncertainty can thus be delimited from the beginning.

It must be noted that for systems with an imperfect state-space model (*i.e.* $\mathbf{Q}(n) \neq \mathbf{0}$), the impact of $\mathbf{\Sigma}_{\mathbf{x}}(0)$ is only perceivable during the transient stage of the filter, causing the filter to reduce the convergence time towards the steady state. Once the steady state is reached, the performance of the Kalman filter does no longer depend on the initialization of the filter, but only on the process noise that lower-saturates the estimation performance,

as explained above. This point will be further developed in Section 3.4.1.

3.3 Kalman Filter State-Space and Observation Models for GNSS Carrier Tracking

For the problem of GNSS carrier tracking, the carrier phase can be considered to evolve according to the carrier dynamics, which originates from the relative motion between the satellites and the receiver. In that sense, we will assume that the discrete-time evolution of the carrier phase coming from the discriminator output for the prompt correlator, denoted herein as $\theta(n)$, follows a third-order dynamic model, also referred to as kinematic [Bar04] or Newtonian [Sim06] model, that can be approximated by a third-order Taylor series expansion:

$$\theta(n) \approx \theta(n-1) + T_s\dot{\theta}(n-1) + \frac{T_s^2}{2!}\ddot{\theta}(n-1) + \frac{T_s^3}{3!}\dddot{\theta}(n-1) \tag{3.14}$$

in radians, where T_s is the sampling time, and $\dot{\theta}(n)$, $\ddot{\theta}(n)$ and $\dddot{\theta}(n)$ are the first, second and third derivatives of $\theta(n)$ over T_s. For the problem at hand, these correspond to carrier frequency, frequency rate and frequency jerk, respectively.

For a third-order Kalman filter, we are interested in tracking the carrier phase, frequency and frequency rate. The discrete-time evolution of the two latter can be derived from (3.14) as,

$$\dot{\theta}(n) \approx \dot{\theta}(n-1) + T_s\ddot{\theta}(n-1) + \frac{T_s^2}{2!}\dddot{\theta}(n-1) \tag{3.15}$$

$$\ddot{\theta}(n) \approx \ddot{\theta}(n-1) + T_s\dddot{\theta}(n-1) \tag{3.16}$$

Eqs. (3.14), (3.15) and (3.16) can be jointly written to form the following state-space model, in normalized matrix notation:

$$\begin{bmatrix} \theta(n) \\ T_s\dot{\theta}(n) \\ T_s^2\ddot{\theta}(n) \end{bmatrix} = \begin{bmatrix} 1 & 1 & 1/2 \\ 0 & 1 & 1 \\ 0 & 0 & 1 \end{bmatrix} \begin{bmatrix} \theta(n-1) \\ T_s\dot{\theta}(n-1) \\ T_s^2\ddot{\theta}(n-1) \end{bmatrix} + \begin{bmatrix} 1/6 \\ 1/2 \\ 1 \end{bmatrix} T_s^3\dddot{\theta}(n-1) \tag{3.17}$$

where $T_s\dot{\theta}(n)$ and $T_s^2\ddot{\theta}(n)$ are the carrier frequency and frequency rate normalized to dimensions of radians through T_s. Equation (3.17) the role of the Kalman state transition equation, based on (3.1),

$$\mathbf{x}_\theta(n) = \mathbf{F}_\theta\mathbf{x}_\theta(n-1) + \mathbf{G}_\theta v(n-1) \tag{3.18}$$

with $\mathbf{x}_\theta(n) \doteq \begin{bmatrix} \theta(n) & T_s\dot{\theta}(n) & T_s^2\ddot{\theta}(n) \end{bmatrix}^T$ the three-dimensional state vector at time instant n, and $v(n) \doteq T_s^3\dddot{\theta}(n)$ the process noise intended to cover the missing higher-order terms in (3.14), which is usually modeled as a zero-mean random process with variance $\sigma_v^2 = T_s^6\sigma_{\dddot{\theta}}^2$ normalized to radians, with $\sigma_{\dddot{\theta}}^2$ the variance of the jerk dynamics in $(\text{rad/s}^3)^2$. We have omitted the time index as we will henceforth consider that σ_v^2 remains fixed. The (3×3) and (3×1) transition and process noise weighting matrices are identified as the following constant matrices,

$$\mathbf{F}_\theta \doteq \begin{bmatrix} 1 & 1 & 1/2 \\ 0 & 1 & 1 \\ 0 & 0 & 1 \end{bmatrix} \tag{3.19}$$

$$\mathbf{G}_\theta \doteq \begin{bmatrix} 1/6 & 1/2 & 1 \end{bmatrix}^T \tag{3.20}$$

the latter leading to the constant process noise covariance matrix $\mathbf{Q}_\theta \doteq \sigma_v^2\mathbf{G}_\theta\mathbf{G}_\theta^T$.

On the other hand, after extracting the phase from the complex prompt correlator output samples, we are typically provided with carrier phase measurements:

$$z_\theta(n) = \mathbf{H}_\theta\mathbf{x}_\theta(n) + w(n) = \theta(n) + w(n) \tag{3.21}$$

which can be understood as a linear transformation of the state vector $\mathbf{x}_\theta(n)$ through the constant observation matrix $\mathbf{H}_\theta \doteq \begin{bmatrix} 1 & 0 & 0 \end{bmatrix}$.

For the problem under analysis, the measurement noise $w(n)$ corrupting the observations in (3.21) is a scalar corresponding to the phase noise at the discriminator output, with zero mean and variance $\sigma_w^2(n)$. We will henceforth consider the four-quadrant arctangent discriminator (ATAN2) presented in Chapter 2, as it is the optimal ML phase extractor at high carrier-to-noise ratio (C/N_0) [Pro01]. Assuming that the output of the prompt correlator is normalized to unit mean power, the variance of $w(n)$ turns out to be a scalar that depends on the instantaneous C/N_0,

$$\sigma_w^2(n) = R(n) \doteq \frac{1}{2T_s\frac{C}{N_0}(n)}\left[1 + \frac{1}{2T_s\frac{C}{N_0}(n)}\right] \tag{3.22}$$

in rad^2, where the second term inside the brackets on the right-hand side accounts for the nonlinear behavior of the ATAN2 discriminator at low C/N_0 [Cur12].

3.4 Performance Bounds

3.4.1 Bayesian Cramér-Rao Bound

The particularity of Kalman filtering is that it addresses the problem of Bayesian filtering. That is, the objective is to track a vector of random parameters that evolve according to some prior statistics. This is in contrast to conventional (*i.e.* non-Bayesian) filtering, where the parameters to be estimated are deterministic unknowns.

In Bayesian filtering, the covariance matrix $\mathbf{\Sigma}_{\mathbf{x}}(n)$ of any estimator $\hat{\mathbf{x}}(z(n), n)$ is lower-bounded by the inverse of the Bayesian information matrix (BIM), $\mathbf{J}_{\mathrm{B}}^{-1}(n)$, leading to the so-called Bayesian Cramér-Rao bound (BCRB) [Tre07], or posterior CRB [Tre68]:

$$\mathbf{\Sigma}_{\mathbf{x}}(n) \doteq \mathrm{E}\left[\left(\hat{\mathbf{x}}(n) - \mathbf{x}(n)\right)\left(\hat{\mathbf{x}}(n) - \mathbf{x}(n)\right)^{H}\right] \geqslant \mathbf{J}_{\mathrm{B}}^{-1}(n) \doteq \mathrm{BCRB}(\mathbf{x}(n)). \tag{3.23}$$

The BIM can be expressed as the sum of two matrices,

$$\mathbf{J}_{\mathrm{B}}(n) = \mathbf{J}_{\mathrm{P}}(n) + \mathbf{J}_{\mathrm{D}}(n) \tag{3.24}$$

where $\mathbf{J}_{\mathrm{P}}(n)$ and $\mathbf{J}_{\mathrm{D}}(n)$ are the contributions owing to the prior information and the observations, respectively. As a matter of fact, the latter represents the Fisher information matrix (FIM), $\mathbf{J}_{\mathrm{F}}(n)$, widely adopted in non-Bayesian estimation theory,

$$\mathbf{J}_{\mathrm{D}}^{-1}(n) = \left(\mathrm{E}\left[\mathbf{J}_{\mathrm{F}}(n)\right]\right)^{-1} \doteq \mathrm{CRB}(\mathbf{x}(n)) \tag{3.25}$$

thus linking the observation contribution to the well-known Cramér-Rao bound (CRB).

From the mathematical standpoint, the BCRB has the form of a discrete algebraic Riccati equation (DARE) that is usually evaluated using numerical methods. However, an interesting observation is that the BCRB can be computed in a recursive manner [Tic98]. That is, for the particular case of the Kalman filter, the covariance matrix $\mathbf{\Sigma}_{\mathbf{x}}(n)$ can recursively be computed according to (3.13) using the recursion given by Eqs. (3.7) and (3.12). Therefore, the recursive version of the BIM, denoted as $\mathbf{J}_{\mathrm{B_{rec}}}(n)$ turns out to be given by,

$$\mathbf{J}_{\mathrm{B_{rec}}}(n) \doteq \mathbf{\Sigma}_{\mathbf{x}}^{-1}(n) \tag{3.26}$$

and can thus be computed using the aforementioned covariance matrix recursion as [Tre07],

$$\mathbf{J}_{\mathrm{B_{rec}}}(n+1) = \left(\mathbf{Q}(n) + \mathbf{F}(n)\mathbf{J}_{\mathrm{B_{rec}}}^{-1}(n)\mathbf{F}^{T}(n)\right)^{-1} + \mathbf{H}^{T}(n)\mathbf{R}^{-1}(n)\mathbf{H}(n) \tag{3.27}$$

where the first term corresponds to the contribution due to the process prediction, and the second term corresponds to the measurement update. The recursive version of the BCRB is then given by the inverse of (3.27):

$$\mathbf{J}_{\mathrm{B_{rec}}}^{-1}(n+1) = \left[\left(\mathbf{Q}(n) + \mathbf{F}(n)\mathbf{J}_{\mathrm{B_{rec}}}^{-1}(n)\mathbf{F}^T(n)\right)^{-1} + \mathbf{H}^T(n)\mathbf{R}^{-1}(n)\mathbf{H}(n) \right]^{-1} \tag{3.28}$$

with all the terms in normalized notation to preserve the generality of (3.28).

3.4.2 Link between BCRB and CRB

The differential characteristic between the CRB and BCRB is given by the Bayesian feature of the latter. The link between both bounds can be made explicit by removing the Bayesian information, which for the problem at hand is given by the system process noise through $\mathbf{Q}(n)$. By doing so, the Kalman state-space model becomes deterministic, and therefore conventional (*i.e.* non-Bayesian) performance lower bounds can be applied. More precisely, the CRB given by $\mathbf{J}_{\mathrm{D}}^{-1}(n)$ can be computed in a recursive manner by considering $\mathbf{Q}(n) = 0$ in Eq. (3.28), which we denote as $\mathbf{J}_{\mathrm{D_{rec}}}^{-1}(n)$:

$$\mathbf{J}_{\mathrm{D_{rec}}}^{-1}(n+1) = \left[\left(\mathbf{F}(n)\mathbf{J}_{\mathrm{D_{rec}}}^{-1}(n)\mathbf{F}^T(n)\right)^{-1} + \mathbf{H}^T(n)\mathbf{R}^{-1}(n)\mathbf{H}(n) \right]^{-1}. \tag{3.29}$$

In order to illustrate the link between the BCRB and the CRB, we consider the example of joint carrier phase and frequency estimation from a snapshot of N noisy measurements. This example is based on the case of GNSS carrier tracking introduced in Section 3.3 but simplified to a second-order dynamic model for simplicity purposes, thus neglecting the effect of frequency rate. For this particular case, the CRB for each magnitude is given by [Kay93, Mor02],

$$\mathrm{CRB}(\theta) = \frac{2N-1}{N(N+1)T_s C/N_0} \tag{3.30}$$

$$\mathrm{CRB}(\dot{\theta}) = \frac{6}{N(N^2-1)T_s C/N_0}. \tag{3.31}$$

both with dimensions of rad^2. For a C/N_0 of 45 dB-Hz, Figure 3.3 compares the CRB given by (3.30) and (3.31) to the recursive CRB in (3.29) and the recursive BCRB in (3.28). We have considered $T_s = 20$ ms as the sampling time employed in the whole document owing to the real scintillation time series that will be analysed later on. As expected, the closed-form expressions for the CRB coincide with the recursive CRB, which decrease without bound. The latter is explained by the fact that the Kalman state-space

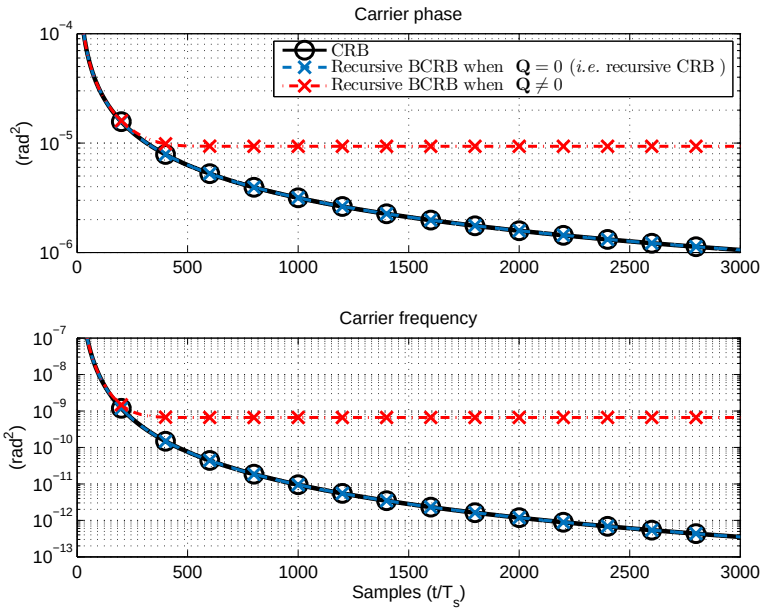

Figure 3.3: Comparison of CRB, recursive CRB (*i.e.* recursive BCRB when $\mathbf{Q} = 0$) and recursive BCRB (*i.e.* when $\mathbf{Q} \neq 0$).

model perfectly matches that of the input signal, and the Kalman filter can thus employ all the measurements in the data record (*i.e.* infinite memory). As a consequence, the filter can gradually improve the estimation performance as the data record increases over time. On the other hand, the BCRB is found to introduce a floor effect that, in contrast to the CRB, limits the estimation performance. This is a well-known phenomenon that is due to the presence of nonzero process noise [Tre07]; the Kalman state-space model does not perfectly match that of the input signal, and the Kalman filter must employ a limited-length data record (*i.e.* limited memory), thus causing the filter to eventually saturate to a steady-state region after some convergence (*i.e.* transient) period. These observations are the basis for the derivation of closed-form expressions for the BCRB up next in Sections 3.5 and 3.7.

3.5 Batch-Mode Formulation of the Kalman Filter

The main inconvenient of the BCRB is that, in general, it does not present a solution in closed form. This often hampers the analysis and tuning of the Kalman filter in practice, thus forcing the designer to resort to numerical evaluations or extensive simulations.

A number of works aiming at circumventing this limitation can be found in the liter-

ature; however, many of them rely on assumptions that are often unrealistic in practice. For instance, this is the case of [Qia09, Ros11], where the results are conditioned upon the availability of an accurate prior. Other works provide simplified versions of the BCRB, yet still require some numerical evaluations [Bay08] or eigendecompositions [Vau70, Ham83]. One last example is the adoption of low-order model restrictions to simplify the mathematical complexity of the problem and provide results that are easily tractable [Shu13]. Therefore, deriving expressions in closed form that facilitate the analysis and tuning of the Kalman filter still remains a difficult task.

In this regard, this section presents an alternative way of formulating the Kalman filter equations that will serve us to derive closed-form expressions for both the convergence time and steady-state performance of kinematic Kalman filters in Sections 3.6 and 3.7, respectively. More precisely, the approach is based on reformulating the Kalman filtering problem in batch mode, thus leaving the estimates at a given time instant n as a function of all past measurements in the data record. After that, it exploits the fact that, when assuming a linear Gaussian model and a diffuse initialization of the Kalman filter (*i.e.* non-informative prior), a parallelism between the KF and the best linear unbiased estimator (BLUE) can be made.

3.5.1 Batch Formulation

The formulation in batch mode of the Kalman filtering problem relies on stacking the measurements in (3.2) for all time instants up to n into an $(n \times 1)$ vector,

$$\mathbf{z}_n \doteq \begin{bmatrix} z(1) & z(2) & \cdots & z(n) \end{bmatrix}^T \tag{3.32}$$

whose elements are to be computed as a function of the state vector at a given time instant n, $\mathbf{x}_p(n)$[1]. To this end, we first start by rewriting the Kalman state transition equation in (3.1) in terms of $\mathbf{x}_p(n)$ as a function of $\mathbf{x}_p(n+1)$ as follows,

$$\mathbf{x}_p(n) = \mathbf{F}_p^{-1} \left[\mathbf{x}_p(n+1) - \mathbf{G}_p v(n) \right] \tag{3.33}$$

where $\mathbf{F}_p$ is assumed to be nonsingular, and therefore the problem is well posed for state estimation[2]. Substituting (3.33) into the measurement equation in (3.2) leads to,

$$z(n) = \mathbf{H}_p \mathbf{F}_p^{-1} \left[\mathbf{x}_p(n+1) - \mathbf{G}_p v(n) \right] + w(n). \tag{3.34}$$

[1]Note the subscript p indicating that the dimension of the Kalman filter is not specified to any particular value.

[2]This makes the system *reachable*, so there exists a finite sequence of $v(n)$ for $n = \{0, 1, \ldots, n'\}$ such that any initial state vector $\mathbf{x}_p(0)$ can be transferred to any final state $\mathbf{x}_p(n'+1)$ [Hen08].

By evaluating (3.34) for different values of n we have,

$$z(n-3) = \mathbf{H}_p\mathbf{F}_p^{-1}\left[\mathbf{x}_p(n-2) - \mathbf{G}_p v(n-3)\right] + w(n-3) \tag{3.35}$$
$$z(n-2) = \mathbf{H}_p\mathbf{F}_p^{-1}\left[\mathbf{x}_p(n-1) - \mathbf{G}_p v(n-2)\right] + w(n-2) \tag{3.36}$$
$$z(n-1) = \mathbf{H}_p\mathbf{F}_p^{-1}\left[\mathbf{x}_p(n) - \mathbf{G}_p v(n-1)\right] + w(n-1) \tag{3.37}$$
$$z(n) = \mathbf{H}_p\mathbf{x}_p(n) + w(n) \tag{3.38}$$

Equations (3.35)-(3.45) stand for the measurements in the data record up to time instant n. In order to formulate the Kalman filtering problem in batch mode, it is of interest that all measurements refer to the state vector at time instant n, $\mathbf{x}_p(n)$. In the example above, this affects equations (3.35) and (3.36). From (3.33) we have that,

$$\mathbf{x}_p(n-1) = \mathbf{F}_p^{-1}\left[\mathbf{x}_p(n) - \mathbf{G}_p v(n-1)\right] \tag{3.39}$$
$$\mathbf{x}_p(n-2) = \mathbf{F}_p^{-1}\left[\mathbf{x}_p(n-1) - \mathbf{G}_p v(n-2)\right]. \tag{3.40}$$

Then, substituting (3.39) into (3.40) leads the latter to become,

$$\mathbf{x}_p(n-2) = \mathbf{F}_p^{-2}\left[\mathbf{x}_p(n) - \mathbf{G}_p v(n-1)\right] - \mathbf{F}_p^{-1}\mathbf{G}_p v(n-2). \tag{3.41}$$

By substituting (3.39) and (3.41) respectively into (3.36) and (3.35), the set of equations (3.35)-(3.45) becomes,

$$\begin{aligned} z(n-3) = {} & \mathbf{H}_p\mathbf{F}_p^{-3}\mathbf{x}_p(n) - \mathbf{H}_p\mathbf{F}_p^{-3}\mathbf{G}_p v(n-1) - \mathbf{H}_p\mathbf{F}_p^{-2}\mathbf{G}_p v(n-2) - \mathbf{H}_p\mathbf{F}_p^{-1}\mathbf{G}_p v(n-3) \\ & + w(n-3) \end{aligned} \tag{3.42}$$
$$z(n-2) = \mathbf{H}_p\mathbf{F}_p^{-2}\mathbf{x}_p(n) - \mathbf{H}_p\mathbf{F}_p^{-2}\mathbf{G}_p v(n-1) - \mathbf{H}_p\mathbf{F}_p^{-1}\mathbf{G}_p v(n-2) + w(n-2) \tag{3.43}$$
$$z(n-1) = \mathbf{H}_p\mathbf{F}_p^{-1}\mathbf{x}_p(n) - \mathbf{H}_p\mathbf{F}_p^{-1}\mathbf{G}_p v(n-1) + w(n-1) \tag{3.44}$$
$$z(n) = \mathbf{H}_p\mathbf{x}_p(n) + w(n). \tag{3.45}$$

In view of this recursion, the measurement model at any $(n-\tau)$, with $\tau \doteq \{1, 2, \ldots, (n-1)\}$, can be written as follows,

$$z(n-\tau) = \mathbf{H}_p\mathbf{F}_p^{-\tau}\mathbf{x}_p(n) - \sum_{l=1}^{\tau}\mathbf{H}_p\mathbf{F}_p^{-(\tau-l+1)}\mathbf{G}_p v(n-l) + w(n-\tau) \tag{3.46}$$

thus leading to the following batch-mode signal model as a function of the Kalman state vector at time n, $\mathbf{x}_p(n)$. That is,

$$\mathbf{z}_n = \mathbf{A}_{n,p}\mathbf{x}_p(n) + \mathbf{B}_{n,p}\mathbf{u}_n \tag{3.47}$$

where $\mathbf{A}_{n,p}$, $\mathbf{B}_{n,p}$ and $\mathbf{u}_n$ are $(n \times p)$, $(n \times (2n-1))$ and $((2n-1) \times 1)$ matrices given by,

$$\mathbf{A}_{n,p} \doteq \left[\mathbf{H}_p\mathbf{F}_p^{-(n-1)};\ \ \mathbf{H}_p\mathbf{F}_p^{-(n-2)};\ \ \cdots;\ \ \mathbf{H}_p\right] \tag{3.48}$$

$$\mathbf{B}_{n,p} \doteq \begin{bmatrix} & \begin{bmatrix} -\mathbf{H}_p\mathbf{F}_p^{-1}\mathbf{G}_p & \cdots & -\mathbf{H}_p\mathbf{F}_p^{-(n-1)}\mathbf{G}_p \\ 0 & \cdots & -\mathbf{H}_p\mathbf{F}_p^{-(n-2)}\mathbf{G}_p \\ \vdots & \ddots & \vdots \\ 0 & \cdots & -\mathbf{H}_p\mathbf{F}_p^{-1}\mathbf{G}_p \\ 0 & \cdots & 0 \end{bmatrix} \\ \mathbf{I}_n, & \end{bmatrix} \tag{3.49}$$

$$\mathbf{u}_n \doteq \begin{bmatrix} w(1) & w(2) & \cdots & w(n) & v(1) & v(2) & \cdots & v(n-1) \end{bmatrix}^T \tag{3.50}$$

with $\mathbf{I}_n$ the $(n \times n)$ identity matrix.

The performance of the Kalman filter in providing an estimate of $\mathbf{x}_p(n)$ is given by the estimation covariance matrix $\boldsymbol{\Sigma}_{\mathbf{x}_p}(n)$, which is lower bounded by the BCRB as explained in Section 3.4.1. Notwithstanding, when considering a diffuse initialization of the Kalman filter, the problem in (3.47) can be reinterpreted as that of estimating a vector of unknown deterministic parameters $\mathbf{x}_p(n)$ from Gaussian measurements $\mathbf{z}_n \sim \mathcal{N}\left(\mathbf{A}_{n,p}\mathbf{x}_p(n), \boldsymbol{\Sigma}_{\mathbf{z}_n}\right)$, with $(n \times n)$ covariance matrix,

$$\boldsymbol{\Sigma}_{\mathbf{z}_n} \doteq \mathrm{E}\left[\mathbf{B}_{n,p}\mathbf{u}_n\mathbf{u}_n^H\mathbf{B}_{n,p}^H\right] = \mathbf{B}_{n,p}\boldsymbol{\Sigma}_{\mathbf{u}_n}\mathbf{B}_{n,p}^H \tag{3.51}$$

where $\boldsymbol{\Sigma}_{\mathbf{u}_n} \doteq \mathrm{diag}\left(\begin{bmatrix}\boldsymbol{\sigma}^2_{w,(1\times n)} & \boldsymbol{\sigma}^2_{v,(1\times(n-1))}\end{bmatrix}\right)$ is a diagonal matrix encompassing both the measurement and process noise variances for all time instants. Given the linear Gaussian nature of the problem, the optimal batch-mode estimator of the state vector $\mathbf{x}_p(n)$ is given by the BLUE [Kay93],

$$\hat{\mathbf{x}}_p(n) = \left(\mathbf{A}_{n,p}^H\boldsymbol{\Sigma}_{\mathbf{z}_n}^{-1}\mathbf{A}_{n,p}\right)^{-1}\mathbf{A}_{n,p}^H\boldsymbol{\Sigma}_{\mathbf{z}_n}^{-1}\mathbf{z}_n \tag{3.52}$$

which is also the MVU estimator, thus attaining the corresponding $(p \times p)$ FIM,

$$\boldsymbol{\Sigma}_{\mathbf{x}_p}(n) \succcurlyeq \mathbf{J}^{-1}(n) = \left(\mathbf{A}_{n,p}^H\boldsymbol{\Sigma}_{\mathbf{z}_n}^{-1}\mathbf{A}_{n,p}\right)^{-1}. \tag{3.53}$$

In the absence of *a priori* information, both the Bayesian and the frequentist approaches coincide [Kay93], thus leading to $\mathbf{J}_{\mathrm{B}}(n) = \mathbf{J}(n)$. Therefore, one can make use of (3.71) to extract the information about the Kalman filter performance when it operates under a diffuse initialization.

3.5.2 Inner Structure of the FIM

In order to determine the behavior of the Kalman filter, we must exploit the knowledge of $\mathbf{B}_{n,p}$ and $\mathbf{\Sigma}_{\mathbf{u}_n}$ to get some insight into the inner structure of the covariance matrix $\mathbf{\Sigma}_{\mathbf{z}_n}$ in the FIM in (3.53). By evaluating $\mathbf{\Sigma}_{\mathbf{z}_n}$ for different values of n, the matrix is found to be decomposed into two terms,

$$\mathbf{\Sigma}_{\mathbf{z}_n} = \sigma_v^2 \mathbf{M}_n + \sigma_w^2 \mathbf{I}_n \tag{3.54}$$

with $\mathbf{M}_n$ a nonnegative $(n \times n)$ symmetric matrix whose constituent elements are formed by cross-products of $\mathbf{H}_p$, $\mathbf{F}_p$ and $\mathbf{G}_p$. On the one hand, the diagonal elements of $\mathbf{M}_n$ are found to be driven by the following expression,

$$[\mathbf{M}_n]_{k,k} = \sum_{m=1}^{n-k} \left(\mathbf{H}_p \mathbf{F}_p^{-m} \mathbf{G}_p\right)^2 \tag{3.55}$$

with $k \doteq [1..n]$, whereas obtaining a closed-form expression as a function of n for the off-diagonal elements becomes quite a mathematical challenge. As a matter of fact, the knowledge of (3.55) is already sufficient to derive closed-form expressions for the Kalman filter performance, as will be shown in the upcoming sections.

3.6 Convergence Time

This section aims at deriving a closed-form upper bound for the convergence time of Kalman filters encompassing kinematic models such as the one presented in Section 3.3, with any non-restricted order. To this end, the KF batch formulation presented in Section 3.5 is employed. In particular, the proposed approach is based on exploiting the knowledge of (3.54) and (3.55). More precisely, we observe the evolution of the trace of $\mathbf{\Sigma}_{\mathbf{z}_n}$ in (3.54) over n. For $p = 2$, this is graphed in Figure 3.4, which also includes the evolution of the two separate components given by $\sigma_v^2 \mathrm{Tr}\left(\mathbf{\Sigma}_{\mathbf{z}_n}\right)$ and $\sigma_w^2 n$, with $\sigma_v^2 = 10^{-8}$ and $\sigma_w^2 = 10^{-5}$ as values for mere illustrative purposes[3]. It is observed that, for small n, $\mathrm{Tr}\left(\mathbf{\Sigma}_{\mathbf{z}_n}\right)$ is dominated by the contribution of the measurement noise σ_w^2 filtered by the Kalman. At a given time instant, a change of state is produced, in which $\mathrm{Tr}\left(\mathbf{\Sigma}_{\mathbf{z}_n}\right)$ starts being dominated by the contribution of the process noise σ_v^2, a situation that remains then for $n \to \infty$. This can be understood as the point at which the BCRB becomes lower-saturated by nonzero process noise. Therefore, the intersection point of both components

[3]Note that we employ normalized (*i.e.* unitless) notation in these derivations in order to preserve the generality of the proposed approach

is considered to determine the time instant at which the Kalman enters the steady state, and thus the point of interest in this section. This point can be found as the solution for n to the equality,

$$\sigma_v^2 \mathrm{Tr}\left(\mathbf{M}_n\right) = \sigma_w^2 n. \tag{3.56}$$

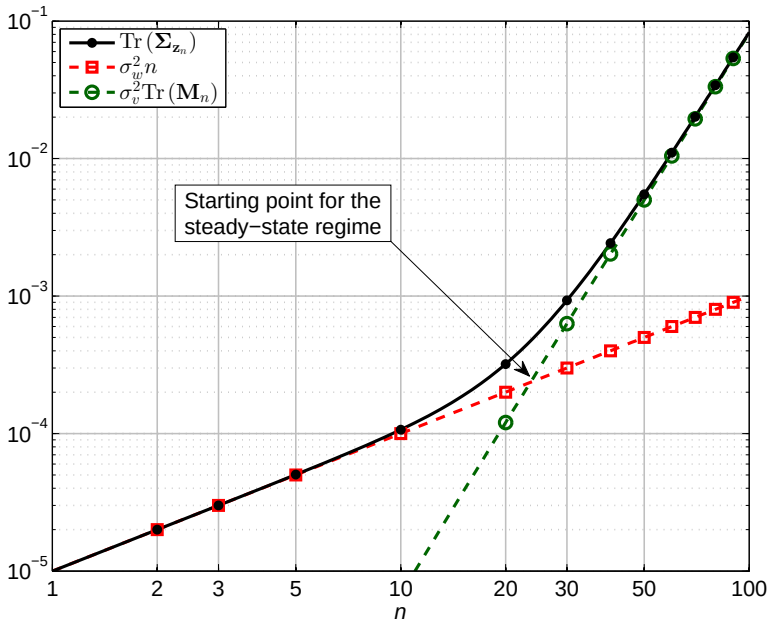

Figure 3.4: Asymptotic evolution of $\mathrm{Tr}(\mathbf{\Sigma}_{\mathbf{z}_n})$ versus the constituent elements of $\mathbf{\Sigma}_{\mathbf{z}_n}$ in (3.54).

The problem of solving (3.56) requires determining the trace of $\mathbf{M}_n$ in closed form. To this end, we fortunately have expression (3.55) to work with. From this, $\mathrm{Tr}\left(\mathbf{M}_n\right)$ can be computed as,

$$\mathrm{Tr}\left(\mathbf{M}_n\right) = \sum_{k=1}^{n} \left[\mathbf{M}_n\right]_{k,k} = \sum_{k=1}^{n} \sum_{m=1}^{n-k} \left(\mathbf{H}_p \mathbf{F}_p^{-m} \mathbf{G}_p\right)^2. \tag{3.57}$$

Substituting the matrices $\mathbf{H}_p$, $\mathbf{F}_p$ and $\mathbf{G}_p$ with those for a kinematic model such as the Taylor series expansion in (3.14), and evaluating for different model orders p, it is found that (3.57) can be rewritten as a polynomial with degree $2p$,

$$\mathrm{Tr}\left(\mathbf{M}_n\right) = \sum_{q=1}^{2p} \beta'_q n^q \tag{3.58}$$

with $\{\beta'_q\}_{q=1}^{2p}$ a set of coefficients whose value is not relevant at this point, but their absolute value is known to be less than one. This latter information will be of great use for the derivation of a closed-form approximation in Section 3.6.1. By substituting (3.58)

into (3.56), the latter can be rewritten as,

$$\sigma_v^2 \sum_{q=1}^{2p} \beta'_q n^q = \sigma_w^2 n. \tag{3.59}$$

where a factor of n can be compensated at both sides of the equal sign. By doing so, one finds that the convergence time of a pth-order Kalman filter, denoted henceforth as $n_{\mathrm{c}}^{(p)}$, can be obtained as the real positive root of the following polynomial with degree $(2p-1)$,

$$f_{\mathrm{c}}(n,p) = \beta_0 + \sum_{q=1}^{2p-1} \beta_q n^q \tag{3.60}$$

with $\beta_q \doteq \beta'_{q+1}$, and β_0 is the independent term defined as,

$$\beta_0 \doteq \beta'_1 - \frac{\sigma_w^2}{\sigma_v^2}. \tag{3.61}$$

Deriving a closed-form solution for the real root of (3.60) may become a rather cumbersome mathematical problem when models with sufficiently high order are considered. For this reason, in Section 3.6.1 we formulate an approximation for $n_{\mathrm{c}}^{(p)}$ that considerably reduces the complexity of the problem.

3.6.1 Derivation of Closed-Form Approximation

In order to derive a closed-form approximation for $n_{\mathrm{c}}^{(p)}$, it is assumed that $\sigma_w^2 \gg \sigma_v^2$, as widely considered in many practical applications such as the radar/sonar tracking problem [Tre07], and the one in which the potential of the Kalman filter can mostly be exploited. In this situation, the Kalman estimates the parameters of interest by sequentially filtering the input measurement noise, down until reaching the floor saturation imposed by nonzero process noise. Such floor effect tends to disappear when $\sigma_v^2 \to 0$, causing the BCRB to decrease without bound and never attain a steady state (*i.e.* as in the CRB), leading to $n_{\mathrm{c}}^{(p)} \to \infty$. On the contrary, the floor becomes more stringent when gradually increasing σ_v^2, causing the convergence time to reduce. When σ_v^2 is such that the condition $\sigma_w^2 \gg \sigma_v^2$ is not fulfilled, the Kalman is left with no margin to filter the measurement noise. Consequently, the process noise becomes rapidly the dominating effect in this situation, thus leading the Kalman filter to saturate at the very first iteration, that is, $n_{\mathrm{c}}^{(p)} \to 1$.

Therefore, as a general rule, the Kalman convergence time is comprised within the range $1 \leqslant n_{\mathrm{c}}^{(p)} < \infty$. In this way, a closed-form approximation of $n_{\mathrm{c}}^{(p)}$ can be derived

through asymptotic analysis as follows. If σ_v^2 is considered small compared to σ_w^2, one can claim from the reasoning above that $n_{\mathrm{c}}^{(p)} > 1$. This value of $n_{\mathrm{c}}^{(p)}$ is raised to different powers in the polynomial in (3.60), resulting in differences of some orders of magnitude between consecutive terms. As a consequence, the polynomial becomes rapidly dominated by the highest-order term, namely the one raised to $(2p-1)$,

$$f_{\mathrm{c}}(n,p) \approx \beta_{2p-1} n^{2p-1} + \beta_0. \tag{3.62}$$

In addition, the assumption of $\sigma_w^2 \gg \sigma_v^2$ and the fact that $|\beta_1'| < 1$ as previously stated, allow the independent term in (3.61) to be approximated by,

$$\beta_0 \approx -\frac{\sigma_w^2}{\sigma_v^2}. \tag{3.63}$$

By substituting (3.63) into (3.62) and equating the latter to zero, an approximation for $n_{\mathrm{c}}^{(p)}$ can be provided as,

$$n_{\mathrm{c}}^{(p)} \approx \left[\beta_{2p-1}^{-1} \frac{\sigma_w^2}{\sigma_v^2} + \alpha\right]^{\frac{1}{2p-1}} \doteq \tilde{n}_{\mathrm{c}}^{(p)} \tag{3.64}$$

where an additional parameter α has been incorporated to provide a valid solution for the convergence time in case the condition $\sigma_w^2 \gg \sigma_v^2$ is not fulfilled. More precisely, the rationale of α is to lower-saturate the approximation in (3.64) and avoid the meaningless result $\tilde{n}_{\mathrm{c}}^{(p)} = 0$ when $\sigma_w^2/\sigma_v^2 \to 0$. Given that the convergence time fulfills $n_{\mathrm{c}}^{(p)} \geqslant 1$, the value of α can be computed by forcing the asymptotic of (3.64) to become,

$$\lim_{\frac{\sigma_w^2}{\sigma_v^2} \to 0} \left[\beta_{2p-1}^{-1} \frac{\sigma_w^2}{\sigma_v^2} + \alpha\right]^{\frac{1}{2p-1}} = 1 \tag{3.65}$$

which leads to $\alpha = 1$.

Even though the complexity of solving $n_{\mathrm{c}}^{(p)}$ for (3.60) has been considerably reduced, the result in (3.64) still lacks the knowledge of β_{2p-1} to become a truly closed-form expression for the Kalman filter convergence time. As a matter of fact, β_{2p-1} is the coefficient of the highest-order term of $\mathrm{Tr}\,(\mathbf{M}_n)$ in (3.58), that is, $\beta_{2p-1} = \beta_{2p}'$, for which an expression can interestingly be obtained in closed form through (3.57) using matrices $\mathbf{H}_p$, $\mathbf{F}_p$ and $\mathbf{G}_p$. To this end, we proceed by computing the highest-order term of (3.57) in a step-by-step basis. First, by evaluating the polynomial $\left(\mathbf{H}_p \mathbf{F}_p^{-m} \mathbf{G}_p\right)^2$ for different values of p, it is found that,

$$\left[\left(\mathbf{H}_p \mathbf{F}_p^{-m} \mathbf{G}_p\right)^2\right]_{\mathrm{HO}} = \frac{m^{2(p-1)}}{\left[(p-1)!\right]^2} \tag{3.66}$$

with the subscript HO on the left-hand side denoting the highest-order term. Then, the result in (3.66) is integrated through the inner summatory,

$$\left[\sum_{m=1}^{n-k}\frac{m^{2(p-1)}}{\left[(p-1)!\right]^2}\right]_{\mathrm{HO}}=\frac{(n-k)^{2p-1}}{(2p-1)\left[(p-1)!\right]^2} \tag{3.67}$$

whose result is then integrated again through the outer summatory in (3.57),

$$\left[\sum_{k=1}^{n}\frac{(n-k)^{2p-1}}{(2p-1)\left[(p-1)!\right]^2}\right]_{\mathrm{HO}}=\frac{n^{2p}}{2p(2p-1)\left[(p-1)!\right]^2}. \tag{3.68}$$

From (3.68) the coefficient of interest can be extracted,

$$\beta_{2p-1}=\frac{1}{2p(2p-1)\left[(p-1)!\right]^2} \tag{3.69}$$

which substituted into (3.64), eventually leads to the following closed-form approximation for the convergence time of a pth-order Kalman filter,

$$\boxed{\tilde{n}_{\mathrm{c}}^{(p)}=\left[2p(2p-1)\left[(p-1)!\right]^2\frac{\sigma_w^2}{\sigma_v^2}+1\right]^{\frac{1}{2p-1}}.} \tag{3.70}$$

It is worth recalling that the result in (3.70) has been obtained by considering a diffuse initialization of the Kalman filter. This means that no *a priori* information about the parameters of interest is available to help the Kalman filter converge more rapidly to the steady state. The filter operates with absolute initial uncertainty, thus causing the convergence time to be maximum. Therefore, the result derived in (3.70) can be understood as an upper bound on the Kalman filter convergence time.

3.6.2 Goodness of Approximation

This section aims at illustrating the goodness of the approximation for the Kalman filter convergence time proposed in (3.70) for a broad range of values of σ_w^2 and σ_v^2. To this end, two different plots are analyzed. On the one hand, the top plots of Figures 3.5 and 3.6 show a comparison of the proposed result $\tilde{n}_{\mathrm{c}}^{(p)}$ in (3.70), to the exact solution $n_{\mathrm{c}}^{(p)}$ given by the real root of (3.60), for $p=3$ and $p=4$, respectively. A very tight match between both lines can be observed for practically all values of σ_w^2 and σ_v^2, even though small discrepancies predictably appear when moving away from the design region (*i.e.* when the assumption $\sigma_w^2 \gg \sigma_v^2$ is not fulfilled). In order to provide a unique real solution for $n_{\mathrm{c}}^{(p)}$, the polynomial in (3.60) is required to have only one real root. This is found to occur

when the process and measurement noise variances meet the condition $\sigma_w^2/\sigma_v^2 \geqslant 10^{1-p}$. For ratios below this value, the polynomial presents multiple real roots, which hinders the distinction of the correct solution for $n_c^{(p)}$. In this situation, the proposed approximation is lower-saturated to $\tilde{n}_c^{(p)} = 1$ as intuitively explained in Section 3.6.1 for large σ_v^2. These results confirm that the applicability of (3.70) can safely be extended to all values of σ_w^2 and σ_v^2.

On the other hand, the bottom plots of Figures 3.5 and 3.6 show the goodness of $\tilde{n}_c^{(p)}$ in terms of the BCRB steady-state completion percentage, measured through the ratio $\gamma \doteq \left[\mathbf{J}_{\mathrm{B_{rec}}}^{-1}(\infty)\right]_{1,1} \Big/ \left[\mathbf{J}_{\mathrm{B_{rec}}}^{-1}(\tilde{n}_c^{(p)})\right]_{1,1}$. The value of γ is desired to be as close to 100% as possible. It is observed that the smaller σ_v^2, the tighter the matching of $\left[\mathbf{J}_{\mathrm{B_{rec}}}^{-1}(\tilde{n}_c^{(p)})\right]_{1,1}$ to $\left[\mathbf{J}_{\mathrm{B_{rec}}}^{-1}(\infty)\right]_{1,1}$, and hence the better the approximation in (3.70), leading to $\gamma \to 100\%$. As σ_v^2 gradually increases and the assumption $\sigma_w^2 \gg \sigma_v^2$ gets compromised, γ worsens, but just slightly below 80% and 70% according to Figures 3.5 and 3.6, respectively. This manifests the limited operation range of the proposed approach, even though an acceptable result can still be provided. When σ_v^2 is too large and $\sigma_w^2 \gg \sigma_v^2$ no longer holds, the lower-saturation in (3.65) comes into action, and interestingly $\gamma \to 100\%$ again. Note that a too large process noise, though, indicates that the Kalman filter state-space model does not quite well fit the incoming measurements, thus causing the former to become ill-posed and consequently not to be able to perform filtering. The result of γ above confirms that in this situation, there is no point in iterating the BCRB further than the very first iteration, as it provides reasonably no benefit in terms of performance enhancement.

3.7 Steady-State Region

Once the convergence region of a pth-order kinematic Kalman filter has been characterized, it remains to evaluate the steady-state region of the filter. In that sense, this section aims at deriving a lower bound for the steady-state performance of Kalman filters in closed form. Similarly to Section 3.6, the result is presented in form of an approximation based on the reasonings and derivations introduced in that section. Even though the approach can eventually be applied to Kalman filters with any model order p, the derivations in this section are restricted to second-order Kalman filters, as shown next.

Recalling from Section 3.5.1, when considering a diffuse initialization of the Kalman filter, the filter performance is lower-bounded by the inverse of the FIM $\mathbf{J}(n)$,

$$\boldsymbol{\Sigma}_{\mathbf{x}}(n) \geqslant \mathbf{J}^{-1}(n) = \left(\mathbf{A}_{n,p}^H \boldsymbol{\Sigma}_{\mathbf{z}_n}^{-1} \mathbf{A}_{n,p}\right)^{-1} \tag{3.71}$$

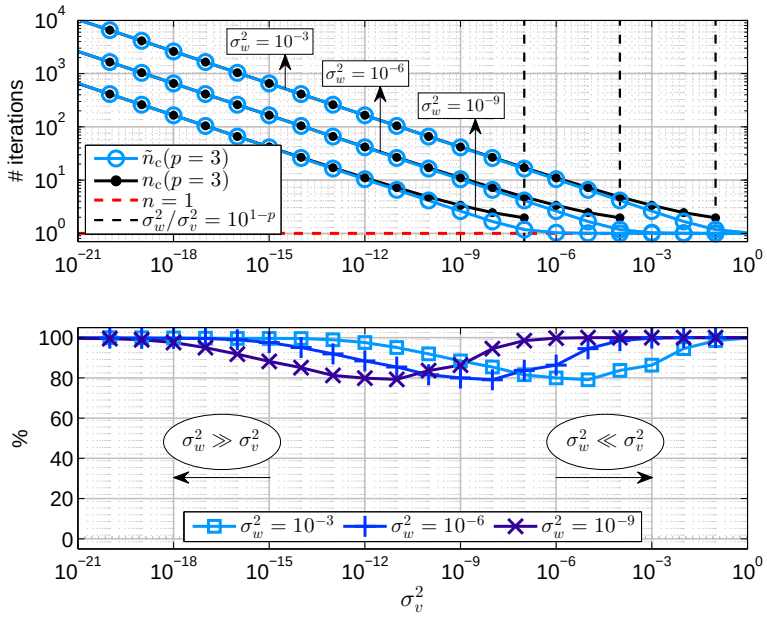

Figure 3.5: (Top) Closed-form approximation for the convergence time $\tilde{n}_c^{(p)}$ in (3.70), versus exact solution $n_c^{(p)}$ for (3.60), with $p = 3$. (Bottom) Goodness of $\tilde{n}_c^{(p)}$ in terms of BCRB steady-state completion percentage $\gamma \doteq \left[\mathbf{J}_B^{-1}(\infty)\right]_{1,1} \Big/ \left[\mathbf{J}_B^{-1}(\tilde{n}_c^{(p)})\right]_{1,1}$.

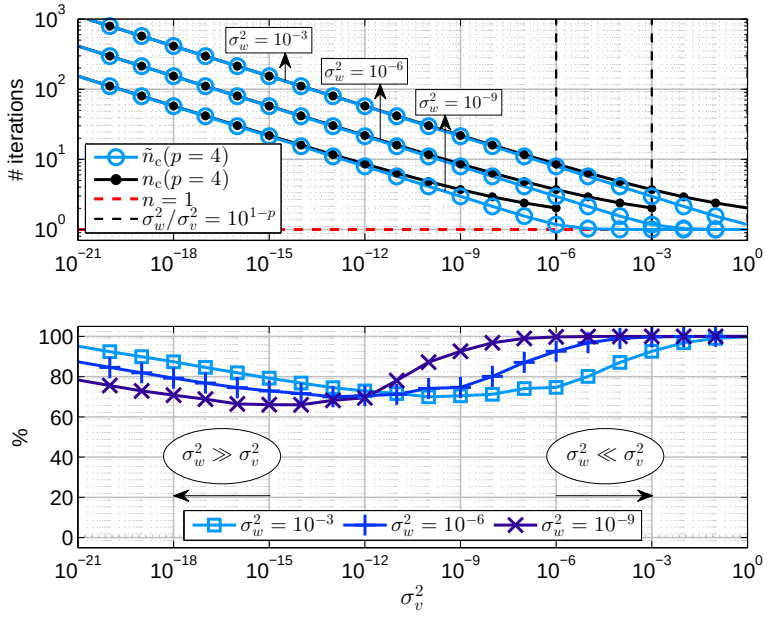

Figure 3.6: Same as Fig. 3.5, but with $p = 4$.

where $\mathbf{J}(n)$ has dimensions $(p \times p)$. This means that finding a closed-form expression for the steady-state performance of the Kalman filter translates into finding a closed-form expression of the $(p \times p)$ inverse of $\mathbf{J}(n)$. This problem becomes practically intractable

from the mathematical standpoint for sufficiently high model orders (*i.e.* $p > 2$). This is the reason why the derivations presented in this section are restricted to second-order Kalman filters (*i.e.* $p = 2$), leaving higher model orders out of the scope of this thesis.

In that sense, a second-order kinematic model, which can be understood as a random walk with a random-walk drift, adopts the following state-space model:

$$\begin{bmatrix} \theta(n) \\ \dot{\theta}(n) \end{bmatrix} = \begin{bmatrix} 1 & 1 \\ 0 & 1 \end{bmatrix} \begin{bmatrix} \theta(n-1) \\ \dot{\theta}(n-1) \end{bmatrix} + \begin{bmatrix} 1/2 \\ 1 \end{bmatrix} v(n) \tag{3.72}$$

where the state vector is defined as $\mathbf{x}(n) \doteq \begin{bmatrix} \theta(n) & \dot{\theta}(n) \end{bmatrix}^T$, and the transition and process noise propagation matrices become $\mathbf{F} \doteq \begin{bmatrix} 1 & 1 \\ 0 & 1 \end{bmatrix}$ and $\mathbf{G} \doteq \begin{bmatrix} 1/2 & 1 \end{bmatrix}^T$. The input measurements remain as in (3.21), being the measurement matrix $\mathbf{H} \doteq \begin{bmatrix} 1 & 0 \end{bmatrix}$ for the two-dimensional case.

3.7.1 Determination of Kalman Filter Steady-State Performance

Let us define the (2×2) FIM for the problem at hand as,

$$\mathbf{J}(n) = \begin{bmatrix} [\mathbf{J}(n)]_{1,1} & [\mathbf{J}(n)]_{1,2} \\ [\mathbf{J}(n)]_{2,1} & [\mathbf{J}(n)]_{2,2} \end{bmatrix} \tag{3.73}$$

which is a symmetric matrix, and thus $[\mathbf{J}(n)]_{1,2} = [\mathbf{J}(n)]_{2,1}$. As stated before, we are interested in finding a closed-form expression for the elements of the inverse FIM. As a matter of fact, when the dimensions are (2×2), the computation is straightforward,

$$\mathbf{J}^{-1}(n) = \frac{1}{[\mathbf{J}(n)]_{1,1}[\mathbf{J}(n)]_{2,2} - [\mathbf{J}(n)]_{1,2}^2} \begin{bmatrix} [\mathbf{J}(n)]_{2,2} & -[\mathbf{J}(n)]_{1,2} \\ -[\mathbf{J}(n)]_{1,2} & [\mathbf{J}(n)]_{1,1} \end{bmatrix}. \tag{3.74}$$

By inspection of (3.71) through the matrices $\mathbf{A}_{n,p}$ and $\mathbf{\Sigma}_{\mathbf{z}_n}$, which depend on the matrices $\mathbf{H}_p$, $\mathbf{F}_p$ and $\mathbf{G}_p$ for $p = 2$, the entries of the FIM are given by,

$$[\mathbf{J}(n)]_{1,1} = \mathbf{1}^T \mathbf{\Sigma}_{\mathbf{z}_n}^{-1} \mathbf{1} \tag{3.75}$$

$$[\mathbf{J}(n)]_{1,2} = -\boldsymbol{\eta}_n^T \mathbf{\Sigma}_{\mathbf{z}_n}^{-1} \mathbf{1} \tag{3.76}$$

$$[\mathbf{J}(n)]_{2,2} = \boldsymbol{\eta}_n^T \mathbf{\Sigma}_{\mathbf{z}_n}^{-1} \boldsymbol{\eta}_n \tag{3.77}$$

where $[\mathbf{J}(n)]_{1,2} = [\mathbf{J}(n)]_{2,1}$, and $\boldsymbol{\eta}_n \doteq [(n-1),\ (n-2),\ \ldots,\ 0]^T$. By substituting these elements into (3.74), the estimation performance of the Kalman filter at hand is found to be lower-bounded by,

$$\mathbf{J}^{-1}(n) = \frac{1}{\mathbf{1}^T\boldsymbol{\Sigma}_{\mathbf{z}_n}^{-1}\mathbf{1}\boldsymbol{\eta}_n^T\boldsymbol{\Sigma}_{\mathbf{z}_n}^{-1}\boldsymbol{\eta}_n - \left(-\boldsymbol{\eta}_n^T\boldsymbol{\Sigma}_{\mathbf{z}_n}^{-1}\mathbf{1}\right)^2}\begin{bmatrix}\boldsymbol{\eta}_n^T\boldsymbol{\Sigma}_{\mathbf{z}_n}^{-1}\boldsymbol{\eta}_n & \boldsymbol{\eta}_n^T\boldsymbol{\Sigma}_{\mathbf{z}_n}^{-1}\mathbf{1}\\ \boldsymbol{\eta}_n^T\boldsymbol{\Sigma}_{\mathbf{z}_n}^{-1}\mathbf{1} & \mathbf{1}^T\boldsymbol{\Sigma}_{\mathbf{z}_n}^{-1}\mathbf{1}\end{bmatrix} \tag{3.78}$$

The expressions above manifest that $\mathbf{J}(n)$ in (3.71) requires computing the inverse matrix of $\boldsymbol{\Sigma}_{\mathbf{z}_n}$. For the purpose at hand, it is of interest to compute $\boldsymbol{\Sigma}_{\mathbf{z}_n}^{-1}$ using a closed-form expression that avoids the inverse operation as such. However, we face again the problem that finding a closed-form expression for the inverse of an $(n\times n)$ matrix becomes quite a mathematical challenge, since n can take any integer value. For this reason, an approximation that considerably simplifies the complexity of the problem is proposed in Section 3.7.2.

3.7.2 Derivation of Closed-Form Approximation

By taking advantage of the knowledge of $\mathbf{M}_n$, the following approximation for $\boldsymbol{\Sigma}_{\mathbf{z}_n}$ is proposed:

$$\widetilde{\boldsymbol{\Sigma}}_{\mathbf{z}_n} \doteq \sigma_v^2\widetilde{\mathbf{M}}_n + \sigma_w^2\mathbf{I}_n \tag{3.79}$$

where $\widetilde{\mathbf{M}}_n \doteq \mathbf{d}_{\mathbf{M}_n}\mathbf{d}_{\mathbf{M}_n}^H$ is defined herein as an approximated version of $\mathbf{M}_n$ with $\mathbf{d}_{\mathbf{M}_n} \doteq \sqrt{\text{diag}(\mathbf{M}_n)}$ the $(n\times 1)$ vector containing the diagonal elements of $\mathbf{M}_n$ found in Section 3.5.2, Eq. (3.55),

$$[\mathbf{M}_n]_{k,k} = \sum_{m=1}^{n-k}\left(\mathbf{H}_p\mathbf{F}_p^{-m}\mathbf{G}_p\right)^2 \tag{3.80}$$

We proceed by finding an expression driving the elements in (3.55) as a function of k for the problem at hand. Substituting the matrices $\mathbf{H}_p$, $\mathbf{F}_p$ and $\mathbf{G}_p$ by those in (3.72) for a second-order kinematic model, it is found that,

$$\mathbf{H}\mathbf{F}^{-m}\mathbf{G} = \frac{1}{2} - m \Longrightarrow \left(\mathbf{H}\mathbf{F}^{-m}\mathbf{G}\right)^2 = m^2 - 2m + 1. \tag{3.81}$$

Then, the summatory in (3.55) is applied to the result in (3.81), and after some mathematical manipulations, it is found that,

$$[\mathbf{M}_n]_{(n-k),(n-k)} = \frac{k}{12}\left(4k^2-1\right) \Longrightarrow [\mathbf{d}_{\mathbf{M}_n}]_{n-k} = \sqrt{\frac{k}{12}\left(4k^2-1\right)}. \tag{3.82}$$

In Figure 3.7 we evaluate the tightness of the approximation above employing the same values of σ_w^2 and σ_v^2 as in Figure 3.4 consistently with the assumption that $\sigma_w^2 \gg \sigma_v^2$. Figure 3.7 depicts the BCRB for $[\mathbf{J}_{\mathrm{B}}^{-1}(n)]_{1,1}$ compared to $[\mathbf{J}^{-1}(n)]_{1,1}$ under the approximated version of $\mathbf{M}_n$ and also when neglecting $\mathbf{M}_n$ in $\mathbf{\Sigma}_{\mathbf{z}_n}$ (*i.e.* zero process-noise). The approximation is seen to provide a tight match with the BCRB while the Kalman filter is in its transient stage and also at the starting region of the steady state. In contrast, when neglecting $\mathbf{M}_n$, such steady state is never reached. This observation supports the importance of $\mathbf{M}_n$ and its proposed approximation.

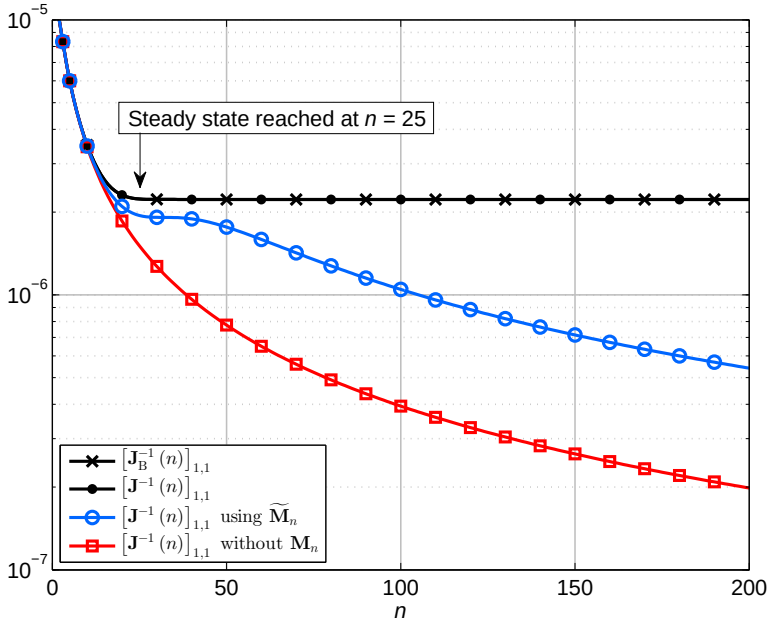

Figure 3.7: Comparison between recursive BCRB for $[\mathbf{J}_{\mathrm{B}}^{-1}(n)]_{1,1}$ and CRB for $[\mathbf{J}^{-1}(n)]_{1,1}$ with different versions of $\mathbf{M}_n$.

The advantage of the proposed approximation is that it allows finding the corresponding inverse of $\mathbf{\Sigma}_{\mathbf{z}_n}$ in a straightforward manner. The Woodbury's identity matrix (*i.e.* matrix inversion lemma) can be applied on the inverse of (3.79) to obtain,

$$\widetilde{\mathbf{\Sigma}}_{\mathbf{z}_n}^{-1} = \frac{1}{\sigma_w^2}\left(\mathbf{I}_n - \frac{6\sigma_v^2}{24\sigma_w^2 + \gamma(n)\sigma_v^2}\mathbf{d}_{\mathbf{M}_n}\mathbf{d}_{\mathbf{M}_n}^T\right). \tag{3.83}$$

Replacing the matrix $\mathbf{\Sigma}_{\mathbf{z}_n}^{-1}$ in (3.78) with the approximated version in (3.83), the following closed-form approximation for the inverse FIM is obtained,

$$\widetilde{\mathbf{J}}^{-1}(n) = \frac{1}{\mathbf{1}^T\widetilde{\mathbf{\Sigma}}_{\mathbf{z}_n}^{-1}\mathbf{1}\boldsymbol{\eta}_n^T\widetilde{\mathbf{\Sigma}}_{\mathbf{z}_n}^{-1}\boldsymbol{\eta}_n - \left(-\boldsymbol{\eta}_n^T\widetilde{\mathbf{\Sigma}}_{\mathbf{z}_n}^{-1}\mathbf{1}\right)^2}\begin{bmatrix}\boldsymbol{\eta}_n^T\widetilde{\mathbf{\Sigma}}_{\mathbf{z}_n}^{-1}\boldsymbol{\eta}_n & \boldsymbol{\eta}_n^T\widetilde{\mathbf{\Sigma}}_{\mathbf{z}_n}^{-1}\mathbf{1} \\ \boldsymbol{\eta}_n^T\widetilde{\mathbf{\Sigma}}_{\mathbf{z}_n}^{-1}\mathbf{1} & \mathbf{1}^T\widetilde{\mathbf{\Sigma}}_{\mathbf{z}_n}^{-1}\mathbf{1}\end{bmatrix}. \tag{3.84}$$

At this point, it must be recalled that this approximation can be applied up to the beginning of the steady state, $n = n_{\mathrm{c}}$, whereas it loses its validity when $n \to \infty$. Therefore, the performance lower bounds for the parameters of interest in steady state can be approximated by,

$$\lim_{n\to\infty} \left[\mathbf{J}_{\mathrm{B}}^{-1}(n)\right]_{1,1} \approx \left[\widetilde{\mathbf{J}}^{-1}(n_{\mathrm{c}})\right]_{1,1} = \frac{\boldsymbol{\eta}_{n_{\mathrm{c}}}^T \widetilde{\boldsymbol{\Sigma}}_{\mathbf{z}_{n_{\mathrm{c}}}}^{-1} \boldsymbol{\eta}_{n_{\mathrm{c}}}}{\mathbf{1}^T \widetilde{\boldsymbol{\Sigma}}_{\mathbf{z}_{n_{\mathrm{c}}}}^{-1} \mathbf{1} \boldsymbol{\eta}_{n_{\mathrm{c}}}^T \widetilde{\boldsymbol{\Sigma}}_{\mathbf{z}_{n_{\mathrm{c}}}}^{-1} \boldsymbol{\eta}_{n_{\mathrm{c}}} - \left(-\boldsymbol{\eta}_{n_{\mathrm{c}}}^T \widetilde{\boldsymbol{\Sigma}}_{\mathbf{z}_{n_{\mathrm{c}}}}^{-1} \mathbf{1}\right)^2} \tag{3.85}$$

$$\lim_{n\to\infty} \left[\mathbf{J}_{\mathrm{B}}^{-1}(n)\right]_{2,2} \approx \left[\widetilde{\mathbf{J}}^{-1}(n_{\mathrm{c}})\right]_{2,2} = \frac{\mathbf{1}^T \widetilde{\boldsymbol{\Sigma}}_{\mathbf{z}_{n_{\mathrm{c}}}}^{-1} \mathbf{1}}{\mathbf{1}^T \widetilde{\boldsymbol{\Sigma}}_{\mathbf{z}_{n_{\mathrm{c}}}}^{-1} \mathbf{1} \boldsymbol{\eta}_{n_{\mathrm{c}}}^T \widetilde{\boldsymbol{\Sigma}}_{\mathbf{z}_{n_{\mathrm{c}}}}^{-1} \boldsymbol{\eta}_{n_{\mathrm{c}}} - \left(-\boldsymbol{\eta}_{n_{\mathrm{c}}}^T \widetilde{\boldsymbol{\Sigma}}_{\mathbf{z}_{n_{\mathrm{c}}}}^{-1} \mathbf{1}\right)^2} \tag{3.86}$$

where n_{c} can be computed using the result in Section 3.6.1, Eq. (3.70) for the Kalman filter convergence time using $p = 2$.

3.7.3 Goodness of Approximation

This section aims at illustrating the applicability of the result in (3.85) and (3.86) for a broad range of values of σ_w^2 and σ_v^2, under the condition $\sigma_w^2 \gg \sigma_v^2$. To this end, some simulation results are provided in Figure 3.8. The experimental performance of the Kalman filter given by the variance of $\left[\hat{\mathbf{x}}\,(n)\right]_1$ in steady state is compared to the approximation of $\left[\mathbf{J}^{-1}(n)\right]_{1,1}$ in (3.85) using $\tilde{n}_{\mathrm{c}}^{(2)}$ in (3.70). A tight match between the exact result and the proposed approach can be drawn in the central operating region. Some discrepancies appear when $\sigma_v^2 \to 0$, but this is consistent with the fact that the proposed method is applicable on the performance floor of the Kalman filter, which appears under the steady-state regime whenever $\sigma_v^2 \neq 0$. It is for this reason that mismatches tend to attenuate when σ_v^2 departs from zero, as observed in the figure. With this, we can confirm the effectiveness of the proposed approach for low-medium (*i.e.* $\sigma_v^2 \sim 10^{-10}$) to high σ_v^2, up to the point where the condition $\sigma_w^2 \gg \sigma_v^2$ no longer holds.

3.8 Conclusions

An interesting feature of the Kalman filter is that the BCRB tool allows predicting its estimation performance without resorting to the implementation of the filter and running several Montecarlo realizations. Since numerical or recursive evaluations are still required to solve for the BCRB, the main contribution of this chapter has been the derivation

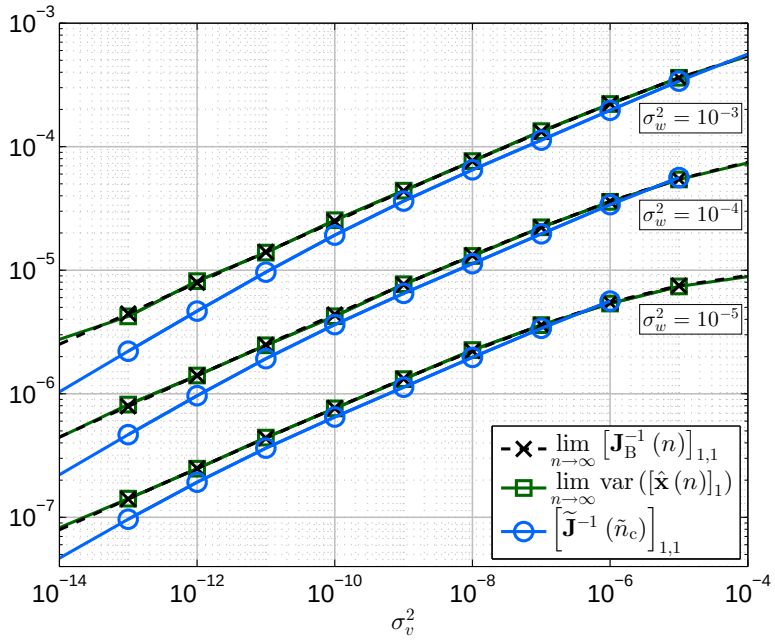

Figure 3.8: Comparison between steady state estimation performance and proposed approximation for $\left[\mathbf{J}^{-1}(n)\right]_{1,1}$ in (3.85).

of closed-form approximations to the convergence time of any-order kinematic Kalman filters through asymptotic analysis, and to the steady-state performance of second-order kinematic ones. In both cases, this has been done by reformulating the Kalman filter in batch mode and analyzing the problem using the tools from classical estimation theory. Simulation results have validated the goodness of the proposed approaches under the design assumption that the measurement noise is much larger than the process noise, which is actually the common situation in practice.

To obtain the results above, in the first part of this chapter the fundamental concepts of the Kalman filter have been introduced. The state-space model has been presented as the way to propagate and track the parameters of interest, and the observation model has been presented as the interaction between the Kalman states and the data provided at the system output. In addition, the Kalman recursive equations have been presented as the way for updating the Kalman gains as a function of the parameters of the problem. The main guidelines for the set-up and tuning of the Kalman filter have been provided, with special emphasis on the process noise covariance matrix, which ultimately determines the transient and steady-state performance by introducing a floor effect in the latter.

Then, in the second part of this chapter, the Kalman filter formulation has been particularized for the problem of GNSS carrier tracking, detailing the corresponding state-space

and observation models to deal with carrier phase measurements whose evolution is assumed to follow a kinematic model approximated by a third-order Taylor series expansion. The information provided in this chapter constitutes the baseline from which the hybrid autoregressive Kalman filter will be designed in the subsequent chapters.

Chapter 4

Autoregressive Modeling of Ionospheric Scintillation

4.1 Motivation

Ionospheric scintillation is a disturbance caused by electron density irregularities that introduce rapidly time-varying amplitude fades and random phase fluctuations into GNSS signals when propagating through the ionosphere. This severely degrades the operation of GNSS receivers, which are prone to suffer from severe carrier phase jitter and to fall into frequent losses of lock when affected by ionospheric scintillation.

Scintillation presents a random nature. As a consequence, it can be modeled using a random process following some probability function. For the amplitude, a correlated Nakagami-M distribution may provide a good match with empirical measurements [Heg01], whereas at the phase level a correlated Gaussian distribution is often considered as a first-order approximation [Hum10b]. This latter observation is of particular interest for scintillation to be encompassed by Kalman filter-based techniques and thus take advantage of their optimality properties under Gaussian disturbances. This opens the door to the possibility of modeling scintillation phase variations using a linear-model random process, which can be embedded into the linear Kalman filter formulation in such a way that they can be dealt with in a natural manner. An example of random processes following a linear model is the class of autoregressive (AR) processes, which have already been employed in other applications such as modeling signal strength measurements in wireless links [How92] or pseudorange variations caused by multipath [De-11].

Therefore, the aim of this chapter is to evaluate how well scintillation phase variations can be modeled using AR processes. To this end, Section 4.2 presents the signal model of an AR process, as well as two equivalent methods to determine the parameters defining such model. The problem of scintillation phase AR fitting is then addressed in Section 4.3. To do so, we will consider two different cases of input scintillation, namely synthetic data using the Cornell scintillation model, and a sample of captured data containing real scintillation time series.

4.2 AR Signal Model and Parameter Determination

Let $\varphi(n)$ be a unitless autoregressive time series at time instant n with order p, denoted henceforth as AR(p). Its time-domain representation is given by [Kay93],

$$\varphi(n) = \sum_{k=1}^{p} \beta_k \varphi(n-k) + s_p(n) \tag{4.1}$$

where $\{\beta_k\}_{k=1}^{p}$ is the set of AR coefficients, and $s_p(n)$ is the so-called AR driving noise for a given pth order, which is usually modeled as a zero-mean Gaussian process with variance $\sigma_{s_p}^2$, that is, $s_p(n) \sim \mathcal{N}\left(0,\ \sigma_{s_p}^2\right)$. These parameters are the ones determining the all-pole frequency response, or power spectral density (PSD), of an AR(p) process:

$$S_\varphi\left(e^{j\omega}\right) = \frac{\sigma_{s_p}^2}{|1 - \sum_{k=1}^{p} \beta_k e^{-j\omega}|^2}. \tag{4.2}$$

Eqs. (4.1) and (4.2) manifest that the problem of AR modeling boils down to determining the set of AR coefficients and driving noise variance. To this end, two equivalent approaches are usually employed, namely the *Yule-Walker* equations and the *least squares* method.

4.2.1 The Yule-Walker Equations

The Yule-Walker (YW) method relies on the fact that the autocorrelation function (ACF) of an AR(p) process can be related to the AR coefficients according to the following recursion [Kay93]:

$$r_\varphi[k] = \begin{cases} \sum_{m=1}^{p} \beta_m r_\varphi[k-m] & k \geqslant 1 \\ \sum_{m=1}^{p} \beta_m r_\varphi[m] + \sigma_{s_p}^2 & k = 0 \end{cases} \tag{4.3}$$

which is termed the YW equations. In matrix form, these become,

$$\begin{bmatrix} r_\varphi[0] & r_\varphi[1] & \cdots & r_\varphi[p-1] \\ r_\varphi[0] & r_\varphi[0] & \cdots & r_\varphi[0] \\ \vdots & \vdots & \ddots & \vdots \\ r_\varphi[p-1] & r_\varphi[p-2] & \cdots & r_\varphi[0] \end{bmatrix} \begin{bmatrix} \beta_1 \\ \beta_2 \\ \vdots \\ \beta_p \end{bmatrix} = \begin{bmatrix} r_\varphi[1] \\ r_\varphi[2] \\ \vdots \\ r_\varphi[p] \end{bmatrix} \tag{4.4}$$

where the matrix at the left-hand side is the autocorrelation matrix of $\varphi(n)$, $\mathbf{R}_\varphi$. We denote (4.4) in vector notation as follows,

$$\mathbf{R}_\varphi \boldsymbol{\beta} = \mathbf{r}_\varphi. \tag{4.5}$$

On the other hand, in view of the second case in (4.3), the AR driving noise variance can be expressed as,

$$\sigma_{s_p}^2 = r_\varphi[0] - \sum_{k=1}^{p} \beta_k r_\varphi[k]. \tag{4.6}$$

The YW method consists in solving the YW equations in (4.4), (4.5) for the AR coefficients $\boldsymbol{\beta}$, and then use the result to obtain the AR driving noise variance in (4.6). To this end, the approach adopted in practice is to obtain an estimated version of the ACF from the available data using either the unbiased or the biased ACF estimators in (4.7) and (4.8), respectively [Sto97]:

$$\hat{r}_{\varphi,\text{unbiased}}[k] \doteq \frac{1}{N-k} \sum_{m=0}^{N-1} \varphi(k+m)\varphi^*(m) \tag{4.7}$$

$$\hat{r}_{\varphi,\text{biased}}[k] \doteq \frac{1}{N} \sum_{m=0}^{N-1} \varphi(k+m)\varphi^*(m) \tag{4.8}$$

with N the number of data samples. However, the most commonly used ACF estimator is the biased one. The reason is twofold:

- Whereas the two estimators behave similarly for small k, the biased one provides better accuracy for large k. This is because the ACF decays rapidly with k for most stationary signals. In this sense, the unbiased estimator may provide large and erratic values for large k owing to the small averaging (for instance, only one product for $k = N-1$), whereas the biased estimator provides small values.

- The biased estimator is guaranteed to be positive semidefinite, while it is not in the unbiased one, which may thus lead to negative spectral estimates.

It is for these reasons that we employ the biased ACF estimator, which we will henceforth denote as simply $\hat{r}_\varphi[k]$ for convenience. By replacing the ACFs in (4.3) with their estimated versions, and isolating $\boldsymbol{\beta}$, the AR coefficients are obtained as,

$$\hat{\boldsymbol{\beta}} = \hat{\mathbf{R}}_\varphi^{-1}\hat{\mathbf{r}}_\varphi \tag{4.9}$$

and the AR driving noise variance can therefore be estimated as,

$$\hat{\sigma}_{s_p}^2 = \hat{r}_x(0) - \sum_{k=1}^{p} \hat{\beta}_k \hat{r}_x(k) = \hat{r}_x(0) - \hat{\boldsymbol{\beta}}^T \hat{\mathbf{r}}_x. \tag{4.10}$$

4.2.2 The Least-Squares Approach

The least squares (LS) approach relies on the fact that the recursion in (4.1) can be written as follows:

$$s_p(n) = \varphi(n) - \hat{\varphi}(n) \tag{4.11}$$

where we define $\hat{\varphi}(n) \doteq \sum_{k=1}^{p} \beta_k \varphi(n-k)$. The objective of the least squares approach is to find the coefficients $\{\beta_k\}_{k=1}^{p}$ that minimize the power of the error in (4.11). That is, those that make $\hat{\varphi}(n)$ as close to $\varphi(n)$ as possible. Therefore, $\hat{\varphi}(n)$ can be understood as an estimation or prediction of $\varphi(n)$ by means of a linear combination of previous values of $\varphi(n)$ in the interval $[n-p,\ n-1]$. For this reason, the least squares approach for AR parameter estimation is also referred to as a linear prediction problem, where $\{\beta_k\}_{k=1}^{p}$ are the linear prediction coefficients and $s_p(n)$ is the linear prediction error with power,

$$\sigma_{s_p}^2 = \mathrm{E}\left[|\varphi(n) - \hat{\varphi}(n)|^2\right]. \tag{4.12}$$

The linear prediction coefficients are obtained as those $\{\beta_k\}_{k=1}^{p}$ that minimize the linear prediction error power. The LS solution to this problem is that which minimizes the following cost function,

$$J\left(\beta_k\right) = \sum_{n=0}^{N-1} \left| \varphi(n) - \sum_{k=1}^{p} \beta_k \varphi(n-k) \right|^2 \tag{4.13}$$

which is based on a given segment of $\varphi(n)$ with length N samples. By defining,

$$\boldsymbol{\varphi} \doteq \begin{bmatrix} \varphi(0) & \varphi(1) & \cdots & \varphi(N-1) \end{bmatrix}^T \tag{4.14}$$

$$\boldsymbol{\Phi} \doteq \begin{bmatrix} \varphi(-1) & \varphi(-2) & \cdots & \varphi(-p) \\ \varphi(0) & \varphi(-1) & \cdots & \varphi(-p+1) \\ \vdots & \vdots & \ddots & \vdots \\ \varphi(N-2) & \varphi(N-3) & \cdots & \varphi(N-1-p) \end{bmatrix} \tag{4.15}$$

the LS solution for $\{\beta_k\}_{k=1}^{p}$ is found to be given by,

$$\hat{\boldsymbol{\beta}} = \left(\boldsymbol{\Phi}^T\boldsymbol{\Phi}\right)^{-1}\boldsymbol{\Phi}^T\boldsymbol{\varphi} \tag{4.16}$$

while the linear prediction error power can be obtained by resorting to the maximum likelihood (ML) estimate using $\hat{\boldsymbol{\beta}}$ as follows,

$$\hat{\sigma}_{s_p}^2 = \frac{1}{N}\left\|\boldsymbol{\varphi} - \boldsymbol{\Phi}\hat{\boldsymbol{\beta}}\right\|^2. \tag{4.17}$$

The LS approach can be interpreted as an approximation to the Yule-Walker method by recognizing that the terms $\boldsymbol{\Phi}^T\boldsymbol{\Phi}$ and $\boldsymbol{\Phi}^T\boldsymbol{\varphi}$ in (4.16) are, to within a multiplicative constant, finite-sample estimates of $\mathbf{R}_\varphi$ and $\mathbf{r}_\varphi$, respectively. As a matter of fact, when the data sample length N employed in the least squares method tends to that employed in the Yule-Walker equations, the terms $\boldsymbol{\Phi}^T\boldsymbol{\Phi}/N$ and $\boldsymbol{\Phi}^T\boldsymbol{\varphi}/N$ are exactly the biased ACF estimates used in the Yule-Walker method [Sto05]. Hence, as the term $1/N$ cancels out in (4.16), both methods are asymptotically equivalent approaches for AR parameter estimation for the problem at hand.

One of the drawbacks of the LS method in contrast to the YW one is that its stability is not guaranteed for small N. However, such instability is reported to be rather infrequent, and not a serious issue, being readily circumvented by using a sufficiently large N [Sto05]. As an important advantage, the LS method is more accurate than the YW one. In addition, the latter presents the drawback of requiring to compute an estimate of the ACF, which is time- and resource-consuming, plus the inverse of a $(p \times p)$ matrix. In contrast, the LS method requires computing only the latter, thus being a rather simpler approach. For the above reasons, we will henceforth employ the LS method for estimating the AR model parameters.

4.3 AR Modeling of Scintillation Phase Variations

4.3.1 Goodness of Scintillation AR Modeling

The methods presented in Sections 4.2.1 and 4.2.2 allow to find the parameters of an AR process that best fit a given set of measurements. In that sense, we now explore the feasibility of modeling scintillation phase variations through an AR(p) process as follows. First, the estimated AR parameters $\{\hat{\boldsymbol{\beta}},\ \hat{\sigma}_{s_p}^2\}$ are employed in (4.2) to compute the power

spectral density (PSD) of the resulting AR process as,

$$\hat{S}_{\varphi}(f) = \frac{\hat{\sigma}^2_{s_p}}{\left|1 - \sum_{k=1}^{p} \hat{\beta}_k \exp\left(-j2\pi f k\right)\right|^2}. \tag{4.18}$$

This is then compared to the actual PSD of the true scintillation phase. The simplest way to compute the latter is by means of a non-parametric spectral estimation method. That is, estimate spectra without making any prior assumption on the underlying structure of the data under analysis. The most straightforward estimator is the periodogram, defined in terms of the Fourier transform of the data,

$$S_{\varphi}(f) = \frac{1}{N}\left|\sum_{n=0}^{N-1} \varphi(n) \exp\left(-j2\pi f n\right)\right|^2. \tag{4.19}$$

with $\varphi(n)$ now in dimensions of radians. This whole process is termed AR model fitting, and the objective here is to validate how well scintillation phase variations can be modeled through an AR process. To do so, we will consider AR models with different orders, namely $p = \{1, 2, 3\}$, for both synthetic and real scintillation time series, as shown next.

4.3.1.1 Synthetic Cornell Scintillation Time Series

Ionospheric scintillation can be understood as a multiplicative channel introducing signal amplitude $A_s(n)$ and phase $\varphi_s(n)$ variations to the received baseband signal $r(n)$:

$$\epsilon_s(n) = A_s(n)\exp\left(j\varphi_s(n)\right) r(n). \tag{4.20}$$

In that sense, scintillation is usually characterized in the literature though two different indexes: S_4 for amplitude scintillation, and σ_{φ_s} for phase scintillation [Van93]. S_4 is an indicator of the scintillation intensity in terms of amplitude, and it is defined as [Hum10a],

$$S_4 = \sqrt{\frac{\mathrm{E}\left[A_s^2(n)\right] - \mathrm{E}\left[A_s(n)\right]^2}{\mathrm{E}\left[A_s(n)\right]^2}} \tag{4.21}$$

whereas σ_{φ_s} is the standard deviation of scintillation phase over a given period of time, usually one minute. Scintillation is declared present when σ_{φ_s} exceeds a given threshold, typically 0.25 radians [Dub06].

An alternative approach that can also be found in the literature to characterize scintillation is by means of the S_4 and τ_0 indexes, the latter termed the decorrelation time and defined as the time lag at which the auto correlation function of a scintillating complex

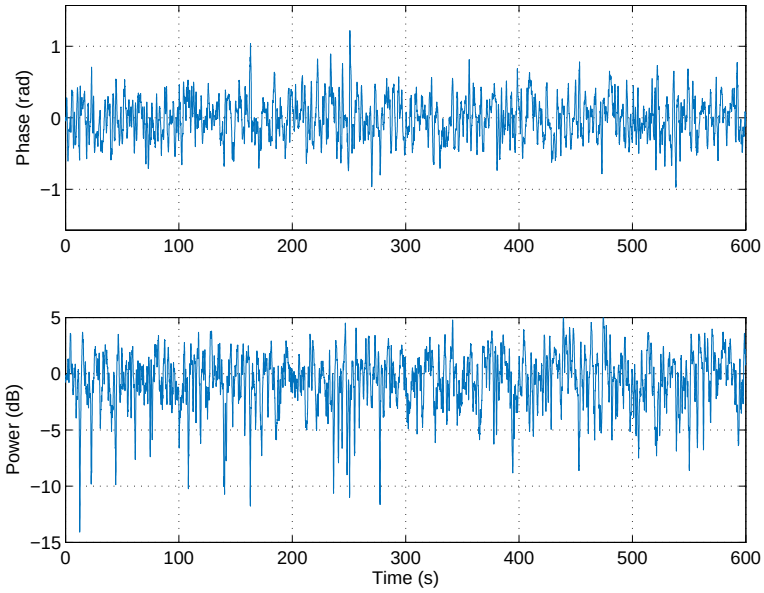

Figure 4.1: Example of a realization of Cornell moderate scintillation time series illustrating phase variations (top) and signal power fades (bottom).

baseband signal falls off by a factor 1/exp(1) [Hum10b]. In the sequel, we will consider a class of synthetic scintillation data that is generated using the so-called *Cornell scintillation model* (CSM), as a first approach for synthesizing scintillation time series using the set of indexes $\{S_4, \tau_0$. As a rule of thumb, the higher S_4 and lower τ_0, the more severe scintillation. We will distinguish between two different operation regions in terms of Cornell scintillation intensity: moderate scintillation, with $S_4 = 0.5$ and $\tau_0 = 0.8$ seconds corresponding to $\sigma_{\varphi_s} = 0.3$ rad, and severe scintillation, with $S_4 = 0.8$ and $\tau_0 = 0.4$ seconds corresponding to $\sigma_{\varphi_s} = 0.8$ rad.

An example of a realization of Cornell moderate scintillation is shown in Figure 4.1. As can be observed, scintillation phase variations are mainly comprised within ± 1 rad, while accompanied by power fades that typically do not exceed -10 dB. On the other hand, Figure 4.2 shows an example of a realization of Cornell severe scintillation. This is a much more extreme situation where phase variations reach the ATAN2 discriminator pull-in range of $\pm\pi$ rad, and the power fades can readily exceed -30 dB. It is worth noting that this is quite a critical case, meaning that the working conditions are often slightly milder. However, we find reasonable to consider this situation, so that the design of the carrier tracking loop can be pushed to the limits of such a worst-case scenario.

The set of AR parameters $\{\boldsymbol{\beta},\ \sigma^2_{s_p}\}$ that are found to best fit the two above situations are computed using (4.16) and (4.17), and the results are summarized in Table 4.1 for

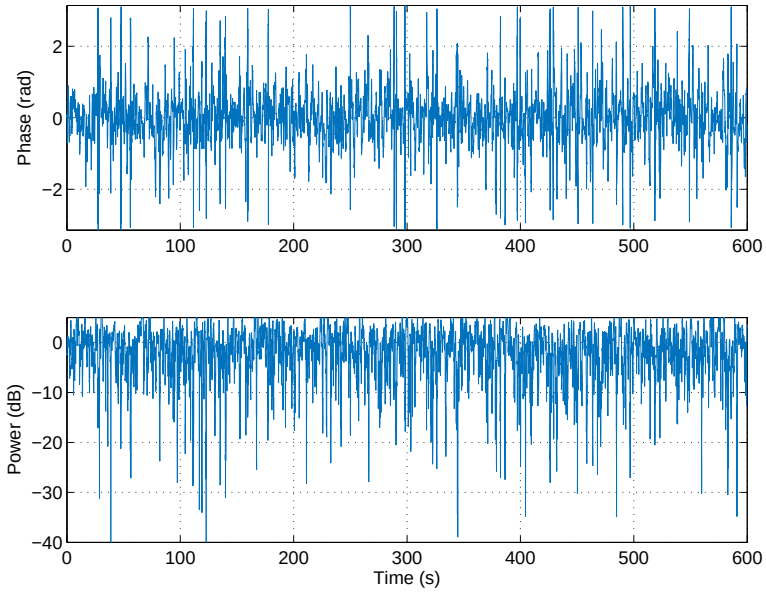

Figure 4.2: Example of a realization of Cornell severe scintillation time series illustrating phase variations (top) and signal power fades (bottom).

AR model orders up to $p = 3$, with $\sigma^2_{s_p}$ now in dimensions of rad^2. The results for the AR model fitting using the values in Table 4.1 are shown in Figures 4.3 and 4.4 for Cornell severe and moderate scintillation, respectively. The former indicates that severe scintillation can be modeled using any pth-order AR process, owing to the short decorrelation between adjacent samples. Hence, increasing the order of the AR model does not provide a major benefit. This suggests that a good model can be obtained for severe scintillation by just keeping the lowest AR order. As a matter of fact, this result can already be anticipated by noting in Table 4.1 that the β_2 and $\{\beta_2, \beta_3\}$ coefficients for AR(2) and AR(3) processes, respectively, are close to zero, and the AR process is mainly driven by β_1, thus resembling an AR(1) process. On the other hand, Figure 4.4 stands out the misfit of moderate scintillation with an AR(1) process, thus manifesting the need to resort to AR models with higher order, namely $p \geqslant 2$. This result is consistent with the fact that moderate scintillation tends to have a longer correlation between adjacent samples, an effect that can be simulated by using more coefficients in the AR model. Even though moderate scintillation can be modeled using either AR(2) or AR(3), the latter is found to provide a slightly better fit, a fact that can be confirmed by noting in Table 4.1 that AR(3) is the model providing smaller prediction error.

	Moderate scintillation		Severe scintillation	
	$\hat{\boldsymbol{\beta}}$ (unitless)	$\hat{\sigma}^2_{s_p}$ (rad^2)	$\hat{\boldsymbol{\beta}}$ (unitless)	$\hat{\sigma}^2_{s_p}$ (rad^2)
AR(1)	0.9972	$1.6337 \cdot 10^{-4}$	0.9631	$3.5756 \cdot 10^{-2}$
AR(2)	[1.9735, -0.9755]	$7.9407 \cdot 10^{-6}$	[1.0394, -0.0793]	$3.5531 \cdot 10^{-2}$
AR(3)	[2.6243, -2.2921, 0.6672]	$4.4066 \cdot 10^{-6}$	[1.0373, -0.0515, -0.0267]	$3.5506 \cdot 10^{-2}$

Table 4.1: Optimal AR parameters for the AR fitting of the CSM.

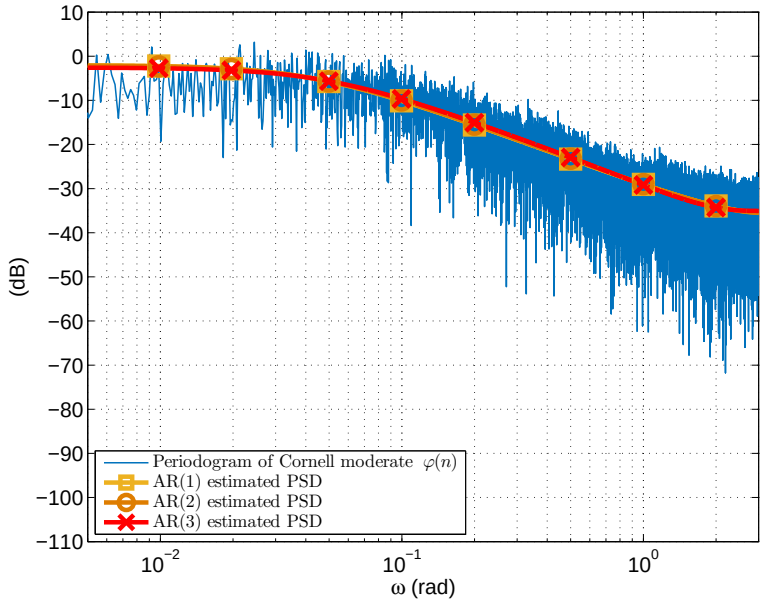

Figure 4.3: Periodogram of Cornell severe scintillation versus PSD of optimal AR(1, 2, 3) processes.

4.3.1.2 Real Scintillation Time Series

Once Cornell synthetic data has been evaluated, we consider now the problem of AR fitting for real scintillation data. The time series used in this thesis comes from ESA's Ionospheric Monitoring Network, which is provided with a number of scintillation monitoring stations placed at strategic locations worldwide, as shown in Figure 4.5. However, the obtained data must undergo a data-detrending process prior to processing ionospheric scintillation, as explained next.

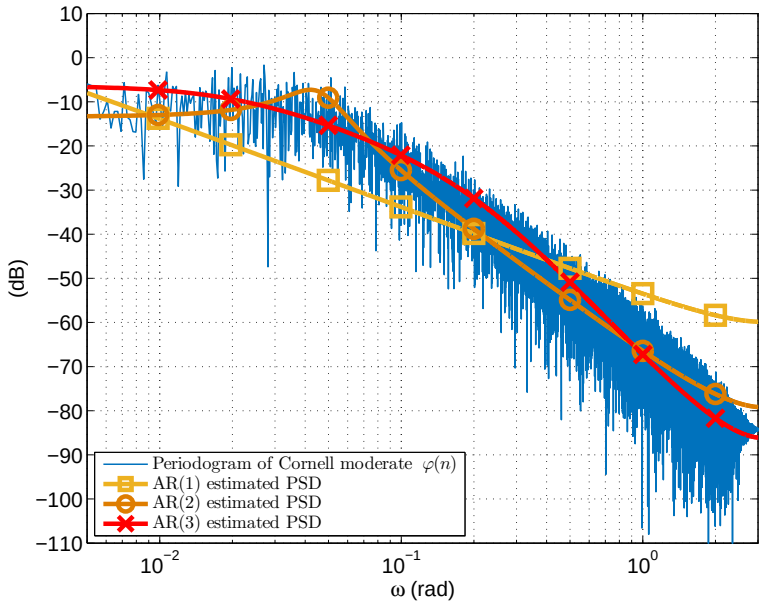

Figure 4.4: Periodogram of Cornell moderate scintillation versus PSD of optimal AR(1, 2, 3) processes.

Data Detrending

The time series received from ESA's monitoring network are affected by residual low-frequency systematic effects such as those from the troposphere, satellite geometry, and receiver oscillator instabilities, particularly when using TCXO [Van93]. These effects introduce undesired phase fluctuations that add up to the scintillation phase variations and must therefore be removed beforehand. Such removal process is termed *data detrending*, and includes both signal phase and power detrending [Des12]. In general, the errors can be eliminated by subtracting carrier and IQ phase of a non-scintillating reference channel from those of scintillating channels. In case all channels are scintillating, the reference channel is chosen to be that with lowest scintillation power ratio [O'H11].

The process of data detrending is explained in detail in [Des12, For02], and the required steps are briefly summarized next. In order to obtain detrended phase data:

1. Using carrier phase measurements from different channels, subtract the carrier phase of a non-scintillating reference channel $\varphi_{c_{\text{ref}}}(n)$ to the carrier phase of the ith tracking channel affected by scintillation $\varphi_{c_i}(n)$:

$$\varphi_c(n) \doteq \varphi_{c_i}(n) - \varphi_{c_{\text{ref}}}(n). \tag{4.22}$$

   In this way, the common receiver clock errors are canceled out.

Figure 4.5: Distribution of ESA's Ionospheric Monitoring stations around the world.

2. Elimination of clock errors is followed by removal of satellite geometry effects. To this end, subtract a polynomial fit of $\varphi_c(n)$, denoted as $\tilde{\varphi}_c(n)$, to the original $\varphi_c(n)$:

$$\tilde{\varphi}(n) \doteq \varphi_c(n) - \tilde{\varphi}_c(n). \tag{4.23}$$

3. The high-frequency variations of interest introduced by scintillation are not present in $\tilde{\varphi}(n)$. In order to recover them, we can exploit the IQ phase data provided by the receiver, which is defined in terms of the in-phase and quadrature phase components as $\arctan(Q/I)$. From this, subtract the IQ phase of the non-scintillating reference $\varphi_{\mathrm{IQ}_{\mathrm{ref}}}(n)$ to the IQ phase of the ith scintillating channel of interest $\varphi_{\mathrm{IQ}_i}(n)$:

$$\varphi_{\mathrm{IQ}}(n) \doteq \varphi_{\mathrm{IQ}_i}(n) - \varphi_{\mathrm{IQ}_{\mathrm{ref}}}(n). \tag{4.24}$$

4. Add the differenced IQ phase $\varphi_{\mathrm{IQ}}(n)$ to the differenced carrier phase $\tilde{\varphi}(n)$:

$$\varphi(n) \doteq \tilde{\varphi}(n) + \varphi_{\mathrm{IQ}}(n). \tag{4.25}$$

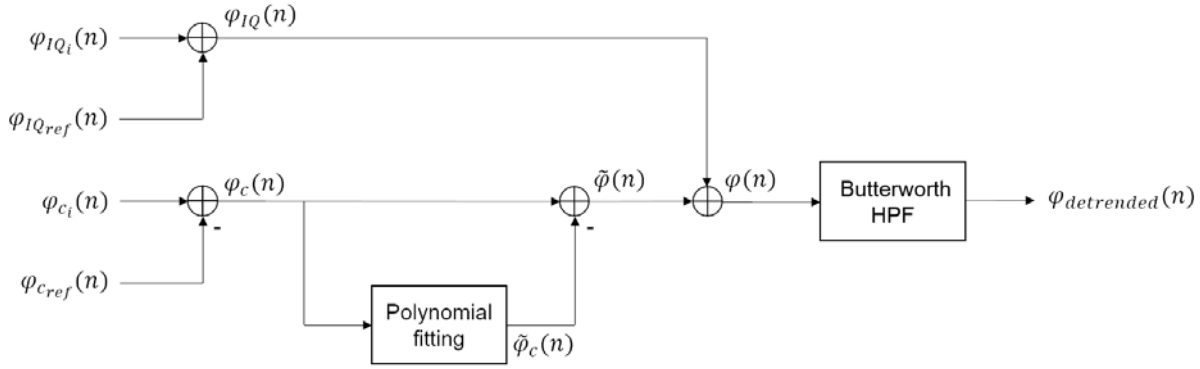

Figure 4.6: Block diagram summarizing the process of phase data detrending to obtain real scintillation time series [Des12].

5. Apply a high-pass sixth-order Butterworth filter to $\varphi(n)$ to wipe all residual low-frequency fluctuations not belonging to scintillation, while high-frequency variations introduced by scintillation do remain [Van01]. In this way, the detrended phase $\varphi_{\text{detrended}}(n)$ is eventually obtained.

The steps for phase data detrending can be observed in form of a block diagram in Figure 4.6.

On the other hand, for signal power detrending, the following two steps are required:

1. Apply a low-pass sixth-order Butterworth filter to the raw power data $\left(\mathrm{I}^2 + \mathrm{Q}^2\right)$ of the ith scintillating channel of interest $P_{r_i}(n)$. The low-pass filtered output is denoted as $P_{\mathrm{LPF}_i}(n)$.

2. Divide $P_{\mathrm{r}_i}(n)$ by the low-pass-filtered version $P_{\mathrm{LPF}_i}(n)$ obtained in the previous step:

$$P(n) = \frac{P_{\mathrm{r}_i}(n)}{P_{\mathrm{LPF}_i}(n)} \tag{4.26}$$

thus obtaining as a result the instantaneous power normalized to the mean one.

Once detrended phase and power have been obtained following the steps above, the resulting is a signal containing only scintillation phase and amplitude effects, which can now be processed as done for Cornell synthetic data.

AR Fitting for Real Scintillation

As stated in the introduction of this dissertation, scintillation is more prominent in equatorial regions. Therefore, in order to carry out a representative analysis of real

scintillation, in this thesis we select the monitoring station placed in Dakar, at a longitude of 352.623897 degrees and small latitude of 14.764939 degrees. Furthermore, scintillation is also dependent on the season of the year and the time of the day [Aar82]. More precisely, scintillation is found to be more intense at the dark times of the day (sunset-midnight) and year (autumn-winter). Following this idea, in this thesis we analyze a time series captured on December 1st, 2014, from 22:00 to 23:00 hours, for GPS SV #24. After the data-detrending process, the look of scintillation phase and power variations is shown in Figure 4.7 top and bottom, respectively.

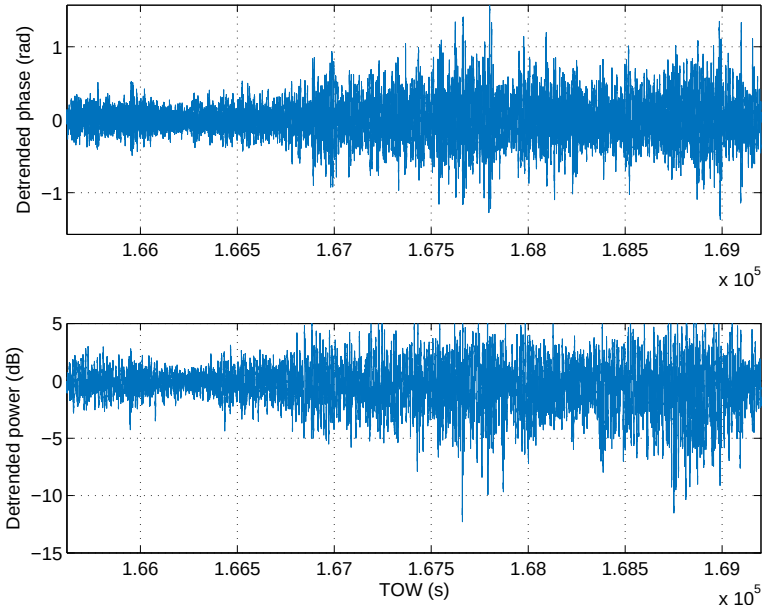

Figure 4.7: Detrended scintillation phase (top) and power (bottom) of DAK2.2014.335.22.GPS24 real time series from ESA's Ionospheric Monitoring Network.

Once data has been detrended, the problem of AR fitting can now be evaluated. In Figure 4.7 it can be noticed that the scintillation intensity is not uniform over the observation interval, but presents a rather time-varying behavior. That is, starting at low intensity at the beginning, it gradually increases over time until reaching maximum activity from TOW 167500s on. This phenomenon also manifests when estimating the AR fitting parameters, as shown in Figure 4.8, where both the AR coefficient and driving noise increase until reaching values above the mean one (in black dotted line).

We will hence focus on the time period above TOW 167500s on, so as to work with a more representative scintillation time series. Using the LS method for AR parameter estimation previously described in Section 4.2.2, the set of AR parameters $\{\boldsymbol{\beta},\ \sigma^2_{s_p}\}$ that

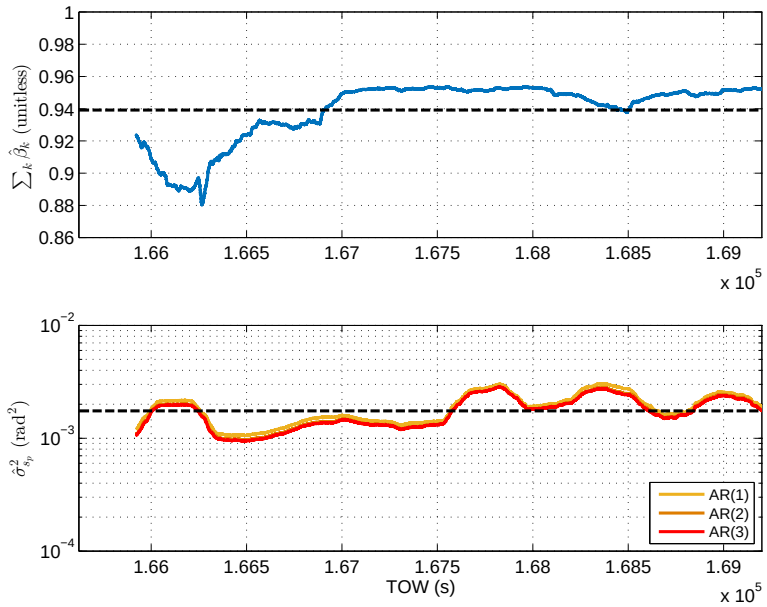

Figure 4.8: Time evolution of estimated AR coefficients (top) and driving noise (bottom) for DAK2.2014.335.22.GPS24 real time series.

are found to best fit the real time series under analysis are summarized in Table 4.2 for AR model orders up to $p = 3$.

	DAK2.2014.335.22.GPS24	
	$\hat{\boldsymbol{\beta}}$ (unitless)	$\hat{\sigma}^2_{s_p}$ (rad^2)
AR(1)	0.9501	$2.3223 \cdot 10^{-3}$
AR(2)	[0.7210, 0.2316]	$2.1753 \cdot 10^{-3}$
AR(3)	[0.7024, 0.1637, 0.0874]	$2.1533 \cdot 10^{-3}$

Table 4.2: Optimal AR parameters for the AR fitting of DAK2.2014.335.22.GPS24 real scintillation time series.

The results for the AR model fitting using the values in Table 4.2 are shown in Figure 4.9. As can be observed, real scintillation phase can be modeled using an AR process with the lowest order, even though higher-order models are found to slightly better fit this data capture. The latter can actually be noticed from Table 4.2 or the bottom plot of Figure 4.8, where the AR(2) provides smaller prediction error power, while further increasing the AR model order provides no major benefit. Therefore, real scintillation presents a behavior in between that of Cornell moderate and severe scintillation analyzed in Section 4.3.1.1.

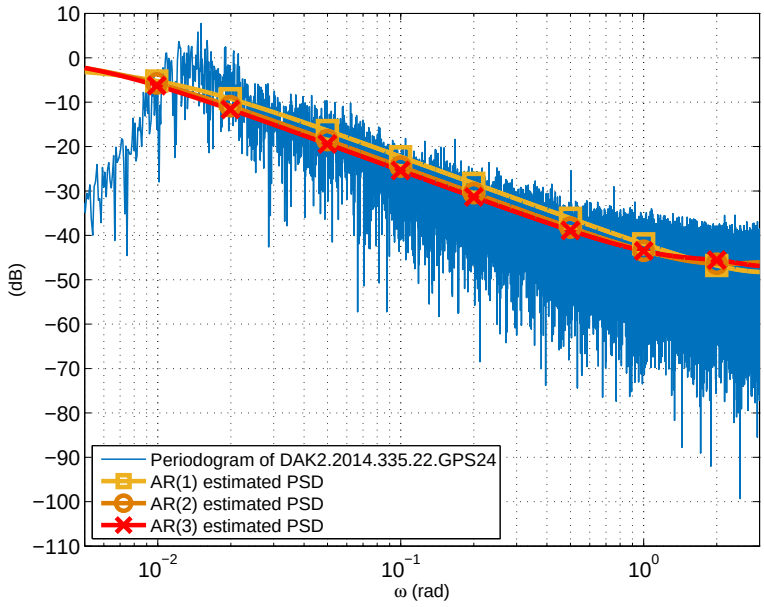

Figure 4.9: Periodogram of real scintillation versus PSD of optimal AR(1, 2, 3) processes.

4.3.2 Optimal AR Model Order Selection

It has been shown in Section 4.3.1 that severe scintillation phase variations can actually be modeled using an AR(1) process, whereas moderate variations are better modeled using AR processes with higher order (*i.e.* $p \geqslant 2$). These results manifest the need for some selection mechanism in order to choose the best model order to be used at every time instant, or even disable the AR module and switch to the dynamics-only KF in the absence of scintillation, also referred to as AR(0). This is thought to be a very convenient approach, as it fits very well into the time-varying behavior of scintillation disturbances in real environments.

Determining the optimal order of a statistical model is a well-known problem in the field of signal processing that is often referred to as model-order selection [Sto04]. In that sense, the statement of the problem is briefly introduced in Section 4.3.2.1 along with some of the selection criteria typically found in the literature. Then, we will focus on the criterion employed in this work, termed the minimum description length criterion.

4.3.2.1 Model Order Selectors

Optimal model order selection is a well-known problem that typically arises in AR spectral estimation, and follows a similar fashion to classical ML estimation, where the

parameter (*i.e.* the model order in our case) that has most likely produced a given set of data is to be chosen. An underestimated model order results in a smoothed spectral estimate, whereas an overestimated model order introduces statistical instability [Kay88]. For the case of AR scintillation modeling, the problem is addressed as follows.

Recalling the matrix notation of AR processes introduced in Section 4.2.2, the AR prediction error in (4.11) can be written as,

$$\mathbf{s}_p(n) = \boldsymbol{\varphi} - \boldsymbol{\Phi}\boldsymbol{\beta} \tag{4.27}$$

where $\mathbf{s}_p(n) \doteq \begin{bmatrix} s_p(0) & s_p(1) & \cdots & s_p(N-1) \end{bmatrix}$ and $[\boldsymbol{\varphi},\ \boldsymbol{\Phi}]$ contain time-shifted replicas of $\varphi(n)$ as in (4.14) and (4.15), respectively.

Since we assume the AR driving noise to be Gaussian distributed, the likelihood function for the problem at hand is given by,

$$f_p\left(\boldsymbol{\varphi}|\boldsymbol{\beta}, \sigma^2_{s_p}\right) = \frac{1}{(2\pi)^{\frac{N}{2}}\,\sigma^N_{s_p}} e^{-\frac{1}{2\sigma^2_{s_p}}\|\boldsymbol{\varphi}-\boldsymbol{\Phi}\boldsymbol{\beta}\|^2} \tag{4.28}$$

whose compressed log-likelihood becomes,

$$-2\log\left(f_p\left(\boldsymbol{\varphi}|\boldsymbol{\beta}, \sigma^2_{s_p}\right)\right) = C + N\log\left(\sigma^2_{s_p}\right) \tag{4.29}$$

with some term C. The rationale of such term relies on the fact that, in essence, model order estimators are based on the estimated prediction power, which is guaranteed to decrease or stay the same as the model order increases [Kay88]. For this reason, the model order selection cannot be carried out by monitoring only the decrease in such power, but must also contemplate some penalty term accounting for the variance enhancement when increasing p. Such penalty term is indeed given by C.

Once the compressed log-likelihood function is available, different model order selection criteria can be applied to find the order p that best fits the measurements:

- A common approach is given by the **Akaike's information criterion** (AIC) [Aka74], which seeks the value of p that minimizes the following cost function:

$$\mathrm{AIC}(p) = N\log\left(\hat{\sigma}^2_{s_p}\right) + 2p. \tag{4.30}$$

  However, the AIC presents two drawbacks. First, it tends to overfit when enlarging the data record. Second, it is not a consistent criterion, understanding by "consistency" the fact that the probability of estimating the correct model order tends to 1 when increasing N.

- The **corrected AIC** [Cav97, Sug78] aims at reducing the overfitting of the AIC by employing a larger penalty term:

$$\mathrm{AIC_c}(p) = N \log\left(\hat{\sigma}^2_{s_p}\right) + 2pC_N \tag{4.31}$$

where $C_N = \frac{N}{N-p-1}$. However, the opposite effect to the AIC may occur. That is, the $\mathrm{AIC_c}$ presents the risk of underfitting.

- The AIC and $\mathrm{AIC_c}$ criteria can actually be grouped in a more general framework, the so-called **generalized information criteria** (GIC) [Sto04],

$$\mathrm{GIC} = N \log\left(\hat{\sigma}^2_{s_p}\right) + 2pC'_N \tag{4.32}$$

which actually equals the $\mathrm{AIC_c}$ when $C'_N = C_N$ and the AIC when $C'_N = 1$, and can often outperform the AIC when setting $C'_N > 1$ [Zou13].

- The **minimum description length** (MDL) [Ris78], also referred to as the Bayesian information criterion (BIC) [Sch78, Dju99] is a model order selector that finds the optimal model order of an AR process as that value of p that minimizes the MDL cost function:

$$\hat{p}_{\mathrm{MDL}} = \arg\min_p J_{\mathrm{MDL}}(p) \tag{4.33}$$

with $J_{\mathrm{MDL}}(p) = -2\log\left(f_p\left(\boldsymbol{\varphi}|\boldsymbol{\beta}, \sigma^2_{s_p}\right)\right) + p\log(N)$ which, for the problem at hand, can be simplified after some mathematical manipulations to,

$$J_{\mathrm{MDL}}(p) = N \log\left(\sigma^2_{s_p}\right) + p\log(N) \tag{4.34}$$

which is nothing but the compressed log-likelihood function in (4.29) with penalty term $C = p\log(N)$. Therefore, the optimal MDL model order can be obtained as,

$$\hat{p}_{\mathrm{MDL}} = \arg\min_p \left(N \log\left(\hat{\sigma}^2_{s_p}\right) + p\log(N)\right) \tag{4.35}$$

with $\hat{\sigma}^2_{s_p}$ the estimated prediction error power of an AR model with given pth order.

The most relevant advantage of the MDL criterion is that, in contrast to the rest of model order selectors presented in this section, it is a consistent criterion. It is for this reason that the MDL is the order selector of choice in the remainder of this document.

4.3.2.2 MDL Test with CSM Time Series

In order to test the MDL criterion for our problem, we first consider the case of synthetic data; we generate the Cornell scintillation phase in the same way as in Section 4.3.1.1. In order to provide reliable results, a simulation with length 10 minutes is carried out, with a sampling time of 20 ms so as to be consistent with that of the DAK2.2014.335.22.GPS24 real scintillation capture.

The model order is estimated by using a limited-length set of data in form of a sliding window that moves forward along the time axis in a sample-by-sample basis. As in many other signal processing applications, the length of such window becomes a trade-off between sensitivity to data variations and estimation accuracy. In our case, a long window preserves the consistency feature of the MDL criterion; a short window is however desirable so as to be able to monitor rapid variations in the scintillation phase. Therefore, it is important to select the proper balance between both contributions. As a rule of thumb, we will henceforth use a window with length 5 seconds.

Simulation results are shown in Figure 4.10 in terms of the percentage of time each model order is selected, considering up to $p = 3$. It is observed that the results are in accordance with the results in Section 4.3.1.1. That is, low-order models are found not to fit moderate scintillation quite well, and the MDL tends to select high-order AR models, mainly AR(3). For severe scintillation, the three model orders are indistinctly chosen, meaning that severe scintillation can already be modeled using an AR(1) process. Even so, a trend to select high-order models can also be appreciated; an AR(3) is preferable over an AR(1, 2), meaning that high-order AR models are found to provide slightly smaller prediction error.

4.3.2.3 MDL Test with Real Scintillation Time Series

We now evaluate the MDL criterion for the DAK2.2014.335.22.GPS24 real scintillation time series. Figure 4.11 shows the percentage of time each model order is selected, considering up to $p = 3$. As can be observed, all three model orders can be selected, but models with $p \geqslant 2$ are found to be the ones mainly chosen by the MDL, rather than an AR(1). Both AR(2) and AR(3) are chosen indistinctly, meaning that they provide a very similar fit to the real scintillation capture with very similar prediction error power as shown previously in Table 4.2. These results are in accordance with the ones in Section 4.3.1.2.

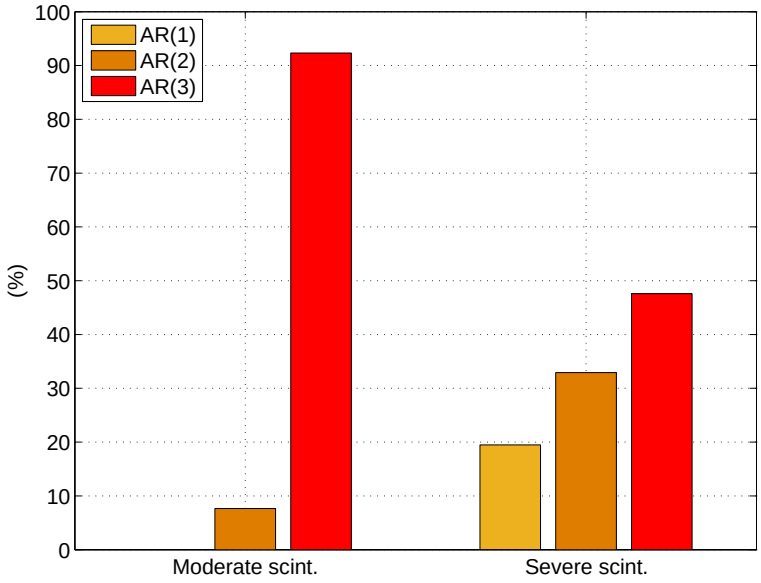

Figure 4.10: Percentage of time that each AR model order is selected by the MDL criterion, for Cornell moderate and severe scintillation.

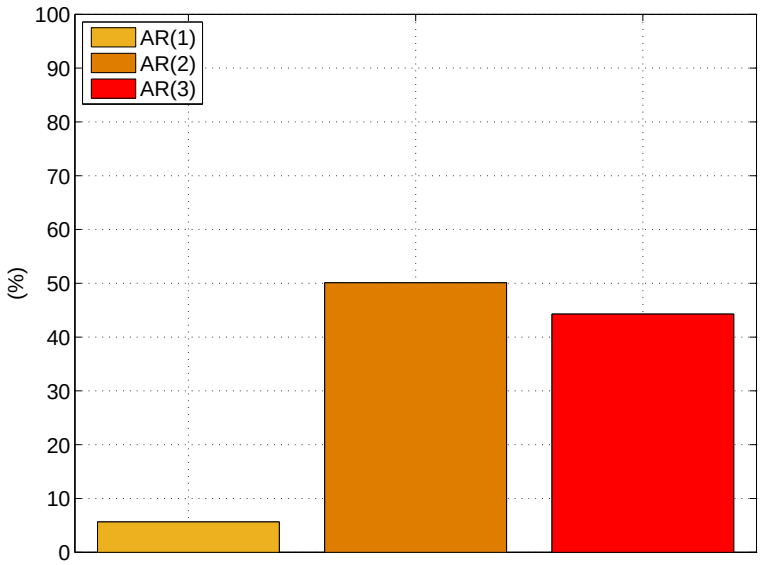

Figure 4.11: Percentage of time that each AR model order is selected by the MDL criterion, for DAK2.2014.335.22.GPS24 real scintillation time series.

4.4 Conclusions

In this chapter, ionospheric scintillation has been introduced as a disturbance caused by the time-varying electron density of the Earth's ionospheric layer. It affects GNSS signals by introducing rapid signal amplitude fades and random carrier phase variations.

In that sense, this chapter has contributed with a thorough analysis on exploring the feasibility of modeling the latter using autoregressive processes. To this end, the problem of AR model fitting to scintillation phase variations has been addressed. Two different situations have been considered. First, the fitting to synthetic data using the Cornell scintillation model. Second, the fitting to a real data capture containing representative time series of scintillation activity in equatorial regions and at dark times of the day and year.

The obtained results have shown the goodness of modeling scintillation phase variations using AR processes. For severe scintillation, the lowest AR model order has been found to already fit well, whereas higher-order models have been concluded to better fit moderate scintillation events. The latter has been confirmed by the AR fitting of real scintillation. For this reason, this chapter has also addressed the problem of model order fitting in order to determine the optimal AR model order of a given data time series, placing the main focus on the minimum description length criterion. The test results have been shown consistent with the statements above.

In view of these conclusions, we are now ready to embed AR signal models into the Kalman filter formulation to deal with scintillation phase variations.

Chapter 5

Robust Carrier Tracking under Ionospheric Scintillation Conditions

5.1 Introduction

Chapter 3 introduced the Kalman filter as the natural improvement to conventional PLLs for GNSS carrier tracking in harsh environments. The carrier dynamics have been modeled using a third-order kinematic model, while also deriving the corresponding Kalman state-space model. Chapter 4 introduced ionospheric scintillation as a detrimental effect onto both signal power and carrier phase measurements. Scintillation phase variations have been found to be well modeled using AR processes, an observation that becomes of great interest; since the latter are linear processes with a correlated Gaussian distribution, we can formulate a state-space model for the Kalman filter to encompass scintillation in a natural manner and exploit its optimality properties in the presence of Gaussian disturbances. This can further be combined with the kinematic model for the carrier dynamics, giving rise to a novel hybrid formulation: the hybrid autoregressive Kalman filter, denoted henceforth as the so-called KF-AR or KF-AR(p).

The use of the KF-AR for GNSS carrier tracking under the presence of ionospheric scintillation has recently started to gain interest in the literature, where early contributions analyze the performance of such technique encompassing a fixed AR(1) model as a first approach [Vil13]. Furthermore, the need for continuously estimating and tracking the optimal AR model parameters for scintillation modeling has been shortly identified in [Foh18]. Therefore, in this chapter we make a leap forward in the design of KF-AR

techniques by introducing novel adaptive KF-AR implementations to deal with scintillation disturbances, which are rather time-varying in practice both in the phase and signal amplitude domains. The idea is to estimate the AR parameters in an online manner for the Kalman filter to self-adapt to the actual working conditions and provide optimal performance irrespective of them. In addition, in this chapter we also derive close-form expressions for the BCRB convergence time and steady-state performance of this kind of techniques.

This chapter is organized as follows. Section 5.2 presents the core of the KF-AR as a Kalman filter with an augmented state-space model to track both the carrier dynamics and scintillation phase variations simultaneously, in the presence of one another but in a decoupled manner. The aim of this technique is to virtually dissociate scintillation from carrier dynamics to further provide clean estimates of each of them, focusing on the latter in navigation and positioning applications. In Section 5.3 we provide a qualitative evaluation of the performance bounds of the KF-AR, while also deriving closed-form expressions for characterizing the KF-AR in a straightforward manner. In Section 5.7 the properties of controllability and observability are presented as a tool for checking on the filter feasibility and proper operation. Section 5.8 presents the adaptive implementations mentioned above. A phenomenon that has been so far overlooked is the fact that GNSS signals entering the Kalman filter are inherently corrupted by some nonzero measurement noise. In terms of AR parameter identification this is an important problem because, even if the input is a pure AR process, the presence of AWGN causes the aggregated random process to depart from a truly AR model. In this sense, during the design of the adaptive implementations we provide a brief analysis on how the presence of AWGN degrades the proper determination of AR parameters is also conducted. In addition, we also propose a novel method to easily deal with non-linear scintillation amplitude fades. Last, in Section 5.9 we present a semi-adaptive version of the KF-AR with the goal of still providing optimal performance but employing an implementation with reduced complexity that is less time- and resource-consuming than the fully-adaptive technique.

5.2 Formulation of Hybrid Autoregressive Kalman Filter

5.2.1 State-Space Formulation and Measurement Model of AR Processes

The time-domain representation of an AR(p) time series was given in (4.1) and is recalled next,

$$\varphi(n) = \sum_{k=1}^{p} \beta_k \varphi(n-k) + s_p(n). \tag{5.1}$$

with $\varphi(n)$ henceforth in radians. The linear nature of (5.1) fits very well into the Kalman filter formulation, and it can be written as the following state-space model,

$$\begin{bmatrix} \varphi(n) \\ \varphi(n-1) \\ \varphi(n-2) \\ \vdots \\ \varphi(n-p+1) \end{bmatrix} = \begin{bmatrix} \beta_1 & \beta_2 & \beta_3 & \cdots & \beta_p \\ 1 & 0 & 0 & \cdots & 0 \\ 0 & 1 & 0 & \cdots & 0 \\ \vdots & 0 & \ddots & \ddots & \vdots \\ 0 & \cdots & 0 & 1 & 0 \end{bmatrix} \begin{bmatrix} \varphi(n-1) \\ \varphi(n-2) \\ \varphi(n-3) \\ \vdots \\ \varphi(n-p) \end{bmatrix} + \begin{bmatrix} 1 \\ 0 \\ 0 \\ \vdots \\ 0 \end{bmatrix} s_p(n) \tag{5.2}$$

which plays the role of the Kalman state transition equation. Therefore, it can be rewritten as,

$$\mathbf{x}_\varphi(n) = \mathbf{F}_\varphi \mathbf{x}_\varphi(n-1) + \mathbf{G}_\varphi s_p(n) \tag{5.3}$$

with $\mathbf{x}_\varphi(n) \doteq \begin{bmatrix} \varphi(n) & \varphi(n-1) & \varphi(n-2) & \cdots & \varphi(n-p+1) \end{bmatrix}^T$ the p-dimensional state vector at time instant n, and $s_p(n)$ the AR driving noise playing now the role of the Kalman process noise. Comparing Eqs. (5.2) and (5.3), the $(p \times p)$ and $(p \times 1)$ transition and process noise weighting matrices are identified as,

$$\mathbf{F}_\varphi \doteq \begin{bmatrix} \beta_1 & \beta_2 & \beta_3 & \cdots & \beta_p \\ 1 & 0 & 0 & \cdots & 0 \\ 0 & 1 & 0 & \cdots & 0 \\ \vdots & 0 & \ddots & \ddots & \vdots \\ 0 & \cdots & 0 & 1 & 0 \end{bmatrix} \tag{5.4}$$

$$\mathbf{G}_\varphi \doteq \begin{bmatrix} 1 & 0 & 0 & \cdots & 0 \end{bmatrix}^T \tag{5.5}$$

the latter leading to the process noise covariance matrix,

$$\mathbf{Q}_{\varphi} \doteq \sigma_{s_p}^2 \mathbf{G}_{\varphi}\mathbf{G}_{\varphi}^T = \begin{bmatrix} \sigma_{s_p}^2 & 0 & \dots & 0 \\ 0 & 0 & \dots & 0 \\ \vdots & \vdots & \ddots & \vdots \\ 0 & 0 & \dots & 0 \end{bmatrix}. \tag{5.6}$$

Similarly to Section 3.3, after some phase extraction at the prompt correlator output we are provided with scintillation phase measurements:

$$z_{\varphi}(n) = \mathbf{H}_{\varphi}\mathbf{x}_{\varphi}(n) + w(n) = \varphi(n) + w(n) \tag{5.7}$$

from which the $(p \times 1)$ observation matrix is identified as $\mathbf{H}_{\varphi} \doteq \begin{bmatrix} 1 & 0 & \cdots & 0 \end{bmatrix}$.

5.2.2 KF-AR(p) State-Space and Observation Models

In the sequel we will consider that the carrier phase evolves according to two separate contributions. On the one hand, the carrier dynamics, which has been modeled as a third-order kinematic process. On the other hand, the scintillation phase, which has been modeled using AR(p) processes. This means that our system needs to keep track of $\theta(n)$, $\dot{\theta}(n)$ and $\ddot{\theta}(n)$ as for the former, and $\varphi(n-k)$ as for the latter, with $k \doteq 0..p-1$.

The Kalman state-space and observation models for both contributions have been presented in Sections 3.3 and 5.2.1, respectively. Interestingly, their linear nature allows to merge both of them into a single state-space model, and thus formulate an augmented Kalman filter embedding the two models simultaneously. More precisely, we can think of a Kalman filter with the following state transition equation:

$$\begin{bmatrix} \mathbf{x}_{\theta}(n) \\ \mathbf{x}_{\varphi}(n) \end{bmatrix} = \begin{bmatrix} \mathbf{F}_{\theta} & \mathbf{0}_{3\times p} \\ \mathbf{0}_{p\times 3} & \mathbf{F}_{\varphi} \end{bmatrix} \begin{bmatrix} \mathbf{x}_{\theta}(n-1) \\ \mathbf{x}_{\varphi}(n-1) \end{bmatrix} + \begin{bmatrix} \mathbf{G}_{\theta} & \mathbf{0}_{3\times 1} \\ \mathbf{0}_{p\times 1} & \mathbf{G}_{\varphi} \end{bmatrix} \begin{bmatrix} v(n) \\ s_p(n) \end{bmatrix} \tag{5.8}$$

which can be written in compact form as,

$$\mathbf{x}(n) = \mathbf{F}\mathbf{x}(n-1) + \mathbf{G}\mathbf{q}(n) \tag{5.9}$$

thus giving raise to the so-called hybrid autoregressive Kalman filter, KF-AR, with $\mathbf{x}(n) \doteq \begin{bmatrix} \mathbf{x}_{\theta}(n) & \mathbf{x}_{\varphi}(n) \end{bmatrix}^T$ the augmented $(3+p)$-dimensional state vector, and $\mathbf{q}(n) \doteq$

$\begin{bmatrix} v(n) & s_p(n) \end{bmatrix}^T$ the process noise. By direct comparison of Eqs. (5.8) and (5.9), the augmented KF-AR transition and process noise weighting matrices can be identified:

$$\mathbf{F} \doteq \begin{bmatrix} \mathbf{F}_\theta & \mathbf{0}_{3\times p} \\ \mathbf{0}_{p\times 3} & \mathbf{F}_\varphi \end{bmatrix} \tag{5.10}$$

$$\mathbf{G} \doteq \begin{bmatrix} \mathbf{G}_\theta & \mathbf{0}_{3\times 1} \\ \mathbf{0}_{p\times 1} & \mathbf{G}_\varphi \end{bmatrix} \tag{5.11}$$

while the process noise covariance matrix becomes,

$$\mathbf{Q} \doteq \mathrm{E}\left[\mathbf{G}\mathbf{q}(n)\mathbf{q}(n)^H\mathbf{G}^H\right] = \begin{bmatrix} \mathbf{Q}_\theta & \mathbf{0}_{3\times p} \\ \mathbf{0}_{p\times 3} & \mathbf{Q}_\varphi \end{bmatrix}. \tag{5.12}$$

On the other hand, the prompt discriminator output provides measurements combining carrier phase and scintillation phase,

$$z(n) = \mathbf{H}\mathbf{x}(n) + w(n) = z_\theta(n) + \varphi(n) = \theta(n) + \varphi(n) + w(n) \tag{5.13}$$

from which the $((3+p)\times 1)$ observation matrix is identified as $\mathbf{H} \doteq \begin{bmatrix} \mathbf{H}_\theta & \mathbf{H}_\varphi \end{bmatrix}$, and where the measurement noise $w(n)$ remains a scalar value as in Eq. (3.22).

5.3 Bayesian Cramér-Rao Bound

Once the KF-AR state-space and observation models have been introduced, it is interesting to evaluate the general performance of the KF-AR where, apart from carrier phase, frequency and frequency rate, the scintillation disturbance $\varphi(n)$ is also jointly estimated. Similarly to Section 3.4.1, the analysis is performed by evaluating the recursive BCRB introduced in (3.28), which is recalled next:

$$\mathbf{J}^{-1}_{\mathrm{B_{rec}}}(n+1) = \left[\left(\mathbf{Q}(n) + \mathbf{F}(n)\mathbf{J}^{-1}_{\mathrm{B_{rec}}}(n)\mathbf{F}^T(n)\right)^{-1} + \mathbf{H}^T(n)\mathbf{R}^{-1}(n)\mathbf{H}(n)\right]^{-1}. \tag{5.14}$$

For $C/N_0 = 45$ dB-Hz and $\sigma_v^2 = 4\cdot 10^{-16}$ rad^2, Figure 5.1 illustrates the BCRB for carrier phase in steady state as a function of the AR process noise $\sigma_{s_p}^2$ using a KF-AR(1) with different values of β. From the interpretation of an AR process as a linear prediction problem, $\sigma_{s_p}^2 \to 0$ means that the process can perfectly be predicted. That is, the scintillation disturbance can perfectly be reproduced, and thus the Kalman filter performs as if scintillation is not present. For this reason, the BCRB coincides with that

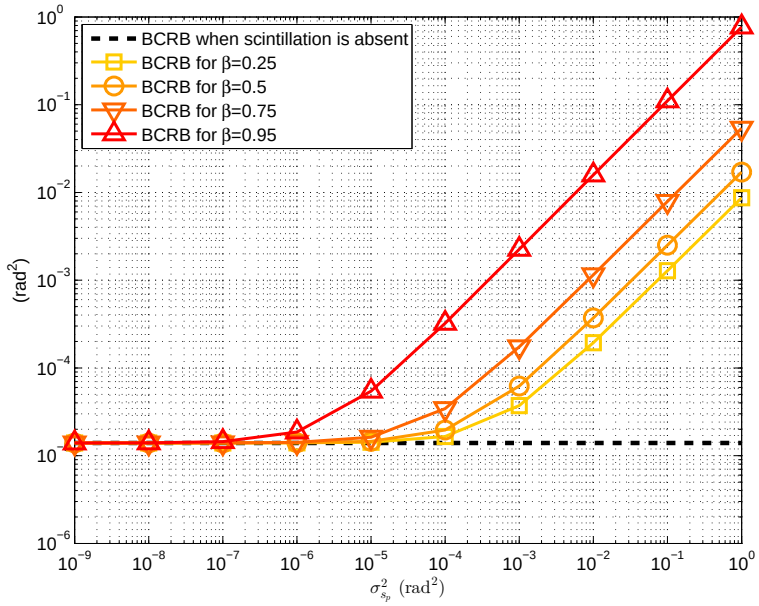

Figure 5.1: Recursive BCRB in steady state of KF-AR(1) for $C/N_0 = 45$ dB-Hz and and $\sigma_v^2 = 4 \cdot 10^{-16}$ rad^2, and different values of β as a function of AR prediction error $\sigma^2_{s_p}$.

of the KF for very low values of $\sigma^2_{s_p}$. However, increasing the AR prediction error $\sigma^2_{s_p}$ induces a degradation in the BCRB, meaning that the main limiting effect in the KF-AR estimation performance becomes the scintillation prediction error. That is, errors in the estimated scintillation hamper the dissociation between carrier dynamics and scintillation phase variations and propagate to the rest of Kalman states, thus leaving some irrecoverable errors onto the estimated phase of interest. As can be observed, this phenomenon becomes more prominent when scintillation phase samples are more correlated (*i.e.* larger β), an observation that goes in the line of moderate scintillation requiring more complex models than severe scintillation.

This is then the cost of having scintillation to be dealt with and introducing extra states into the KF to keep track of it, with respect to the case when there is no scintillation. The performance in the latter case will be obtained when $\sigma^2_{s_p} \to 0$, or when the C/N_0 is so low that the thermal noise becomes the main limiting effect, leaving scintillation hidden below the noise floor. This phenomenon is emphasized in Figure 5.2 with fixed $\beta = 0.95$ and $\sigma^2_{s_p} = 4 \cdot 10^{-5}$ rad^2; the top plot shows that, for a C/N_0 of 25 dB-Hz, the BCRBs when in the absence and in the presence of scintillation tend to converge, in contrast to the bottom plot for $C/N_0 = 45$ dB-Hz.

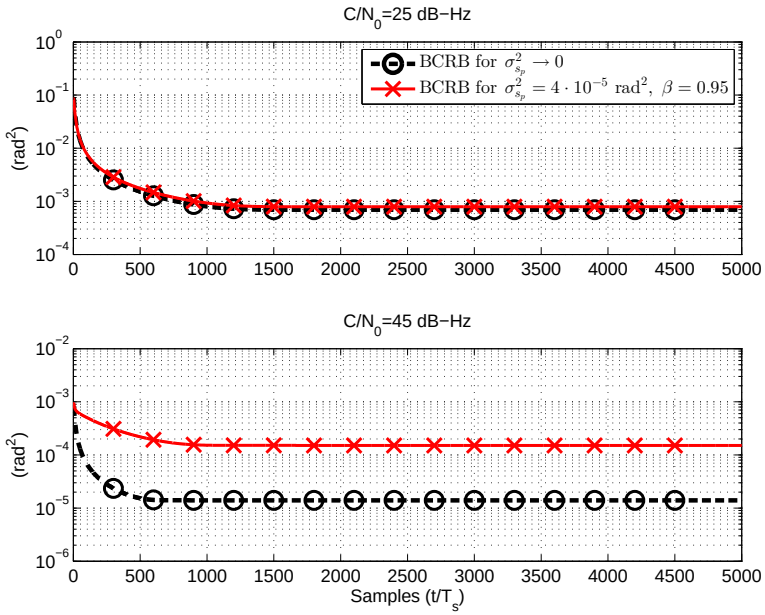

Figure 5.2: Recursive BCRB of KF-AR(1) with $\beta = 0.95$ and $\sigma_{s_p}^2 = 4 \cdot 10^{-5}$ rad^2 for $C/N_0 = 25$ dB-Hz (top) and $C/N_0 = 45$ dB-Hz (bottom).

5.4 Batch-Mode Formulation of Hybrid Autoregressive Kalman Filter

Chapter 3 presented the derivation of closed-form expressions for the convergence time and steady-state performance of Kalman filters following kinematic models with nonzero process noise. Notwithstanding, the Kalman filter can also be found in plenty of applications devoted to tracking magnitudes of any kind, such as the case of AR processes, as shown in this chapter. This is the case of [Kom02, Che04, Sim11], where a Kalman filter with an AR model is employed for channel estimation and equalization, as well as for manoeuvring target tracking [Jin15] and signal dereverberation [Bra16]. Another example is given by [Tat13], where a random-walk model is used within the Kalman filter to compute the coefficients of an AR process to estimate physiological trembling in medical robotic applications.

In that sense, this section introduces the formulation of hybrid autoregressive Kalman filters in batch mode that will serve us to derive closed-form expressions for the convergence time of these kind of techniques. Again, we will exploit the parallelism between the Kalman filter and the BLUE estimator when considering a diffuse initialization of the filter and a linear Gaussian model for the input measurements. To illustrate the method,

the derivation is restricted to a hybrid KF-AR combining a second-order kinematic model and a first-order AR process. In the sequel, this particular configuration will be referred to as KF(2)-AR(1). The proposed approach could eventually be extended to any order of the kinematic and AR models, even though the derivations become rather cumbersome from the mathematical standpoint and thus remain out of the scope of this thesis.

5.4.1 Batch Formulation

Recall the batch-mode signal model for the input measurements as a function of the Kalman state vector $\mathbf{x}(n)$,

$$\mathbf{z}_n = \mathbf{A}_n \mathbf{x}(n) + \mathbf{B}_n \mathbf{u}_n \tag{5.15}$$

where, for the KF(2)-AR(1), $\mathbf{A}_n$ and $\mathbf{B}_n$ are $(n \times 3)$ and $(n \times (3n-2))$ matrices given by,

$$\mathbf{A}_n \doteq \left[\mathbf{H}\mathbf{F}^{-(n-1)};\ \ \mathbf{H}\mathbf{F}^{-(n-2)};\ \ \cdots;\ \ \mathbf{H}\right] \tag{5.16}$$

$$\mathbf{B}_n \doteq \left[\mathbf{I}_n,\ \ \mathbf{B}_{n,\theta},\ \ \mathbf{B}_{n,\varphi}\right] \tag{5.17}$$

with

$$\mathbf{B}_{n,\theta} \doteq \begin{bmatrix} -\mathbf{H}_\theta \mathbf{F}_\theta^{-1} \mathbf{G}_\theta & \cdots & -\mathbf{H}_\theta \mathbf{F}_\theta^{-(n-1)} \mathbf{G}_\theta \\ 0 & \cdots & -\mathbf{H}_\theta \mathbf{F}_\theta^{-(n-2)} \mathbf{G}_\theta \\ \vdots & \ddots & \vdots \\ 0 & \cdots & -\mathbf{H}_\theta \mathbf{F}_\theta^{-1} \mathbf{G}_\theta \\ 0 & \cdots & 0 \end{bmatrix} \tag{5.18}$$

$$\mathbf{B}_{n,\varphi} \doteq \begin{bmatrix} -\beta^{-1} & \cdots & -\beta^{-(n-1)} \\ 0 & \cdots & -\beta^{-(n-2)} \\ \vdots & \ddots & \vdots \\ 0 & \cdots & -\beta^{-1} \\ 0 & \cdots & 0 \end{bmatrix}. \tag{5.19}$$

In (5.15), $\mathbf{u}_n \doteq \begin{bmatrix}\mathbf{w}_n, & \mathbf{v}_n, & \mathbf{s}_n\end{bmatrix}^T$ is a $((3n-2)\times 1)$ vector containing the measurement and process noise samples, with

$$\mathbf{w}_n \doteq \begin{bmatrix} w(1) & w(2) & \cdots & w(n)\end{bmatrix} \tag{5.20}$$

$$\mathbf{v}_n \doteq \begin{bmatrix} v(1) & v(2) & \cdots & v(n-1)\end{bmatrix} \tag{5.21}$$

$$\mathbf{s}_n \doteq \begin{bmatrix} s(1) & s(2) & \cdots & s(n-1)\end{bmatrix}. \tag{5.22}$$

The FIM associated to the BLUE estimator of $\mathbf{x}(n)$ from the measurements $\mathbf{z}_n \sim \mathcal{N}\left(\mathbf{A}_n\mathbf{x}(n), \mathbf{\Sigma}_{\mathbf{z}_n}\right)$ remains the same as in Section 3.5,

$$\mathbf{J}(n) = \mathbf{A}_n^H \mathbf{\Sigma}_{\mathbf{z}_n}^{-1}\mathbf{A}_n \tag{5.23}$$

with $\mathbf{\Sigma}_{\mathbf{z}_n}$ the measurements covariance matrix,

$$\mathbf{\Sigma}_{\mathbf{z}_n} \doteq \mathrm{E}\left[\mathbf{B}_n\mathbf{u}_n\mathbf{u}_n^H\mathbf{B}_n^H\right] = \mathbf{B}_n\mathbf{\Sigma}_{\mathbf{u}_n}\mathbf{B}_n^H. \tag{5.24}$$

The FIM in (5.23) coincides with the BIM $\mathbf{J}_{\mathrm{B}}(n)$ when in the absence of an informative prior. Therefore, one can exploit the known structure of $\mathbf{\Sigma}_{\mathbf{z}_n}$ within the FIM in (5.23) to evaluate the performance of the KF(2)-AR(1).

5.4.2 Inner Structure of the FIM

By inspection of (5.24) it is found that $\mathbf{\Sigma}_{\mathbf{z}_n}$ follows the fashion of (3.54), but a new term $\sigma_s^2\mathbf{S}_n$ arises owing to the contribution of the AR model,

$$\mathbf{\Sigma}_{\mathbf{z}_n} = \sigma_v^2\mathbf{M}_n + \sigma_s^2\mathbf{S}_n + \sigma_w^2\mathbf{I}_n \tag{5.25}$$

with $\mathbf{S}_n$ a nonnegative $(n\times n)$ symmetric matrix[1]. The diagonal elements of $\mathbf{M}_n$ are already known to be driven by (5.26), whereas it is easily found that the ones for $\mathbf{S}_n$ are given by (5.27),

$$[\mathbf{M}_n]_{k,k} = \sum_{m=1}^{n-k}\left(\mathbf{H}_\theta\mathbf{F}_\theta^{-m}\mathbf{G}_\theta\right)^2 \tag{5.26}$$

$$[\mathbf{S}_n]_{k,k} = \sum_{m=1}^{n-k}\beta^{-2m}. \tag{5.27}$$

In Section 3.5, we focused particularly on the diagonal elements of $\mathbf{\Sigma}_{\mathbf{z}_n}$, since it was the information from which the convergence time of the Kalman filter could be characterized. We will follow the same approach for the KF(2)-AR(1), as shown up next.

[1]Note that we have omitted the subscript p in σ_s^2 since it has now a specific value.

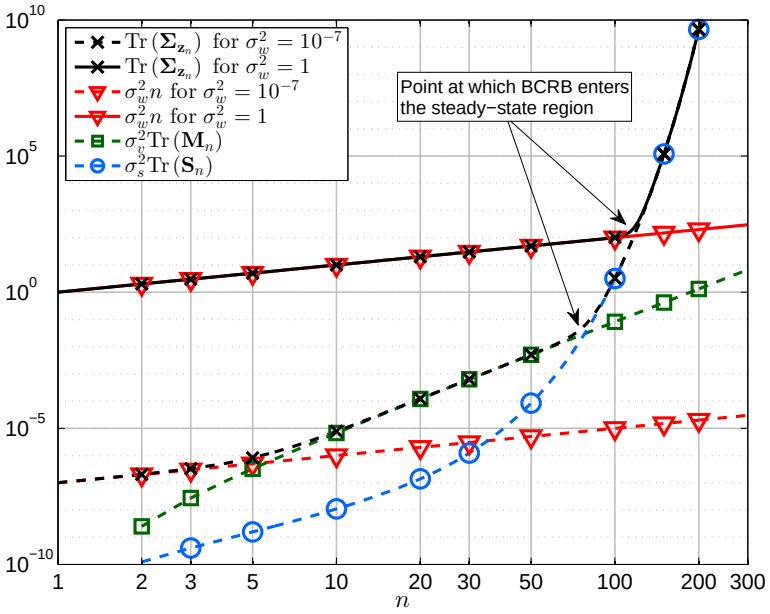

Figure 5.3: Asymptotic evolution of $\mathrm{Tr}(\mathbf{\Sigma}_{\mathbf{z}_n})$ versus the constituent elements of $\mathbf{\Sigma}_{\mathbf{z}_n}$ in (5.25), for $\sigma_w^2 = \{10^{-7},\ 1\}$.

5.5 KF(2)-AR(1) Convergence Time

This section aims at deriving closed-form upper bounds for the convergence time of the KF(2)-AR(1) by making use of the batch-mode formulation presented in Section 5.4. Here the results are derived through asymptotic analysis by distinguishing between two different operating regions, namely for small and large measurement noise (*i.e.* high and low C/N_0, respectively).

We proceed by again observing the evolution of the trace of $\mathbf{\Sigma}_{\mathbf{z}_n}$ in (5.25) over n. This is depicted in Figure 5.3, along with the trace of the three separate components. For illustrative purposes, the values $\beta = 0.9$, $\sigma_s^2 = 10^{-10}$ and $\sigma_v^2 = 10^{-8}$ are used[2]. To illustrate the approach, we consider $\sigma_w^2 = 10^{-7}$ and $\sigma_w^2 = 1$ for the two different operating regions of small and large measurement noise, respectively.

[2]We use again normalized notation to preserve the generality of the approach.

5.5.1 Closed-Form Approximation for Small Measurement Noise

For small n, the trace of $\mathbf{\Sigma}_{\mathbf{z}_n}$ is dominated by the contribution of σ_w^2. At some point, a change of roles is produced and the component of σ_v^2 starts being dominant. In Section 3.5 this point was considered to determine the Kalman convergence time, denoting that the BCRB entered the steady state imposed by nonzero process noise. However, in the KF(2)-AR(1) a new change of trend occurs later, in which the new contribution given by σ_s^2 becomes the dominating one, a situation that then remains for $n \to \infty$. For small measurement noise, this can thus be understood as the turning point at which the KF(2)-AR(1) enters the steady-state region. As observed in Figure 5.3, this occurs when the contributions of σ_v^2 and σ_s^2 intersect. Therefore, the convergence time for the KF(2)-AR(1) with small σ_w^2, denoted henceforth as $n_{\mathrm{c}}^{\sigma_w^2 \downarrow}$, can be found as the real solution for n to the following equality,

$$\sigma_v^2 \mathrm{Tr}\left(\mathbf{M}_n\right) = \sigma_s^2 \mathrm{Tr}\left(\mathbf{S}_n\right). \tag{5.28}$$

The problem of solving (5.28) requires determining the traces of $\mathbf{M}_n$ and $\mathbf{S}_n$. For a second-order kinematic model, the former is obtained as,

$$\mathrm{Tr}\left(\mathbf{M}_n\right) = \frac{n}{24}\left(n-1\right)\left(2n^2-2n-1\right) \tag{5.29}$$

whereas the latter can be computed by summing the elements in (5.27) for $k \doteq [1\,..\,n]$, which results in a set of geometric series that after some mathematical manipulations equals to,

$$\mathrm{Tr}\left(\mathbf{S}_n\right) = n\left(\frac{1}{1-\beta^{-2}} - 1\right) - \frac{\beta^{-2}}{\left(1-\beta^{-2}\right)^2}\left(1-\beta^{-2n}\right). \tag{5.30}$$

As can be observed, expressions (5.29) and (5.30) as such pose a considerable mathematical difficulty for deriving a closed-form solution for $n_{\mathrm{c}}^{\sigma_w^2 \downarrow}$ using (5.28). For this reason, we propose an approximation of reduced complexity that relies on the following observations. Recalling Section 3.6.1, the convergence time of a Kalman filter meets $1 \leqslant n_{\mathrm{c}}^{(p)} < \infty$. Being this raised to the fourth power in (5.29), the trace of $\mathbf{M}_n$ becomes rapidly dominated by the highest-order term of the polynomial, namely,

$$\mathrm{Tr}\left(\mathbf{M}_n\right) \approx \frac{n^4}{12}. \tag{5.31}$$

In addition, the coefficient β must fulfill $|\beta| < 1$ for an AR(1) process to be stable. As a result of both observations, the trace of $\mathbf{S}_n$ in (5.30) is empirically found to be dominated

by the second term on the right-hand side, where one can also resort to $(1-\beta^{-2n}) \approx -\beta^{-2n}$, thus boiling down to,

$$\mathrm{Tr}\left(\mathbf{S}_n\right) \approx \frac{\beta^{-2(n+1)}}{\left(1-\beta^{-2}\right)^2}. \tag{5.32}$$

Substituting (5.31) and (5.32) into (5.28) and solving for n, an approximation for the KF(2)-AR(1) convergence time with small measurement noise can be provided as,

$$n_{\mathrm{c}}^{\sigma_w^2\downarrow} \approx \frac{2}{\ln\left(\beta\right)} W_{-1}\left(-\left(\frac{3\ln\left(\beta\right)^4\beta^2\sigma_s^2}{4\sigma_v^2\left(\beta^4-2\beta^2+1\right)}\right)^{\frac{1}{4}}\right) \tag{5.33}$$

where $W_{-1}\left(\cdot\right)$ refers to the -1 real branch of the so-called Lambert W function. It is defined in the interval $[-\exp(-1),\ 0)$ [Cha02]. Therefore, the result in (5.33) provides a valid solution as long as the following relationship is fulfilled,

$$0 < \sigma_s^2 \leqslant \frac{4\sigma_v^2\left(\beta^4-2\beta^2+1\right)}{3\ln\left(\beta\right)^4\beta^2\exp(4)}. \tag{5.34}$$

After some polynomial fitting analysis, it is found that the $W_{-1}\left(x\right)$ function can be approximated by,

$$W_{-1}\left(x\right) \approx 2.4\log_{10}\left(-x\right) - 2.24. \tag{5.35}$$

Therefore, substituting x by the argument of $W_{-1}\left(\cdot\right)$ in (5.33), an approximation for $n_{\mathrm{c}}^{\sigma_w^2\downarrow}$ can be provided in closed form as,

$$\boxed{n_{\mathrm{c}}^{\sigma_w^2\downarrow} \approx \frac{4.8\log_{10}\left(\left(\frac{3\ln(\beta)^4\beta^2\sigma_s^2}{4\sigma_v^2(\beta^4-2\beta^2+1)}\right)^{\frac{1}{4}}\right)-4.48}{\ln\left(\beta\right)} \doteq \tilde{n}_{\mathrm{c}}^{\sigma_w^2\downarrow}.} \tag{5.36}$$

5.5.2 Closed-Form Approximation for Large Measurement Noise

When n is small, $\mathrm{Tr}\left(\mathbf{\Sigma}_{\mathbf{z}_n}\right)$ is also dominated by the contribution of σ_w^2. Then, a change of state is produced when intersecting with the contribution of σ_s^2, which dominates in the steady state. This can be observed in Fig. 5.3, where the effect of σ_v^2 becomes neglected here, in contrast to the case for small measurement noise. Therefore, the convergence time for the KF(2)-AR(1) with large measurement noise, denoted henceforth as $n_{\mathrm{c}}^{\sigma_w^2\uparrow}$, can be found as the real solution for n to the equality,

$$\sigma_s^2\mathrm{Tr}\left(\mathbf{S}_n\right) = \sigma_w^2 n. \tag{5.37}$$

At this point we can take advantage of the approximation for $\mathrm{Tr}\left(\mathbf{S}_n\right)$ in (5.32). If this is substituted into (5.37) and the equation is solved for n, an approximation for $\tilde{n}_{\mathrm{c}}^{\sigma_w^2\uparrow}$ can be provided as,

$$n_{\mathrm{c}}^{\sigma_w^2\uparrow} \approx \frac{W_{-1}\left(\frac{2\ln(\beta)\beta^2\sigma_s^2}{\sigma_w^2(\beta^4-2\beta^2+1)}\right)}{2\ln\left(\beta\right)} \tag{5.38}$$

which, since is also given by the -1 real branch of a Lambert W function, provides a valid solution when,

$$0 < \sigma_s^2 \leqslant \frac{\sigma_w^2\left(2\beta^2-\beta^4-1\right)}{2\ln\left(\beta\right)\beta^2\exp(1)}. \tag{5.39}$$

Similarly to the case for small measurement noise, substituting x in (5.35) by the argument of $W_{-1}\left(\cdot\right)$ in (5.38), an approximation for $n_{\mathrm{c}}^{\sigma_w^2\uparrow}$ can be provided in closed form as,

$$\boxed{n_{\mathrm{c}}^{\sigma_w^2\uparrow} \approx \frac{1.2\log_{10}\left(\frac{2\ln(\beta)\beta^2\sigma_s^2}{\sigma_w^2(2\beta^2-\beta^4-1)}\right)-1.12}{\ln\left(\beta\right)} \doteq \tilde{n}_{\mathrm{c}}^{\sigma_w^2\uparrow}.} \tag{5.40}$$

It is worth noting that, due to the non-dependence of (5.38) with σ_v^2, this result also applies to non-hybrid autoregressive Kalman filters. That is, Kalman filters that are configured to merely track an AR process, in this case an AR(1). This kind of filters will be studied with more detail in Section 5.6.

Lastly, as in Section 3.5, the results in (5.36) and (5.40) have been derived assuming a diffuse initialization of the Kalman filter, meaning that the convergence time is maximum. Therefore, these results can also be understood as upper bounds on the KF(2)-AR(1) convergence time.

5.5.3 Goodness of Approximations

This section aims at illustrating the goodness of the approximations for the KF(2)-AR(1) convergence time in (5.36) and (5.40). To this end, Figure 5.4 depicts the matching of our results with the empirical convergence time n_{c}, measured through the metrics $\Delta\tilde{n}_{\mathrm{c}}^{\sigma_w^2\downarrow} \doteq (\tilde{n}_{\mathrm{c}}^{\sigma_w^2\downarrow} - n_{\mathrm{c}})/n_{\mathrm{c}}$ and $\Delta\tilde{n}_{\mathrm{c}}^{\sigma_w^2\uparrow} \doteq (\tilde{n}_{\mathrm{c}}^{\sigma_w^2\uparrow} - n_{\mathrm{c}})/n_{\mathrm{c}}$. The results are plotted as a function of σ_w^2 for different values of σ_s^2, while the values of β and σ_v^2 remain as in Figure 5.3. The term n_{c} is computed as the time sample for which the BCRB reaches $\left[\mathbf{J}_{\mathrm{Brec}}^{-1}(\infty)\right]_{1,1}\big/\left[\mathbf{J}_{\mathrm{Brec}}^{-1}(n_{\mathrm{c}}^{(p)})\right]_{1,1} = 0.99$, with 0.99 a conservative value. In the figure, positive values indicate an overestimated convergence time, meaning that the BCRB reached the steady state some iterations ago. On the contrary, negative values denote an underestimation where the BCRB is still to reach the steady state. A tight match between our

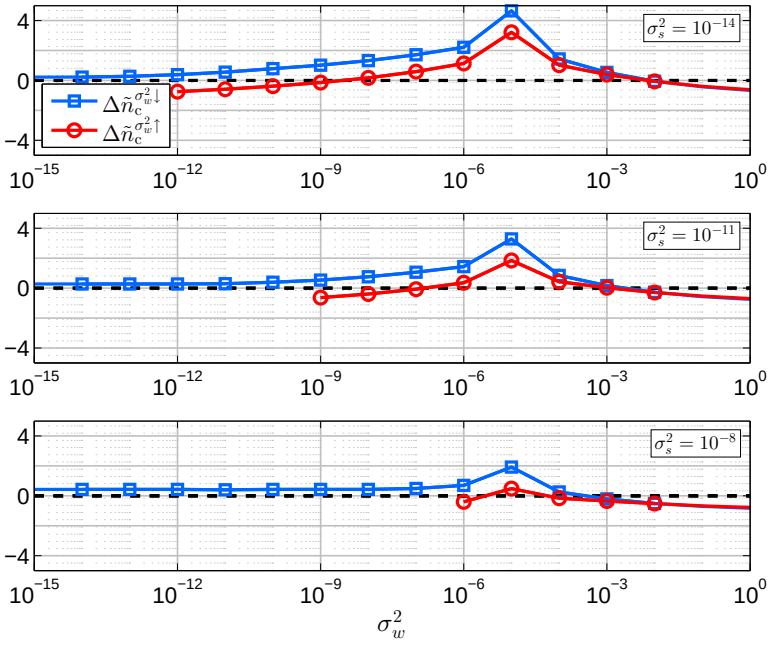

Figure 5.4: Differences between approximations and empirical convergence time, $\Delta\tilde{n}_c^{\sigma_w^2\downarrow} \doteq (\tilde{n}_c^{\sigma_w^2\downarrow} - n_c)/n_c$ and $\Delta\tilde{n}_c^{\sigma_w^2\uparrow} \doteq (\tilde{n}_c^{\sigma_w^2\uparrow} - n_c)/n_c$.

results and the empirical convergence time can be observed, with the previous metrics surrounding the ideal zero. Some discrepancies appear for small σ_s^2 or when increasing σ_w^2. This is explained by the fact that the steady-state region tends to disappear when the AR process noise variance σ_s^2 gets much smaller than σ_w^2. In this situation, it becomes thus more difficult to properly characterize the convergence time of the KF(2)-AR(1). As in Section 3.5, our results apply when the presence of the steady-state region is evident. For this reason, mismatches tend to attenuate for moderate σ_w^2 and σ_s^2. For small σ_w^2, the approximation $\tilde{n}_c^{\sigma_w^2\downarrow}$ provides very good accuracy. However, when σ_s^2 and σ_w^2 fulfill the condition in (5.39) and $\tilde{n}_c^{\sigma_w^2\uparrow}$ comes into play, it is seen to provide a benefit over $\tilde{n}_c^{\sigma_w^2\downarrow}$, with $\Delta\tilde{n}_c^{\sigma_w^2\uparrow}$ closer to zero. These results confirm the validity of our approach when the conditions in (5.34) and (5.39) are fulfilled.

5.6 Steady-State Region of Non-Hybrid Autoregressive Kalman Filters

This section aims at obtaining expressions in closed form for the performance lower bounds of non-hybrid autoregressive Kalman filters. These are Kalman filters whose

state-space models encompass only autoregressive processes with no other disturbances (*i.e.* no kinematic models). As introduced in Section 5.4, this kind of techniques can be found in plenty of applications in practice. For the sake of mathematical complexity, the derivations in this section are restricted to low-order AR models, namely AR(1) and AR(2).

This contribution arises from a twofold observation. First, the fact that the Kalman state covariance matrices introduced in Section 3.2.2 do contain the information of the BCRB. Second, it can be noticed that the recursion employed to obtain such matrices, see Eqs. (3.7), (3.12) and (3.13), does actually not depend on the actual input measurements. This is an interesting point, meaning that such matrices can be computed in an offline manner.

As a matter of fact, the derivations presented in this section adopt a different approach to the batch-mode formulation one, based on simply analyzing the abovementioned recursion when the steady state has been reached. As already explained, the presence of nonzero process noise introduces a floor effect in the BCRB that causes the estimation performance to saturate at some point, thus remaining in such steady-state region for $n \to \infty$. In this situation, the temporary index of the covariance matrix $\mathbf{\Sigma}_{\mathbf{x}}(n)$ can thus be ignored. By doing so, the recursion to obtain such matrix is shown next in Eqs. (5.41)-(5.43), where we also rename some of the involved matrices for convenience:

1. Predicted covariance matrix:

$$\mathbf{P} \doteq \mathbf{\Sigma}_{\mathbf{x}}(n|n-1)|_{n\to\infty} = \mathbf{F}\mathbf{C}\mathbf{F}^T + \mathbf{Q} \tag{5.41}$$

2. Kalman gains:

$$\mathbf{K} \doteq \mathbf{K}(n)|_{n\to\infty} = \mathbf{P}\mathbf{H}^T \left(\mathbf{R} + \mathbf{H}\mathbf{P}\mathbf{H}^T\right)^{-1} \tag{5.42}$$

3. Corrected covariance matrix:

$$\mathbf{C} \doteq \mathbf{\Sigma}_{\mathbf{x}}(n)|_{n\to\infty} = (\mathbf{I} - \mathbf{K}\mathbf{H})\,\mathbf{P}. \tag{5.43}$$

5.6.1 Performance Lower-Bound for AR(1) Kalman Filter

Following the signal model for an AR(p) process introduced in (4.1), an AR(1) process is driven by,

$$\varphi(n) = \beta\varphi(n-1) + s(n) \tag{5.44}$$

which, in terms of a Kalman state-space model, $\mathbf{F} \doteq \beta$ and $\mathbf{Q} \doteq \sigma_s^2$ are identified as the transition matrix and process noise covariance matrix. With these, the predicted covariance matrix in (5.41) can be written as,

$$\mathbf{P}^{\mathrm{AR}(1)} = \beta^2 \mathbf{C}^{\mathrm{AR}(1)} + \sigma_s^2 \tag{5.45}$$

where, for the case of an AR(1), $\mathbf{P}^{\mathrm{AR}(1)}$ and $\mathbf{C}^{\mathrm{AR}(1)}$ reduce to scalar values. On the other hand, the Kalman input measurements are considered to be given by the AR(1) process $\varphi(n)$, and thus $\mathbf{H} \doteq 1$, whereas $\mathbf{R} \doteq \sigma_w^2$ refers to the scalar variance of the input noise. With this, the Kalman gains in (5.42) can be written as,

$$\mathbf{K}^{\mathrm{AR}(1)} = \frac{\mathbf{P}^{\mathrm{AR}(1)}}{\mathbf{P}^{\mathrm{AR}(1)} + \sigma_w^2}. \tag{5.46}$$

By substituting (5.46) into the corrected covariance matrix in (5.43), the latter becomes,

$$\mathbf{C}^{\mathrm{AR}(1)} = \mathbf{P}^{\mathrm{AR}(1)} \left(1 - \frac{\mathbf{P}^{\mathrm{AR}(1)}}{\mathbf{P}^{\mathrm{AR}(1)} + \sigma_w^2}\right). \tag{5.47}$$

The recursion is closed by introducing the result in (5.47) into the prediction equation (5.45) again, which leads to,

$$\mathbf{P}^{\mathrm{AR}(1)} = \beta^2 \mathbf{P}^{\mathrm{AR}(1)} \left(1 - \frac{\mathbf{P}^{\mathrm{AR}(1)}}{\mathbf{P}^{\mathrm{AR}(1)} + \sigma_w^2}\right) + \sigma_s^2 \tag{5.48}$$

thus leaving the covariance matrix as a function of itself. By solving for $\mathbf{P}^{\mathrm{AR}(1)}$ in (5.48) and after some mathematical manipulations, the following closed-form expression for the steady-state performance of an AR(1) Kalman filter is obtained,

$$\boxed{\mathbf{P}^{\mathrm{AR}(1)} = \frac{\sigma_s^2 + \sigma_w^2\left(\beta^2 - 1\right) + \sqrt{\left[\sigma_w^2\left(\beta^2 - 1\right)\right]^2 + 2\sigma_w^2\sigma_s^2\left(\beta^2 + 1\right) + \sigma_s^4}}{2}.} \tag{5.49}$$

5.6.2 Performance Lower-Bounds for AR(2) Kalman Filter

An AR(2) process is given by the following signal model:

$$\varphi(n) = \beta_1 \varphi(n-1) + \beta_2 \varphi(n-2) + s(n) \tag{5.50}$$

which, in terms of the Kalman state-space model, $\mathbf{F} \doteq \begin{bmatrix} \beta_1 & \beta_2 \\ 1 & 0 \end{bmatrix}$ and $\mathbf{Q} \doteq \begin{bmatrix} \sigma_s^2 & 0 \\ 0 & 0 \end{bmatrix}$. The predicted covariance matrix in (5.41) depends on $\mathbf{C}$, which for the AR(2) case corresponds

to a (2×2) symmetric matrix defined as $\mathbf{C}^{\mathrm{AR}(2)} \doteq \begin{bmatrix} \mathbf{C}_{1,1}^{\mathrm{AR}(2)} & \mathbf{C}_{1,2}^{\mathrm{AR}(2)} \\ \mathbf{C}_{1,2}^{\mathrm{AR}(2)} & \mathbf{C}_{2,2}^{\mathrm{AR}(2)} \end{bmatrix}$. With this, after doing the operation in (5.41), the predicted covariance matrix becomes,

$$\mathbf{P}^{\mathrm{AR}(2)} = \begin{bmatrix} \beta_1 \left(\mathbf{C}_{1,1}^{\mathrm{AR}(2)} \beta_1 + \mathbf{C}_{1,2}^{\mathrm{AR}(2)} \beta_2 \right) + \beta_2 \left(\mathbf{C}_{1,2}^{\mathrm{AR}(2)} \beta_1 + \mathbf{C}_{2,2}^{\mathrm{AR}(2)} \beta_2 \right) + \sigma_s^2 & \beta_1 \mathbf{C}_{1,1}^{\mathrm{AR}(2)} + \beta_2 \mathbf{C}_{1,2}^{\mathrm{AR}(2)} \\ \beta_1 \mathbf{C}_{1,1}^{\mathrm{AR}(2)} + \beta_2 \mathbf{C}_{1,2}^{\mathrm{AR}(2)} & \mathbf{C}_{1,1}^{\mathrm{AR}(2)} \end{bmatrix} \tag{5.51}$$

to whose elements we will refer for the moment as $\mathbf{P}^{\mathrm{AR}(2)} \doteq \begin{bmatrix} \mathbf{P}_{1,1}^{\mathrm{AR}(2)} & \mathbf{P}_{1,2}^{\mathrm{AR}(2)} \\ \mathbf{P}_{1,2}^{\mathrm{AR}(2)} & \mathbf{P}_{2,2}^{\mathrm{AR}(2)} \end{bmatrix}$.

Similarly to Section 5.6.1, the input measurements are given by $\varphi(n)$ and thus $\mathbf{H} \doteq \begin{bmatrix} 1 & 0 \end{bmatrix}$, while $\mathbf{R} \doteq \sigma_w^2$ remains as the input noise variance. With this, the Kalman gains in (5.42) can be written as a function of the elements of $\mathbf{P}^{\mathrm{AR}(2)}$ as,

$$\mathbf{K}^{\mathrm{AR}(2)} = \begin{bmatrix} \frac{\mathbf{P}_{1,1}^{\mathrm{AR}(2)}}{\mathbf{P}_{1,1}^{\mathrm{AR}(2)} + \sigma_w^2} & \frac{\mathbf{P}_{1,2}^{\mathrm{AR}(2)}}{\mathbf{P}_{1,1}^{\mathrm{AR}(2)} + \sigma_w^2} \end{bmatrix}^T. \tag{5.52}$$

By substituting (5.52) into the corrected covariance matrix in (5.43), the latter becomes,

$$\mathbf{C}^{\mathrm{AR}(2)} = \begin{bmatrix} \mathbf{P}_{1,1}^{\mathrm{AR}(2)} \left(1 - \frac{\mathbf{P}_{1,1}^{\mathrm{AR}(2)}}{\mathbf{P}_{1,1}^{\mathrm{AR}(2)} + \sigma_w^2} \right) & \mathbf{P}_{1,2}^{\mathrm{AR}(2)} \left(1 - \frac{\mathbf{P}_{1,1}^{\mathrm{AR}(2)}}{\mathbf{P}_{1,1}^{\mathrm{AR}(2)} + \sigma_w^2} \right) \\ \mathbf{P}_{1,2}^{\mathrm{AR}(2)} \left(1 - \frac{\mathbf{P}_{1,1}^{\mathrm{AR}(2)}}{\mathbf{P}_{1,1}^{\mathrm{AR}(2)} + \sigma_w^2} \right) & \mathbf{P}_{2,2}^{\mathrm{AR}(2)} - \frac{\left(\mathbf{P}_{1,2}^{\mathrm{AR}(2)} \right)^2}{\mathbf{P}_{1,1}^{\mathrm{AR}(2)} + \sigma_w^2} \end{bmatrix}. \tag{5.53}$$

The recursion is closed by introducing the result in (5.53) into the prediction equation (5.51) again. This leads to the covariance matrix being left as a function of its own elements. By doing so, the following elements are obtained:

$$\begin{aligned} \mathbf{P}_{1,1}^{\mathrm{AR}(2)} = \; & \beta_1 \left(\left(\beta_1 \mathbf{P}_{1,1}^{\mathrm{AR}(2)} + \beta_2 \mathbf{P}_{1,2}^{\mathrm{AR}(2)} \right) \left(1 - \frac{\mathbf{P}_{1,1}^{\mathrm{AR}(2)}}{\mathbf{P}_{1,1}^{\mathrm{AR}(2)} + \sigma_w^2} \right) \right) + \\ & + \beta_2 \left(\beta_1 \mathbf{P}_{1,2}^{\mathrm{AR}(2)} \left(1 - \frac{\mathbf{P}_{1,1}^{\mathrm{AR}(2)}}{\mathbf{P}_{1,1}^{\mathrm{AR}(2)} + \sigma_w^2} \right) + \beta_2 \left(\mathbf{P}_{2,2}^{\mathrm{AR}(2)} - \frac{\left(\mathbf{P}_{1,2}^{\mathrm{AR}(2)} \right)^2}{\mathbf{P}_{1,1}^{\mathrm{AR}(2)} + \sigma_w^2} \right) \right) + \sigma_s^2 \end{aligned} \tag{5.54}$$

$$\mathbf{P}_{1,2}^{\mathrm{AR}(2)} = \left(\beta_1 \mathbf{P}_{1,1}^{\mathrm{AR}(2)} + \beta_2 \mathbf{P}_{1,2}^{\mathrm{AR}(2)} \right) \left(1 - \frac{\mathbf{P}_{1,1}^{\mathrm{AR}(2)}}{\mathbf{P}_{1,1}^{\mathrm{AR}(2)} + \sigma_w^2} \right) \tag{5.55}$$

$$\mathbf{P}_{2,2}^{\mathrm{AR}(2)} = \mathbf{P}_{1,1}^{\mathrm{AR}(2)} \left(1 - \frac{\mathbf{P}_{1,1}^{\mathrm{AR}(2)}}{\mathbf{P}_{1,1}^{\mathrm{AR}(2)} + \sigma_w^2} \right). \tag{5.56}$$

At this point, it is of interest to write the results for $\mathbf{P}_{1,2}^{\mathrm{AR}(2)}$ and $\mathbf{P}_{2,2}^{\mathrm{AR}(2)}$ as a function of $\mathbf{P}_{1,1}^{\mathrm{AR}(2)}$, and then employ these results to solve for $\mathbf{P}_{1,1}^{\mathrm{AR}(2)}$ in (5.54) and leave it as a

function of the Kalman parameters. By solving (5.55) for $\mathbf{P}_{1,2}^{\mathrm{AR}(2)}$ the result is,

$$\mathbf{P}_{1,2}^{\mathrm{AR}(2)} = \frac{\beta_1 \sigma_w^2 \mathbf{P}_{1,1}^{\mathrm{AR}(2)}}{\sigma_w^2 \left(1-\beta_2\right) + \mathbf{P}_{1,1}^{\mathrm{AR}(2)}} \tag{5.57}$$

whereas the result for $\mathbf{P}_{2,2}^{\mathrm{AR}(2)}$ in (5.56) already fulfills this point. With this, solving for $\mathbf{P}_{1,1}^{\mathrm{AR}(2)}$ in (5.54) results in a fourth-order polynomial whose coefficients are determined by the Kalman parameters as follows:

$$\begin{aligned}
&\left(\mathbf{P}_{1,1}^{\mathrm{AR}(2)}\right)^4 - \left(\mathbf{P}_{1,1}^{\mathrm{AR}(2)}\right)^3 \left(\sigma_w^2 \left(\beta_1^2 + \beta_2^2 + 2\beta_2 - 3\right) + \sigma_s^2\right) + \\
&\quad + \left(\mathbf{P}_{1,1}^{\mathrm{AR}(2)}\right)^2 \left(\sigma_w^4 \left(\beta_1^2\beta_2^2 + 2\beta_2^3 - 2\beta_1^2 - \beta_2^2 - 4\beta_2 + 3\right) + \sigma_w^2\sigma_s^2 \left(2\beta_2 - 3\right)\right) + \\
&\quad + \mathbf{P}_{1,1}^{\mathrm{AR}(2)} \left(\sigma_w^6 \left(\beta_1^2\beta_2^2 - \beta_2^4 + 2\beta_2^3 - \beta_1^2 - 2\beta_2 + 1\right) - \sigma_w^4\sigma_s^2 \left(\beta_2^2 - 4\beta_2 + 3\right)\right) - \\
&\quad - \sigma_w^6\sigma_s^2 \left(\beta_2^2 - 2\beta_2 + 1\right) = 0
\end{aligned} \tag{5.58}$$

thus leaving the first element of the covariance matrix as a function of itself.

As can be anticipated, finding a closed-form solution to the fourth-order polynomial in (5.58) becomes quite a mathematical challenge. For this reason, a closed-form approximation that considerably reduces the complexity of the problem is presented next.

5.6.3 Derivation of Closed-Form Approximation for AR(2) Kalman Filter

The proposed closed-form approximation is based on the observation that the estimation variance is expected to be much smaller than 1, $\mathbf{P}_{1,1}^{\mathrm{AR}(2)} \ll 1$, as can be concluded from observing the recursive BCRB in (5.14). This will occur as long as the KF-AR operates in nominal conditions, that is, $\sigma_s^2 \ll \sigma_w^2$. This observation allows the polynomial in (5.58) to be approximated by the first-order and the independent terms, namely,

$$\begin{aligned}
&\mathbf{P}_{1,1}^{\mathrm{AR}(2)} \left(\sigma_w^6 \left(\beta_1^2\beta_2^2 - \beta_2^4 + 2\beta_2^3 - \beta_1^2 - 2\beta_2 + 1\right) - \sigma_w^4\sigma_s^2 \left(\beta_2^2 - 4\beta_2 + 3\right)\right) - \\
&\quad - \sigma_w^6\sigma_s^2 \left(\beta_2^2 - 2\beta_2 + 1\right) = 0
\end{aligned} \tag{5.59}$$

which, after some mathematical manipulations, leads to the following closed-form approximation for $\mathbf{P}_{1,1}^{\mathrm{AR}(2)}$:

$$\boxed{\mathbf{P}_{1,1}^{\mathrm{AR}(2)} \approx \frac{\sigma_w^2\sigma_s^2 \left(\beta_2 - 1\right)^2}{\sigma_w^2 \left(\beta_2^2 - 1\right) \left[\beta_1^2 - \left(\beta_2 - 1\right)^2\right] - \sigma_s^2 \left(\beta_2 - 1\right) \left(\beta_2 - 3\right)} \doteq \tilde{\mathbf{P}}_{1,1}^{\mathrm{AR}(2)}} \tag{5.60}$$

while the elements $\mathbf{P}_{1,2}^{\mathrm{AR}(2)}$ and $\mathbf{P}_{2,2}^{\mathrm{AR}(2)}$ can be approximated as a function of $\tilde{\mathbf{P}}_{1,1}^{\mathrm{AR}(2)}$ as follows,

$$\mathbf{P}_{1,2}^{\mathrm{AR}(2)} \approx \frac{\beta_1 \sigma_w^2}{1 - \frac{\sigma_w^2(\beta_2 - 1)}{\tilde{\mathbf{P}}_{1,1}^{\mathrm{AR}(2)}}} \doteq \tilde{\mathbf{P}}_{1,2}^{\mathrm{AR}(2)} \tag{5.61}$$

$$\mathbf{P}_{2,2}^{\mathrm{AR}(2)} \approx \frac{\sigma_w^2}{1 + \frac{\sigma_w^2}{\tilde{\mathbf{P}}_{1,1}^{\mathrm{AR}(2)}}} \doteq \tilde{\mathbf{P}}_{2,2}^{\mathrm{AR}(2)}. \tag{5.62}$$

5.6.4 Goodness of Approach

The aim of this section is to illustrate the goodness of the closed-form expressions in (5.49) and (5.60) for the steady-state performance lower bounds of first- and second-order autoregressive Kalman filters. For the former, Figure 5.5 shows a comparison of the closed-form expression for $\mathbf{P}^{\mathrm{AR}(1)}$ to the empirical value obtained by iterating over equations (5.41)-(5.43). As expected, a perfect match between both lines is observed, while obtaining very similar results for the different values of β since no disturbing dynamics process noise is present. This result confirms the validity of the derived closed-form expression in (5.49). On the other hand, Figure 5.6 shows a comparison of the closed-form approximation $\tilde{\mathbf{P}}_{1,1}^{\mathrm{AR}(2)}$ to the empirical result. A very tight match is observed when working under nominal conditions, $\sigma_s^2 \ll \sigma_w^2$. However, this holds until up to a point in terms of the ratio σ_s^2/σ_w^2 beyond which no meaningful results can be provided, where the blue lines in Figure 5.6 get truncated. This is explained by the fact that, in this region, the first-order polynomial approximation in (5.59) is no longer applicable, as the neglected higher-order terms start gaining some importance. This takes place when approaching the noncompliance of the $\sigma_s^2 \ll \sigma_w^2$ condition. Notwithstanding, the behavior of $\mathbf{P}_{1,1}^{\mathrm{AR}(2)}$ is found to be well-defined by the approximation $\tilde{\mathbf{P}}_{1,1}^{\mathrm{AR}(2)}$ when the condition $\sigma_s^2 \ll \sigma_w^2$ is fulfilled, thus confirming the validity of the proposed approach in this region.

5.7 Controllability and Observability

The properties of controllability and observability [Jaz70, Gop84] of the Kalman filter constitute a set of tools of great practical interest to analyze the state transition and observation equations, and give insights into the filter's viability during the design stage [Sou98]. Therefore, they must be checked to confirm the feasibility of the KF-AR.

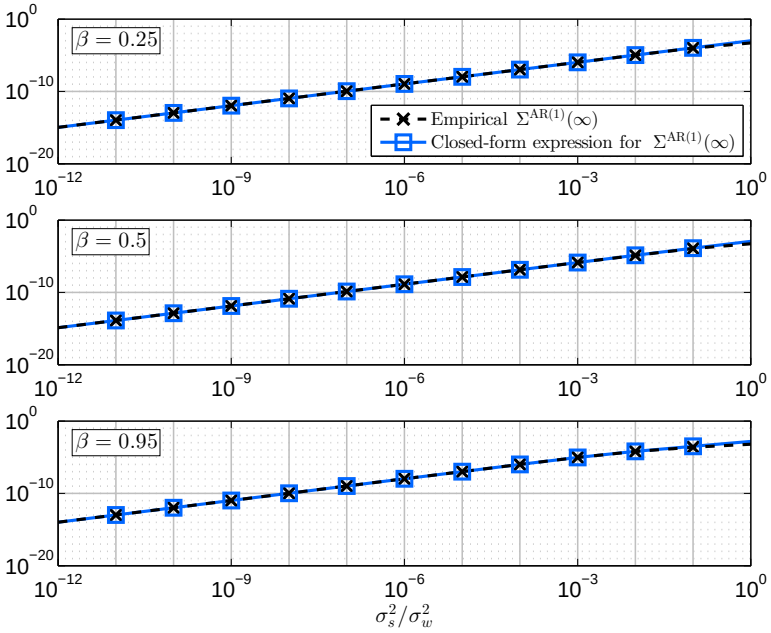

Figure 5.5: Empirical $\mathbf{P}^{\mathrm{AR}(1)}$ versus closed-form expression in (5.49).

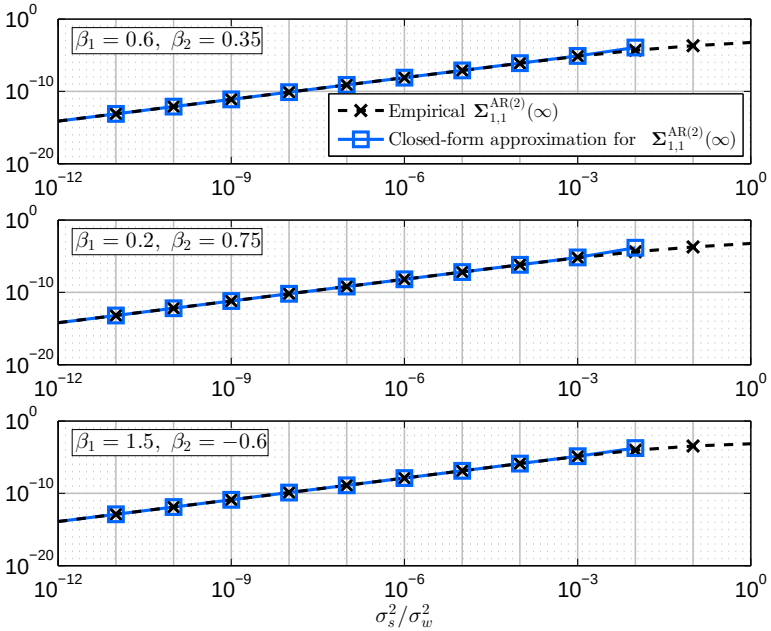

Figure 5.6: Empirical $\mathbf{P}_{1,1}^{\mathrm{AR}(2)}$ versus closed-form approximation in (5.60).

Controllability

A linear Kalman filter is controllable if for any initial state vector $\mathbf{x}(n_0)$ and any given time instant n, there exists a control force driving the initial state to any desired value of $\mathbf{x}(n)$ [Sim06]. That is, an initial state vector can be driven to any desired state

by the application of any unconstrained control inputs $\mathbf{q}(n)$. A simple test to check the controllability of a linear system is based on analyzing the so-called *controllability matrix*:

$$\mathbf{C} \doteq \begin{bmatrix} \mathbf{G} & \mathbf{FG} & \mathbf{F}^2\mathbf{G} & \cdots & \mathbf{F}^{k-1}\mathbf{G} \end{bmatrix} \tag{5.63}$$

where k is the dimension of the Kalman state vector. With this, the system is controllable if and only if the controllability matrix $\mathbf{C}$ has rank k. Otherwise, the system is said to be uncontrollable, meaning that some elements in the state vector are not affected by the control input.

Observability

On the other hand, a linear Kalman filter is observable if for any initial state vector $\mathbf{x}(n_0)$ and any given time instant n, the system can be uniquely determined with the knowledge of the process noise $\mathbf{q}$ and the observations $\mathbf{z}(n)$ for all n [Sim06]. A simple way to check the observability of a linear system is based on analyzing the so-called *observability matrix*:

$$\mathbf{O} \doteq \begin{bmatrix} \mathbf{H} \\ \mathbf{HF} \\ \mathbf{HF}^2 \\ \vdots \\ \mathbf{HF}^{k-1} \end{bmatrix}. \tag{5.64}$$

With this, the system is observable if and only if the observability matrix $\mathbf{O}$ has rank k. Otherwise, the system is said to be unobservable, meaning that some elements in the state vector at a given time instant n may not be determined from examination of the input observables, regardless of how many measurements are taken. The property of observability can also be understood as the ability of the Kalman filter to dissociate among the different parameters to be estimated based on the available set of observables.

By checking Eqs. (5.63) and (5.64) using the defined $\mathbf{H}$, $\mathbf{F}$ and $\mathbf{G}$ matrices, it is found that the KF-AR fulfills both controllability and observability properties, thus being well-posed for carrier dynamics plus scintillation phase tracking.

5.8 Doubly-Adaptive KF-AR Implementation. The AHL-KF-A2R(p)

When characterizing the DAK2.2014.335.22.GPS24 real scintillation time series in Chapter 4, it has been found that ionospheric scintillation presents a rather time-varying behavior in practice. This means that KF-AR techniques with fixed AR model parameters may fail at providing optimal performance when scintillation varies from that for which they are designed. Therefore, it is reasonable to provide the KF-AR with some adaptability so that it can nimbly self-adapt to the actual working conditions and perform in an optimal manner irrespective of them. In that sense, this section presents a doubly-adaptive implementation of the KF-AR, the so-called AHL-KF-A2R(p), which consists of two online adaptive algorithms. On the one hand, an online estimator of the AR model parameters and order, whose output is fed back to the Kalman filter in order for the corresponding matrices to match the working conditions at each time instant. On the other hand, a novel adaptive hard-limiting (AHL) method to deal with the non-linear signal amplitude fades introduced by scintillation. In order to confirm the reliability of the above online estimators, we will compare their performance to that obtained offline (*i.e.* with no Kalman filter closed-loop architecture involved) considered as the theoretical reference, where we will also see how the presence of AWGN may degrade the AR estimation, particularly the AR model parameters.

5.8.1 Online Estimation of AR Model Parameters

The parameters of an AR process can be determined by employing either the YW or the LS methods, as explained in Chapter 4. These rely on a sample data record with some length. From this observation, the online estimation of AR model parameters consists in determining the optimal set of $\{\boldsymbol{\beta}, \sigma^2_{s_p}\}$ to be employed at a given time instant n based on a record of past data samples in form of a sliding window that moves forward when gradually increasing n. The block diagram of this implementation is shown in Figure 5.7, where the output of the AR parameter estimation box is correspondingly employed to adapt the transition matrix $\mathbf{F}$, thus depending on time, $\mathbf{F}(n)$, and the Kalman gains through $\mathbf{Q}(\hat{\sigma}^2_{s_p}(n), n)$. The key aspect of this implementation is that the scintillation must be visible without dynamics. That is, it must be applied after correcting dynamics but before correcting the scintillation phase in the local replica. To this end, Figure 5.7 implements a second carrier discriminator that derives from this in-between point.

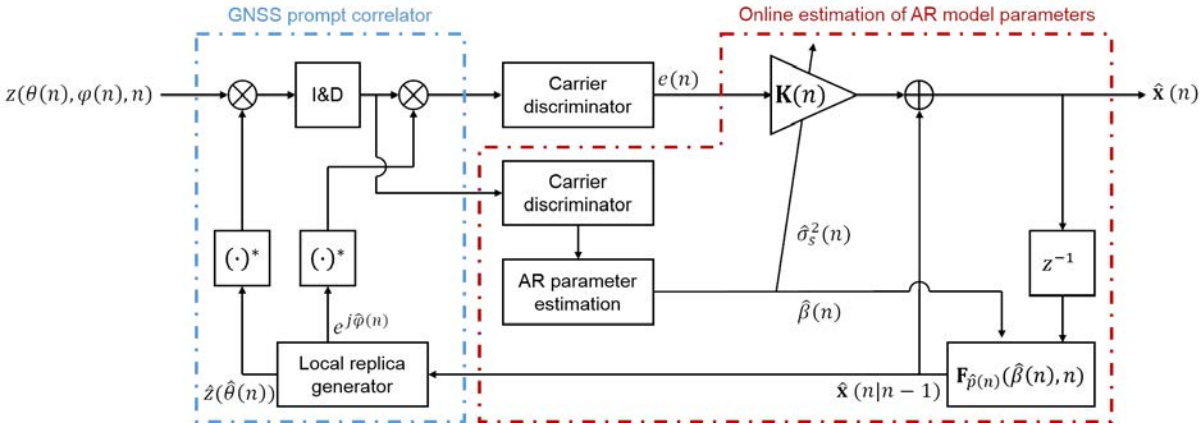

Figure 5.7: Block diagram of KF-AR with adaptive (*i.e.* online estimation) AR parameters.

In practice, though, the second carrier discriminator in Figure 5.7 observes not only scintillation, but also the AWGN measurement noise introduced by the receiver, and thus the resulting random process departs from an AR process. This phenomenon can be explained by the fact that an AR process is characterized by an all-pole transfer function, as shown previously in Eq. (4.2). However, AWGN is characterized by a flat PSD in the form $S_{\text{AWGN}}\left(e^{j\omega}\right) = \sigma^2_{\text{AWGN}}$. If both processes are assumed uncorrelated with one another, the resulting PSD becomes,

$$S_{\text{TOTAL}}\left(e^{j\omega}\right) = S_{\text{AR}}\left(e^{j\omega}\right) + S_{\text{AWGN}}\left(e^{j\omega}\right) = \frac{\sigma^2_{s_p} + \sigma^2_{\text{AWGN}}|1 - \sum_{k=1}^{p}\beta_k e^{-j\omega}|^2}{|1 - \sum_{k=1}^{p}\beta_k e^{-j\omega}|^2} \tag{5.65}$$

which does not present an AR structure anymore, but the one for an *autoregressive moving average* (ARMA) process, with a pole-zero transfer function, thus posing serious concerns to the AR modeling of the process of interest if the C/N_0 is sufficiently low.

5.8.1.1 Estimation of AR(p) Parameters for Moderate CSM under AWGN

When determining the AR model parameters $\{\boldsymbol{\beta}, \sigma^2_{s_p}\}$, the key point to be taken into account is the power of the prediction error that the estimated AR coefficients produce. For the case of Cornell moderate scintillation, this is shown in Figure 5.8 for AR(1, 2, 3) processes, where we also consider the presence of AWGN through a C/N_0 ranging from 30 to 60 dB-Hz. As can be observed, the online estimation matches very tightly the theoretical offline one, thus being an indicator of its proper operation. The small mismatches that can be appreciated are due to the online estimator being involved within a Kalman filter processing the input samples and applying some corrections to the local

replica at the same time, thus having some effect on the next samples to be processed. On the other hand, it is found that the estimated AR coefficients produce a prediction error that truly departs from the minimum error power when in the presence of AWGN, and it further degrades when the C/N_0 decreases. A very high C/N_0 is required in order to properly identify the AR model parameters under moderate scintillation. However, a nominal C/N_0 around 45-50 dB-Hz is usually observed in practical open-sky conditions, where the estimated $\sigma^2_{s_p}$ is degraded by some orders of magnitude. At this point it is important to note that, similarly to the conventional PLL, the Kalman filter is a closed-loop architecture that can thus be characterized by some equivalent loop bandwidth, which indeed depends on $\sigma^2_{s_p}$ in a direct way [Jwo01]. Since increasing the bandwidth translates into larger jitter at the filter output, we should therefore expect the presented adaptive implementation to incur into some performance degradation when estimating moderate scintillation. However, keep in mind that the advantage of this adaptive implementation is the agility of the KF-AR to rapidly adapt to the actual working conditions.

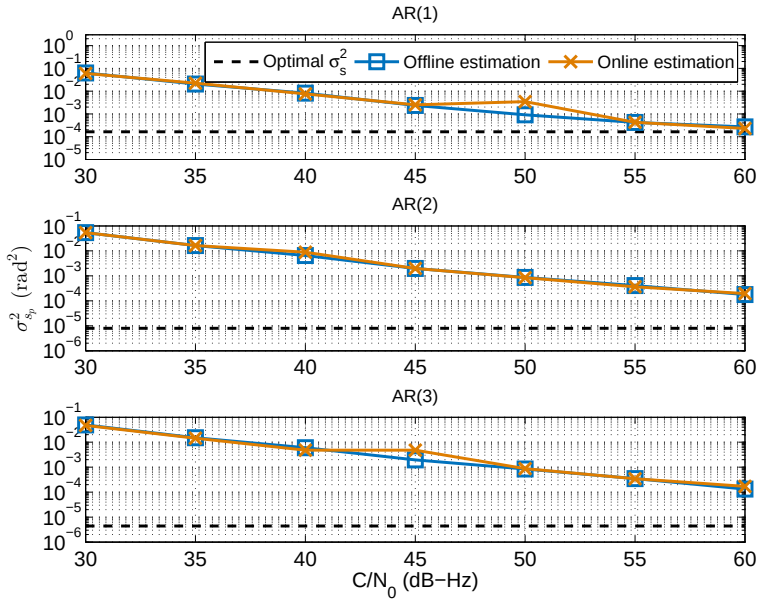

Figure 5.8: Online estimation of AR(1) (top), AR(2) (middle) and AR(3) (bottom) prediction noise power for Cornell moderate scintillation. Comparison to offline estimation as a function of the C/N_0.

5.8.1.2 Estimation of AR(p) Parameters for Severe CSM under AWGN

Figure 5.9 shows the power of the prediction error when estimating the AR(1, 2, 3) coefficients under severe scintillation, as a function of the C/N_0. Again, a very tight match

between the offline and online estimates is observed. As for the presence of AWGN, the degradation with respect to the minimum error power is not so critical as in the moderate case, already obtaining acceptable results for C/N_0 above 40 dB-Hz. This is explained by the fact that, for a given C/N_0, the effect of severe scintillation is more prominent than moderate scintillation, and thus easier to detect and estimate. In nominal conditions (*i.e.* 45-50 dB-Hz), the estimated AR coefficients introduce an error power that is very close to the minimum value. Therefore, we should expect the presented adaptive implementation to successfully estimate severe scintillation events, incurring into very small performance degradation.

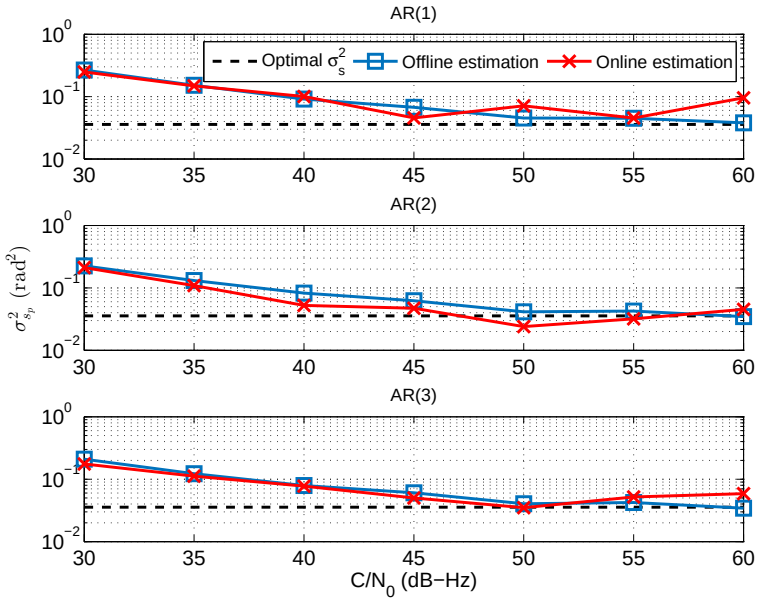

Figure 5.9: Online estimation of AR(1) (top), AR(2) (middle) and AR(3) (bottom) prediction noise power for Cornell severe scintillation. Comparison to offline estimation as a function of the C/N_0.

5.8.2 Online Estimation of AR Model Order

Similarly to the estimation of the AR model parameters, the MDL can also be implemented in an online manner in order to find the AR model order that best fits the actual input scintillation phase at a given time instant n. To this end, the same sliding window feature of Section 5.8.1 can be employed. As a matter of fact, the online MDL estimator employs the output of the online AR parameter estimator. The block diagram of this implementation is shown in Figure 5.10. It follows the same rationale as the previous

Figure 5.7, and the MDL estimator box has been added right after the AR parameter estimator.

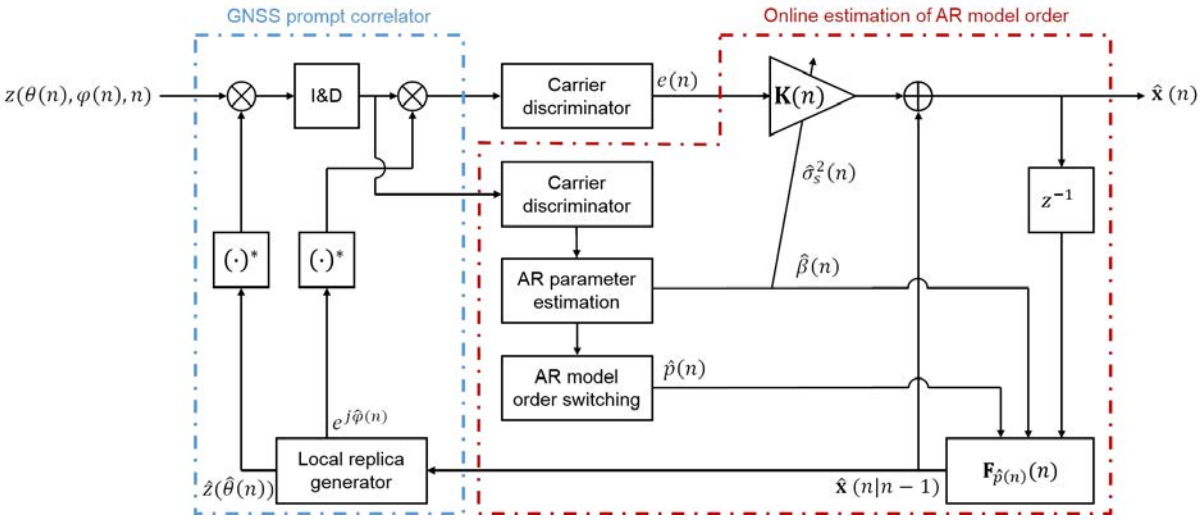

Figure 5.10: Block diagram of KF-AR with adaptive (*i.e.* online estimation) AR model order.

5.8.2.1 Estimation of AR Model Order under AWGN

We will now explore the reliability of the online MDL estimator by comparing it to the reference offline estimator, as well as the impact of AWGN in the estimation of the AR model order. The first test is that of estimating the order when there is no scintillation, but only the effect of AWGN. The result is shown in Figure 5.11. As expected, the MDL mainly selects an AR(0) regardless of the C/N_0. This situation corresponds to the KF, the Kalman filter that only tracks carrier dynamics. This result confirms the capability of the MDL of disabling the AR module within the Kalman filter when there is no scintillation.

5.8.2.2 Estimation of AR Model Order for Moderate CSM under AWGN

The result of estimating the optimal AR model order for Cornell moderate scintillation is shown in Figure 5.12 with the C/N_0 ranging from 30 to 60 dB-Hz. As can be observed, the online estimation yields practically the same result as the offline one, thus indicating the feasibility of the online MDL estimator. As expected, the MDL tends to select AR(2, 3) models rather than an AR(1), and this occurs irrespective of the C/N_0. These results are in accordance with those from previous Figure 4.10, in which the trend is to choose high

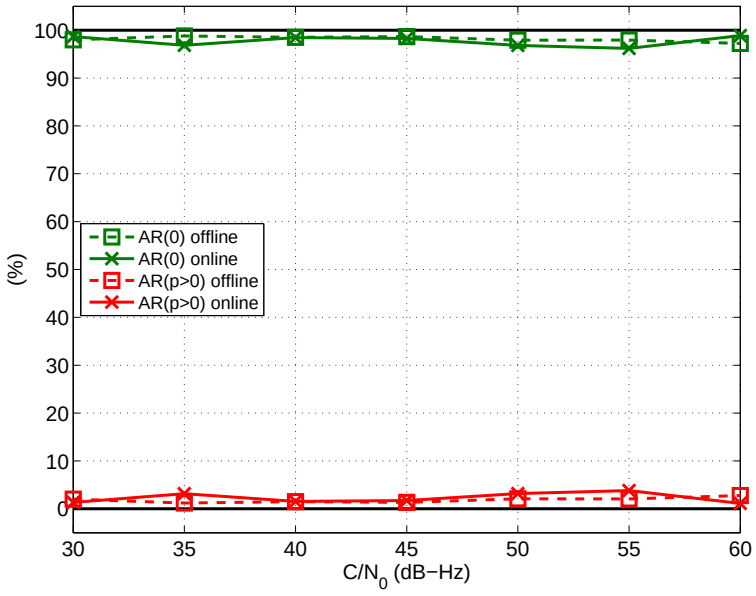

Figure 5.11: Online estimation of AR model order in the absence of ionospheric scintillation. Comparison to offline estimation as a function of the C/N_0.

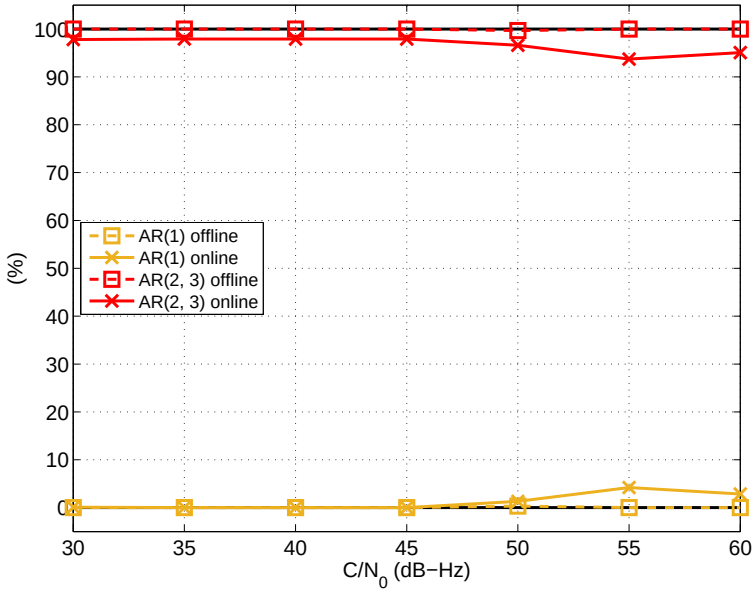

Figure 5.12: Online estimation of AR model order for Cornell moderate scintillation. Comparison to offline estimation as a function of the C/N_0.

AR model orders, whereas AR(1) models are found not to fully fit moderate scintillation events.

5.8.2.3 Estimation of AR Model Order for Severe CSM under AWGN

The result of estimating the optimal AR model order for Cornell severe scintillation is shown in Figure 5.13. Similarly to the case for moderate scintillation, the results for the online estimation tightly match those for the offline estimation, except for some small discrepancies. For high C/N_0 it is observed that an AR(1) model is selected with a probability of 30%, whereas higher-order models are selected with a probability of 70%. These values are also consistent with the results in previous Figure 4.10, where an AR(1) already fits severe scintillation, although higher-order models are found to provide slightly smaller prediction errors. When the C/N_0 decreases, the AR(1) probability is found to gradually decrease in the same quantity as the AR(2, 3) probability increases. This is a known fact where the estimated AR model order tends to overfit when the noise becomes more dominant, in an attempt to resemble the real ARMA process in (5.65). A more illustrative example of this claim is given by Figure 5.14, which shows the probability of AR order selection as a function of the C/N_0 for an ideal AR(1) process. As can be observed, the MDL truly departs from the ideal AR(1) when decreasing the C/N_0, as the selected model order gradually increases. Therefore, the presence of AWGN is shown to have some impact onto the AR model order determination under severe scintillation. These observations support the need for the MDL criterion to properly select the AR model order and estimate scintillation also accounting for the different nominal values the C/N_0 may take.

5.8.3 Adaptive Hard-Limited Measurement Noise Variance

The presence of scintillation disturbances is not limited to random phase variations, but also introduces deep fades in the signal amplitude. Such fades are often accompanied by abrupt phase changes. This joint phenomenon is known as canonical fade [Psi07], and an illustrative example is shown in Figure 5.15, which depicts a realization of Cornell moderate scintillation plotting the scintillation phase as a function of the scintillation power. As can be seen, most of the phase deviations caused by scintillation are contained in the $\pm$1-rad region, and they are accompanied by fades ranging from [-10, 0] dB. Nevertheless, when fades on the order of 25-30 dB appear, they are usually accompanied by abrupt phase jumps close to $\pm\pi$ rad.

The presence of canonical fades poses a serious concern to the linearity of the arctangent operator and may thus become a major source of misbehavior of the KF-AR. In

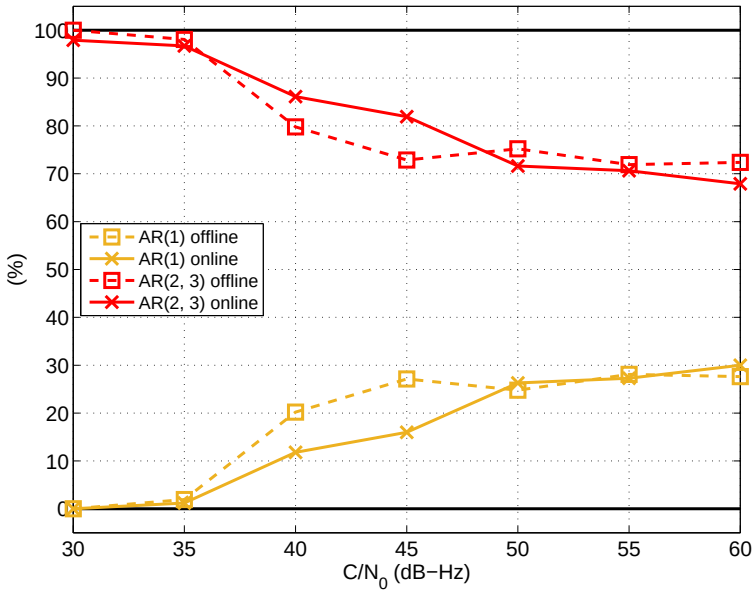

Figure 5.13: Online estimation of AR model order for Cornell severe scintillation. Comparison to offline estimation as a function of the C/N_0.

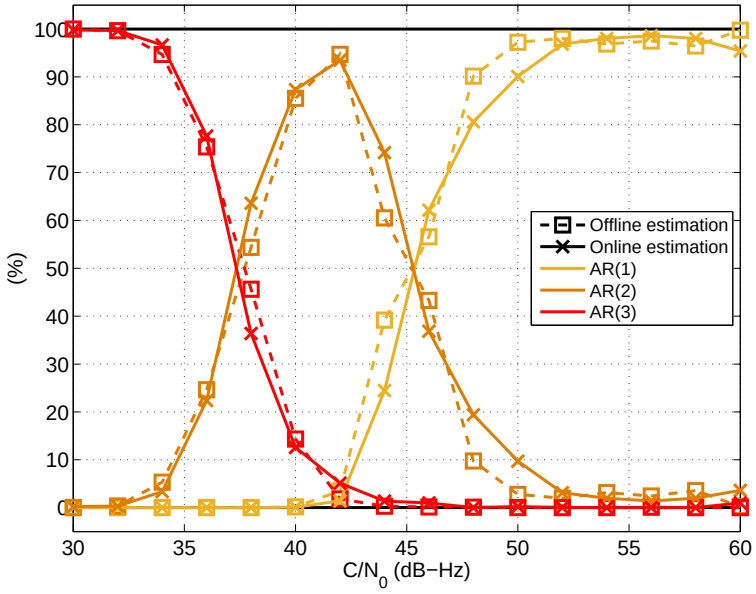

Figure 5.14: Example of online estimation of AR model order for ideal AR(1) process. Comparison to offline estimation as a function of the C/N_0.

that sense, this section proposes an adaptive implementation of the measurement noise covariance matrix of the Kalman filter that mitigates this effect.

Figure 5.16 shows the evolution over time of the C/N_0 under the presence of CSM

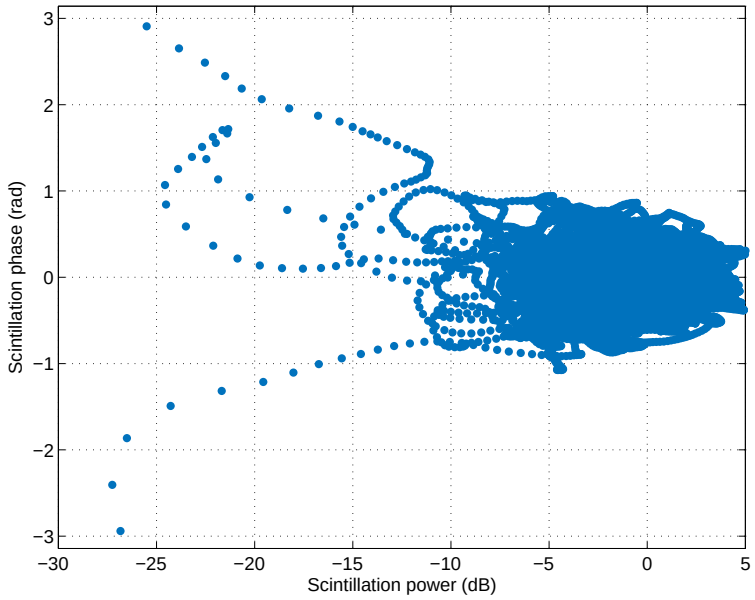

Figure 5.15: Example of Cornell moderate scintillation time series, showing scintillation phase as a function of scintillation power.

moderate and severe scintillation. The variations are given with respect to a nominal C/N_0 of 45 dB-Hz. As can be observed, the effect becomes particularly critical under severe scintillation, introducing fades that frequently exceed 30 dB. In this situation, the KF-AR is affected by abnormal measurements that severely degrade the performance and may even drive the tracking loop to lose lock.

From the Kalman filter perspective, the canonical fades introduced above have a rather nonlinear nature, and thus it is difficult to deal with them through a linear approach, such as the one considered for the scintillation phase. In that sense, the proposed approach consists in an adaptive hard-limiting (AHL) condition that is based on the measured C/N_0. The underlying idea is to exploit the fact that the Kalman equations explicitly indicate the time dependence of the measurement noise variance $R(n)$, thus allowing it to be dynamically adjusted to match the actual working conditions. This parameter plays a key role in the Kalman filter performance, as it determines the value of the Kalman gains [Kay93] and, interestingly, it depends on the instantaneous C/N_0 for the problem at hand, as already shown in (3.22),

$$R(n) = \frac{1}{2T_s \frac{C}{N_0}(n)} \left[1 + \frac{1}{2T_s \frac{C}{N_0}(n)} \right] \text{ rad}^2. \tag{5.66}$$

Therefore, the approach consists in adapting $R(n)$ in (5.66) based on actual estimates of the instantaneous C/N_0 in order to consistently adjust the Kalman gains, but subject to

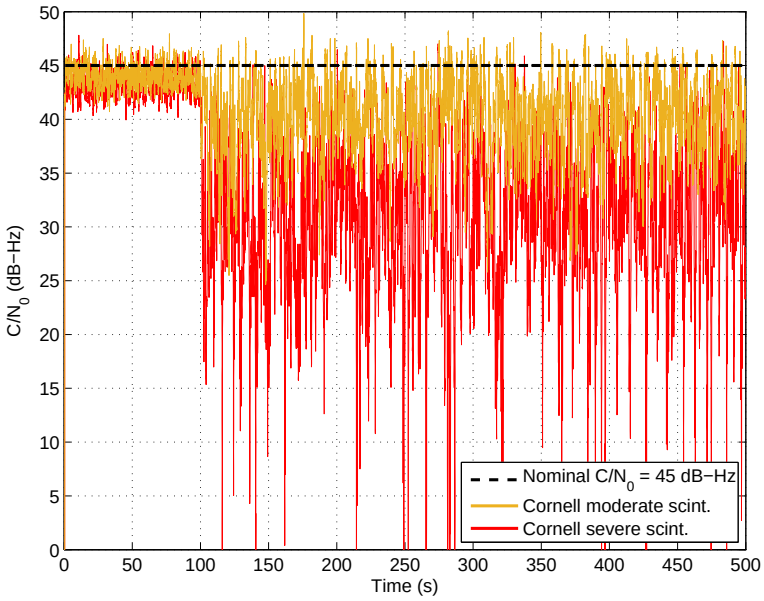

Figure 5.16: Illustrative example of canonical fades introduced by Cornell moderate and severe scintillation as a function of time, with respect to nominal C/N_0 of 45 dB-Hz.

a hard-limiting value such that,

$$R(n) = \begin{cases} \hat{R}(n) & \text{if } \frac{\hat{C}}{N_0}(n) \geqslant \gamma \\ \infty & \text{otherwise} \end{cases} \tag{5.67}$$

for some threshold γ, and where $\hat{R}(n)$ refers to the estimated measurement noise variance, obtained by substituting the instantaneous C/N_0 in (5.67) by an estimated version. The implementation of Eq. (5.67) is shown in Figure 5.17 in form of a block diagram. We can see a block devoted to the C/N_0 estimation and a switching block that commutes between the weighted innovation sequence when $C/N_0 > \gamma$ and an open-circuit when $C/N_0 < \gamma$. In the latter, by setting $R(n) = \infty$ in (5.66), the Kalman gains are driven to zero whenever the C/N_0 drops below γ. In this situation, the Kalman filter is totally isolated from the carrier discriminator output, and the state propagation relies only on the Kalman internal state-space model, thus protecting the loop from abnormal measurements when deep fades occur, and keeping it in lock until the C/N_0 recovers to nominal conditions. This implementation is thought to provide an added robustness to the technique in the presence of potential outliers introduced by scintillation.

In view of this, the problem of the proposed approach boils down to estimating the C/N_0 so as to adjust the measurement noise covariance matrix $\hat{R}(n)$. To this end, we will make use of the so-called narrow-wideband power ratio method [Van96], featured by

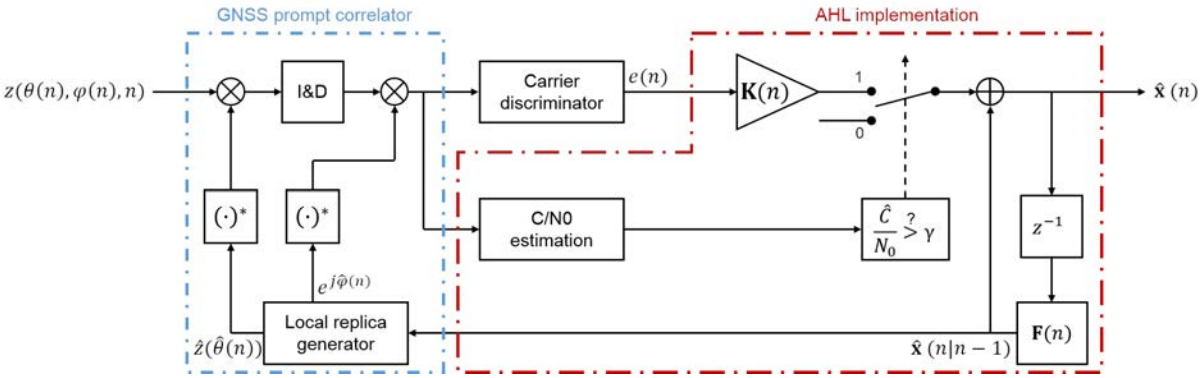

Figure 5.17: Block diagram of KF-AR implementing the adaptive hard-limiting (AHL) C/N_0 estimation.

providing sufficiently good C/N_0 estimates with ease of implementation.

Narrow-Wideband Power Ratio Algorithm for C/N_0 Estimation

The *narrow-wideband power ratio* (NWPR) estimator is based on dissociating the noise power at the prompt correlator output into a narrow and a wide bandwidth components,

$$\mathrm{NBP}(n) = \left| \sum_{m=1}^{M} y_{\mathrm{P}}(n-m) \right|^2 \tag{5.68}$$

$$\mathrm{WBP}(n) = \sum_{m=1}^{M} |y_{\mathrm{P}}(n-m)|^2 \tag{5.69}$$

where $y_p(n)$ is the prompt correlator output at time sample n. As can be observed, the NWPR method employs M past samples of $y_p(n)$, in the interval $[n-M..n-1]$, to estimate the C/N_0 at the current time sample. The value of M becomes a trade-off between estimation accuracy and agility to C/N_0 variations. Thus, it should be chosen neither too large so as to misdetect spurious deep fades, nor too small to make the Kalman unstable due to the rapid variations of the estimated C/N_0.

The next step is to compute the averaged power ratio using an exponential filter as follows,

$$\hat{\mu}(n) = \alpha \frac{\mathrm{NBP}(n)}{\mathrm{WBP}(n)} + (1-\alpha)\hat{\mu}(n-1) \tag{5.70}$$

with α the weighting factor between the new data and past measurements, whose value determines a trade-off between the convergence speed of (5.70) and the estimation accuracy (*i.e.* variance) in steady state. Expression (5.70) is then used to eventually estimate

the instantaneous C/N_0 as,

$$\frac{\hat{C}}{N_0}(n) = \frac{1}{T_s}\frac{\hat{\mu}(n)-1}{M-\hat{\mu}(n)}. \tag{5.71}$$

5.8.4 Adaptive Hard-Limited KF-AR with Adaptive Autoregressive Model. AHL-KF-A2R(p)

On the one hand, Sections 5.8.1 and 5.8.2 have presented a method to estimate the optimal AR model parameters and order in an online manner, so that the Kalman state-space model can be self-adapted to match the actual input working conditions. On the other hand, Section 5.8.3 has presented a way to optimally adapt the Kalman measurement noise variance, subject to a hard-limiting threshold that isolates the filter from the input measurements when the C/N_0 falls below a given value. The latter has been thought to deal with deep fades introduced by ionospheric scintillation, particularly by severe scintillation, that cause the C/N_0 to drastically drop.

Both of these implementations fit very well into the time-varying nature of scintillation disturbances, and are found to take place simultaneously in reality. Therefore, it is natural to think of a single configuration that combines both functionalities. That is, a configuration that merges both implementations into the same closed-loop architecture. The result is an augmented KF-AR technique that we denote herein as AHL-KF-A2R(p), whose block diagram is shown in Figure 5.18.

The GNSS code correlator correlates the incoming signal with a local replica that is generated using the Kalman predicted phase for time instant n, which is based on the estimated phase at time instant $n-1$. It contains both user dynamics and scintillation phase, and hence the phase at the carrier discriminator output contains the difference between the incoming phase and the Kalman predicted phase. The resulting signal is the Kalman innovation sequence, or prediction error. On the other hand, the correlator presents a second output before the local replica is compensated with the estimated scintillation phase. This is used to implement a second carrier discriminator whose output contains the difference between the incoming phase and the estimated user dynamics, thus leaving only the input scintillation phase that is eventually used to apply the MDL to estimate the optimal AR model order for the current time instant n. The transition matrix is then updated accordingly, as well as the Kalman gains using the corresponding value of $\sigma^2_{s_p}$. The Kalman filter carries out the state correction, with the AHL commuter isolating the loop from the Kalman prediction error at low C/N_0, and the state prediction for the next

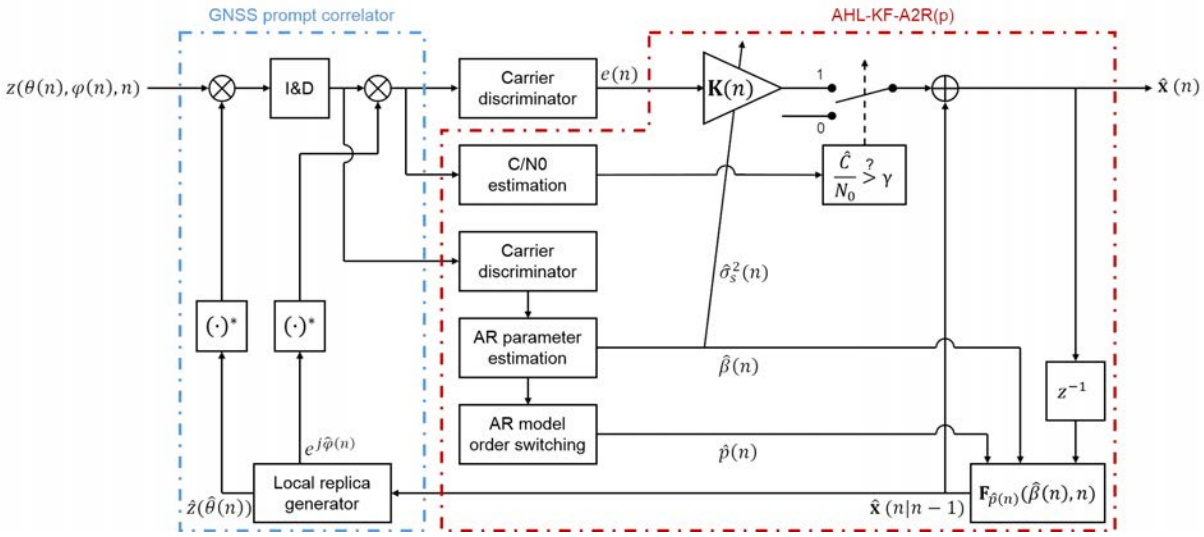

Figure 5.18: Block diagram of proposed adaptive hard-limited KF-AR with adaptive autoregressive model, referred to as AHL-KF-A2R(p).

time instant is then computed. The GNSS signal generator takes the predicted Kalman state as input to further obtain the predicted measurement and update the local replica. This is then correlated with the input signal, thus closing the loop.

5.9 Semi-Adaptive KF-AR Implementation. The AHL-KF-AR(0, 1)

One of the drawbacks of the AHL-KF-A2R(p) is the fact of requiring that three estimation modules be operating at each time instant, namely for AR parameter, model order and C/N_0 estimation. This translates into a high resource and computational load that may become unsuitable for handheld receivers. In this sense, the major contributor to this effect is the online AR parameter estimator due to the involvement of autocorrelation or inverse matrix operations at each time instant. On the other hand, there are evidences in Section 5.8.1 that show the AHL-KF-A2R(p) to underestimate the AR parameters due to the presence of AWGN, a phenomenon that is expected to incur into some performance degradation.

With this information, it is natural to think of a simplified technique that circumvents the computational limitations posed by the AHL-KF-A2R(p), while attempting to provide optimal performance without compromising agility. We propose a semi-adaptive

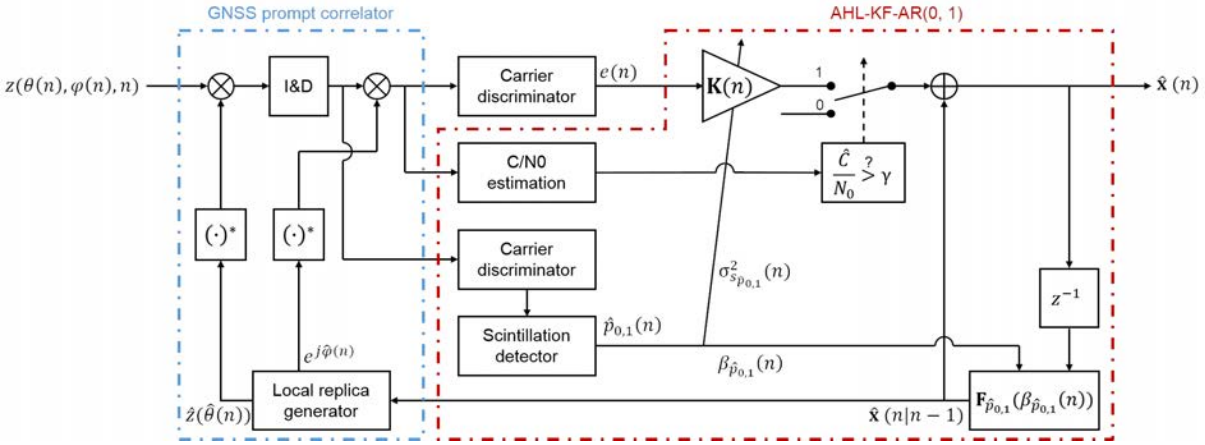

Figure 5.19: Block diagram of proposed semi-adaptive KF-AR, referred to as AHL-KF-AR(0, 1).

implementation that uses a fixed set of AR model parameters, while partially preserving the other estimation modules: the AHL implementation remains as in the AHL-KF-A2R(p), whereas the MDL is truncated to switch between the KF and a fixed KF-AR. This semi-adaptive technique will be henceforth termed AHL-KF-AR(0, 1), and its particular features are described in detail next.

5.9.1 Determination of Optimal AR Model Parameters

In order to avoid the online estimation of the AR model parameters, we must find a set of fixed parameters with which both moderate and severe scintillation can be simultaneously dealt with. The proposed way to do so stems from considering that the filter must be able to track up to severe scintillation phase variations, understood as the worst-case scenario (*i.e.* strongest intensity scintillation can have). From the analysis in Chapter 4, severe scintillation was found to be mainly fitted by an AR(1) process. Even when forcing higher-order models, the obtained AR parameters converged to those of an AR(1) process. That is, β_1 was the predominant coefficient, whereas β_2 and β_3 were very close to zero. In addition, the AR prediction errors for all model orders were very similar.

Therefore, the semi-adaptive KF-AR must also be able to track moderate scintillation, subject to the statements above. That is, using an AR(1) model. In Chapter 4, AR(2, 3) models were found to better fit moderate scintillation events. However, an AR(1) can ultimately be used if noting that $\sigma^2_{s_p}$ plays a key role in the estimation performance as follows. Being $\sigma^2_{s_p}$ the process noise variance for scintillation tracking, it determines the

Kalman filter equivalent loop bandwidth [Jwo01], as previously stated, and therefore the trade-off between the measurement noise filtering capabilities and the ability to track scintillation phase variations.

Using higher-order AR models for moderate scintillation fitting can be understood as the natural solution since higher-order models present smaller prediction errors, thus not compromising the KF-AR equivalent loop bandwidth. It is therefore the optimal solution, the most robust one in terms of noise filtering. However, this phenomenon can also be interpreted from the KF-AR standpoint as follows. Using the AR(1) parameters for moderate scintillation in Table 4.1, the KF-AR is not able to perform well because $\sigma^2_{s_p}$ is such that the equivalent loop bandwidth is not enough to faithfully track moderate scintillation variations. Therefore, another solution is to increase the equivalent loop bandwidth by increasing $\sigma^2_{s_p}$. In this way, the KF-AR is expected to track moderate scintillation using an AR(1) process.

As a matter of fact, this is the solution that must inevitably be adopted by the semi-adaptive KF-AR implementation, since $\sigma^2_{s_p}$ is required to increase from the order of 10^{-6} up to $4 \cdot 10^{-2}$ rad^2 so as to be able to track severe scintillation. It is though a suboptimal approach since it requires increasing the KF-AR equivalent loop bandwidth, thus reducing the noise filtering capabilities under moderate scintillation and the operational range in terms of C/N_0 as a consequence. In contrast, this solution presents the following advantages:

1. It enables tracking moderate scintillation using an AR(1) model, the least complex solution in terms of KF-AR state-space formulation.

2. It is expected to perform optimally at high C/N_0 regardless of the nature of the input signal.

At this point, it remains to determine the optimal AR(1) coefficient β. This can be obtained by simply fixing $\sigma^2_{s_p} = 4 \cdot 10^{-2}$ rad^2 as required by severe scintillation, and finding the value of β that leads to the optimal BCRB. By analysing the recursive BCRB in (5.14) as a function of β, this requirement is found to be fulfilled for $\beta = 0.9$.

Therefore, the optimal AR model parameters are summarized in Table 5.1. These values will be the ones used in the simulation campaign in Chapter 6.

	AHL-KF-AR(0, 1)	
	$\hat{\beta}$ (unitless)	$\hat{\sigma}_s^2$ (rad^2)
AR(1)	0.9	4E-2

Table 5.1: Optimal AR parameters to be used by AHL-KF-AR(0, 1) for the AR fitting of the CSM.

5.9.2 Truncated Online Estimation of AR Model Order

A critical aspect of the AHL-KF-AR(0, 1) to avoid loss of agility is the capability of disabling the AR part when scintillation is absent (*i.e.* AR(0)), which must be preserved for the AR module not to incur into any performance degradation when only AWGN is present. For this purpose, the AHL-KF-AR(0, 1) utilizes the AR model order selector from the AHL-KF-A2R(p), but a truncated version that commutes only between an AR(0) and an AR(1) process in the absence and in the presence of scintillation, respectively. Therefore, the MDL can be now understood as a scintillation detector, and the problem can be thought of as a *hypothesis testing* problem, where $\mathcal{H}_0$ corresponds to a scintillation-free situation, whereas $\mathcal{H}_1$ corresponds to a situation where any kind of scintillation is present.

Hypothesis Testing under AWGN

For a simulation with 10 minutes length, Figure 5.20 shows the percentage of time either AR(0) or AR(1) is selected in the presence of only AWGN with no scintillation. As expected, the MDL commuter is fully selecting an AR(0) model for all C/N_0, thus confirming the ability to switch to the non-hybrid KF that only tracks carrier dynamics when scintillation is absent.

Hypothesis Testing under CSM plus AWGN

The results when in the presence of AWGN plus moderate and severe scintillation are shown in Figures 5.21 and 5.22, respectively. As can be observed, at low C/N_0 the truncated MDL is reacting as if there were no scintillation. This behavior can be explained by the fact that, at low C/N_0, the noise power is such that it ends up masking scintillation; the Kalman input measurements are mainly corrupted by AWGN, thus neglecting the effect of scintillation that is located below the noise floor. For this reason, this phenomenon

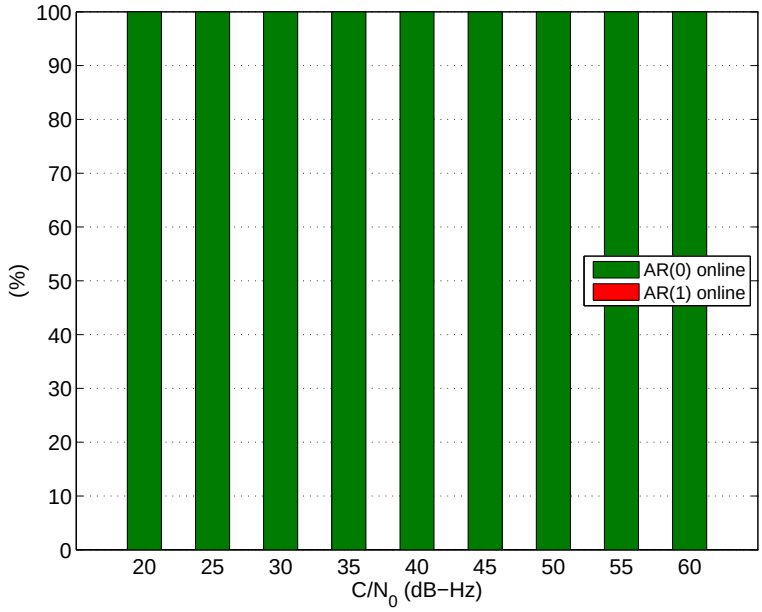

Figure 5.20: Online AR commuting mechanism in the absence of ionospheric scintillation. Percentage of time either AR(0) or AR(1) models are selected.

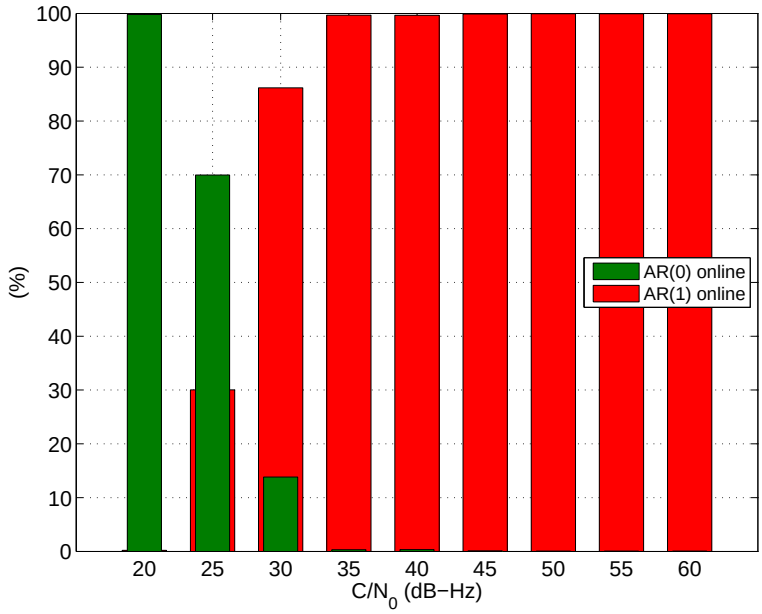

Figure 5.21: Online AR commuting mechanism in the presence of Cornell moderate scintillation. Percentage of time either AR(0) or AR(1) models are selected.

ameliorates when increasing the C/N_0. In this situation, the MDL is able to successfully detect the presence of scintillation, thus confirming the ability to switch to the hybrid Kalman configuration when needed.

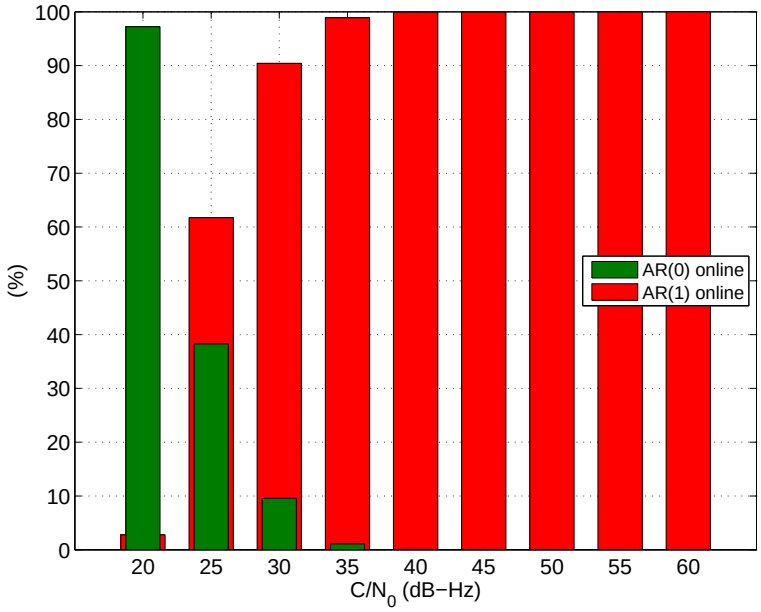

Figure 5.22: Online AR commuting mechanism in the presence of Cornell severe scintillation. Percentage of time either AR(0) or AR(1) models are selected.

5.10 Conclusions

The main contributions of this chapter have been two. On the one hand, the derivation of novel closed-form approximations for the convergence time and steady-state performance of autoregressive Kalman filters. Results for both hybrid and non-hybrid autoregressive filters have been obtained. To this end, the core of the hybrid formulation has been presented in the first part of the chapter as a fusion of the carrier dynamics and scintillation phase state-space models into an embedded setup. Then, a qualitative evaluation of the KF-AR performance bounds has been provided, highlighting that the steady-state BCRB tends to increase when scintillation is above the noise floor. It is concluded that, when this occurs, the dynamics and scintillation phase estimates are coupled, meaning that estimation errors in one of them induce estimation errors in the other.

On the other hand, this chapter has proposed two KF-AR adaptive approaches to self-adapt to time-varying scintillation and circumvent the limitations of fixed techniques. The first one is the AHL-KF-A2R(p), a doubly-adaptive technique implementing two separate estimation modules. First, an online estimator of the AR model parameters and order. Second, an adaptive estimation of the measurement noise power based on the measured C/N_0 to deal with the nonlinear amplitude fades introduced by scintillation. In order to test the online estimation under realistic conditions, this chapter has also provided a

detailed analysis on the problem of AR fitting when in the presence of AWGN. Preliminary simulation results have shown that the proper identification of the AR model parameters becomes hindered, particularly under moderate scintillation. Therefore, the AHL-KF-A2R(p) provides agility of self-adaptation when the working conditions vary, but at the expense of some performance degradation in the estimated scintillation. As for the AR order selector, it has been shown to favor higher-order models when decreasing the C/N_0, in an attempt to approximate to the real ARMA process underlying in the input signal. However, this phenomenon has no direct impact onto the KF-AR estimation performance.

As a consequence, the AHL-KF-AR(0, 1) technique has been proposed in order to circumvent the limitations of the AHL-KF-A2R(p). It implements the AHL as in the AHL-KF-A2R(p), whereas the MDL has been reduced to a mere scintillation detector that commutes between a KF-AR(0) and a KF-AR(1) with fixed parameters. Preliminary simulation results have shown the MDL to successfully detect the absence and presence of scintillation for C/N_0 above 30 dB-Hz. On the contrary situation, when scintillation is below the noise floor, the MDL mainly selects an AR(0). The fixed AR(1) parameters have been designed to provide optimal performance under both moderate and severe scintillation, and thus no performance degradation is expected with the AHL-KF-AR(0, 1).

At this point we are ready to thoroughly evaluate the performance of the above techniques, which is the aim of Chapter 6 and will include fixed KF-AR techniques and the AHL-KF-A2R(p) and AHL-KF-AR(0, 1) adaptive implementations under synthetic CSM and realistic scintillation time series.

Chapter 6

KF-AR Test and Experimental Results

6.1 Introduction

The main purpose of this chapter is to test the KF-AR implementations proposed in Chapter 5 and compare their performance to that of conventional PLL architectures. To this end, an extensive simulation campaing has been carried out by using a GNSS carrier tracking simulator that has been implemented in MATLAB for GPS L1 C/A signals (*i.e.* BPSK modulation). The simulations presented in this chapter are divided into three main categories:

- Simulations with stationary Cornell scintillation, in order to test the performance of fixed KF-AR configurations in comparison to conventional PLLs and evaluate the closeness to the optimal (*i.e.* expected) performance given by the BCRB.
- Simulations under time-varying Cornell scintillation, aimed at testing the self-configuring capabilities of the adaptive implementations (*i.e.* AHL-KF-A2R(p) and AHL-KF-AR(0, 3)) introduced in Chapter 5 when working conditions change over time.
- Simulations using real scintillation time series obtained from the ESA scintillation monitoring network. The objective is to test the performance of KF-AR techniques using real scintillation measurements and to validate the results obtained for synthetic data.

6.2 Metrics for Performance Evaluation

Root Mean Square Error

The *root mean squared error* (RMSE) is widely adopted in the field of signal processing to evaluate the quality of a given estimator. It measures the average root mean squared deviation of the estimator from the true value [Kay93],

$$\mathrm{RMSE}(n) \doteq \sqrt{\mathrm{E}\left[\left(\hat{\theta}(n) - \theta(n)\right)^2\right]} \tag{6.1}$$

which must reach the root BCRB in order to truly conclude that the Kalman filter performs optimally.

The RMSE will be determined by performing several Montecarlo realizations of the Kalman filter. In this simulation campaign we will run the techniques for 100 Montecarlo iterations. It is important to note that only those iterations that have not lost lock will be employed in the computation of the RMSE, in order to obtain a meaningful result. Otherwise, a distorted RMSE metric would be obtained. Those realizations that have lost lock will be discarded, and will be treated separately to determine the metric of probability of loss of lock.

Probability of Loss of Lock

For the problem of GNSS tracking, the *loss-of-lock probability* (LoL) is the probability that the tracking loses the lock to the signal, and it is mainly determined by the given channel working conditions and tracking loop set-up. As stated above, the need for measuring the LoL is initially motivated by the RMSE computation, where those out-of-lock realizations have to be discarded to avoid introducing outliers and abnormal measurements into the RMSE metric. The LoL is computed by looking at the errors of the Kalman filter estimates along the time, and the method employed in this thesis relies on the following two considerations.

At first glance, the LoL computation is based on observing whether the instantaneous phase error measurements exceed the tracking threshold. The latter must be set in such a way that it allows to clearly detect the presence of abnormal phase errors. To this end, the rule of thumb is to consider half the pull-in range of the phase discriminator, since this value is indeed the border that separates two adjacent stable points of the discriminator S-curve [Ló12]. Thus, it can intuitively be understood as the point that phase errors should

not exceed. For the ATAN2 discriminator, half the pull-in range equals to a threshold of $\pm\pi$ radians. However, phase errors of this magnitude can never be observed since they coincide with the edges at which the ATAN2 phase values are wrapped, that is, at $[-\pi,\ \pi)$ radians. For this reason, the common approach in practice is to take one additional half, leading to a threshold of $\pm\pi/2$ radians, which is one fourth of the ATAN2 pull-in range. It can be noticed that this threshold preserves the same notion of "one fourth of the pull-in range" as the threshold used for the RMSE, which follows the rule of thumb that $3\sigma_\theta < \frac{\text{pull-in range}}{4}$ [Kap05].

The second consideration to be taken into account is the existence of momentary instants, such as phase jumps or deep fades introduced by scintillation, where the phase error may exceed the LoL threshold but the Kalman filter does actually not lose lock; the error goes below the threshold again after the scintillation peak. This leads us to think that, in order to declare LoL, not only a single error sample must go beyond the threshold, but a whole burst of consecutive samples. In this simulation campaign we will consider a loss-of-lock window of 400 ms.

6.3 Scenario Definition and KF-AR Set-Up

The simulations in this chapter are defined for a static receiver, such as a ground scintillation monitoring station. Notwithstanding, even though the receiver presents zero dynamics, there is still some relative motion between the receiver and GNSS satellites owing to the movement of the latter. This causes the receiver to experience some residual dynamics, which in the sequel are considered to be given by the values in Table 6.1. The normalization to radians in the third column has been performed with $T_s = 20$ ms, so as to be consistent with the sampling time of the DAK2.2014.335.22.GPS24 real scintillation time series that will be processed in Section 6.6.

Parameter	**Value**	**Norm. to rad**
Doppler shift	10 Hz	1.25
Doppler rate	1 Hz/s	$2.5 \cdot 10^{-3}$
Doppler jerk	$2 \cdot 10^{-4}$ Hz/s^2	10^{-8}

Table 6.1: Residual dynamics experienced by static receiver.

For the problem of tracking carrier dynamics, we are considering a third-order Kalman

filter in charge for tracking carrier phase, Doppler shift and Doppler rate. The Doppler jerk, also termed Doppler acceleration, is the missing higher-order term that is modeled through the Kalman process noise $v(n)$ following some random distribution. According to Section 3.2.3, its variance σ_v^2 is one of the parameters to be tuned for the filter to operate. For the simulations in this chapter, a convenient way to do so is to set σ_v^2 as the variance of a uniformly-distributed random variable within $\left[-\dddot{\theta}_{\max},\ \dddot{\theta}_{\max}\right]$, with $\dddot{\theta}_{\max}$ the maximum Doppler jerk. This leads to the following constant,

$$\sigma_v^2 \doteq \frac{\Delta^2}{12} = \frac{\left(2\dddot{\theta}_{\max}\right)^2}{12} = 3.4 \cdot 10^{-17}\ \text{rad}^2. \tag{6.2}$$

On the other hand, the Kalman filter also requires tuning the measurement noise variance $\sigma_w^2(n)$ to operate. For the problem at hand, σ_w^2 refers to the noise power at the phase discriminator output, the ATAN2 in this case, which is recalled next from (3.22):

$$R(n) \doteq \frac{1}{2T_s\frac{C}{N_0}(n)}\left[1 + \frac{1}{2T_s\frac{C}{N_0}(n)}\right]\ \text{rad}^2. \tag{6.3}$$

In the simulations, the receiver is assumed to have clear satellite visibility, and thus it will be affected by AWGN at a nominal C/N_0 of 45 dB-Hz. With these values, the measurement noise variance results in $R(n) = 8 \cdot 10^{-4}$ rad^2.

It remains to tune the initial state covariance matrix. The Kalman filter will be forced to start operating with absolute initial uncertainty about the parameters to be estimated. For this reason, the following initial state covariance matrix is set:

$$\mathbf{\Sigma_x}(0) = \begin{bmatrix} \pi^2/3 & 0 & 0 & 0 & 0 & 0 \\ 0 & 10^6 & 0 & 0 & 0 & 0 \\ 0 & 0 & 10^6 & 0 & 0 & 0 \\ 0 & 0 & 0 & \pi^2/3 & 0 & 0 \\ 0 & 0 & 0 & 0 & \pi^2/3 & 0 \\ 0 & 0 & 0 & 0 & 0 & \pi^2/3 \end{bmatrix} \tag{6.4}$$

with $\pi^2/3$ the variance in rad^2 of a uniformly-distributed random variable within $[-\pi,\ \pi]$ rad. On the other hand, large initial Doppler shift and rate variances of 10^6 indicate the complete lack of knowledge about the true parameter values. Under this configuration, though, it is recommended to start running the Kalman filter during a silent period where no scintillation is present in the input samples. Such silent period at the beginning will

allow the filter to consolidate the estimation of the residual user dynamics. Then, the Kalman filter will be ready to start operating under the presence of scintillation, and distinguishing it from carrier dynamics.

It is important to note that, even though the main focus of the simulation campaign is placed on testing carrier phase tracking, the MATLAB simulator also implements a DLL for code-delay tracking so that the simulator be realistic and the simulation results be meaningful. Given that the dynamics KF is of third-order, a second-order DLL has been implemented following the guidelines in Chapter 2, with a loop bandwidth as small as 0.1 Hz thanks to the carrier aiding feature presented in Section 2.3.3.3.

Finally, the threshold γ for the AHL implementation must be set. The determination of γ is based on the tracking threshold in terms of C/N_0. For the ATAN2 discriminator employed herein, the tracking threshold is set as $3\sigma_\theta < \frac{\pi}{2}$ radians. As already explained, the value of σ_θ is determined by the loop bandwidth and the C/N_0,

$$\sigma_\theta = \sqrt{\frac{B_\mathrm{L}}{C/N_0}\left(1 + \frac{1}{2T_s C/N_0}\right)} \text{ rad.} \tag{6.5}$$

In GNSS, the loop bandwidth of the PLL loop filter does usually not exceed $B_\mathrm{L} = 15$ Hz, in order to remain stable [Kap05]. If this value is employed in (6.5) and $T_s = 20$ ms, it is found that the C/N_0 tracking threshold is located below 20 dB-Hz. With these observations, the threshold γ will be set at $\gamma = 25$ dB-Hz so as to leave some margin and not push the AHL to the limit imposed by the C/N_0 tracking threshold.

6.4 Simulation Results with CSM Time Series

6.4.1 Scenarios with Stationary Scintillation

The aim of this section is twofold. First, to evaluate the estimation performance of fixed (*i.e.* non-adaptive) KF-AR configurations using the optimal AR parameters in Table 4.1. Second, to compare the KF-AR performance with the one provided by a conventional PLL. In this latter, the comparison must be fair (*i.e.* under equal set-up conditions), so that the extracted conclusions about the advantages and inconvenients of each technique be meaningful.

Technique	**KF-AR RMSE (rad)**	**PLL equiv. bandwidth (Hz)**
KF-AR for moderate scint.	$6.8 \cdot 10^{-3}$	2
KF-AR for severe scint.	$2.5 \cdot 10^{-3}$	0.2

Table 6.2: Equivalent loop bandwidth for a PLL to perform equally as the KF-AR under dynamics plus AWGN only.

6.4.1.1 Equivalent PLL Loop Bandwidth

As explained in Section 2.3.3.1, the PLL performance is determined by its loop bandwidth, being this a trade-off between the noise filtering capabilities and the maximum supported input dynamic stress. As already explained, the Kalman filter can also be understood as a loop filter with some equivalent loop bandwidth given by a combination of the tuning parameters σ_v^2 and $\sigma_w^2(n)$ [Jwo01][1]. Since these have already been set in Section 6.3 for the scenario under analysis, the idea is to design a PLL with loop bandwidth such that its phase jitter equals the steady-state phase MSE of the KF-AR, $[\mathbf{\Sigma_x}]_{1,1}$, when under dynamics plus AWGN only (*i.e.* no scintillation),

$$B_{\mathrm{L_{eq}}} = \frac{[\mathbf{\Sigma_x}]_{1,1}^{(\mathrm{AWGN})} C/N_0}{1 + \frac{1}{2C/N_0 T_s}} \text{ Hz}. \tag{6.6}$$

The results for the KF-AR(p) optimized for both Cornell moderate and severe scintillation are shown in Table 6.2.

6.4.1.2 Scenario #1.1. Cornell Moderate Scintillation

This section presents the performance results of the fixed KF-AR techniques versus conventional PLLs for stationary Cornell moderate scintillation. Figure 6.1 compares the optimal KF-AR(1) to the conventional PLL in terms of RMSE. The mean steady-state RMSE values are summarized in Table 6.3, as well as the metric of LoL probability for each technique. Table 6.3 also shows the normalized computational cost (CPU) of the different techniques relative to that of the basic KF-AR(p) implementation, which is taken as the reference. All techniques perform similarly in terms of LoL probability. However, even though at the expense of higher computational burden, the KF-AR(1) is clearly outperforming the PLL, particularly in terms of RMSE and stability over time. The

[1]Note that σ_v^2 and $\sigma_w^2(n)$ also refer to dynamic stress and noise power, respectively, thus linking these tuning parameters with the concept of equivalent loop bandwidth.

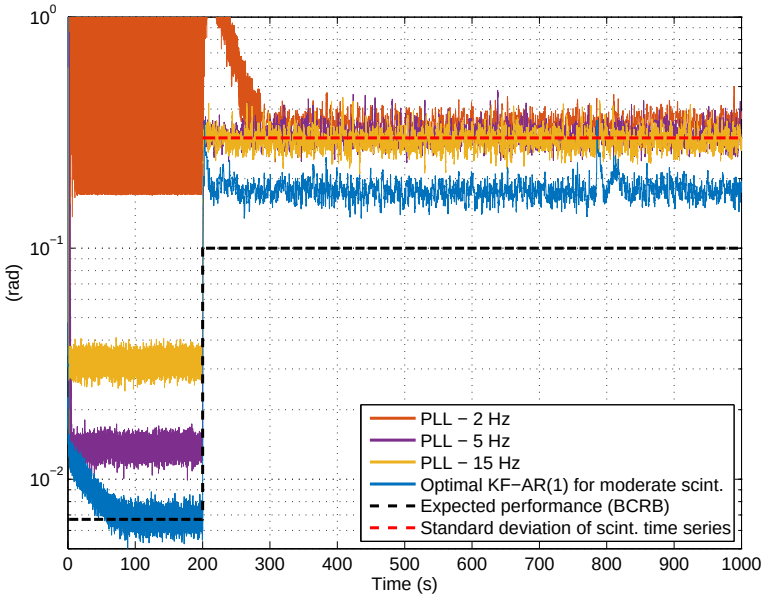

Figure 6.1: Phase RMSE of optimal KF-AR(1) for Cornell moderate scintillation, versus PLL with loop bandwidths $\{2,\ 5,\ 15\}$ Hz. Test scenario #1.1.

KF-AR(1) is able to lock during the initial silent period, whereas the 2-Hz PLL is not, suffering from several cycle slips. For this reason, Figure 6.1 and Table 6.3 also include the performance metrics for the PLL with 5- and 15-Hz loop bandwidth. Nonetheless it is found that whereas increasing the PLL loop bandwidth allows to practically eradicate the cycle slips, it does not provide any major improvement in terms of RMSE. While the KF-AR(1) provides a steady-state RMSE of around 0.2 rad, it worsens to 0.3 rad for any PLL. The latter is explained by the fact that the PLL interprets scintillation phase variations as part of carrier dynamics. That is, when in lock, it tracks both carrier dynamics and scintillation as a whole, as shown in Figure 6.2. Therefore, when computing the phase estimation error by subtracting the true carrier dynamics from the estimated phase, the result is the scintillation phase variations themselves. Given that these have zero mean (*i.e.* zero bias), the PLL RMSE equals thus the standard deviation of scintillation time series, which is around $\sigma_{\varphi_{s,\mathrm{mod}}} = 0.3$ rad for the Cornell moderate scintillation under study.

Even though the PLL is outperformed by the KF-AR(1), Figure 6.1 also shows that the latter is not reaching the expected performance given by the BCRB in the presence of scintillation. This manifests that the KF-AR(1) state-space model parameters do not fully match the input signal model. This is though an expected phenomenon since AR(1) models with the optimal parameters in Table 4.1 have been found not to well fit moderate

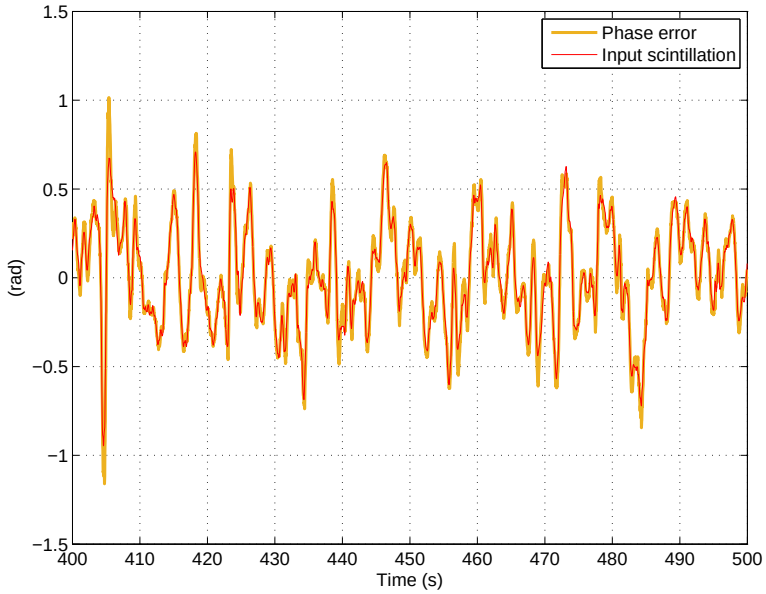

Figure 6.2: Illustrative example of PLL tracking both carrier dynamics and scintillation as a whole, thus not being able to dissociate between both components.

scintillation. As explained in Section 5.9, this can be solved in two ways: by either increasing the KF-AR equivalent loop bandwidth by enhancing $\sigma_s^2(n)$, or using higher-order AR models. The latter is the optimal (*i.e.* natural) solution, the robust one since it preserves the KF-AR loop bandwidth. In that sense, Figure 6.3 compares the phase RMSE of the KF-AR(1) to that of the KF-AR(2, 3) techniques. Higher-order AR models are found to reach the BCRB, thus confirming their suitability for fitting moderate scintillation events, while presenting the smallest LoL probability, according to Table 6.3.

Lastly, the AHL implementation is tested. Figure 6.3 also includes the RMSE performance of the optimal KF-AR(3) with the AHL enabled. As can be observed, the AHL is found to provide very similar performance to the non-AHL KF-AR(3), owing to the fact that moderate scintillation does not introduce major deep fades in the signal amplitude. However, even though at the expense of higher computational load, the AHL does improve the KF-AR performance when under severe scintillation as we will see next.

6.4.1.3 Scenario #1.2. Cornell Severe Scintillation

This section presents the performance results of the fixed KF-AR techniques versus conventional PLLs for stationary Cornell severe scintillation. Figure 6.4 compares the optimal KF-AR(1) to the conventional PLL in terms of RMSE. The mean steady-state

Technique	RMSE (rad)	Prob. LoL (%)	CPU (norm.)
2-Hz PLL	0.3535	1	0.5
5-Hz PLL	0.3081	<1	
15-Hz PLL	0.2941	1	
KF-AR(1)	0.1816	1	1
KF-AR(2)	0.1088	<1	
KF-AR(3)	0.0951	<1	
AHL-KF-AR(3)	0.0953	<1	1.25

Table 6.3: Performance results of PLL and KF-AR techniques for Cornell moderate scintillation. Test scenario #1.1.

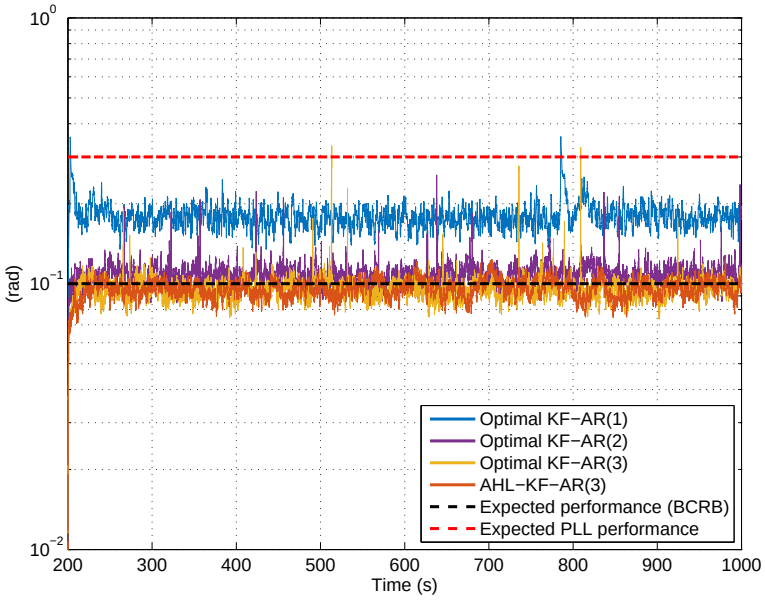

Figure 6.3: Phase RMSE of optimal KF-AR(1, 2, 3) techniques for Cornell moderate scintillation. Test scenario #1.1.

RMSE values are summarized in Table 6.4, as well as the LoL probability of each technique and the relative CPU cost. As can be observed, the KF-AR outperforming the PLL is more evident than in the case for moderate scintillation. The KF-AR(1) is able to lock to the loop and reach the BCRB in the absence of scintillation (even though after a convergence period of more than 100 seconds), whereas the equivalent 0.2-Hz PLL loses lock in all Montecarlo iterations. Increasing the PLL loop bandwidth allows the filter

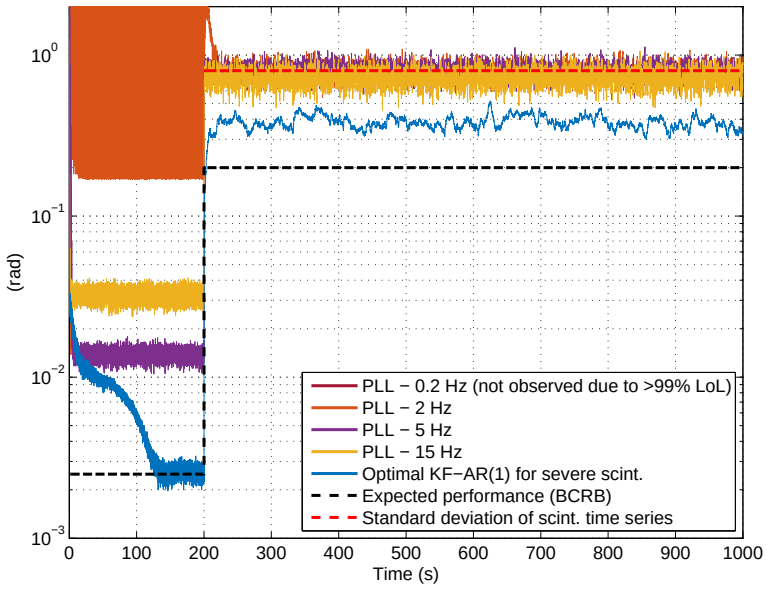

Figure 6.4: Phase RMSE of optimal KF-AR(1) for Cornell severe scintillation, versus PLL with loop bandwidths $\{0.2,\ 2,\ 5,\ 15\}$ Hz. Test scenario #1.2.

to lock with significantly smaller LoL probability, around 15-20%. However, the same conclusions as in the moderate scintillation case apply here, in the sense that the RMSE of any PLL equals the standard deviation of scintillation time series, which is around $\sigma_{\varphi_{s,\text{sev}}} = 0.8$ rad for the severe case. The KF-AR(1) clearly outperforms these results by reducing the RMSE by a factor of more than 2 with much smaller LoL probability, around 5%.

As expected, the KF-AR provides very similar performance for any AR model order p. In the simulations, this phenomenon can be observed in the previous Table 6.4, and also in Figure 6.5, which depicts the phase RMSE for the KF-AR(1, 2, 3). However, the KF-AR(p) does not reach the expected performance given by the BCRB in the presence of scintillation. This manifests a mismatch between the KF-AR configuration and the actual input measurements. In this case, such mismatch is due to the canonical fades present in the input signal; the BCRB is computed for a nominal constant C/N_0 of 45 dB-Hz, and the amplitude fades introduced by severe scintillation are not accounted for. This is when the AHL implementation introduced in Section 5.8.3 comes into play in order to palliate such amplitude fades and prevent them from affecting the KF-AR loop. In that sense, Figure 6.5 also includes the RMSE performance for the AHL-KF-AR(p). The AHL further reduces the RMSE down to 0.2 rad, allowing the KF-AR to eventually reach the BCRB. In addition, it also provides the smallest LoL probability according to

Technique	RMSE (rad)	Prob. LoL (%)	CPU (norm.)
0.2-Hz PLL	N/A	>99	0.5
2-Hz PLL	0.7959	17	
5-Hz PLL	0.7958	16	
15-Hz PLL	0.7311	15	
KF-AR(1)	0.3684	4	1
KF-AR(2)	0.3599	5	
KF-AR(3)	0.3465	4	
AHL-KF-AR(p)	0.1968	<1	1.25

Table 6.4: Performance results of PLL and KF-AR techniques for Cornell severe scintillation. Test scenario #1.2.

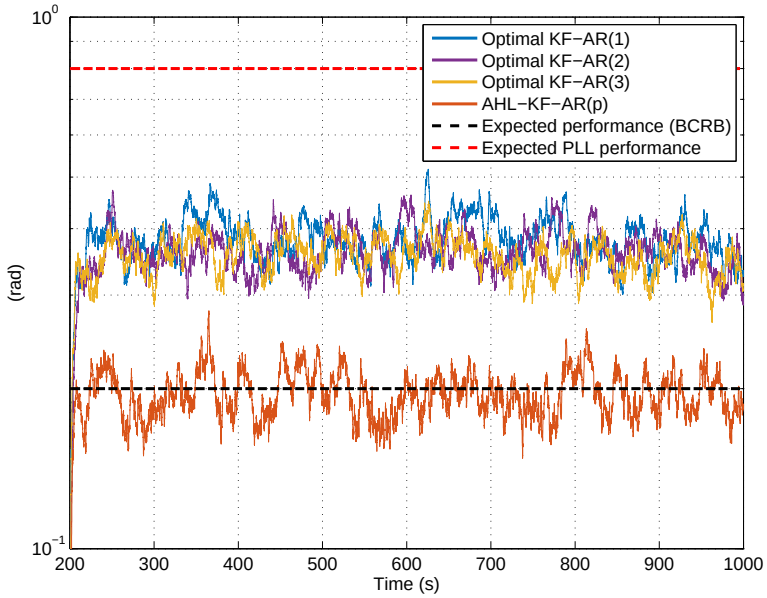

Figure 6.5: Phase RMSE of optimal KF-AR(1, 2, 3) techniques for Cornell severe scintillation. Test scenario #1.2.

Table 6.4, where no Montecarlo iteration has lost lock. Even though this comes at the expense of requiring more CPU resources due to the online estimation of the C/N_0, these results confirm the usefulness of the AHL implementation.

6.4.2 Scenarios with Time-Varying Scintillation

In this section, two scenarios will be considered in order to simulate realistic time-varying scintillation conditions:

1. Scenario #2.1 presents an initial silent period where only AWGN is present. Then, the input signal starts experiencing moderate scintillation events that last for some time, until they vanish and the signal is again scintillation-free. This is a representative scenario of a real case where scintillation suddenly appears at a given moment, and then disappears after a while. The objective here is to evaluate the ability of the adaptive KF-AR implementations to self-switch between the KF and the KF-AR.

2. Scenario #2.2 also starts with an initial silent period, before the receiver starts experiencing moderate scintillation events. Then, scintillation steps up to severe, and after some time the intensity decreases back to moderate. This scenario simulates a real case of how scintillation events evolve during the day time. There is no scintillation during the day, but it starts appearing near sunset. It gradually increases its intensity until reaching maximum activity at midnight. Then, scintillation gradually decreases its intensity again when approaching dawn. The goal of this scenario is to evaluate the robustness of the adaptive KF-AR implementations when dealing with severe scintillation.

The two test scenarios above have been selected with a twofold objective. First, to evaluate the agility of adaptive KF-AR implementations to self-configure when the working conditions change, and the ability to provide optimal performance regardless of the nature of the input signal. Second, to compare their convergence and steady-state performance to that of fixed KF-AR techniques.

6.4.2.1 Scenario #2.1. Transition from AWGN to Moderate Scintillation

For scenario #2.1, Figure 6.6 compares the RMSE performance of the adaptive and semi-adaptive KF-AR implementations (AHL-KF-A2R(p) and AHL-KF-AR(0, 1)) to the expected one given by the optimal fixed KF-AR(p) techniques. The mean steady-state RMSE and LoL probability values are summarized in Table 6.5, as well as the relative CPU cost of the different techniques. While all techniques perform similarly in terms of LoL probability, the AHL-KF-A2R(p) expectedly provides near-optimal performance, meaning that there exists some RMSE gap that prevents the performance from fully

reaching the BCRB. This phenomenon was already anticipated throughout Sections 5.8 and 5.9, where the presence of AWGN causes an underestimation of the AR(p) coefficients that leads to a divergence of $\sigma_s^2(n)$ with respect to its optimal value. In addition, the online estimation of the AR parameters significantly increases the required CPU load, rising up to 2.75 times the one needed by fixed KF-AR techniques, see Table 6.5.

Notwithstanding, the main advantage of the AHL-KF-A2R(p) is the agility and flexibility in front of time-varying working conditions. In Figure 6.6 this can be observed in the initial silent period and when switching from moderate scintillation to AWGN only, where the AHL-KF-A2R(p) readily reaches the BCRB, in contrast to the fixed implementations which may take more than 100 seconds to converge since the AR module is being forced when there is no scintillation. In contrast to the AHL-KF-A2R(p), though, fixed KF-AR techniques do provide optimal performance when scintillation is present, as they are designed for that particular situation. The KF-AR for severe scintillation also supports moderate scintillation, since its configuration only implies an increment of the KF-AR equivalent loop bandwidth. Notwithstanding, fixed techniques fail at providing optimal performance when pulled out of their design scenario, either in convergence or steady state. The clear example is the KF-AR for moderate scintillation, which is not able to reach the BCRB when scintillation is absent.

These observations give support to the AHL-KF-AR(0, 1), a technique that simply employs a carrier-dynamics-only KF (*i.e.* KF-AR(0)) and a KF-AR with fixed AR(1) model to deal with scintillation when present, and commutes between one another using the MDL as a scintillation detector. In that sense, Figure 6.6 includes the RMSE performance of the AHL-KF-AR(0, 1), while Figure 6.7 illustrates the scintillation detection over time for one Montecarlo realization, while also indicating the percentage of time the AR(0, 1) models are correctly selected throughout all Montecarlo iterations. Both figures show very promising results. As expected, the technique commutes to the KF-AR(0) when under AWGN only, and to the fixed KF-AR(1) when in the presence of scintillation, reaching the BCRB in both cases. Therefore, the AHL-KF-AR(0, 1) is able to provide optimal performance regardless of the nature of the input signal. Moreover, the agility of the AHL-KF-A2R(p) when switching between scenarios is preserved. What is more, since the MDL is employed as a scintillation detector only, the sliding window can be shortened so as to minimize the transient from moderate scintillation to AWGN only, and vice versa. By reducing the window from 5 to 2 seconds, this can actually be noticed in Figure 6.6, thus outperforming the AHL-KF-A2R(p) while considerably reducing the required CPU load down to 1.75 times the one for the fixed KF-AR, in contrast to the

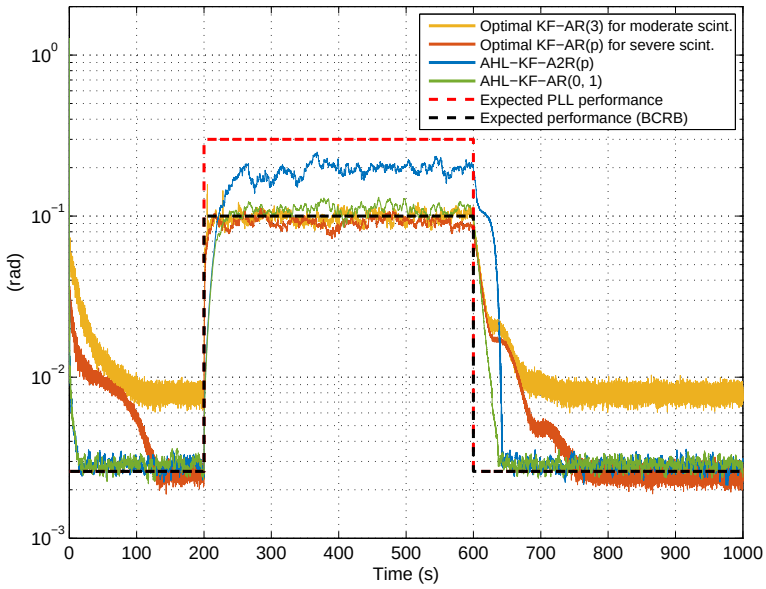

Figure 6.6: Phase RMSE of adaptive and semi-adaptive KF-AR implementations (AHL-KF-A2R(p) and AHL-KF-AR(0, 1)) versus optimal fixed KF-AR(p) techniques for time-varying scenario #2.1.

	RMSE (rad)		**LoL prob. (%)**	**CPU (norm.)**
	No scint.	Moderate		
AHL-KF-A2R(p)	$2.8 \cdot 10^{-3}$	0.1976	1	2.75
AHL-KF-AR(0, 1)	$2.8 \cdot 10^{-3}$	0.1030	<1	1.75
Opt. KF-AR(3) mod.	$8.0 \cdot 10^{-3}$	0.0989	<1	1
Opt. KF-AR(p) sev.	$2.6 \cdot 10^{-3}$	0.0951	<1	1

Table 6.5: Performance results of fixed and (semi-)adaptive KF techniques for test scenario #2.1.

AHL-KF-A2R(p) which requires 2.75 units.

These results confirm the suitability and goodness of the AHL-KF-AR(0, 1) under moderate scintillation, for which an example of three different Montecarlo realizations on the scintillation estimation is illustrated in Figure 6.8 to show how well the technique estimates moderate scintillation in the presence of carrier dynamics.

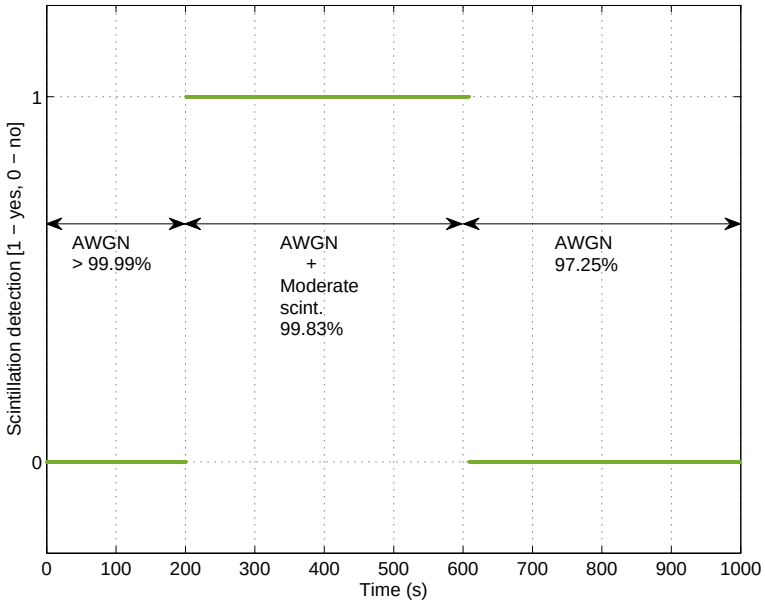

Figure 6.7: Scintillation detector of AHL-KF-AR(0, 1) as a function of time for time-varying scenario #2.1.

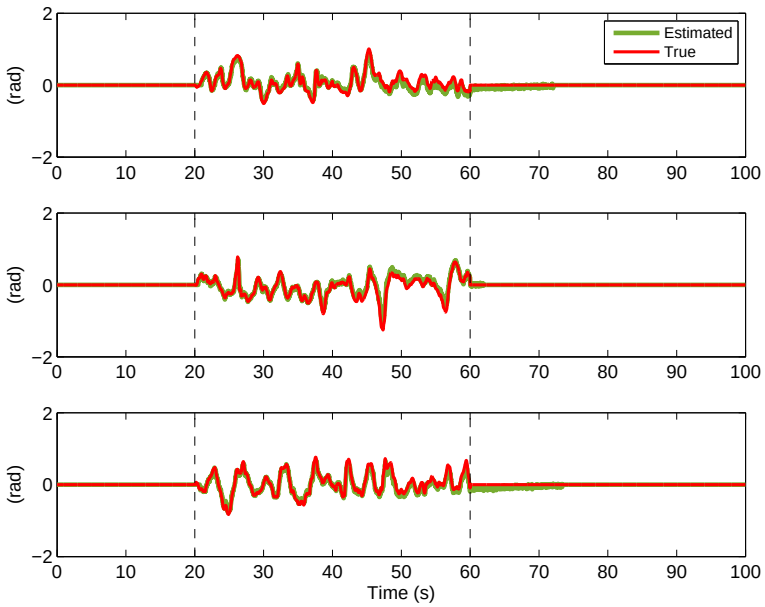

Figure 6.8: Example of three Montecarlo iterations on the estimation of scintillation provided by the AHL-KF-AR(0, 1) as a function of time for time-varying scenario #2.1.

6.4.2.2 Scenario #2.2. Transition from Moderate to Severe Scintillation

For scenario #2.2, Figure 6.9 compares the RMSE performance of the AHL-KF-A2R(p) and AHL-KF-AR(0, 1) to the expected one given by the optimal fixed KF-AR(p)

techniques. The mean steady-state RMSE and LoL probability values are summarized in Table 6.6. Similar conclusions to those from scenario #2.1 can be drawn. The AHL-KF-A2R(p) successfully selects an AR(0) during the AWGN-only initial silent period, whereas it enables the AR part features when scintillation appears. It presents good agility and flexibility when switching between scenarios, in contrast to fixed KF-AR implementations. However, whereas the latter do reach the BCRB when scintillation is present, some gap exists in the AHL-KF-A2R(p), due to the AR parameters being underestimated because of AWGN. This affects moderate scintillation in particular, where the underestimation of $\sigma_s^2(n)$ was found to be more prominent; given its lower intensity, it becomes more affected by AWGN than severe scintillation for a given C/N_0. This result is confirmed in Figure 6.6 and Table 6.5, where the RMSE degradation with respect to the BCRB is more noticeable in the moderate-scintillation regions.

As for the fixed techniques, the optimal AHL-KF-AR(p) for severe scintillation is expectedly providing optimal performance regardless of the scintillation intensity, whereas the optimal AHL-KF-AR(p) for moderate scintillation is not working properly. It presents extremely large LoL probability, around 80%, which explains the RMSE being so noisy in comparison to the rest of techniques, as a great number of Montecarlo iterations have been discarded so as not to distort the RMSE metric. As anticipated in Section 5.9, the reason for this behavior lies in such a small optimal $\sigma_s^2(n)$ for moderate scintillation leading to an equivalent loop bandwidth that is not enough to withstand severe scintillation.

Similarly to scenario #2.1, these drawbacks are overcome by the AHL-KF-AR(0, 1). As observed in Figure 6.9 and Table 6.6, it is able to provide optimal RMSE performance regardless of the nature of the input signal, with practically zero LoL probability as no Montecarlo iteration has lost lock. It successfully detects the presence of scintillation and commutes between the KF-AR(0) and KF-AR(1) as shown in Figure 6.10. In addition, it preserves (or even improves) the agility of the AHL-KF-A2R(p) with significantly lower computational cost. In view of these results, the AHL-KF-AR(0, 1) becomes the optimal technique to perform tracking in GNSS receivers when affected by ionospheric scintillation disturbances.

These results confirm the suitability and goodness of the AHL-KF-AR(0, 1) under severe scintillation, for which an example of three different Montecarlo realizations on the scintillation estimation is illustrated in Figure 6.11 to show how well the technique estimates severe scintillation in the presence of carrier dynamics.

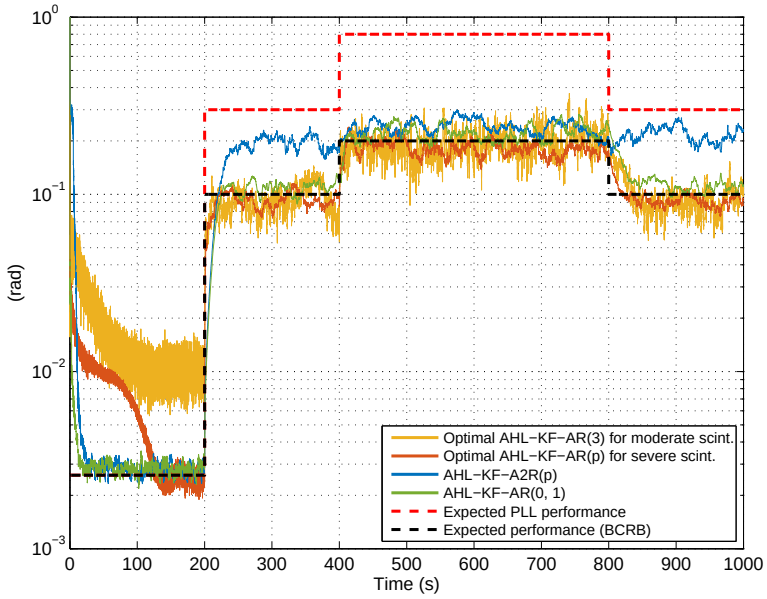

Figure 6.9: Phase RMSE of adaptive and semi-adaptive KF-AR implementations (AHL-KF-A2R(p) and AHL-KF-AR(0, 1)) versus optimal fixed KF-AR(p) techniques for time-varying scenario #2.2.

	RMSE (rad)			**LoL prob.**	**CPU**
	No scint.	Moderate	Severe	**(%)**	**(norm.)**
AHL-KF-A2R(p)	$2.8 \cdot 10^{-3}$	0.1976	0.2372	1	2.75
AHL-KF-AR(0, 1)	$2.8 \cdot 10^{-3}$	0.1030	0.2129	<1	1.75
AHL-KF-AR(3) mod.	$1.0 \cdot 10^{-2}$	0.0989	0.2053	78	1
AHL-KF-AR(p) sev.	$2.6 \cdot 10^{-3}$	0.0951	0.1908	<1	1

Table 6.6: Performance results of fixed and (semi-)adaptive KF techniques for test scenario #2.2.

6.5 KF-AR Outperformance Region over PLL

When comparing the performance of KF-AR techniques versus the conventional PLL, both implementations have to be configured with the same loop bandwidth so as to provide equal RMSE performance when only dynamics and AWGN are present. In Section 6.4.1.1, the KF-AR state-space formulation was fixed, and the PLL loop bandwidth was consistently adjusted so as to provide the same performance.

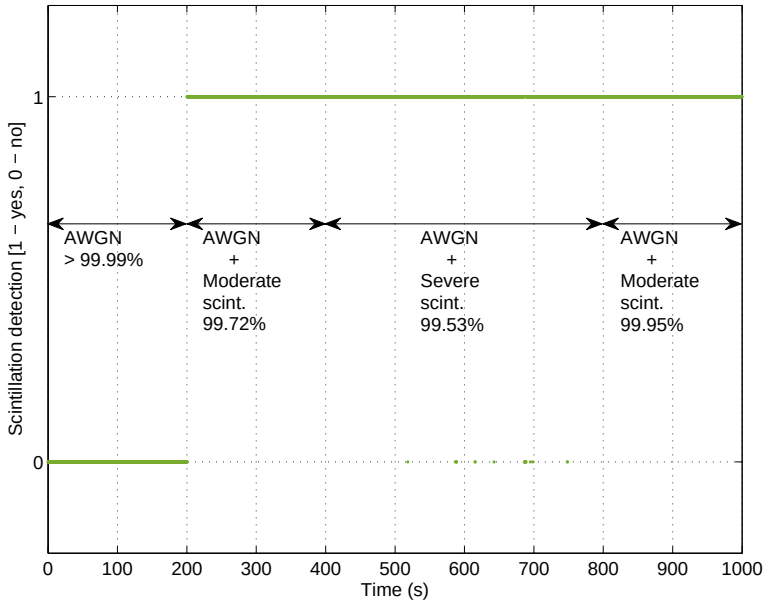

Figure 6.10: Scintillation detector of AHL-KF-AR(0, 1) as a function of time for time-varying scenario #2.2.

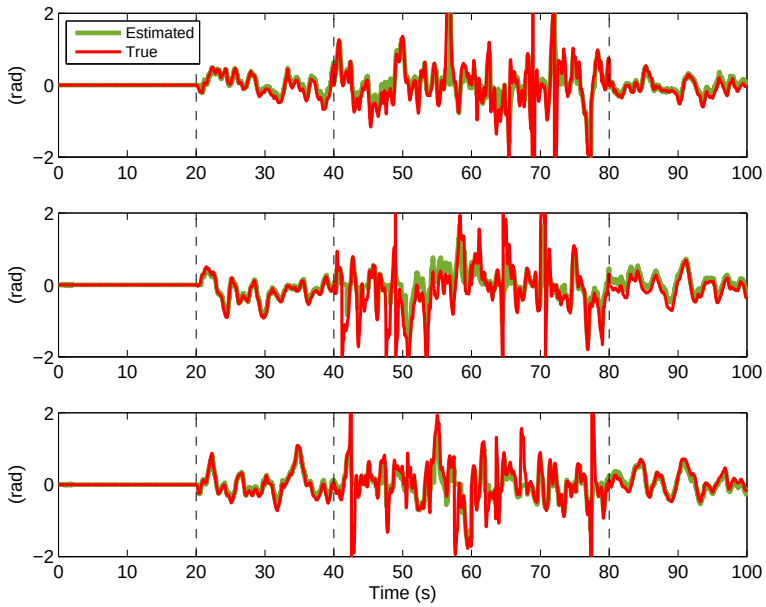

Figure 6.11: Example of three Montecarlo iterations on the estimation of scintillation provided by the AHL-KF-AR(0, 1) as a function of time for time-varying scenario #2.2.

In this section, the analysis is carried out the other way around. That is, by fixing a PLL loop bandwidth and adjusting the KF-AR equivalent one. Since this must be done when only carrier dynamics plus AWGN are present, we must focus on tuning the KF-AR equivalent loop bandwidth through the dynamics process noise variance σ_v^2. The

higher σ_v^2, the higher the bandwidth [Jwo01]. This parameter denotes thus the maximum dynamic stress that the Kalman filter can tolerate, in a similar way to when increasing the PLL loop bandwidth.

Taking for instance the 5-Hz PLL as a reference, it is found that, for the problem at hand, the AHL-KF-AR(0, 1) performs equally under carrier dynamics plus AWGN only when $\sigma_v^2 = 2 \cdot 10^{-9}$ rad^2. In that sense, Figure 6.12 compares the corresponding RMSE performance to that of the PLL when in the absence and in the presence of scintillation. Interestingly, in the latter the AHL-KF-AR(0, 1) departs from the BCRB and shows very similar performance to the 5-Hz PLL. It is found that with such a large σ_v^2, the Kalman filter prioritizes the estimation of the carrier-phase dynamics. The AR module becomes practically neglected, and the Kalman estimates scintillation phase as part of the user dynamics, thus resembling the behavior of the PLL in the previous sections.

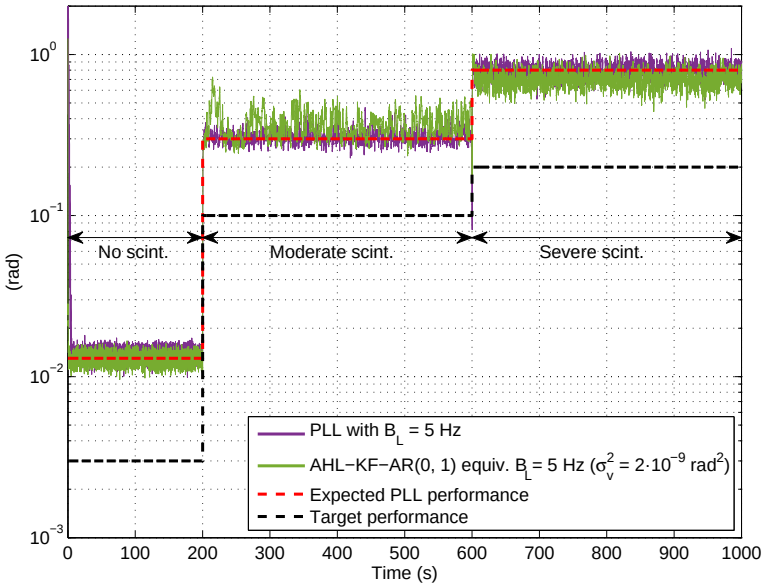

Figure 6.12: Phase RMSE performance comparison between 5-Hz PLL and AHL-KF-AR(0, 1) with the same loop bandwidth.

These observations suggest the existence of an upper bound in terms of dynamic stress beyond which the use of the AHL-KF-AR(0, 1) no longer provides a benefit over a PLL. In addition, as the loop bandwidth also plays a key role on the noise filtering capabilities, it is realistic to think that such upper bound may also vary with the C/N_0. Therefore, this section culminates with the quantification of the AHL-KF-AR(0, 1) performance limits as a function of both the C/N_0 and σ_v^2 below which the technique outperforms conventional PLLs.

6.5.1 Outperformance Region for Moderate Scintillation

Figure 6.13 shows a 3D plot of the KF-AR(0, 1) phase RMSE under moderate scintillation. The gray plane stands for the best performance that could be expected from PLLs. The performance limits are given by the curve originated when both plots intersect, see the plant view in Figure 6.14. Note that since moderate scintillation is found not to introduce major deep fades, the AHL implementation has been disabled so as to maximize the outperformance region in terms of C/N_0. As anticipated, the intersection takes place at smaller σ_v^2 when the C/N_0 decreases. The region where the KF-AR(0, 3) performance lies below the one for the PLL is bounded by a C/N_0 around 15 dB-Hz, with σ_v^2 restricted to 10^{-17} rad^2, whereas at high C/N_0 this can be relaxed up to 10^{-9} rad^2.

The values above can be translated into the maximum Doppler jerk supported by the KF-AR(0, 3) as a function of the C/N_0. With the process noise being uniformly distributed, it can be computed reverting the operation in (6.2) as follows,

$$\dddot{\theta}_{\max} = \pm \frac{\sqrt{12\sigma_v^2}}{2T_s^3} \text{ rad/s}^3. \tag{6.7}$$

Therefore, for the specifications at hand, the Doppler jerk is limited down to $\pm 7 \cdot 10^{-4}$ rad/s^3 for a C/N_0 of 15 dB-Hz, whereas under good signal conditions the KF-AR(0, 3) can support up to ± 7 rad/s^3 Doppler jerk. These values can also be expressed in pure dimensions of Doppler jerk, leading to $\pm 10^{-4}$ Hz/s^2 and ± 1 Hz/s^2, respectively.

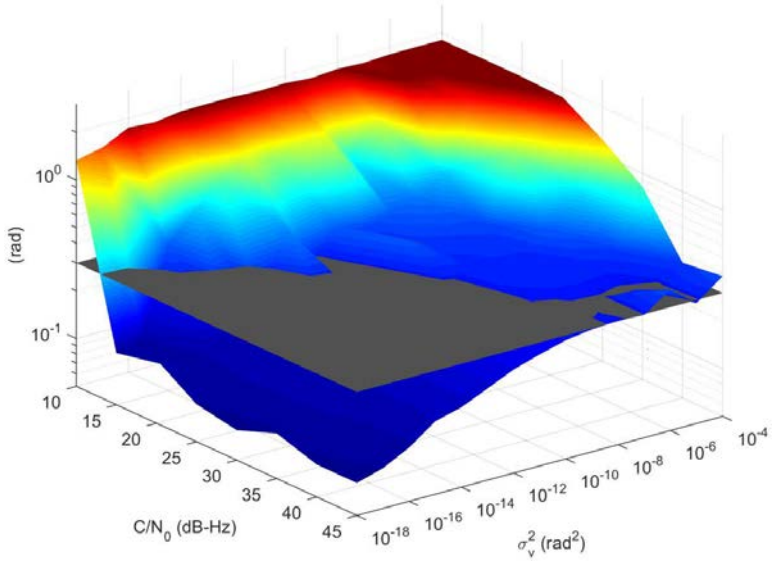

Figure 6.13: 3D plot of phase RMSE as a function of C/N_0 and σ_v^2 for Cornell moderate scintillation.

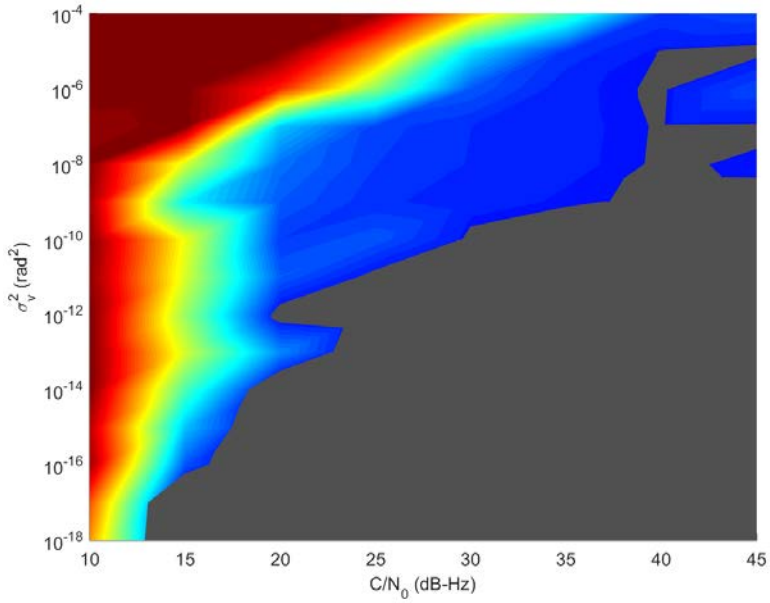

Figure 6.14: Plant view of Figure 6.13.

6.5.2 Outperformance Region for Severe Scintillation

For the case of severe scintillation, the results are shown in Figure 6.15 with the AHL implementation now enabled. The plant view is shown in Figure 6.16. The figure shows that, as expected, the AHL-KF-AR(0, 1) outperforms the PLL for a C/N_0 bounded at 25 dB-Hz, as it is the tracking threshold to which the AHL threshold γ has been set, while σ_v^2 is limited to 10^{-12} rad^2. Nonetheless, in this second analysis it must be noted that the tracking techniques are more prone to suffer from LoL owing to the stronger intensity of severe scintillation. Therefore, the LoL probability is also a constraining parameter under severe scintillation that must be taken into account. Figure 6.17 shows a 3D plot of the LoL probability for both the AHL-KF-AR(0, 1) and the PLL, and the corresponding plant view in Figure 6.17 confirms that, indeed, the LoL probability is further constraining the AHL-KF-AR(0, 1) outperformance region. More precisely, the C/N_0 is bounded to around 30 dB-Hz. Above this value, σ_v^2 is limited to 10^{-15} rad^2, which applying (6.7) corresponds to a maximum Doppler jerk of $\pm 7 \cdot 10^{-3}$ rad/s^3 $\approx \pm 10^{-3}$ Hz/s^2.

To conclude Section 6.5, the performance limits of the AHL-KF-AR(0, 1) for both moderate and severe scintillation are summarized in Table 6.7.

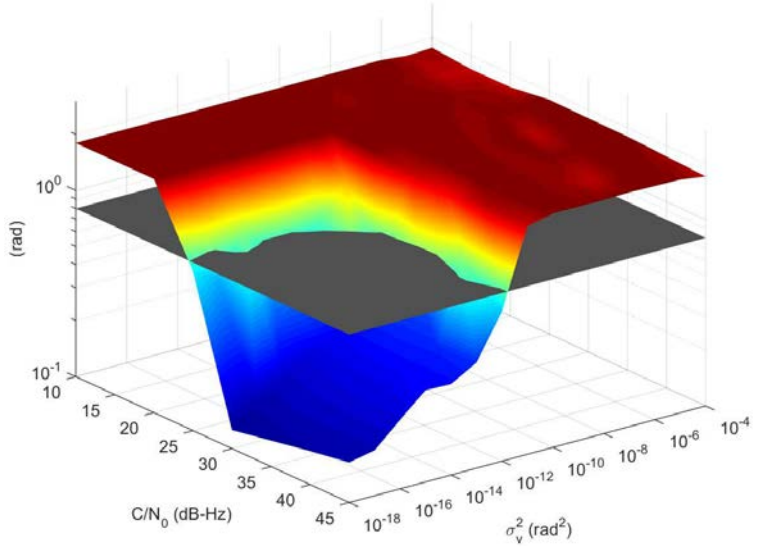

Figure 6.15: 3D plot of phase RMSE as a function of C/N_0 and σ_v^2 for Cornell severe scintillation.

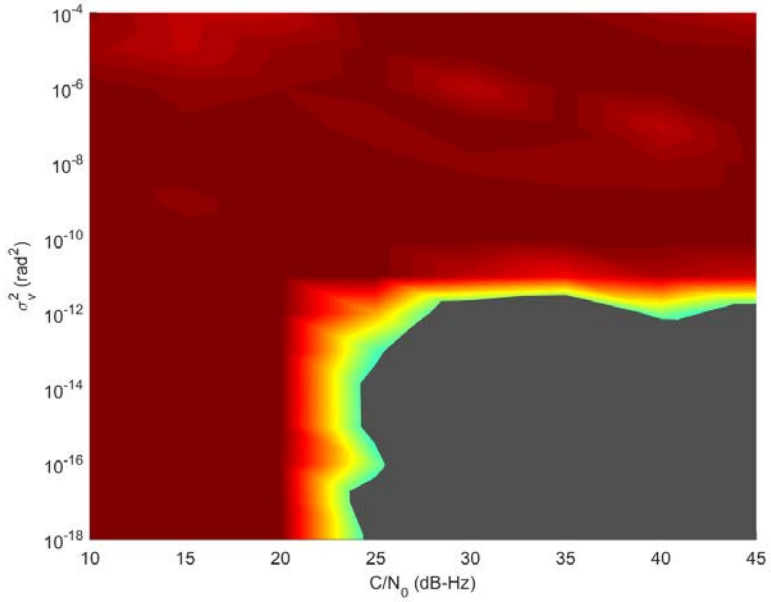

Figure 6.16: Plant view of Figure 6.15.

6.6 Results with Real Scintillation Time Series from ESA Monitoring Network

This section aims at validating the goodness and performance of KF-AR techniques obtained in the previous sections using real scintillation data. In Chapter 4 we performed an AR characterization of a representative real scintillation time series obtained from the

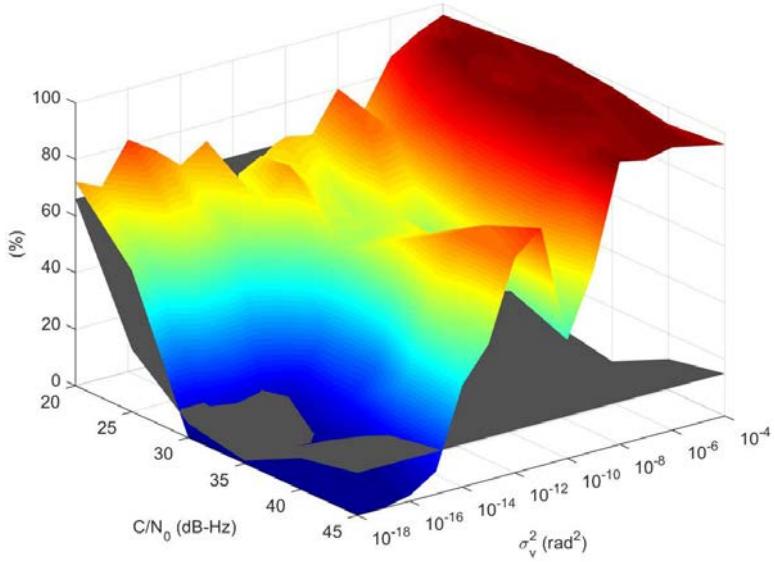

Figure 6.17: 3D plot of LoL probability as a function of C/N_0 and σ_v^2 for Cornell severe scintillation.

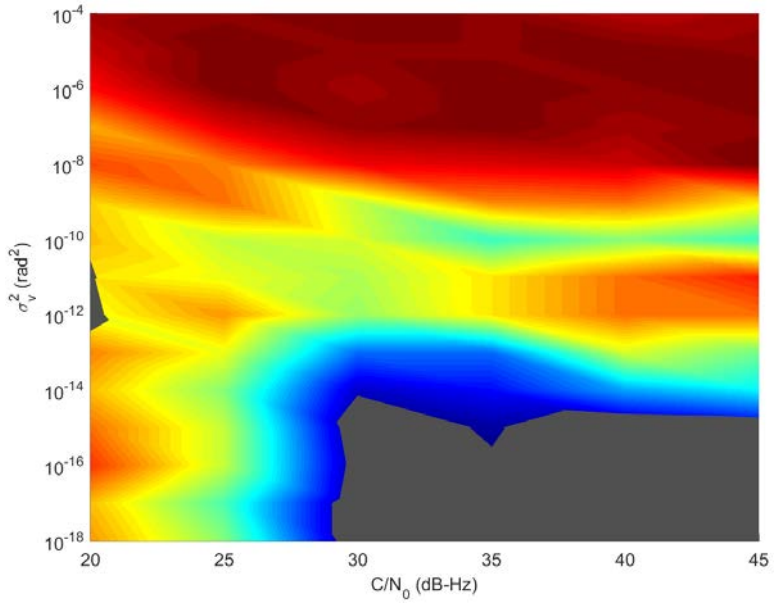

Figure 6.18: Plant view of Figure 6.17.

ESA scintillation monitoring network. That is, the DAK2.2014.335.22.GPS24 capture obtained from the station in Dakar on December 1st, 2014, from 22:00 to 23:00 hours, for GPS SV #24. In the sequel, we will employ the same capture.

Figure 6.19 shows the RMSE performance of the adaptive KF-AR implementations, which is compared to the expected one for fixed KF-AR techniques employing the op-

Moderate scintillation			**Severe scintillation**		
C/N_0 (dB-Hz)	$\dddot{\theta}_{\max}$ (rad/s^3)	$\ddot{\theta}_{\max}$ (Hz/s^2)	C/N_0 (dB-Hz)	$\dddot{\theta}_{\max}$ (rad/s^3)	$\ddot{\theta}_{\max}$ (Hz/s^2)
15	$\pm 7 \cdot 10^{-4}$	$\pm 10^{-4}$	25-30	$\pm 7 \cdot 10^{-3}$	$\pm 10^{-3}$
45	± 7	± 1			

Table 6.7: Summary of AHL-KF-AR(0, 1) performance limits.

timal AR parameters obtained in Table 4.2. In addition, the mean steady-state RMSE and LoL probability values are summarized in Table 6.8. As observed, all techniques present close-to-zero LoL probability (*i.e.* no Montecarlo iteration has lost lock), while also outperforming the RMSE performance that would be obtained with a conventional PLL, which is also depicted in Figure 6.19. As previously stated, the PLL RMSE equals the standard deviation of the scintillation time series under study.

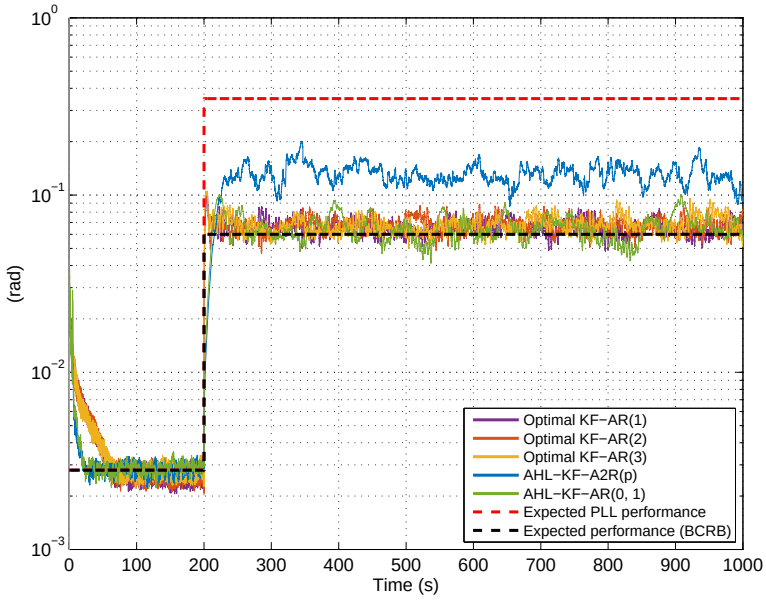

Figure 6.19: Phase RMSE of adaptive and semi-adaptive KF-AR implementations (AHL-KF-A2R(p) and AHL-KF-AR(0, 1)) versus optimal fixed KF-AR(p) techniques for DAK2.2014.335.22.GPS24 real scintillation time series.

As expected, the optimal fixed techniques provide practically equal performance, and are able to fully reach the expected one given by the BCRB, both in the presence of AWGN only and added scintillation. In the former, though, fixed techniques require a large transient. As already seen, this is the penalty incurred by forcing a fixed AR module in the Kalman filter when in the absence of scintillation. This is overcome by the use of

	RMSE (rad)		**LoL prob. (%)**
	No scint.	DAK2.2014.335.22.GPS24	
Optimal KF-AR(1)	$2.6 \cdot 10^{-3}$	$6.5 \cdot 10^{-2}$	<1
Optimal KF-AR(2)	$2.7 \cdot 10^{-3}$	$6.8 \cdot 10^{-2}$	<1
Optimal KF-AR(3)	$2.7 \cdot 10^{-3}$	$6.7 \cdot 10^{-2}$	<1
AHL-KF-A2R(p)	$2.8 \cdot 10^{-3}$	$1.3 \cdot 10^{-1}$	<1
AHL-KF-AR(0, 1)	$2.8 \cdot 10^{-3}$	$6.4 \cdot 10^{-2}$	<1

Table 6.8: Performance results of fixed and (semi-)adaptive KF techniques for DAK2.2014.335.22.GPS24 real scintillation time series.

the AHL-KF-A2R(p), which rapidly detects the absence of scintillation and thus disables the AR module thanks to its enhanced agility. Notwithstanding, the presence of AWGN hampers the optimal estimation of the AR parameters, which are online-estimated for each time instant. Such an underestimation eventually leads to the RMSE performance being degraded by a factor of 2 with respect to the optimal one, as can be noticed in Figure 6.19.

In view of these inconvenients, the AHL-KF-AR(0, 1) comes into play. As in previous sections, it is able to fully reach the BCRB when both in the absence and in the presence of scintillation, thus providing optimal performance regardless of the working conditions. The fixed non-AHL techniques reaching the BCRB manifest that the AHL could be disabled in this simulation. This is explained by the fact that the fades introduced by the scintillation in the DAK2.2014.335.22.GPS24 capture are not major, and resemble those for moderate scintillation. Such fades become visible in Figure 6.20 where, for a nominal C/N_0 of 45 dB-Hz, the estimated C/N_0 is mainly above the AHL threshold, with only very few punctual time instants in different Montecarlo iterations exceeding such threshold. Even so, the AHL implementation is recommended to remain enabled in order to ensure optimal and robust KF-AR operation in front of the possibility of stronger scintillation activity.

On the other hand, the AHL-KF-AR(0, 1) preserves the agility of the AHL-KF-A2R(p) in front of scenario variations since it successfully detects whether scintillation is present or not. This is depicted in Figure 6.21, which shows the scintillation detection over time, indicating the percentage of time either AR(0) or AR(1) are correctly selected throughout all Montecarlo iterations. These observations are similar to those in Section 6.4.2 for

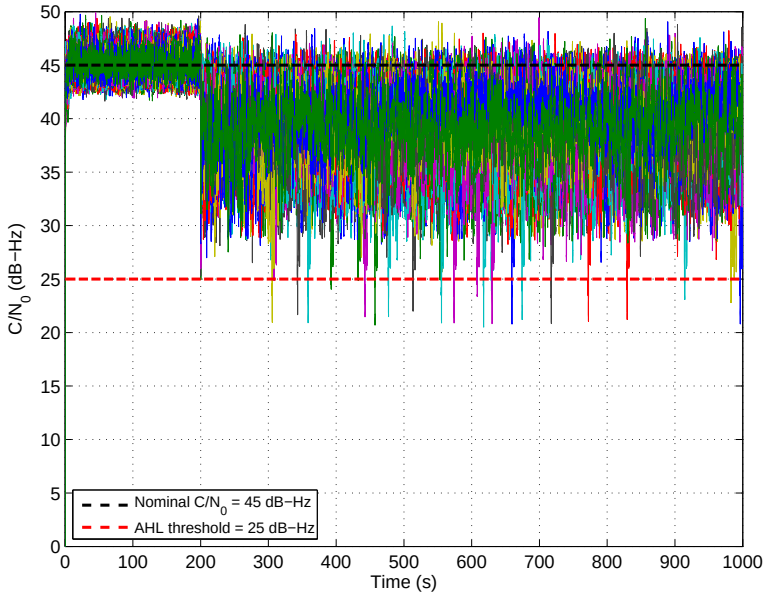

Figure 6.20: Estimated C/N_0 by AHL-KF-AR(0, 1) for all Montecarlo iterations using DAK2.2014.335.22.GPS24 real scintillation time series.

synthetic time-varying scintillation and confirm the goodness of the AHL-KF-AR(0, 1) technique.

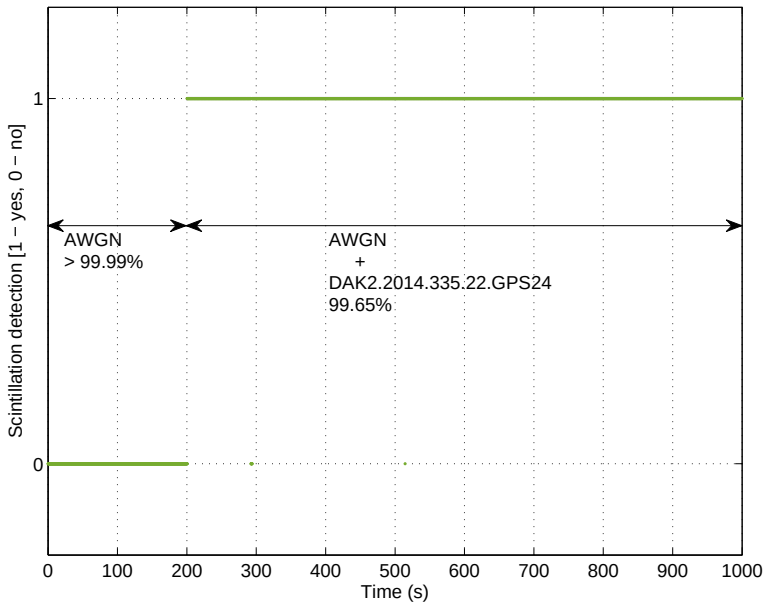

Figure 6.21: Scintillation detector of AHL-KF-AR(0, 1) as a function of time for DAK2.2014.335.22.GPS24 real scintillation time series.

Figure 6.22 shows an example of three different Montecarlo realizations on the estimation of scintillation provided by the AHL-KF-AR(0, 1) technique, and shows how well

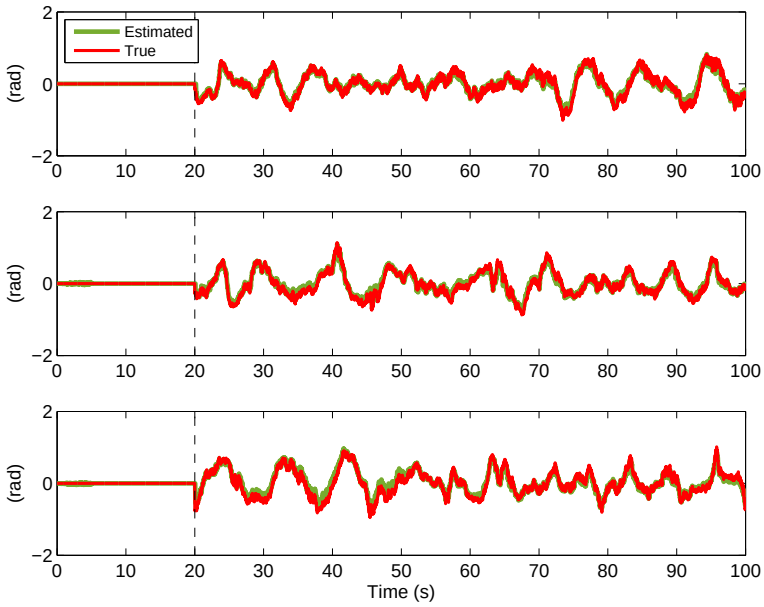

Figure 6.22: Example of three Montecarlo iterations on the estimation of scintillation provided by the AHL-KF-AR(0, 1) as a function of time for DAK2.2014.335.22.GPS24 real scintillation time series.

it can estimate real scintillation when in the presence of carrier dynamics.

6.7 Conclusions

In this chapter, an extensive simulation campaign to test the KF-AR techniques has been carried out, and the performance of KF-AR techniques has been compared to that of conventional PLLs. A first set of simulations using synthetic Cornell scintillation under stationary conditions has been performed using fixed techniques. The results have shown that, even though the KF-AR incurs into a higher computational load, it clearly outperforms the conventional PLL, particularly under severe scintillation. The PLL estimates carrier dynamics and scintillation phase variations as a whole, whereas the KF-AR dissociates between both components as desired. For moderate scintillation, the importance of employing high-order AR processes has been confirmed, reaching the expected RMSE performance given by the BCRB. The same conclusion applies for severe scintillation in regard to the AHL implementation, showing no loss-of-lock in any Montecarlo realization, even though at the expense of requiring more CPU resources.

Then, a set of simulations considering realistic time-varying scintillation conditions

has been performed to test the adaptive KF-AR implementations and compare their performance to that of fixed techniques. Both of them actually have advantages and inconvenients that complement with one another. The AHL-KF-A2R(p) presents the best agility in front of scintillation variations, rapidly adapting to the actual working conditions and disabling the Kalman AR module when scintillation disappears. However, the technique has been found not to fully reach the BCRB when in the presence of scintillation. This is explained by an underestimation of the optimal AR parameters owing to the presence of AWGN. In addition, it also incurs into a high computational burden. On the contrary, the fixed KF-AR(p) is able to reach the BCRB when dealing with scintillation as it is the scenario for which it has been conceived, while also presenting the smallest computational cost. However, it fails at providing optimal performance when pulled out of its design operation, requiring large transients to converge under AWGN only due to the unnecessary AR module being forced.

In this sense, the AHL-KF-AR(0, 3) has been found to perform as a hybrid implementation that combines the best of the fixed KF-AR(p) and the AHL-KF-A2R(p). It uses the MDL criterion as a simple scintillation detector that commutes between a non-AR Kalman filter and a fixed AHL-KF-AR(1) that can deal with both moderate and severe scintillation. The technique successfully adapts to the actual working conditions and provides optimal RMSE and LoL probability performance irrespective of the nature of the input signal. Furthermore, it preserves the agility of the AHL-KF-A2R(p) and operates at a significantly reduced computational cost. Then, the advantageous operational region of the AHL-KF-AR(0, 1) with respect to that of the conventional PLL has been determined. That is, the region in terms of maximum dynamic stress and noise power within which the AHL-KF-AR(0, 1) outperforms the PLL has been quantified. As expected, the operational region has been found smaller under severe scintillation owing to its stronger intensity.

Finally, the KF-AR techniques have been tested using a representative capture of real scintillation time series in order to validate the results obtained for synthetic data. The conclusions above have been confirmed, where fixed techniques provide optimal performance when in the presence of scintillation, whereas the AHL-KF-A2R(p) presents the best agility at the expense of a degraded RMSE performance and enhanced computational cost. The AHL-KF-AR(0, 1) has been found to overcome the issues of each of the above implementations, providing the best performance and agility with a significantly reduced computational complexity. These conclusions confirm the goodness of the AHL-KF-AR(0, 1) implementation.

Chapter 7

Thesis Conclusions and Future Work

This thesis has tackled the problem of robust carrier phase tracking with the aim of overcoming the technological challenges to be faced by next-generation GNSS receivers. The focus has been placed on the effect of ionospheric scintillation, which introduces random amplitude and phase variations to GNSS signals crossing the ionosphere and poses a serious concern to carrier dynamics tracking. To deal with ionospheric scintillation, a detailed analysis on modeling scintillation phase variations using autoregressive processes has been first carried out. The conclusions have led to proposing the hybrid autoregressive Kalman filter, a promising approach consisting of a linear Kalman filter with a novel hybrid formulation that allows tracking scintillation and virtually eliminating it, thus providing clean estimates of the carrier dynamics of interest. In this sense, several adaptive implementations have been proposed in order to deal with the time-varying behavior of scintillation and provide optimal estimation performance irrespective of the nature of the input measurements. Such adaptive implementations include a hard-limiting technique based on the measured signal power that is thought to provide an added robustness in front of the signal amplitude fades introduced by scintillation. In addition, this thesis has also contributed with the derivation of closed-form expressions for the performance characterization of non-hybrid and hybrid Kalman filters. This has arisen from the lack of a closed-form solution for the Bayesian Cramér-Rao bound, thus hampering the tuning of the Kalman filter. The obtained derivations include results for both the transient and steady-state regimes of the filter, and are thought to be a tool of great practical interest during the design stage of the problem.

The main conclusions of this work are drawn next, as well as some possible future research lines are also proposed.

7.1 Thesis Conclusions

Chapter 2 has introduced the fundamentals of GNSS technologies. The GNSS trilateration positioning principle has been presented, and the generic architecture of GNSS receivers has been explained. It consists mainly of the front end, acquisition, tracking and PVT stages. In the latter, some guidelines for multi-constellation hybridization in high-sensitivity receivers have been provided, mainly consisting in determining the user's position without having to decode the navigation message. As a matter of fact, this is related to the tasks performed by the author during his research stay at ESTEC. This chapter has though provided a more detailed description of the tracking stage, since it is the main scope of this dissertation. The well-known phase- and delay-locked loops have been presented as the solutions adopted by conventional GNSS receivers.

In Chapter 3 the problem of GNSS carrier tracking has been revisited by making use of the general framework of optimal minimum mean squared error estimation. In that sense, the Kalman filter has been presented as the natural improvement to conventional phase-locked loops to perform precise carrier tracking in the presence of propagation disturbances. The basic notions of the Kalman filter have been explained, and the formulation has then been particularized to the problem of GNSS carrier tracking. Some useful guidelines for the tuning of the filter have also been provided. At this point, this thesis has contributed with the derivation of novel closed-form expressions for the Bayesian Cramér-Rao bound: an upper bound for the convergence time and a lower bound for the steady-state performance of kinematic Kalman filters. To this end, the BCRB has been presented as a tool of practical interest to predict the Kalman filter performance, linking it to the classical Cramér-Rao bound when in the absence of process noise. The proposed approach has been based on reformulating the filtering problem in batch mode and analyzing the resulting matrices when a diffuse initialization of the filter is considered. A set of simulation results has been provided that confirms the applicability of the proposed approach.

Chapter 4 has tackled the characterization of scintillation disturbances, particularly the random phase variations. The class of autoregressive processes has been proposed, and the problem of autoregressive fitting has been addressed. Two equivalent approaches for the determination of the model parameters have been introduced, namely the Yule-Walker equations and the Least Squares method, the latter presenting slightly smaller computational load. The fitting of autoregressive processes has been carried out by means of two different types of scintillation time series. On the one hand, synthetic data using the

Cornell scintillation model. On the other hand, real scintillation data obtained from ESA's scintillation monitoring network, for which a detrending algorithm has been explained. The main outcome here is the confirmation that scintillation phase variations can actually be modeled using autoregressive processes. For strong scintillation events, a simple first-order model suffices, whereas higher-order models have been found to better fit events that are more correlated. In view of these conclusions, the problem of optimal model order selection has been addressed. A literature review on the most commonly used criteria has been provided, with the advantages and drawbacks of each of them. Then, the minimum description length criterion has been presented as the chosen one in this thesis, since it is a consistent criterion that reduces its estimation error as the length of the employed data record increases. The above synthetic and real scintillation time series have been employed to test the order selection, and the obtained results have confirmed those for the problem of scintillation autoregressive fitting.

Chapter 4 has led to interesting conclusions, in the sense that the modeling of scintillation phase variations using a linear Gaussian process has opened the door to encompassing them within the linear Kalman filter in a natural manner, and take advantage of its Gaussianity optimality properties. This has been the main goal of Chapter 5: to formulate an augmented Kalman filter with a novel hybrid formulation to track dynamics and scintillation separately, in the presence of one another. The underlying idea of this approach is to estimate scintillation phase variations so that they can be virtually removed and clean estimates of the carrier dynamics can be provided. The proposed technique has been termed hybrid autoregressive Kalman filter, KF-AR(p). An analysis of the Bayesian Cramér-Rao bound for this technique has been carried out, concluding that the scintillation power above the noise floor induces a slight performance degradation in the carrier dynamics estimates caused by the possible errors in the estimation of scintillation. Here, this thesis has contributed with the derivation of novel closed-form expressions for the convergence time and steady-state performances of hybrid and pure autoregressive Kalman filters. A set of simulation results has been provided that confirms the applicability of the proposed approach. Then, in this chapter we have made a leap forward to dealing with the time-varying nature of scintillation: we have proposed adaptive implementations in order for the KF-AR to nimbly self-tune to the actual scintillation conditions and provide optimal performance in time-varying scenarios. First, the fully-adaptive implementation AHL-KF-A2R(p) has consisted of an online estimator of the autoregressive model parameters and order. At this point we have also considered the presence of thermal noise, as an approach to realistic working conditions. After some analysis it has been found that thermal noise causes the input signal to depart from an autoregressive process, partic-

ularly under moderate scintillation. Therefore, we have derived an adaptive technique thought to be agile and flexible in front of time-varying working conditions, even though at the expense of some performance degradation owing to the underestimation of autoregressive parameters. To circumvent this drawback, we have derived the semi-adaptive approach AHL-KF-AR(0, 1) that employs a first-order autoregressive process with fixed parameters designed to deal with any kind of scintillation intensity. Moreover, the MDL criterion has been employed as a mere scintillation detector with the ability to commute to a dynamics-only Kalman filter when scintillation is absent. This semi-adaptive technique has been thought to provide optimal performance while preserving the agility of the fully-adaptive approach at a significantly reduced computational cost. In addition, a hard-limiting threshold has been also implemented in order to deal with the nonlinear signal amplitude fades introduced by severe scintillation, particularly, thus providing an added degree of robustness to the KF-AR.

In Chapter 6 the KF-AR techniques proposed in Chapter 5 have been tested by means of an extensive simulation campaign. Very promising results have been obtained, with the proposed approaches clearly outperforming conventional PLLs. The hard-limiting threshold has been found to provide an additional gain particularly under the presence of severe scintillation, reaching the expected performance given by the BCRB. In time-varying scenarios, fixed KF-AR techniques have failed at providing optimal performance. In this sense, the AHL-KF-A2R(p) has shown to be fully agile when the working conditions change, even though at the expense of some performance degradation in the presence of scintillation and significant computational cost. The AHL-KF-AR(0, 1) has shown to successfully overcome these limitations while preserving the agility of the AHL-KF-A2R(p). This chapter has also contributed with the determination of the limits in terms of thermal noise and input dynamic stress below which the proposed technique does provide a gain over conventional PLLs. These bounds are thought to become useful guidelines for the application of the AHL-KF-AR(0, 1) in practice. The results obtained with Cornell synthetic data have been validated by processing real data measurements. Therefore, we can conclude on the goodness and applicability of the proposed AHL-KF-AR(0, 1) for next-generation GNSS receivers to obtain accurate carrier phase estimates in the presence of scintillation disturbances.

7.2 Future Research Lines

From the work presented in this dissertation, the following future research lines can be derived:

- Research on the accurate estimation of autoregressive parameters in the presence of AWGN. In the AHL-KF-AR(0, 1), a large loop bandwidth is employed to cope with up to severe scintillation, thus limiting the operational range of the technique under moderate scintillation, particularly. By properly estimating the AR parameters in the AHL-KF-A2R(p), a smaller loop bandwidth could be employed, thus improving the noise filtering capabilities, and the maximum dynamic stress may be expected to increase at low C/N_0. Some of the baseline techniques that can be found in the literature are the unbiased least squares method, the modified Yule-Walker equations and the use of two interacting Kalman filters.

- Extend the problem to the arena of multi-frequency GNSS receivers, and evaluate the proposed techniques for the case of multi-frequency carrier phase measurements.

- Evaluate the gain of determining scintillation amplitude variations by means of a tracking stage, as done herein with the carrier phase, and employ an extended Kalman filter (EKF) for tracking both amplitude and phase.

- Evaluate whether the parameters $\{S_4, \sigma_{\varphi_s}\}$ can be exploited to extract additional information; for instance, use S_4 as an indicator on the presence of scintillation.

- Perform a thorough analysis on scintillation phase fitting using more complex signal models, such as autoregressive integrated moving average (ARIMA) and ARMA.

Bibliography

[Aar82] J. Aarons, "Global Morphology of Ionospheric Scintillations", *Proceedings of the IEEE*, Vol. 70, nº 4, pags. 360–378, April 1982.

[Aka74] H. Akaike, "A New Look at the Statistical Model Identification", *IEEE Transactions on Automatic Control*, Vol. 19, nº 6, pags. 716–723, December 1974.

[Ako02] D. Akopian, J. Syrjarinne, "A network aided iterated LS method for GPS positioning and time recovery without navigation message decoding", *2002 IEEE Position Location and Navigation Symposium*, pags. 77–84, April 2002.

[Ako09] D. Akopian, J. Syrjarinne, "A Fast Positioning Method Without Navigation Data Decoding for Assisted GPS Receivers", *IEEE Transactions on Vehicular Technology*, Vol. 58, nº 8, pags. 4640–4645, Oct 2009.

[Alb14] Brian Albright, *Essentials of mathematical statistics*, Jones & Bartlett Learning, 2014.

[Ban85] S. Bancroft, "An Algebraic Solution of the GPS Equations", *IEEE Transactions on Aerospace and Electronic Systems*, Vol. AES-21, nº 1, pags. 56–59, Jan 1985.

[Bar04] Y. Bar-Shalom, X. R. Li, T Kirubarajan, *Estimation with Applications to Tracking and Navigation: Theory Algorithms and Software*, John Wiley & Sons, 2004.

[Bay08] S. Bay, C. Herzet, J. M. Brossier, J. P. Barbot, B. Geller, "Analytic and asymptotic analysis of Bayesian Cramér-Rao bound for dynamical phase offset estimation", *IEEE Trans. Signal Process.*, Vol. 56, nº 1, pags. 61–70, Jan 2008.

[Bra16] S. Braun, E. A. P. Habets, "Online Dereverberation for Dynamic Scenarios Using a Kalman Filter With an Autoregressive Model", *IEEE Signal Process. Lett.*, Vol. 23, nº 12, pags. 1741–1745, Dec 2016.

[Bur06] A. Burian, E. S. Lohan, M. Renfors, "BPSK-like Methods for Hybrid-Search Acquisition of Galileo Signals", *2006 IEEE International Conference on Communications*, Vol. 11, pags. 5211–5216, June 2006.

[Cas80] F. R. Castella, "An Adaptive Two-Dimensional Kalman Tracking Filter", *IEEE Transactions on Aerospace and Electronic Systems*, Vol. AES-16, nº 6, pags. 822–829, Nov 1980.

[Cav97] Joseph E Cavanaugh, *et al.*, "Unifying the Derivations for the Akaike and Corrected Akaike Information Criteria", *Statistics & Probability Letters*, Vol. 33, nº 2, pags. 201–208, 1997.

[Cha02] F. Chapeau-Blondeau, A. Monir, "Numerical Evaluation of the Lambert W Function and Application to Generation of Generalized Gaussian Noise with Exponent 1/2", *IEEE Trans. Signal Process.*, Vol. 50, nº 9, pags. 2160–2165, Sept 2002.

[Che04] Wei Chen, Ruifeng Zhang, "Kalman-Filter Channel Estimator for OFDM Systems in Time and Frequency-Selective Fading Environment", *Proc. Int. Conf. on Acoustics, Speech, and Signal Processing (ICASSP)*, Vol. 4, pags. 377–380, May 2004.

[Cla93] H. J. Clayton, P. Fines, A. H. Aghvami, "Kalman algorithm frequency estimator for dynamic Doppler shift environments", *Electronics Letters*, Vol. 29, nº 7, pags. 597–598, April 1993.

[Cur12] J. T. Curran, G. Lachapelle, C. C. Murphy, "Improving the Design of Frequency Lock Loops for GNSS Receivers", *IEEE Transactions on Aerospace and Electronic Systems*, Vol. 48, nº 1, pags. 850–868, Jan 2012.

[De-11] P. F. De-Bakker, "Modeling Pseudo Range Multipath as an Autoregressive Process", *Proceedings of the 24th International Technical Meeting of The Satellite Division of the Institute of Navigation (ION GNSS)*, pags. 1737–1750, 2011.

[Del10] J. A. Del Peral-Rosado, J. A. López-Salcedo, G. Seco-Granados, J. M. López-Almansa, J. Cosmen, "Kalman filter-based architecture for robust and high-sensitivity tracking in GNSS receivers", *2010 5th ESA Workshop on Satellite Navigation Technologies and European Workshop on GNSS Signals and Signal Processing (NAVITEC)*, pags. 1–8, Dec 2010.

[Des12] K. B. Deshpande, G. S. Bust, C. R. Clauer, H. Kim, J. E. Macon, T. E. Humphreys, J. A. Bhatti, S. B. Musko, G. Crowley, A. T. Weatherwax, "Initial GPS Scintillation Results from CASES Receiver at South Pole, Antarctica", *Radio Science*, Vol. 47, nº 5, pags. 1–10, Oct 2012.

[Dju99] P. M. Djuric, S. M. Kay, K. M. Vijay, B. W. Douglas, "Spectrum Estimation and Modeling", *Digital Signal Processing Handbook, CRC Press*, 1999.

[Dub06] Smita Dubey, Rashmi Wahi, A. K. Gwal, "Ionospheric effects on GPS positioning", *Advances in Space Research*, Vol. 38, nº 11, pags. 2478–2484, 2006.

[Ege15] Daniel Egea-Roca, Gonzalo Seco-Granados, José A. López-Salcedo, F. Dovis, "Signal-level integrity and metrics based on the application of quickest detection theory to multipath detection", *Proceedings of the 28th International Technical Meeting of the Satellite Division of the Institute of Navigation (ION GNSS+ 2015), Tampa, FL, USA*, pags. 2926–2938, 2015.

[Ege17] Daniel Egea-Roca, Gonzalo Seco-Granados, José A. López-Salcedo, "Comprehensive overview of quickest detection theory and its application to GNSS threat detection", *Gyroscopy and Navigation*, Vol. 8, nº 1, pags. 1–14, 2017.

[ESA11a] ESA, "BeiDou General Introduction", `https://gssc.esa.int/navipedia`, 2011, accessed 01 Feb 2019.

[ESA11b] ESA, "Front End", `https://gssc.esa.int/navipedia`, 2011, accessed 04 May 2019.

[ESA11c] ESA, "GLONASS General Introduction", `https://gssc.esa.int/navipedia`, 2011, accessed 01 Feb 2019.

[ESA17] ESA, "What is Galileo?", `https://www.esa.int/Our_Activities`, 2017, accessed 01 Feb 2019.

[Fin99] P. Fine, W. Wilson, "Tracking algorithm for GPS offset carrier signals", *Proceeding of ION National Technical Meeting, 1999*, pags. 671–676, San Diego, CA, 1999.

[Foh18] F. Fohlmeister, F. Antreich, J. A. Nossek, "Dual Kalman filtering based GNSS phase tracking for scintillation mitigation", *2018 IEEE/ION Position, Location and Navigation Symposium (PLANS)*, pags. 1151–1158, April 2018.

[For02] B. Forte, S. M. Radicella, "Problems in Data Treatment for Ionospheric Scintillation Measurements", *Radio Science*, Vol. 37, nº 6, pags. 1–5, Dec 2002.

[For08] Borje Forssell, *Radionavigation Systems*, GNSS Technology and Applications, 2008.

[Fre96] G. T. French, *Understanding the GPS: An Introduction to the Global Positioning System: what it is and how it works*, GeoResearch, 1996.

[Gó16] D. Gómez-Casco, J. A. López-Salcedo, G. Seco-Granados, "Generalized Integration Techniques for High-Sensitivity GNSS Receivers Affected by Oscillator Phase Noise", *2016 IEEE Statistical Signal Processing Workshop (SSP)*, pags. 1–5, June 2016.

[Gó18] David Gómez-Casco, *Non-coherent acquisition techniques for high-sensitivity GNSS receivers, PhD dissertation*, PhD Thesis, Universitat Autònoma de Barcelona (UAB), 2018.

[Gal13] M. N. Gallardo, G. S. Granados, G. L. Risueño, M. Crisci, "Code smoothing for BOC ambiguity mitigation", *2013 International Conference on Localization and GNSS (ICL-GNSS)*, pags. 1–6, June 2013.

[Gar14] J. A. García-Molina, M. Navarro-Gallardo, G. Lopez-Risueño, M. Crisci, "Unambiguous tracking of high-order BOC signals in urban environments: Channel considerations", *2014 7th ESA Workshop on Satellite Navigation Technologies and European Workshop on GNSS Signals and Signal Processing (NAVITEC)*, pags. 1–6, Dec 2014.

[Gar15] J. A. Garcia-Molina, M. Navarro-Gallardo, G. Lopez-Risueño, M. Crisci, "Robust unambiguous tracking of high-order BOC Signals: a multi-Correlator approach", *ION GNSS*, pags. 1–6, 2015.

[Gop84] M. Gopal, *Modern Control System Theory*, Wiley Eastern Ltd., 1984.

[GSA17] European GNSS Agency GSA, "GNSS Market Report, Issue 5", 2017.

[Hae89] R. Haeb, H. Meyr, "A systematic approach to carrier recovery and detection of digitally phase modulated signals of fading channels", *IEEE Transactions on Communications*, Vol. 37, nº 7, pags. 748–754, July 1989.

[Ham83] F. M. Ham, R. G. Brown, "Observability, eigenvalues, and Kalman filtering", *IEEE Trans. Aerosp. Electron. Syst.*, Vol. AES-19, nº 2, pags. 269–273, March 1983.

[Heg01] C. Hegarty, M. B. El-Arini, T. Kim, S. Ericson, "Scintillation Modeling for GPS-Wide Area Augmentation System Receivers", *Radio Science*, Vol. 36, nº 5, pags. 1221–1231, Sept 2001.

[Hen08] E. Hendricks, O. Jannerup, P. Haase, *Linear Systems Control. Deterministic and Stochastic Methods*, Springer, New York, NY, USA, 2008.

[Hin88] S Hinedi, "An extended Kalman filter based automatic frequency control loop", 1988.

[Hod08] M. Stephen Hodgart, Paul D. Blunt, Martin Unwin, "Double estimator — a new receiver principle for tracking BOC signals", *Inside GNSS*, Vol. 3, nº 3, pags. 26–36, 2008.

[How92] S. J. Howard, K. Pahlavan, "Autoregressive Modeling of Wide-Band Indoor Radio Propagation", *IEEE Transactions on Communications*, Vol. 40, nº 9, pags. 1540–1552, Sept 1992.

[Hum10a] T. E. Humphreys, M. L. Psiaki, P. M. Kintner, "Modeling the Effects of Ionospheric Scintillation on GPS Carrier Phase Tracking", *IEEE Transactions on Aerospace and Electronic Systems*, Vol. 46, nº 4, pags. 1624–1637, Oct 2010.

[Hum10b] T. E. Humphreys, M. L. Psiaki, B. M. Ledvina, A. P. Cerruti, P. M. Kintner, "Data-Driven Testbed for Evaluating GPS Carrier Tracking Loops in Ionospheric Scintillation", *IEEE Transactions on Aerospace and Electronic Systems*, Vol. 46, nº 4, pags. 1609–1623, Oct 2010.

[Jaz70] A. H. Jazwinski, *Stochastic Process and Filtering Theory*, Academic Press, 1970.

[Jia13] Y. Jiao, Y. T. Morton, S. Taylor, W. Pelgrum, "Characterization of high-latitude ionospheric scintillation of GPS signals", *Radio Science*, Vol. 48, nº 6, pags. 698–708, Nov 2013.

[Jia15] Y. Jiao, Y. T. Morton, "Comparison of the effect of high-latitude and equatorial ionospheric scintillation on GPS signals during the maximum of solar cycle 24", *Radio Science*, Vol. 50, nº 9, pags. 886–903, Sep. 2015.

[Jin15] B. Jin, B. Jiu, T. Su, H. Liu, G. Liu, "Switched Kalman Filter-Interacting Multiple Model Algorithm Based on Optimal Autoregressive Model for Manoeuvring Target Tracking", *IET Radar, Sonar and Navigation*, Vol. 9, nº 2, pags. 199–209, 2015.

[Jwo01] D. J. Jwo, "Optimisation and Sensitivity Analysis of GPS Receiver Tracking Loops in Dynamic Environments", *IEE Proceedings - Radar, Sonar and Navigation*, Vol. 148, nº 4, pags. 241–250, Aug 2001.

[Kal60] R. E. Kalman, "A New Approach to Linear Filtering and Prediction Problems", *Journal of Basic Engineering*, Vol. 82, nº 1, pags. 35–45, 1960.

[Kap05] E. Kaplan, C. Hegarty, *Understanding GPS: Principles and Applications*, Artech House, 2005.

[Kar07] John Karl, *Celestial Navigation in the GPS Age*, Paradise Cay Publications, 2007.

[Kay88] S. M. Kay, *Modern Spectral Estimation*, Pearson Education, 1988.

[Kay93] Steven M. Kay, *Fundamentals of Statistical Signal Processing. Volume I: Estimation Theory*, Prentice-Hall, Upper Saddle River, NJ, USA, 1993.

[Kin07] P. M. Kintner, B. M. Ledvina, E. R. De Paula, "GPS and Ionospheric Scintillations", *Space Weather*, Vol. 5, nº 9, 2007.

[Kin09] P. M. Kintner, T. E. Humphreys, J. Hinks, "GNSS and Ionospheric Scintillation. How to Survive the Next Solar Maximum", *Inside GNSS*, pags. 22–33, July/August 2009.

[Kom02] C. Komninakis, C. Fragouli, A. H. Sayed, R. D. Wesel, "Multi-Input Multi-Output Fading Channel Tracking and Equalization using Kalman Estimation", *IEEE Trans. Signal Process.*, Vol. 50, nº 5, pags. 1065–1076, May 2002.

[Ló12] J. A. López-Salcedo, J. López-Vicario, G. Seco-Granados, *Sistemas de Radionavegación. El Sistema GPS*, Universitat Oberta de Catalunya (UOC), 2012.

[Lac04] G. Lachapelle, H. Kuusniemi, D. T. H. Dao, G. MacGougan, M. E. Cannon, "HSGPS Signal Analysis and Performance under Various Indoor Conditions", *Navigation: Journal of the Institute of Navigation*, Vol. 51, nº 1, pags. 29–43, 2004.

[Lee17] J. Lee, Y. T. J. Morton, J. Lee, H. Moon, J. Seo, "Monitoring and Mitigation of Ionospheric Anomalies for GNSS-Based Safety Critical Systems: A review of up-to-date signal processing techniques", *IEEE Signal Processing Magazine*, Vol. 34, nº 5, pags. 96–110, Sep. 2017.

[Li11] L. Li, J. Zhong, M. Zhao, "Doppler-Aided GNSS Position Estimation With Weighted Least Squares", *IEEE Transactions on Vehicular Technology*, Vol. 60, nº 8, pags. 3615–3624, Oct 2011.

[Loc17] S. Locubiche-Serra, D. Gómez-Casco, A. Gusi-Amigó, J. A. López-Salcedo, G. Seco-Granados, J. A. García-Molina, "Positioning Performance Analysis of High-Order BOC Signals in Advanced Multi-Constellation High-Sensitivity GNSS Receivers", *Proc. 6th International Colloquium on Scientific and Fundamental Aspects of GNSS / Galileo*, Oct 2017.

[Lop06] G. Lopez-Risueno, G. Seco-Granados, "Method of Processing Positioning Signals, in Particular for Indoor Applications", Mar 03 2006, patent number EP1994423B1, US2010/0061427, PCT/EP2006/002581, WO/2007/098787.

[Luc16a] V. Lucas-Sabola, G. Seco-Granados, J. A. López-Salcedo, J. A. García-Molina, M. Crisci, "Cloud GNSS receivers: New advanced applications made possible", *2016 International Conference on Localization and GNSS (ICL-GNSS)*, pags. 1–6, June 2016.

[Luc16b] Vicente Lucas-Sabola, Gonzalo Seco-Granados, José A López-Salcedo, J García-Molina, M Crisci, "Demonstration of Cloud GNSS Signal Processing", *Proc. ION GNSS*, 2016.

[Mac03] D. J. C. MacKay, *Information Theory, Inference and Learning Algorithms*, Cambridge University Press, 2003.

[Mac12] Christophe Macabiau, Lina Deambrogio, Valentin Barreau, Willy Vigneau, Jean-Jacques Valette, Géraldine Artaud, Paul Thevenon, Lionel Ries, "Kalman filter based robust GNSS signal tracking algorithm in presence of ionospheric scintillations", *ION GNSS 2012, 25th International Technical Meeting of The Satellite Division of the Institute of Navigation*, pag. pp. 3420, 2012.

[Mis06] P. Misra, P. Enge, *Global Positioning System: signals, measurements and performance*, Ganga-Jamuna Press, 2nd ed., 2006.

[Mit13] R. H. Mitch, M. L. Psiaki, D. M. Tong, "Local Ionosphere Model Estimation from Dual-Frequency Global Navigation Satellite System Observables", *Radio science*, Vol. 48, nº 6, pags. 671–684, 2013.

[Mor02] M. Morelli, "Doppler-Rate Estimation for Burst Digital Transmission", *IEEE Transactions on Communications*, Vol. 50, nº 5, pags. 707–710, May 2002.

[Mor03] Y. T. Morton, J. Tsui, D. M. Lin, M. M. Miller, J. Schamus, Q. Zhou, M. P. French, "Assessment and Handling of CA Code Self-Interference during Weak GPS Signal Acquisition", *Proc. ION GPS*, pags. 646–653, 2003.

[Mou05] Alexandre Moudrak, Andriy Konovaltsev, A. Bauch, S. Bedrich, A. Schroth, J. Furthner, J. Hammesfahr, P. Defraigne, "Interoperability on time: Gps-galileo offset will bias position", *GPS world*, Vol. 16, nº 3, pags. 24–32, 2005.

[Mut12] K. Muthuraman, M. Petovello, "What is Coarse Timing Positioning and how does it work?", *Inside GNSS*, pags. 28–31, April 2012.

[O'H11] B. W. O'Hanlon, M. L. Psiaki, S. Powell, J. A. Bhatti, T. E. Humphreys, G. Crowley, G. S. Bust, "CASES: A Smart, Compact GPS Software Receiver for Space Weather Monitoring", *Radionavigation Laboratory Conference Proceedings*, 2011.

[Par96a] B. W. Parkinson, P. Enge, P. Axelrad, J. J. Spilker Jr, *Global positioning system: Theory and applications, Volume I*, American Institute of Aeronautics and Astronautics, 1996.

[Par96b] B. W. Parkinson, P. Enge, P. Axelrad, J. J. Spilker Jr, *Global Positioning System: Theory and Applications, Volume II*, American Institute of Aeronautics and Astronautics, 1996.

[Pat99] A. Patapoutian, "On Phase-Locked Loops and Kalman Filters", *IEEE Transactions on Communications*, Vol. 47, nº 5, pags. 670–672, May 1999.

[Pin13] M. Pini, B. Motella, M. T. Gamba, "Detection of Correlation Distortions through Application of Statistical Methods", *Proceedings of the ION GNSS*, pags. 3279–3289, 2013.

[Pol73] D. Polk, S. Gupta, "Quasi-Optimum Digital Phase-Locked Loops", *IEEE Transactions on Communications*, Vol. 21, nº 1, pags. 75–82, January 1973.

[Pro01] J. Proakis, *Digital Communications*, McGraw-Hill, 4th ed., New York, NY, USA, 2001.

[Psi07] Mark L. Psiaki, T. Humphreys, A. Cerruti, S. Powell, P. Kintner, "Tracking L1 C/A and L2C Signals through Ionospheric Scintillations", *Proc. ION GNSS*, Vol. 20, pags. 246–268, Sep 2007.

[Qia09] Y. Qian, X. Cui, M. Ku, Z. Feng, "Steady-state performance of Kalman filter for DPLL", *Tsinghua Science and Technology*, Vol. 14, nº 4, pags. 470–473, 2009.

[Rap02] T. S. Rappaport, *Wireless Communications: Principles and Practice*, Prentice Hall, 2nd edition, Upper Saddle River, NJ, 2002.

[Reu11] Nico Reussner, Lambert Wanninger, "GLONASS inter-frequency biases and their effects on RTK and PPP carrier-phase ambiguity resolution", Vol. 1, Jan 2011.

[Ris78] J. Rissanen, "Modeling by shortest data description", *Automatica*, Vol. 14, nº 5, pags. 465–471, 1978.

[Ros11] L. Ros, E. P. Simon, "Second-order modeling for Rayleigh flat fading channel estimation with Kalman filter", *Proc. Intl. Conf. on Digital Signal Processing (DSP)*, pags. 1–6, 2011.

[San13] J. Sanz-Subirana, J. M. Juan-Zornoza, M. Hernández-Pajares, *GNSS Data Processing. Volume I: Fundamentals and Algorithms*, ESA Communications, 2013.

[Sch78] G. Schwarz, "Estimating the Dimension of a Model", *The Annals of Statistics*, Vol. 6, nº 2, pags. 461–464, 1978.

[Sec12] G. Seco-Granados, J. López-Salcedo, D. Jiménez-Baños, G. López-Risueño, "Challenges in Indoor Global Navigation Satellite Systems: Unveiling its core features in signal processing", *IEEE Signal Processing Magazine*, Vol. 29, nº 2, pags. 108–131, March 2012.

[Seo09] J. Seo, T. Walter, T. Chiou, P. Enge, "Characteristics of deep GPS signal fading due to ionospheric scintillation for aviation receiver design", *Radio Science*, Vol. 44, nº 01, pags. 1–10, Feb 2009.

[Shu13] H. Shu, E. P. Simon, L. Ros, "Third-Order Kalman Filter: Tuning and Steady-State Performance", *IEEE Signal Process. Lett.*, Vol. 20, nº 11, pags. 1082–1085, Nov 2013.

[Sim06] Dan Simon, *Optimal State Estimation: Kalman, H Infinity, and Nonlinear Approaches*, John Wiley & Sons, New York, NY, USA, 2006.

[Sim11] E. P. Simon, L. Ros, H. Hijazi, J. Fang, D. P. Gaillot, M. Berbineau, "Joint Carrier Frequency Offset and Fast Time-Varying Channel Estimation for MIMO-OFDM Systems", *IEEE Trans. Veh. Technol.*, Vol. 60, nº 3, pags. 955–965, Mar 2011.

[Sko05] S. Skone, G. Lachapelle, D. Yao, W. Yu, R. Watson, "Investigating the impact of ionospheric scintillation using a GPS software receiver", *Proc. ION GNSS*, pags. 1126–1137, 2005.

[Sou98] B. Southall, B. F. Buxton, J. A. Marchant, "Controllability and Observability: Tools for Kalman Filter Design", *BMVC*, pags. 1–10, 1998.

[Sto97] P. Stoica, R. L. Moses, *Introduction to Spectral Analysis*, Vol. 1, Prentice-Hall, Upper Saddle River, NJ, 1997.

[Sto04] P. Stoica, Y. Selen, "Model-Order Selection: A Review of Information Criterion Rules", *IEEE Signal Processing Magazine*, Vol. 21, nº 4, pags. 36–47, July 2004.

[Sto05] P. Stoica, R. L. Moses, "Spectral analysis of signals", 2005.

[Sug78] N. Sugiura, "Further Analysts of the Data by Akaike's Information Criterion and the Finite Corrections", *Communications in Statistics-Theory and Methods*, Vol. 7, nº 1, pags. 13–26, 1978.

[Tah12] M. Tahir, L. L. Presti, M. Fantino, "A novel quasi open loop frequency estimator for GNSS signal tracking", *Proceedings of the 2012 IEEE/ION Position, Location and Navigation Symposium*, pags. 952–960, April 2012.

[Tat13] S. Tatinati, K. C. Veluvolu, S. M. Hong, W. T. Latt, W. T. Ang, "Physiological Tremor Estimation With Autoregressive (AR) Model and Kalman Filter for Robotics Applications", *IEEE Sensors J.*, Vol. 13, nº 12, pags. 4977–4985, Dec 2013.

[Tay13] Sarab Tay, Juliette Marais, "Weighting models for GPS Pseudorange observations for land transportation in urban canyons", *6th European Workshop on GNSS Signals and Signal Processing*, pag. 4, 2013.

[Tic98] P. Tichavský, C. H. Muravchik, A. Nehorai, "Posterior Cramér-Rao Bounds for Discrete-Time Nonlinear Filtering", *IEEE Trans. Signal Process.*, Vol. 46, nº 5, pags. 1386–1396, May 1998.

[Tre68] H. L. V. Trees, *Detection, Estimation and Modulation Theory*, Vol. 1, Wiley, New York, NY, USA, 1968.

[Tre07] Harry L. Van Trees, Kristine L. Bell, *Bayesian Bounds for Parameter Estimation and Nonlinear Filtering/Tracking*, Wiley, New York, NY, USA, 2007.

[USG19] USGov, "GPS Space Segment", `https://www.gps.gov/systems/gps/space/`, 2019, accessed 01 Feb 2019.

[Van93] A. J. Van Dierendonck, J. Klobuchar, Q. Hua, "Ionospheric Scintillation Monitoring using Commercial Single Frequency C/A Code Receivers", *Proceedings of ION GPS*, Vol. 93, pags. 1333–1342, 1993.

[Van96] A. J. Van Dierendonck, "GPS Receivers", *Global Positioning System: Theory and Applications*, Vol. 1, pags. 329–407, 1996.

[Van01] A. J. Van Dierendonck, Q. Hua, "Measuring Ionospheric Scintillation Effects from GPS Signals", *Proceedings of the 57th Annual Meeting of The Institute of Navigation*, pags. 391–396, June 2001.

[Van02] F. Van Diggelen, "Indoor GPS theory and implementation", *2002 IEEE Position Location and Navigation Symposium*, pags. 240–247, April 2002.

[Van07] I. Vanschoenbeek, B. Bonhoure, M. Boschetti, J. Legenne, "GNSS Time Offset: Effects on GPS-Galileo Interoperability Performance", *Inside GNSS*, pags. 60–70, October 2007.

[Van09] Frank Stephen Tromp Van Diggelen, *A-GPS: Assisted GPS, GNSS, and SBAS*, Artech House, 2009.

[Vau70] D. Vaughan, "A nonrecursive algebraic solution for the discrete Riccati equation", *IEEE Trans. Autom. Control*, Vol. 15, nº 5, pags. 597–599, Oct 1970.

[Vil13] J. Vila-Valls, J. A. Lopez-Salcedo, G. Seco-Granados, "An Interactive Multiple Model Approach for Robust GNSS Carrier Phase Tracking under Scintillation Conditions", *2013 IEEE International Conference on Acoustics, Speech and Signal Processing*, pags. 6392–6396, May 2013.

[Wan11] Lambert Wanninger, "Carrier-phase inter-frequency biases of GLONASS receivers", *Journal of Geodesy*, Vol. 86, pags. 1–10, Feb 2011.

[Wez14] Kinga Wezka, "The Reliability Evaluation of GNSS Observations in the Presence of Ionospheric Perturbations", *Mitigation of Ionospheric Threats to GNSS: an Appraisal of the Scientific and Technological Outputs of the TRANSMIT Project*, InTech, 2014.

[Zha08a] Y. Zhang, M. G. Amin, F. Ahmad, "Application of time-frequency analysis and Kalman filter to range estimation of targets in enclosed structures", *2008 IEEE Radar Conference*, pags. 1–4, May 2008.

[Zha08b] Z. G. Zhang, S. C. Chan, K. M. Tsui, "A Recursive Frequency Estimator Using Linear Prediction and a Kalman-Filter-Based Iterative Algorithm", *IEEE Transactions on Circuits and Systems II: Express Briefs*, Vol. 55, nº 6, pags. 576–580, June 2008.

[Zou13] A. Zoubir, M. Viberg, R. Chellappa, S. Theodoridis, "Academic Press Library in Signal Processing Volume 3: Array and Statistical Signal Processing", 2013.